Reticulon Homology Domain Containing Protein Families of the Endoplasmic Reticulum

Darshan Kumar

Institute of Biotechnology

Doctoral Programme in Integrative Life Science,

Doctoral School in Health Sciences

Molecular and Integrative Biosciences Research Program,

Faculty of Biological and Environmental Sciences

University of Helsinki

ACADEMIC DISSERTATION

To be presented with the permission of the Faculty of Biological and Environmental Sciences of the University of Helsinki for public examination in the auditorium 2041at Biocenter 2 (Viikinkaari 5), on 14th June 2019 at 12 noon.

HELSINKI 2019

Supervisor

Eija Jokitalo, Researcher Director
Institute of Biotechnology
University of Helsinki, Helsinki, Finland

Thesis Advisory committee

Marjomäki Varpu, Adjunct Professor
Department of Biological & Environmental Science
Nanoscience center
University of Jyväskylä, Jyväskylä, Finland

Tero Ahola, Adjunct Professor
Department of Microbiology
Faculty of Agriculture and Forestry
University of Helsinki, Helsinki, Finland

Reviewers

Aki Manninen, Adjunct Professor
Oulu Center for Cell-Matrix Research, Biocenter Oulu
Faculty of Biochemistry & Molecular Medicine
University of Oulu, Oulu, Finland

Mikko Hiltunen, Professor of Tissue & Cell Biology
Institute of Biomedicine
University of Eastern Finland, Kuopio, Finland

Opponent

Jussi Jäntti, Adjunct Professor
VTT Technical Research Centre of Finland
Espoo, Finland

Custodian

Kari Keinänen, Professor, Receptor Biochemistry,
Molecular and Integrative Biosciences Research Programme
University of Helsinki, Helsinki, Finland

ISBN 978-951-51-5266-4 (Paperback)
ISBN 978-951-51-5267-1 (ethesis, PDF)
ISSN 2342-3161 (Print)
ISSN 2342-317X (Online)

Press: Painosalama, Turku 2019

Cover figure: Model generated from serial block-face scanning electron microscopy showing branched tubular endoplasmic reticulum (yellow) in close contact with metaphase chromatin (blue) in REEP3/4 knockdown HeLa cell.

REsearched enthusiastically in this search

'Let action itself be the motive, not the result'

Adapted from the Hindu Scripture - *Shrimad Bhagavad Geeta*

TABLE OF CONTENTS

ABBREVIATIONS

aa	Amino acid
AD	Alzheimer's disease
ALS	Amyotrophic lateral sclerosis
BAR	BIN/Amphiphysin/Rvs
ER	Endoplasmic reticulum
EM	Electron microscopy
ERMES	ER-mitochondria encounter structures
ET	Electron tomography
FAM134C	Family with sequence similarity 134, member C
HSP	Hereditary spastic paraplegia
Immuno-EM	Immuno electron microscopy
INM	Inner nuclear membrane
LBR	Lamin B receptor
LC3	Microtubule-associated protein 1A/1B-light chain 3
LM	Light microscopy
Lnp1	Lunapark
LMN	Lamin
MIB	Microscopy image browser
MS	Multiple sclerosis
NE	Nuclear envelope
NEBD	Nuclear envelope breakdown
NPC	Nuclear pore complexes
ONM	Outer nuclear membrane
PM	Plasma membrane
REEP	Receptor expression enhancing protein
RHD	Reticulon homology domain
RTN	Reticulon family of proteins
SB-EM	Serial block-face scanning electron microscopy
SCG Neurons	Superior cervical ganglia neurons

LIST OF ORIGINAL PUBLICATIONS

This thesis is based on the following articles, which are referred in the text by their Roman numerals.

I Olli Rämö*, Darshan Kumar*, Erika Gucciardo, Merja Joensuu, Maiju Saarekas, Helena Vihinen, Ilya Belevich, Olli-Pekka Smolander, Kui Qian, Petri Auvinen, Eija Jokitalo. 2016. NOGO-A/RTN4A and NOGO-B/ RTN4B are Simultaneously Expressed in Epithelial, Fibroblast and Neuronal Cells and Maintain ER Morphology. *Sci Rep* **6**:35969. https://doi.org/10.1038/srep35969.

II Darshan Kumar*, Banafsheh Golchoubian*, Ilya Belevich, Eija Jokitalo#, Anne-Lore Schlaitz#. REEP3 and REEP4 Determine the Tubular Morphology of the Endoplasmic Reticulum during Mitosis. Accepted 10 April 2019, MBoC, https://doi.org/10.1091/mbc.E18-11-0698.

III Darshan Kumar, Behnam Lak, Taina Suntio, Ilya Belevich, Aki Vartiainen, Tiina Viita, Liu Xiaonan, Maria Vartiainen, Markku Varjosalo, Eija Jokitalo. FAM134C Promotes ER Membrane Curvature and is Elevated upon Starvation in Mammalian Cells (Manuscript).

IV Ilya Belevich, Merja Joensuu, Darshan Kumar, Helena Vihinen, Eija Jokitalo. 2016. Microscopy Image Browser: A Platform for Segmentation and Analysis of Multidimensional Datasets. *PLoS Biol.*, **14**: e1002340.

*These authors contributed equally to this work

Corresponding Authors

Some unpublished data are also included.

SUMMARY

The endoplasmic reticulum (ER) is the largest membrane bound organelle in a cell and has multiple responsibilities. Execution of the various duties performed by the ER requires it to be shaped in a rather complex and intricate manner. ER's two major structural motives, namely sheets and tubules, play very complex yet not fully understood role in giving ER its overall structure and function. The ratio of sheet and tubule conformations differ significantly within cell types and during cell cycle. Such a balance is possible only with a well-functioning set of factors that constantly communicate with each other throughout a cell cycle. These factors are specifically responsible for either shaping the ER sheets or tubules in addition to factors that keep the dynamic nature of the ER sound. During mitosis, ER undergoes a major transformation in its structure, where the sheet-tubule ratio shifts more towards tubules. Specific factors keep this process sound by acting actively during the stage of mitosis for proper cell division to occur. Although research on such factors are still on-going, many in-depth details on such factors (e.g. their precise localization) and their mechanism of action plus novel factors for ER shaping still needs to be resolved using techniques involving high end light and electron microscopy. In addition, a constant battle in data analysis for answering key questions also persists. Development of tools to study and analyse data on the lines of image analysis and processing is an unmet need that needs simultaneous attention. The research in this thesis focuses on three family of proteins that we uncover as responsible candidates in shaping the ER. To aid the study, this thesis also discusses the development of a software platform for analysis of microscopic data generated during this study.

In this research, Reticulon family of proteins (RTN) were characterised using high-end microscopic techniques. We showed RTN4A and RTN4B to localize to ER tubules and sheet edges using pre-embedding immuno electron microscopy (immuno-EM) and electron tomography. Using qPCR, RTN4A and RTN4B were observed to be the most expressed isoforms in neurons and epithelial cells respectively. FAM134C, a poorly characterised protein was identified as one of the RTN4B interacting proteins. FAM134C localised to the ER where it specifically resided at high curvature ER (sheet edges and tubules) similar to RTN4B. FAM134C, similar to the RTN4B also had the capability to promote ER tubules upon overexpression. In addition, another family of proteins belonging to receptor expression enhancing protein (REEP), namely REEP3 and REEP4 were studied for shaping ER during mitotic stage of cell cycle. REEP3 and REEP4 collectively were observed both in tubulating peripheral ER during mitosis and clearing tubular ER from the chromatin for a normal mitosis to take place.

Collectively, this work elaborates on proteins belonging to three classes that shape and position the ER specifically either in interphase or during stages of cell division. Our findings also throws light on the role of different domains in each of these proteins such as the reticulon homology domain (RHD) that was observed to be present in all these proteins under study. The RHD previously known for inserting partially and unsymmetrically in the outer leaflet of the ER gives a strong indication for proteins like RTN4B and FAM134C to localize to ER thus tubulating ER upon overexpression conditions. We uncovered the RHD's crucial role in ER shaping and positioning in REEP3/4 during mitosis. These results showed how various proteins govern the shape of the ER using unique shaping domains like the RHD. In addition, to support this study we developed a set of tools incorporated in a software platform needed for making measurements via automatic and semi-automatic segmentation of images. As the needs in image analysis are dynamic, our tool undergoes constant updating for coping up with new challenges in answering key biological questions.

1 INTRODUCTION

Eukaryotic cells are comprised of organelles, which occur in distinctive shapes and sizes and are bound by membranes (**Figure 1**). These membranes segregate one organelle from the other, physically and functionally. Every organelle is responsible for one or multiple tasks. Collectively, a sound functioning set of organelles not only keeps a cell alive, but also allows that cell to perform its destined function on an organismic level.

1.1 Endoplasmic reticulum, the mother of the cell

The ER is the largest membrane bound organelle in a eukaryotic cell and occupies as

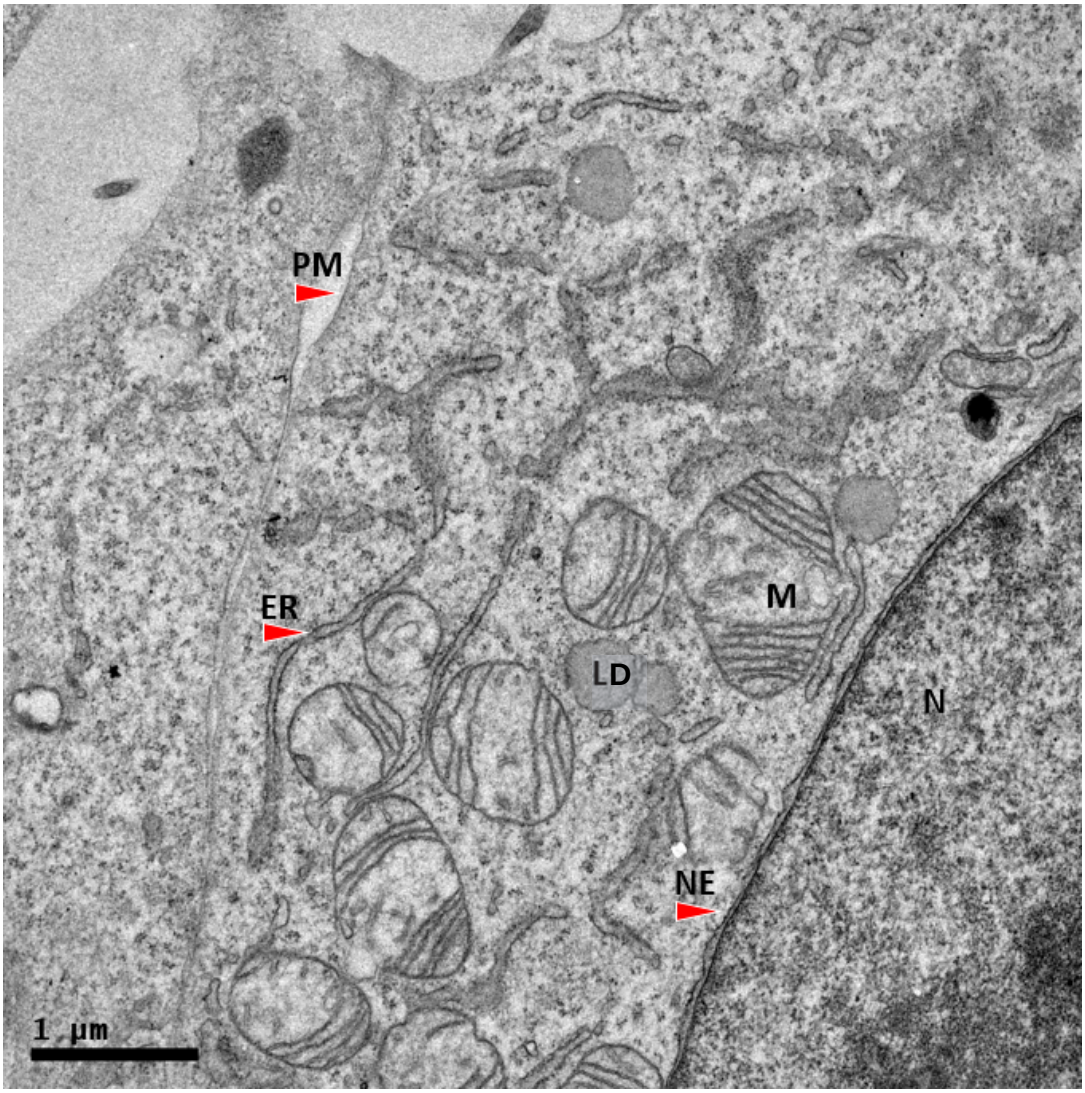

Figure 1. A peek to a human cell. TEM micrograph of a Huh-7 cell showing various membrane bound organelles. Red arrows pointing out some of the organelles denoted as follows; ER (endoplasmic reticulum), LD (lipid droplet), M (mitochondria), NE (nuclear envelope), N (nucleus) and PM (plasma membrane).

much as 60% of the cell volume, varying however from one cell type to the other. Currently, over 400 proteins have been experimentally shown to localize to the ER, which amounts to around 2% of all human proteins (The Human Protein Atlas (proteinatlas.org).

The endoplasmic reticulum (ER) plays a great role in multiple major cellular functions ranging from the synthesis of proteins and lipids, to glycogen and steroids like cholesterol. In case of secreted proteins, ER plays a significant role. The protein synthesis processes in this case involves many resources within a cell where ER acts as an anchor point for the ribosomes allowing translation to take place in a process called co-translational translocation. The ER also acts as a reservoir for these synthesised proteins that it eventually transports via the ER-Golgi intermediate compartments (ERGIC) to the Golgi complex.

At the membrane and within the lumen of the ER, dedicated proteins called chaperons assist newly synthesised proteins in folding and assembly, ultimately leading to a properly folded protein that is fit for the secretory pathway. Misfolded proteins which get retained within the ER are delivered to the proteasomal degradation machinery, a process known as ER-associated degradation (ERAD) (Travers et al., 2000). ER functions can get disrupted by ER stress caused by multiple conditions ranging from hypoxia to glucose deprivation. Such a stress leads to accumulation of unfolded proteins to which the cells adapt by the activation of an integrated signal transduction pathway known as the unfolded protein response (Walter and Ron, 2011).

Ca^{2+} have a variety of functions in context of ER. For a proper protein folding, Ca^{2+} levels are regulated by channels maintained by the ER. In context of muscle cells, the sarcoplasmic reticulum's (ER of muscle cells) release of Ca^{2+} brings about muscular contraction (Block et al., 1988; Takeshima et al., 2000). Detoxification of lipid soluble drugs and various harmful compounds, which are metabolically produced within the cell is another crucial function performed by the ER.

The membranes of the ER are known to give rise to autophagy related compartments which degrade various cellular contents thus recycling resources for the cell. Just like other organelles, the ER also gets recycled via autophagy pathway in a selective manner also known as ER-phagy. ER-phagy is brought about by receptors that reside on the ER's membrane that channel ER and its contents for degradation and recycling (Khaminets et al., 2015). With such an extent of presence throughout the cell and an extensive functional portfolio, the ER forms a vital part of a eukaryotic cell nurturing it during its lifespan.

1.1.1 General ER structure and lipid composition

ER membrane bilayer is an intricate assembly of phospholipids with their polar head groups facing the cytoplasm or the ER lumen, while the hydrophobic tails of both lipid layers face each other. ER sheets are studded with ribosomes (rough ER) while ribosome free ER is mostly tubular (smooth ER). ER includes the nuclear envelope (NE) in addition to peripheral ER. The NE is comprised of the inner and outer nuclear membrane, and shares a common lumen with the peripheral ER. The complexity of the ER structure can be revealed using a combination of LM (light microscopy) and EM (electron microscopy) methods. Such methods revealed ER to have a series of conformations, where these structures have been mainly dissected into ER sheets and ER tubules (**Figure 2**) (adapted from (Puhka et al., 2007)). Previously, ER was categorised primarily into rough and smooth forms, which was based on the

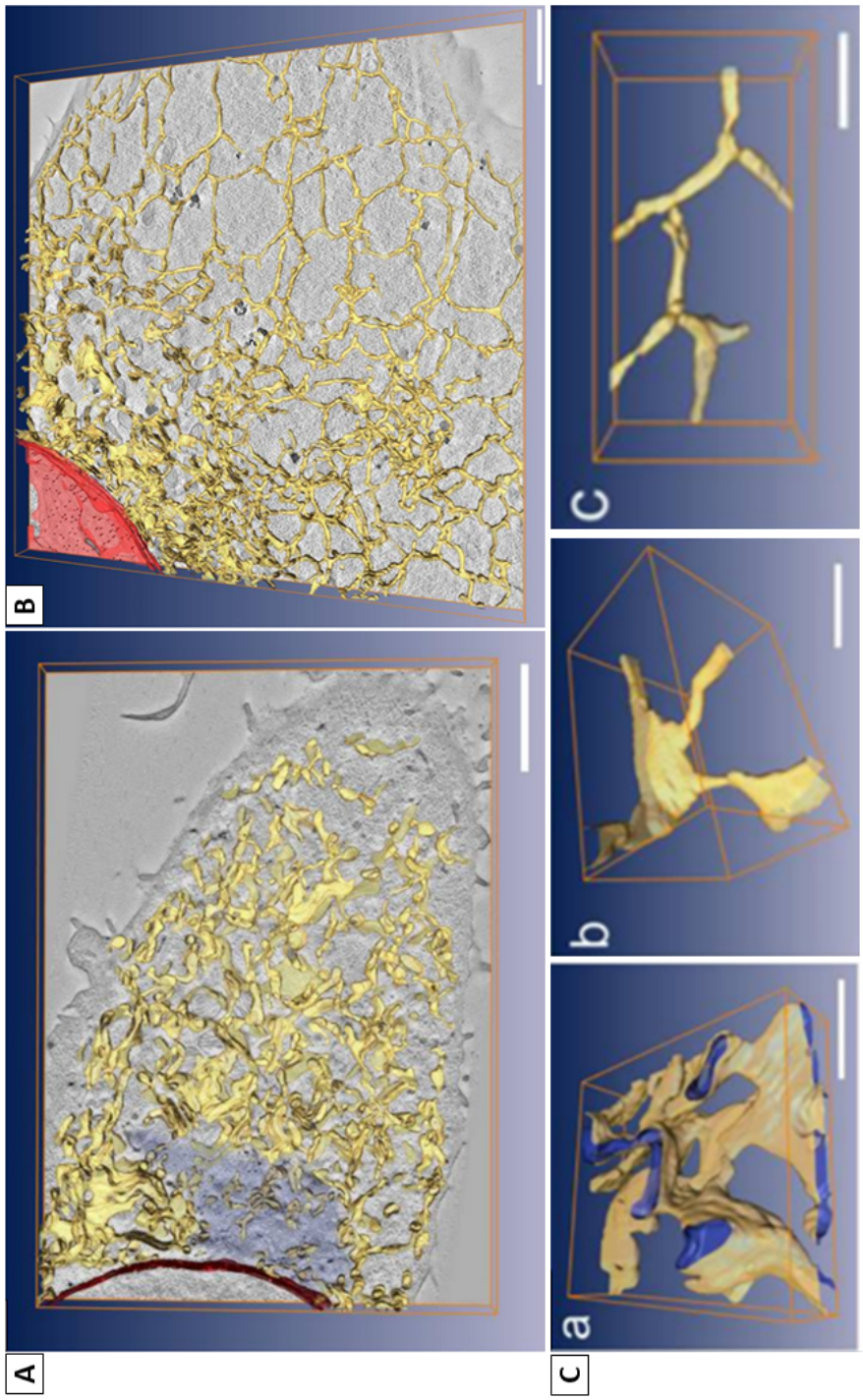

Figure 2. 3D-EM models of the ER. Images showing models of ER (yellow) and nucleus (red) generated from serial section tomography of CHO-K1 cells growing on a flat substratum. Images showing ER at the area in the middle of the cell parallel to the substratum (A) and area close to the bottom of the cell (B). Golgi area in A is highlighted with darker grey colour. ER sheets are found more in the central part of the cell and long interconnected ER tubules at the cell periphery. (C) Models showing different branch points between two sheets (a), a tubule and a sheet (b) or between two tubules (c). Bars, 500nm. (adapted from Puhka et al., 2007).

ribosomal density. Current classification is ER structure dependent denoting ER either in sheet or tubular forms. ER sheets are flat membranes covered with ribosomes at varied densities and tubules with long and highly curved structures often observed branched.

Although the peripheral ER sheets may vary in size, the spacing of the lumen is relatively consistent (around 50 nm and 30 nm in mammalian and yeast cells, respectively) (Bernales et al., 2006). While the sheets and tubules possess vastly different structural features, the luminal thickness for both are similar. Though the ratio of tubules to sheets varies in different cell types (Puhka et al., 2012) depending on cell function, interestingly, both ER tubules and sheets are found in all eukaryotic cells (Staehelin, 1997). Depending on the cell type, sheets can be observed in a stacked conformation (Terasaki et al., 2013). Sheets may be connected to other big or small sheets and tubules, while tubules can be connected to sheets or other tubules forming a branched but continuous network.

There are many kinds and types of phospholipids that make up biological membranes in the cell. The ER is mostly comprised of phosphatidylcholine and phosphatidylethanolamine, while other lipids like cholesterols are found in minor amounts. The absence of such compact lipids like cholesterol makes ER a very fluid structure as compared to the plasma membrane (PM), which is relatively more rigid. This property of flexibility gives ER the possibility to attain intricate shapes.

The ER shape is maintained by a large set of factors ranging from integral membrane proteins to interactions with the cytoskeleton and other organelles. Such interactions are highly dynamic in nature (Lee and Chen, 1988). The nature of such dynamic events of the ER modulate itself differently from events like protein interactions, intracellular signals, cell cycle, cell differentiation or developmental stages. Recent and past research has thrown light on the factors that control the basic shape of ER sheets and tubules. Although it is still unclear how the changes in ER sheet-tubule ratio may occur, it remains to be seen how many more such factors exist out there, which may be complementing the known factors in giving ER its correct conformations thus maintaining its full functionality. With current innovative microscopy, ER characterization has reached a very high level of precision, but designation of which cellular pathways play what role in ER shape determination still needs clarification.

1.1.2 ER tubules

The tubular ER has an average diameter ranging from 60 to 100 nm. The ER tubules are very highly curved structures as compared to the sheets. Tubular structures are maintained by multiple factors. Many protein factors responsible for shaping the ER have been reported previously. Many of these factors shape either the tubular ER or the edges of ER sheets. One of the most commonly referred domains common in most of the proteins shaping the ER, is the reticulon homology domain (RHD). The RHDs shape the membrane by forming a transmembrane hairpin topology thereby acting like a wedge. This wedge displaces the lipids on the outer leaflet of the bilayer thus bending or curving the membranes (**Figure 3**) (Shibata et al., 2010; Voeltz et al., 2006). Because of this property, the RHD containing proteins localize to both ER tubules and sheet edges (Voeltz et al., 2006).

Upon overexpression, some RHD containing proteins give rise to long and unbranched ER tubules while depletion causes reduction in ER tubules, thus, giving rise to more peripheral ER sheets (Voeltz et al., 2006). The RHD is comprised of two hydrophobic stretches of amino acids separated by a cytoplasmic loop. The exact sequence of the RHD may differ from one protein to other or from one isoform to other. The RHD's two transmembrane domains are not long enough to span the entire phospholipid bilayer and reappear back to the cytoplasmic side of the ER. This hence causes the partial insertion in the

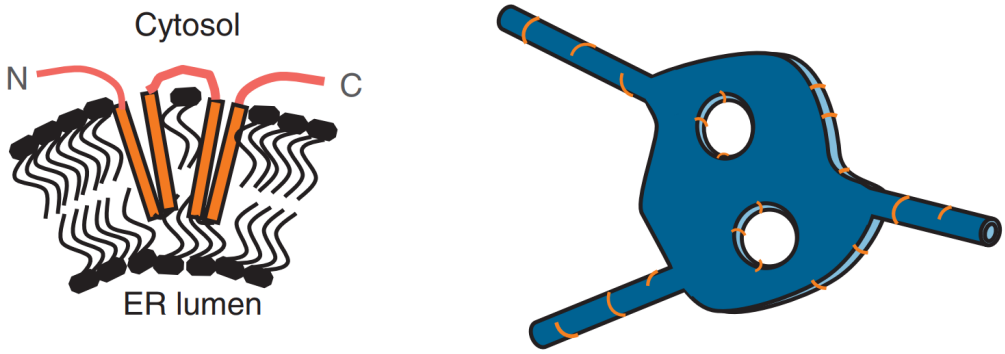

Figure 3. Models showing how RHD of RTNs shape high curvature ER. (Left) A Schematic of RTN topology on the ER membrane. The two hydrophobic segments of the RHD form hairpin loops that insert unsymmetrically on the outer leaflet of the ER membrane thus generating curvature of the membrane. (Right) A model of ER showing tubules, sheets and fenestrations with indication of RTN proteins (orange) observed on the tubules, sheet edges and fenestrations (adapted from Voeltz et al., 2006; Shibata et al., 2010).

membrane thus causing the membranes to curve. For some proteins, the RHD domains are relatively similar in their amino acid (aa) sequences, while in others the RHD may differ greatly from one isoform to other. This difference not only is seen in the aa sequences but also in the length of the transmembrane segments. Such an observation clearly points out to distinct functions pertaining to individual proteins belonging to the same family.

Besides the shaping of ER tubules, the formation of a tubular network also needs to be maintained. Such a network denoted often by three-way junctions (**Figure 4**) are maintained by homotypic fusion events. These junctions of the ER are comprised mostly of three tubules where tubule branching and fusion gives rise to polygons in the network (Lee and Chen, 1988). Such events are mediated by a set of proteins belonging to a member of dynamin-like GTPase family called atlastins. Lack of atlastins leads to a reduction of fusion events causing an abundance of long and unbranched tubules (Hu et al., 2009). Upon depletion of atlastins in *Drosophila*, ER was observed to be fragmented, while purified atlastins were shown to be sufficient for catalysing GTP-dependent fusion of proteoliposomes (Bian et al., 2011; Byrnes and Sondermann, 2011; Orso et al., 2009).

ER tubules continually undergo fusing and branching events (Lee and Chen, 1988). Such events may bring about the creation of new three-way junctions. Events like junction sliding or tubule ring closure leads to a loss of three-way junctions causing the formation of polygonal structure (Friedman et al., 2010). Although less is known about mechanisms keeping these processes in place, findings on lunapark (Lnp1) protein throws some light. Lnp1 has been shown to localize to and stabilize three-way junctions (Chen et al., 2015; Chen et al., 2012). Lnp1 was shown to bind to RHD containing proteins and Yop1, while yeast homolog of atlastin, Sey1, was implicated in regulating Lnp1s localization to junctions (Chen et al., 2012). An exact mechanism for Lnp1's role in junction stabilization still remains to be elucidated, but some findings stated below give possible explanations. Lnp1 has two transmembrane domains in addition to a zinc finger domain located on the cytoplasmic side of the ER (Chen et al., 2015). Upon cysteine mutations at the zinc finger domain, polygons were observed to be smaller (Chen et al., 2012). It could thus be stated that the mutations in the

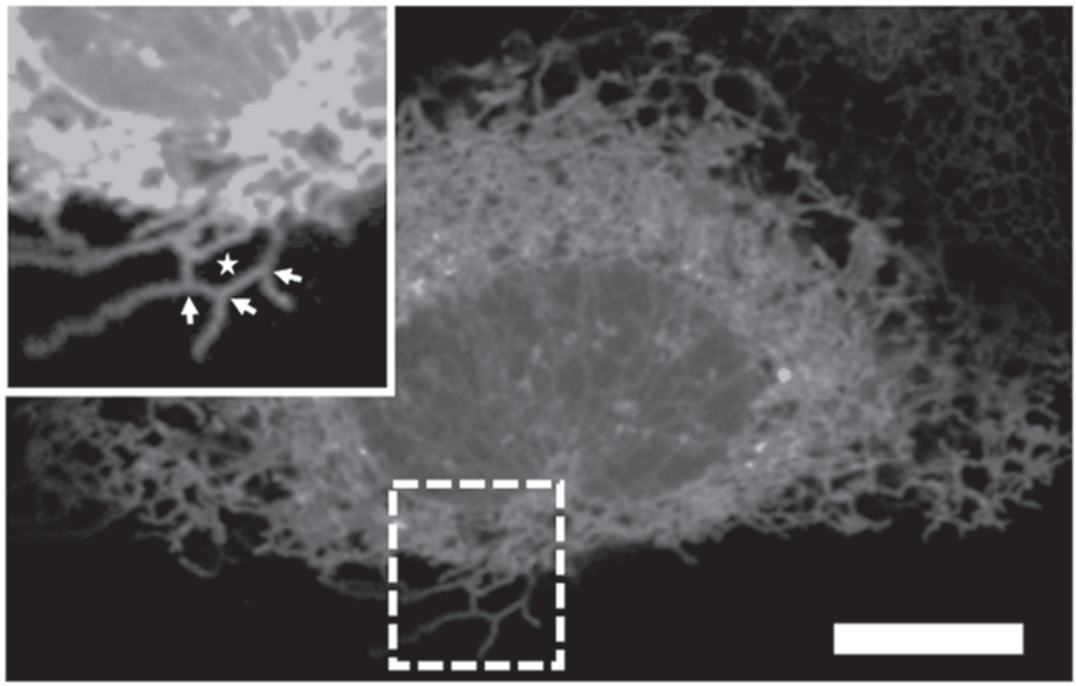

Figure 4. Thee-way junctions and polygons of the ER network. U2-OS cells (human bone osteosarcoma) expressing ER marker RAMP4-GFP. Inset showing zoomed area of ER within the white dashed box. Arrows pointing to three-way junctions and star points to a polygon. Scale bar 10 μm.

zinc finger domain may affect the protein-protein interactions, interfere with lipid distribution on cytoplasmic ER surface or complex formation causing abnormal effects in junction stabilization. Another explanation could be that the transmembrane domains of Lnp1 maybe be curving the membrane using an inverted wedge thus causing a local negative curvature which is characteristic for three-way junctions (Chen et al., 2015).

1.1.3 ER Sheets

The ER sheet's flat cisternal arrangement has evolved most probably because of one of its main function of storing biological components like proteins and calcium within its lumen, thus acting as a reservoir for the cell providing an optimized surface area to volume ratio as compared to tubules. Several sheet shaping factors and their mechanisms have been revealed. One such proposal was for integral membrane proteins to span the intraluminal space of the sheets forming bridges and connecting the lipid bilayers (Senda and Yoshinaga-Hirabayashi, 1998; Shibata et al., 2009; Shibata et al., 2010). Such proteins may either individually or in a complex, form a scaffold, thereby aiding the stabilization of sheets and/or by bringing the two lipid layers in a definite proximity to each other thus defining the sheet thickness or luminal width (Shibata et al., 2009). Proteins like kinectin (microtubule associated protein), p180 and Climp63 have been reported to maintain the ER sheet structure in the above mentioned mechanisms (Shibata et al., 2010). Climp63, a highly abundant protein (Beck et al., 2011; Foster et al., 2006; Nagaraj et al., 2011) localizes to the perinuclear ER while remaining absent from the NE (Klopfenstein et al., 1998; Klopfenstein et al., 2001). Overexpression of Climp63 leads to a significant increase in ER sheets, while

knockdown did not decrease sheet area, but led to a reduction in ER sheet's luminal width/spacing (Shibata et al., 2010).

Depending on the cell type, sheets may have holes, referred to as fenestrations or nanoholes (Puhka et al., 2012; Puhka et al., 2007). The composition and/or the full function of fenestrations is still largely unknown, but they have been shown to let cytoskeletal components pass through to various parts of the cell. These nanoholes have been shown to be dynamic in nature (Schroeder et al., 2019).

Polyribosomes were shown to stabilize ER sheets, where higher ribosomal density was connected to more abundant and larger sheets (Puhka et al., 2007). This work also demonstrated that upon stripping of ribosomes from ER using puromycin (protein translation inhibitor), the ER sheet tubule ratio shifted more towards tubules. In contrary, treatment of cells with cyclohexamide, which blocks translation and stabilizes ribosome-ER binding, did not yield the same effect (Puhka et al., 2007). Overexpression of p180 protein (known to bind ribosomes) was shown to have increased stacked rough ER sheets and an increase in the secretion capacity of the cell (Benyamini et al., 2009). This work also showed that under p180 depletion condition, the cell had not only less ribosomal density on ER but also lowered ER sheet conformations in general, with a reduced secretion capacity.

The ratio of sheet to tubule is cell type dependent. The function of the cell could be directly related to the shape of ER, thus, directly relating to sheet-tubule ratio. For example, B cells, which have a high secretion capacity, not only have large arrays of ER sheets but also high levels of polyribosomes-bound translocation complexes in addition to lower levels of tubule stabilizing proteins as compared to epithelial cells. Such a structure/function balance can also be seen in neurons where the cell body consists mostly of ER sheets that may be stacked, while the neuronal outgrowths (axons and dendrites) are specifically positive for tubular ER (Terasaki, 2018; Wu et al., 2017)(I). With the fast-paced improvements in LM imaging, the ER structures are being further elucidated to a higher resolution. High resolution stimulated emission depletion microscopy (STED) and 4Pi single-molecule switching nanoscopy (4Pi-SMSN) showed ER sheet to be narrower than ER tubules (Schroeder et al., 2019). Similar advancements at LM using lattice light sheet microscopy have also given rise to claims that sheet structures could indeed be clusters of heavily tubulated ER, which were unresolved with conventional confocal microscopy (Nixon-Abell et al., 2016).

1.1.4 ER contacts other organelles

The ER is very dynamic in nature and it reaches out to far edges of the cell. This constantly moving organelle is capable of making contacts with many organelles at the same time. Such contacts may often look random, but a range of studies on this topic has shown the need and the specificity for the ER to span the whole cell. This could be the primary reason by which the ER continually communicates with various parts of the cell. ER has been reported to be closely apposed to organelles such as PM, lipid droplets, endosomes, mitochondria, peroxisomes and Golgi (Friedman and Voeltz, 2011; Toulmay and Prinz, 2011).

ER-PM contacts have been reported to be the sites of non-vesicular transfer of sterols in addition to phosphatidylinositol metabolism and Ca^{2+} level regulation (Baumann et al., 2005; Carrasco and Meyer, 2011; Li and Prinz, 2004; Stefan et al., 2011). Using EM techniques, it was revealed that 20-45% of budding yeast PM's cytoplasmic surface was in tethering distance with the ER (West et al., 2011).

Morphologically, ER-mitochondrial contacts have been very highly conserved feature for eukaryotic cells. These sites have been associated with many crucial functions ranging from Ca^{2+} signalling and lipid biosynthesis to mitochondrial division (Boldogh and Pon, 2007; Friedman et al., 2011; Rizzuto et al., 1998; Vance, 1990). Two apposing membranes in this case may come to 30 nm distance of each other, as seen by ET (electron tomography) (Csordas et al., 2006; West et al., 2011); while in some cases an electron dense structure can be seen resembling protein tethers at the ER-mitochondrial contacts (Csordas et al., 2006; Hayashi et al., 2009). These contacts can also be observed using LM where the time-lapsed imaging has revealed the contacts to be secured while moving along the cytoskeleton (Friedman et al., 2010). The contact sites between ER and mitochondria have also been previously described for being responsible for lipid flipping between the apposed membranes during lipid biosynthesis (Achleitner et al., 1999; Kornmann et al., 2009; Vance, 1990; Voelker, 2000). The biosynthesis of phosphatidylcholine requires the proper functioning of proteins residing at ER and mitochondria. For this process, first, the phosphatidylserine gets synthesised from phosphatidylalanine on the ER membrane, phosphatidylethanolamine is thereby synthesised by phosphatidylserine on the mitochondria, while the phosphatidy-lethanolamine conversion to phosphatidy-lcholine occurs via enzymes localized at the ER (Osman et al., 2011; van Meer et al., 2008). Thus, during the whole process of phospholipid synthesis a shuttling of lipids occurs between the opposing membranes of the two organelles. Many enzymes that are known to be involved in lipid biosynthesis are enriched at the mitochondrial associated membranes also known as MAMs (Stone and Vance, 2000; Vance, 1990), a physical association between the ER and mitochondria.

One interesting finding concerning ER-mitochondrial contact was the observation of ER tubules, which marked the sites of mitochondrial division both in yeast and in mammalian cells (Friedman et al., 2011). These observations were made using ET in combination with confocal live cell imaging. The ER tubules were found wrapping around the mitochondria prior to mitochondria's division. In these points of contacts, the mitochondria were in a constricted conformation. Such observations point to explanations, where either the ER itself takes part in the constriction leading to mitochondrial division or it acts as a scaffold thereby allowing the recruitment of factors that bring about mitochondrial division. As there are multiple functions/activities occurring at the mitochondrial-ER contact sites, it is possible to expect multiple tethers controlling the respective functions. One such tether is the ER-mitochondria encounter structures (ERMES) which was identified as a tether between the two organelles in yeast. The components of ERMES complex comprise of membrane proteins, which localize both to the ER (Mmm1), and mitochondrial membrane (Mdm10 and Mdm34) (Kornmann et al., 2009). Using EM, the ER was shown to also form contacts with endosomes in mammalian cells and with vacuoles in yeast (Eden et al., 2010; Rocha et al., 2009; West et al., 2011). The role of such a contact has been proposed for a direct cholesterol transfer between the ER and the late endosomes (Rocha et al., 2009). In addition, tubules were also shown to be linked to early and late endosome constriction and fission process, thus defining the timing and positioning of endosome fission (Rowland et al., 2014).

1.1.5 Nuclear envelope

Although the ER is continuous with the NE's outer membrane the architecture of the NE differs greatly from the peripheral ER. The

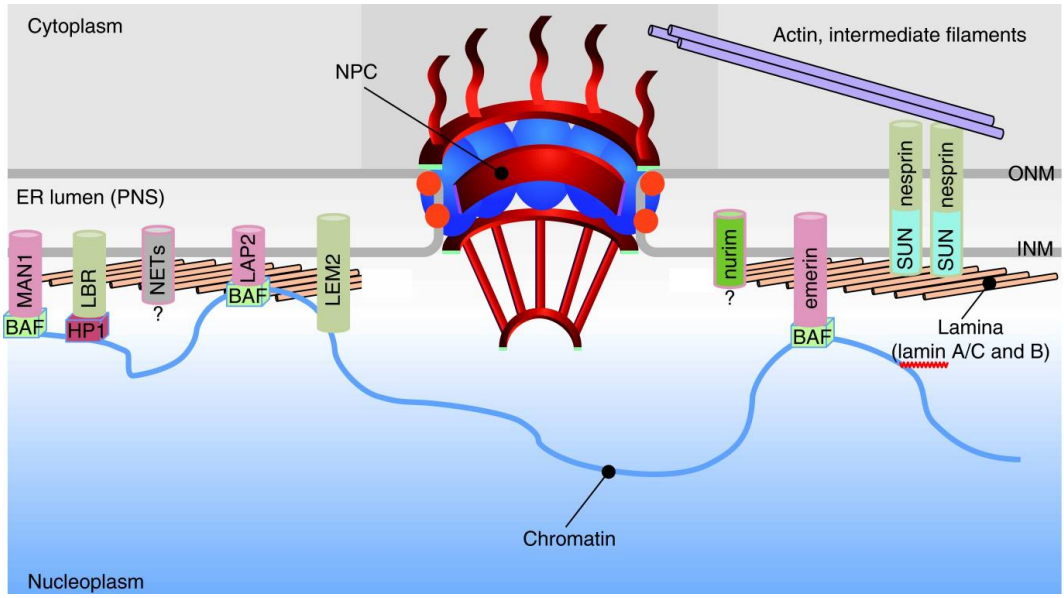

Figure 5. Schematic model showing the topology of the NPC and components of INM. The INM and ONM are separated by the ER lumen, also known as the perinuclear space (PNS). The INM proteins link the chromatin to the lamina while the ONM proteins connect the nucleus to the cytoskeleton. The LBR interacts with chromatin associated heterochromatin protein 1 ((HP1) and the B-type lamins. The lamina-associated proteins LAP2, emerin and MAN1 interact with chromatin via barrier-to autointegration factor (BAF). Nesprins interact with SUN proteins thus forming the LINC complex, which establishes a connection between INM and ONM. Many uncharacterised proteins have been identified via proteomic studies to be at the INM, but still lack functional designations (Hetzer, 2010).

membranes surrounding the nucleus have been distinctively segregated to two membrane bilayers, namely inner nuclear membrane (INM) and outer nuclear membrane (ONM) (**Figure 5**) (Hetzer, 2010). Nuclear pore complexes (NPC) perforate both these membranes (**Figure 5**). The proteome architecture of INM, ONM and NPC differ greatly from each other (Hetzer et al., 2005). NPCs are mostly composed of a family of proteins called the nucleoporins, which are arranged in a rotational symmetry through which the NPCs are able to perform bidirectional exchange of proteins, RNA and ribonucleoprotein complexes (Beck et al., 2004; Tran and Wente, 2006). Proteins from the INM interact with ONM resident proteins. This interaction within the nuclear lumen forms trans-envelope linkages that physically connect the nuclear chromatin to the cytoplasmic filaments in several organisms. An example of such a linkage is the SUN and nesprin proteins that form the LINC complex (King et al., 2008; Starr and Han, 2002). The INM and ONM proteins forming links have been implicated in spacing the two NE membrane leaflets at a constant distance of ~50 nm (Voeltz and Prinz, 2007). The NE thus acts simultaneously in both segregating but physically linking the nucleus and the cytoplasm.

The ONM is continuous with the ER, and contains similar architecture to ER with translocation channels, ribosomes and ER exit sites. One major set of components associated closely with the INM are the intermediate filament proteins called lamins (LMN). LMNs connect the INM, DNA and forms a network connecting the NPCs to each other. LMNs thus help shape the nuclei by maintaining its spherical geometry (Houben et al., 2007).

Human diseases like muscular dystrophy have been associated with mutations in LMNs, nuclear membrane proteins and their binding partners (Schirmer et al., 2003). Although LMNs are not found in fungi and plants, many NPC related INM and ONM proteins are conserved at a structural and functional level, thus stating that the possible mechanisms keeping nuclear contents in an organized manner are conserved partially (Anderson and Hetzer, 2008a).

1.1.5.1 Nuclear envelope during mitosis

At the end of the interphase in G2, the NPCs double in number and nuclei duplicate their genome. The ER network remains continuous with the NE. The entry into mitosis (prophase) marks the NE breakdown (NEBD) which denotes to the disassembly of the NE. This process leads to a loss of nucleo-cytoplasmic compartmentalization (Burke and Ellenberg, 2002). The disassembly of the NE however does not vesiculate the NE membranes; rather it gets merged with the peripheral ER and remains continuous (Anderson and Hetzer, 2008c; Ellenberg et al., 1997; Puhka et al., 2007). At prophase the proteins of the INM tethering the INM and chromatin in addition to lamins get phosphorylated (Hetzer, 2010). The phosphorylation dissociates lamin B receptor (LBR) from its nuclear contact sites, and leads to the nuclear lamin disassembly (Courvalin et al., 1992). From the onset of NEBD until metaphase or early anaphase, the chromatin material is mostly not in contact with membranes (Puhka et al., 2007). Majority of the soluble NE proteins redistribute throughout the cell while the transmembrane NE proteins localize to the mitotic ER (Ellenberg et al., 1997; Puhka et al., 2007). By anaphase, the NE membrane starts to reassemble while enwrapping the chromatin material (Anderson and Hetzer, 2008b). The chromatin thereafter de-condenses, a subset of nucleoporins start to re-associate and the NPC reformation is brought about (Anderson and Hetzer, 2008a). The NE reformation at the end of mitosis brings about the nuclear lamins to reassemble. During this event the LBR gets dephosphorylated while the NE proteins reconnect with the chromatin and the nuclear lamin (Anderson and Hetzer, 2007). The exact nature of membrane structure or architecture that reforms the NE is still under research but a recent research has shown NE to reform from highly fenestrated sheets (Otsuka et al., 2018). NE has also been reported to reform from ER tubules (Anderson and Hetzer, 2008c). At the final stages of cell division, the NE fully reforms and NPCs fully reassemble.

1.1.6 ER during mitosis

The ER at the onset of mitosis gets heavily transformed from its complex interphase architecture. From interphase to mitosis, the cultured cells change their shape dramatically from flat to rounded. This brings a considerable challenge while conducting microscopic analysis of the mitotic events. The ER during mitosis localizes mostly close to the PM and is excluded from the mitotic spindle as compared to a relatively homogenous spread at interphase throughout the cytoplasm (Anderson and Hetzer, 2008c; Lu et al., 2009, 2011; McCullough and Lucocq, 2005; Puhka et al., 2012; Puhka et al., 2007; Smyth et al., 2012).

The mechanisms and the involved factors related to the maintenance of ER during mitosis are questions that still needs to be addressed. Stromal interaction molecule 1 (STIM1), a calcium sensor in the ER (Roos et al., 2005) was recently shown to be involved in ER positioning. It was shown that the phosphorylation of STIM1 was necessary for preventing the ER membrane association to mitotic spindle (Smyth et al., 2012). STIM1, a ER protein, is known to bind to a microtubule

plus end binding protein EB1 (Grigoriev et al., 2008). During mitosis, STIM1 also gets phosphorylated like the lamins, dissociating itself from EB1. Upon expression of a mutated STIM1 lacking the capacity to be phosphorylated, the mutated STIM1 colocalized with EB1 and ER associated itself with the mitotic spindle (Smyth et al., 2012).

The ER transformation on a morphological level during mitosis as compared to interphase still remains controversial. Using LM, EM and ET, ER morphology has been previously reported to transition to a more tubular form during mitosis (Puhka et al., 2012; Puhka et al., 2007), and in agreement with this observation, NEs have been reported to reform from ER tubules that contact chromatin (Anderson and Hetzer, 2007). On the other hand, other research have reported the ER to transition towards a more cisternal form while stating NEs reformation from ER sheets (Lu et al., 2009, 2011; Wang et al., 2013). ER structures at LM appearing to be cisternal were revealed to be highly fenestrated and highly curved upon investigation using high end 3D EM techniques (II)(Puhka et al., 2012). Such a transformation of ER during mitosis states the importance of its high curvature with relation to overall cell structure and the relevance of proteins responsible for shaping ER domains. During mitosis, the extent of ER transformation varies significantly between cell lines (Puhka et al., 2012). This could possibly explain some of the discrepancies.

1.2 Membrane bending proteins

1.2.1 Curvature of biological membranes

Membrane curvature is an important phenomenon keeping the structural and functional integrity of a cell in harmony. Membranes form local subregions, which can be seen as complex membrane shapes within the cell. There are various ways in which membranes can be shaped (**Figure 6**) (McMahon and Boucrot, 2015). This shaping can range from nanoscopic range (a scale at the level of protein domains) to microscopic scale comparable to the level of organelle shaping. Lipid composition and asymmetry can shape membranes. All lipids have various intrinsic shapes that depend on the acyl chain composition and their head group sizes. The shapes of lipids thus affect their side-by-side arrangement, giving a specific shape to the monolayer. Hence, the final curvature of lipid bilayer arises from the difference of curvatures of its inner and outer monolayers. Flat monolayers are formed by lipids like phophatidylcholine and phsphatidylserine that are shaped cylindrically. Lipids such as phosphatic acid, phosphatidylethanolamine, diacylglycerol or cardiolipin form a conical shape due to their smaller head group as compared to phosphatidylcholine. Clustering of such lipids causes membranes to form a negative curvature, where the headgroups come close to each other. On the other hand, lipids with a larger headgroup than the acyl chain, such as phosphatidylinositol phosphates and lysophosphatidylcholine, favour membranes to bend towards a positive curvature (Zimmerberg and Kozlov, 2006).

Proteins with transmembrane domains having an intrinsic inverted conical or conical structure have the ability to bend membranes they are associating with (Aimon et al., 2014). Complementing this method of membrane bending, the non-membrane associated parts of proteins could also shape membranes. Receptor proteins could bring about such a curvature to membranes by locally populating themselves. In such a case, the membrane would bend away from that side which contains proteins with larger domains (Copic et al., 2012). Many proteins may also oligomerize, forming homo- or heteromeric chains resulting in local membrane scaffolding. For example, clustering of low-density lipoprotein or transferrin receptors have been

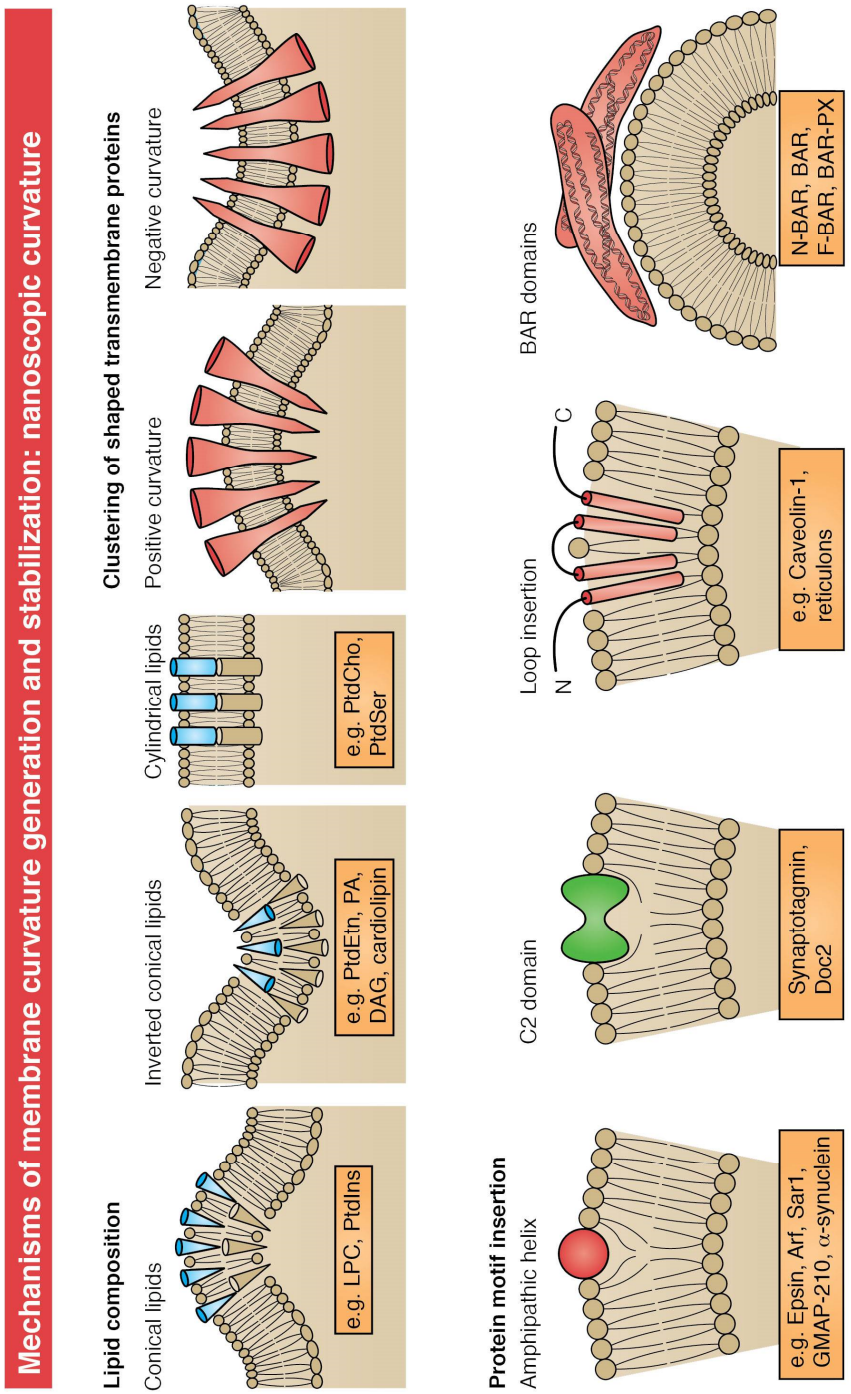

Figure 6. Overview of mechanisms for membrane curvature. Models showing lipid and protein based membrane bending forming positive or negative curvature at a nanoscopic level. Abbreviations: LPC, lysophosphatidylcholine; PtdEtn, phosphatidylethanolamine; PtdIns, phosphatidylinositol; PA, phosphatidic acid; DAG, diacylglycerol; PtdCho, phosphatidylcholine; PtdSer, phosphatidylserine; Arf, ADP ribosylation factor; N-BAR, N-terminal amphipathic helix BAR domain; F-BAR, FCH BAR domain (adapted from McMahon and Boucrot, 2015).

reported at sites of endocytosis forming clathrin –coated pits (Ehrlich et al., 2004). Hence, such a crowding mechanism could not only be a consequence, but also a necessity, giving rise to membrane bending at defined subdomains within the cell.

Local membrane curvature by hydrophobic protein motif insertion is another

robust method utilised by cells. In this case, the transmembrane domains of proteins form a wedge shape. This wedge gets inserted from the apex part into the membrane, finally residing within the lipid bilayer. Such an arrangement thereby causes the membranes to bend. With a single insertion the membrane bending is dissipated rapidly throughout the membrane space, while with insertions from several proteins occurring in close proximity to each other (either with same or between different protein complexes) the membrane curvature observed is of a much higher degree (Campelo et al., 2008).

Membrane curvature by crescent-shaped dimeric BAR (BIN/Amphiphysin/Rvs) domain proteins binding to membrane's hydrophilic surface is yet another novel method utilized by cells. Primarily, the initial binding of BAR proteins is brought about by electrostatic interaction between this protein family and charged lipids. Membrane curvature needed for membrane tubules is favoured by the action of BAR domain proteins while they are not responsible in providing higher curvature structures as in case of membrane scission (Boucrot et al., 2012). The first report on BAR domains to bend membranes via its curved interface architecture was described by Peter and colleagues (Peter et al., 2004). The BAR/N-BAR domains in general are located at the N-terminus of the protein while sometimes it can be found at the central or C-terminal locations (Suetsugu, 2010; Suetsugu et al., 2010). Occasionally, an amphipathic helix at the N-terminus can be found which inserts into the hydrophobic region of the lipid bilayer. Collectively, ER membranes until now are known to be shaped mostly by proteins that form a wedge with their hydrophobic loop insertion to the lipid bilayer.

1.2.2 Reticulon proteins

Reticulon family are a set of proteins that contain the RHD domain, which shape the ER tubules and sheet edges (Voeltz et al., 2006). The reticulon protein family is represented by the expression of a set of genes, namely RTN1, RTN2, RTN3 and RTN4/NOGO (**Figure 7**) (Yang and Strittmatter, 2007). Out of the four RTN genes, the most heavily studied gene has been the RTN4/NOGO. Each of these genes give rise to various isoforms due to promoter usage and differential splicing (Oertle and Schwab, 2003). The RTN1, the first identified RTN, was found from cDNA in neural tissue (Wieczorek and Hughes, 1991). RTNs were originally named as neuroendocrine-specific proteins and were named as reticulons upon their discovery of localization to ER in COS-1 cells (Vandevelde et al., 1994).The RTNs lack the traditional ER localization sequence but their C-terminal RHD keeps them anchored to the ER membrane (Chen et al., 2000; Iwahashi et al., 2007). Reticulons are known to form immobile oligomers (Shibata et al., 2008). The RTN family of proteins have a common C-terminal tail containing the RHD while the N-terminus is variable. This domain of the RTNs have been under intensive study where multiple functions of the RHD have surfaced. The RTNs while being anchored to the ER, resides on the ER membrane's outer leaflet with its C and N-terminus facing the cytoplasm. However, it has also been reported previously that RTN4A (the longest isoform of RTN4) localizes to the relatively flat PM facing the extracellular surface (Dodd et al., 2005; Oertle and Schwab, 2003). Nogo66, the cytoplasmic loop of the RTN4's RHD is involved in several signalling cascades, including Nogo receptor interaction for inhibiting neurite outgrowth (Fournier et al., 2001). The RTN4's Nogo66 loop as compared to RTN1 and RTN3's loop has an identity of 71% and 63% respectively, while mouse RTN1 and RTN3 have an identity of 67% and 59% to human RTN4's loop (Yang

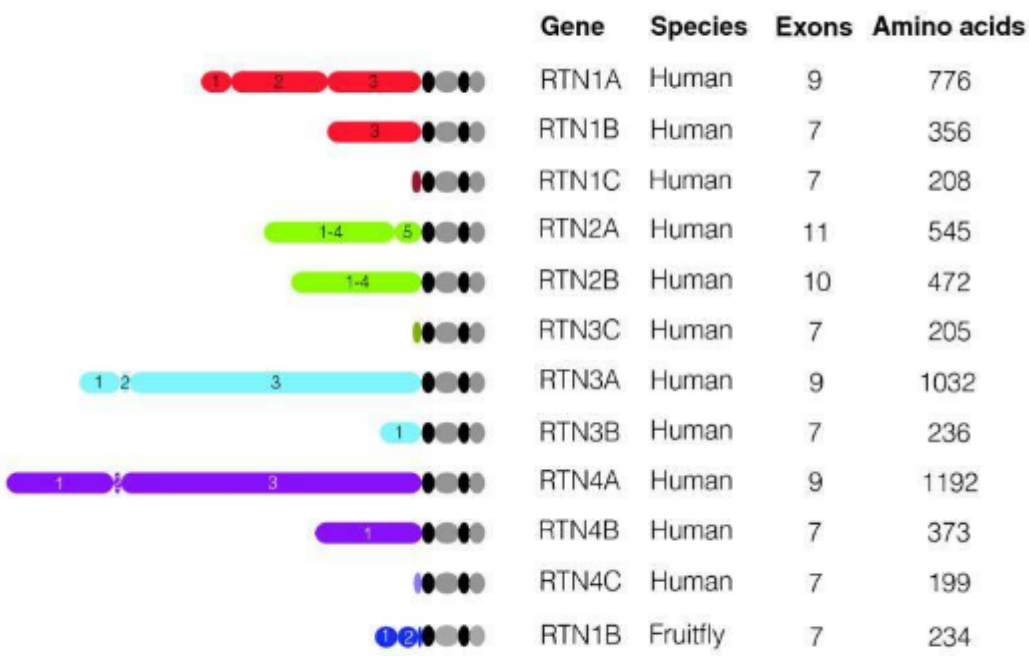

Figure 7. Overview of the RTN proteins. Image displaying a detailed architecture of all the known RTN proteins showing the number of exons encoding the respective RTN isoforms. The black and grey ovals represent the overlapping RHD domain consisting of two hydrophobic regions (black ovals) separated by cytoplasmic regions (grey ovals). (Yang and Strittmatter, 2007)

and Strittmatter, 2007). With such a high similarity, it is interesting to note that the RTN1's loop does not bind to Nogo receptor (Lauren et al., 2007), while the function of RTN1 and RTN3 loops still need further investigation.

Recently, ER nanoholes or fenestrations were reported for being positive for RTN4B/D (Schroeder et al., 2019). Consistently, in yeast, observations have been reported for RTNs to organize membrane curvature at the edges of sheets and fenestrations (West et al., 2011).

RTNs have been implicated to have roles in endocytosis. RTN1 isoforms RTN1A and RTN1B were reported to interact with a component of mammalian endocytosis adaptor complex AP-2. While RTN1C was shown to interact with SNARE proteins VAMP2, syntaxin 13, syntaxin 7 and syntaxin1, stating its possible role in exocytosis (Steiner et al., 2004).

RTNs have been researched previously for their role in intracellular trafficking. RTN3 overexpression was shown to prevent retrograde transport of proteins to ER from Golgi (Wakana et al., 2005). RTNs may also play a role in apoptosis. RTN4A and RTN1C were reported to interact with Bcl-X_L, an apoptotic inhibitor (Tagami et al., 2000). Further study showed RTN1C to inhibit Bcl-X_L, while RTN4A inhibited both Bcl-X_L and Bcl-2, another apoptosis inhibitor. Many other reports also showed RTN3 to enhance apoptosis by interacting with Bcl-2 (Kuang et al., 2005; Wan et al., 2007; Zhu et al., 2007). Though these findings may lead us to believe the possible role of RTNs as anti-cancer agents, there are findings negating such an idea (Oertle and Schwab, 2003). RTN4B was reported not to be a physiological pro-apoptotic protein in some cancer types (Oertle et al., 2003).

In other recent studies, RTNs have also been associated with autophagy as RTN3, exclusively from the RTNs, was reported to regulate the turnover of tubular ER via selective autophagy (Grumati et al., 2017).

Involvement of RTNs in viral infection has received considerable recognition in the last decade. RTNs have been reported to play crucial roles in viral RNA replication and replication compartment formation in brome mosaic virus (Diaz et al., 2010), thus acting as a set of host proteins aiding viral infection. RTN3 on the other hand was reported to be required for efficient viral RNA synthesis in the case of enterovirus 71 (Shih et al., 2011; Tang et al., 2007). The RTN3 was reported to interact with 2C proteins of coxsackievirus A16, poliovirus and enterovirus e71 (Tang et al., 2007). Interaction of RTN3 with non-structural protein 4B of hepatitis C virus was also reported using yeast-two hybrid system (Liu et al., 2005). Plus stranded RNA viruses have been known to induce membrane curvature in cells, aiding in infecting the host (Knoops et al., 2008; Limpens et al., 2011). It can be extrapolated that with the ability of RTNs in bending membranes, the viral replication mechanism could recruit host proteins, specifically pertaining RHDs for membrane shaping of viral compartments in plus stranded RNA viruses, amidst other mechanistic processes for a successful infection.

The real reason for having multiple expressions of various forms of RTNs while having the RHD domain consistent may have several implications. One such reason could possibly be in efficiently achieving multiple functions channelled via the variable N-terminal loops.

1.2.3 Receptor expression enhancing proteins

Receptor expression enhancing protein (REEP) family got their name primarily because of their involvement in targeting of odorant receptors to cell surfaces (Saito et al., 2004). Currently, we know six isoforms, REEP1 to REEP6 (**Figure 8**). REEP1 and REEP2 proteins are reported to be expressed in neuronal and neuronal-like exocytotic tissues (Hurt et al., 2014). REEPs are known to be involved in intracellular trafficking by regulating the ER cargo capacity (Bjork et al., 2013). Maintenance of ER structure by REEPs has gained attention in the past decade, where REEPs involvement in tubule ER network formation was reported (Hu et al., 2009). REEP5 was shown to interact with RTNs. REEP proteins also contain the RHD, which is positioned closer to the N-terminus in contrast to RTNs.

REEP1 to REEP4 are relatively similar to each other in their sequence as compared to REEP5 and REEP6 (**Figure 8**). REEP1-4 are relatively longer in their aa sequence and contain a microtubule binding domain between the two hydrophobic segments belonging to their RHD (Schlaitz et al., 2013).

REEP's role in mitotic ER shaping has been recently addressed, (Schlaitz et al., 2013) although an in-depth investigation on the mechanism of action of REEPs during mitosis is yet to be uncovered. REEP3 and REEP4 were shown to be responsible for not only ER positioning during mitosis but also in shaping the ER. ER, in REEP3/4 silenced cells was shown to localize to the chromatin, while the peripheral ER as compared to controls was observed to be highly cisternal (Schlaitz et al., 2013). The same research also showed defects on recently segregated cells, which were lacking REEP3/4. Although REEP3/4 are less abundant than REEP5 in wild type HeLa, they are specifically responsible in shaping and positioning of ER during mitosis. REEP3/4's

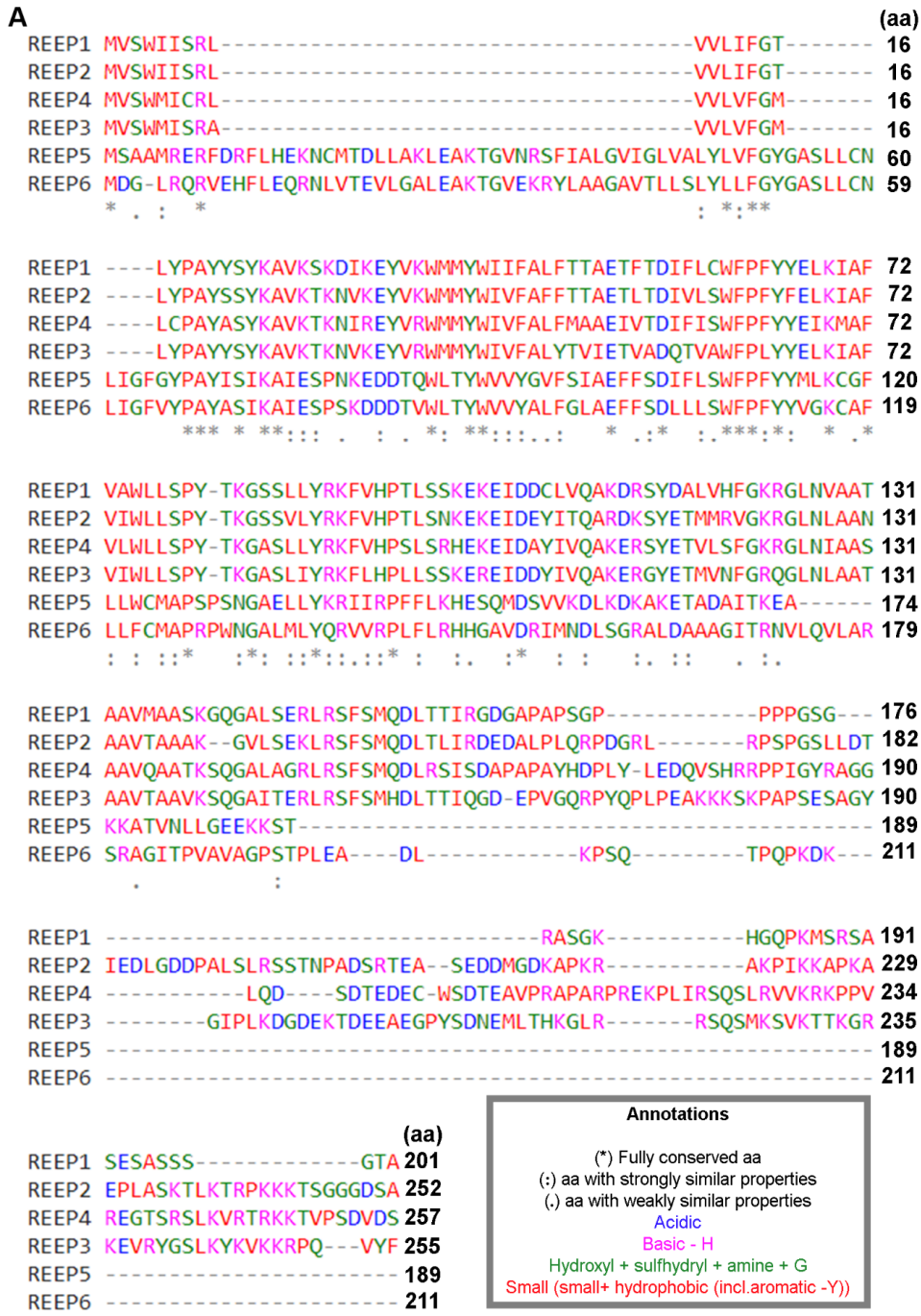

Figure 8. (A) Multiple protein sequence alignment of human REEP 1- 6 for the canonical forms of the respective genes. The alignments were generated using the web based MAFFT FFT-NS-i (v7.397) alignment tool.

RHD domain consists of a microtubule-binding region. A chimera expressing a non-microtubule binding loop of REEP5 was unable to rescue the REEP3/4 knockdown

phenotype. Hence, REEP3/4's cytoplasmic loop was proposed to be responsible for the clearing of ER from chromatin. It was also hypothesised that the REEP3/4's RHD domain kept the peripheral ER tubular in wild type conditions.

In interphase, roles of REEP3 and REEP4 are not yet revealed. However it is known that they are needed for a proper architecture of the NE post mitosis (Schlaitz et al., 2013). REEP5 was shown to be involved in maintaining sarcoplasmic reticulum architecture in adult rat ventricular myocardium, where the levels of REEP5 was observed to be higher than other REEPs (Yao et al., 2018). In addition, REEP5 compromised rats showed a reduced cardiac contractility with depressed sarcoplasmic reticulum Ca^{2+} release. REEP6 from the REEP family of proteins was recently shown to be needed for maintenance of retina in mouse by facilitating ER homeostasis and protein trafficking (Agrawal et al., 2017). Involvement of REEPs in the nervous system and musculature has been investigated further in Xenopus embryo, where REEP4 mutations were observed to be causing paralysis with abnormalities at the tailbud stage of the embryo (Argasinska et al., 2009). REEP3's association to autism, another neuropathy related disorder (Castermans et al., 2007), brings REEPs in close connection with the observed pattern of ER related pathological disorders affecting the human kind.

1.2.4 Family with sequence similarity 134

The protein family with sequence similarity 134 (FAM134) are a family of relatively uncharacterised set of proteins that have recently received attention. FAM134 family currently has three known forms, namely FAM134A, B and C (Khaminets et al., 2015). In humans, all these three forms are expressed from genes residing at different chromosomes (www.uniprot.org). From these three, FAM134B has been the most studied.

FAM134B is also called reticulophagy regulator 1 (RETREG1) because it was found to be associated with selective autophagy. FAM134B was observed to selectively target parts of the ER to autophagy, mediated by using the LC3 binding domain at the C-terminus (Khaminets et al., 2015). This observation/finding has opened up a new class of autophagy related receptors. The LC3 domain is consistently present in all the FAM134 forms although the abolishing of just the FAM134B form was shown to be enough for hindering the ER-phagy (selective autophagy of the ER) (Khaminets et al., 2015). The same publication also showed changes in the ER structure upon FAM134B manipulation in cultured cells and mouse tissue, where FAM134B knockdown caused an expansion of the ER while overexpression led to fragmentation of the ER. Interestingly, all FAM134 proteins also contain the RHD domain. This very domain, which is responsible for shaping ER membranes, hence could be directly linked to the membrane deformation capability for the FAM134 proteins. It must be noted that the sequence of the RHD varied from the RTNs. In addition, the RHD's sequence varied from FAM134A to C as well, but all revealed the presence of 2 to 3 hydrophobic domains, which are characteristic to phospholipid bilayer inserted domains.

Although the FAM134B was shown by immuno-fluorescence LM to be an ER resident protein, localization of FAM134B with ER sheet marker CLIMP63 was more prominent than with ER-tubule marker RTN4 (Khaminets et al., 2015). It is interesting to note such a localization although it has a RHD and is capable of ER fragmentation upon overexpression. Controversially, another research stated FAM134B to be a Golgi residing protein (Kurth et al., 2009). An interspecies sequence similarity for FAM134B

showed the protein to be highly conserved (Khaminets et al., 2015). It would be interesting to know where FAM134C and FAM134A localize in the cell and thereafter map its evolutionary conservation.

In relation to neuropathy, FAM134 family have already started to emerge as important factors keeping the nervous system's architecture stable. This protein family has also been associated previously to human disorders, where mutations in FAM134B were reported to cause severe sensory and autonomic neuropathy (Kurth et al., 2009), and severe hereditary sensory neuropathy (Murphy et al., 2012).

FAM134B's role in virus replication, have also recently emerged, similar to RTNs. Dengue virus and Zika virus both enhanced in their replication at an early viral life cycle stage upon FAM134B knockdown conditions. This research also showed that the viruses cleaved FAM134B, thus hampering reticulophagy (Lennemann and Coyne, 2017). Such interesting findings also can be extrapolated to possible therapeutic angles of FAM134 family towards their application in preventing/curing viral infections.

1.2.5 Human diseases in context of membrane shaping proteins of the ER

As organisms are comprised of an intricate assembly of cells, which represent the building blocks of life, impressions of grievous diseases affecting the human race can be observed at the cellular level. ER in the context of human diseases has been discussed often, specially highlighting its importance in neurodegenerative disorders. Structural protein families have been associated with hampering normal brain function in several neurodegenerative disorders as well as schizophrenia (GrandPre et al., 2000; Yang and Strittmatter, 2007), where the disorders have been observed with abnormal protein levels. ER stress on the other hand has been observed as a common denominator in many neurodegenerative diseases.

1.2.5.1 Alzheimer's disease

Alzheimer's disease (AD) is one of the most common neurodegenerative diseases that still needs clarification in its etiology. AD is characterised by the presence of brain amyloid plaques and neurofibrillary tangles, accumulation of which causes extensive neuronal loss followed by progressive decline of cognitive function (Chiurchiu and Maccarrone, 2011; Huang and Mucke, 2012). RTN1-4 all have been implicated to be involved in AD equally as the BACE1 enzyme, which cleaves the amyloid precursor protein into β-amyloid peptide. BACE1 were reported to co-immunoprecipate with RTN1-4 (He et al., 2004). RTN3 overexpression reduced the levels of β-amyloid peptide, while the knockdown increased the β-amyloid peptide levels, implicating that RTN3 is responsible for inhibiting BACE1 (He et al., 2004). In direct translation to this, RTN3 in the temporal lobes of AD patients was observed to be downregulated (Yokota et al., 2006). Oligomerization and accumulation of RTN3 has been shown in a subpopulation of dystrophic neurites in AD post-mortem brain (Hu et al., 2007). In agreement to this, mice overexpressing RTN3 were observed to develop dystrophic neurites, which were morphologically similar to those observed in AD brains (Hu et al., 2007). It must be noted that this is in contrary to another finding, where no difference in RTN3 expression levels were observed from AD brains to controls (Kume et al., 2009a; Kume et al., 2009b).

1.2.5.2 Amyotrophic lateral sclerosis

Amyotrophic lateral sclerosis (ALS) is a fatal neurodegenerative disorder,

characterized by upper and lower motor neuron deaths of the brain, brain stem and spinal cord. This leads to the overall progressive weakness and atrophy of skeletal muscles (Chiurchiu and Maccarrone, 2011; Mitchell and Borasio, 2007). The RTN4A/B and RTN4C mRNA levels were seen to be differentially up- and downregulated in both post-mortem muscular samples of ALS patients and in ALS mouse models as compared to wild-type mice (Dupuis et al., 2000). In pre-symptomatic mice, RTN4A and RTN4B mRNA levels (to a lesser extent) were seen elevated, while RTN4C levels were high only in asymptomatic mice (Dupuis et al., 2000). In agreement to this, the RTN4A and RTN4B levels which are low in adult mice, were also shown to be increased in ALS mice correlating with disease severity (Jokic et al., 2005). On the contrary, the highly expressed RTN4C in wild type had lower levels (Dupuis et al., 2002). The involvement of RTN4s in ALS conversely have also been reported to not be specific to this disorder (Askanas et al., 2007; Harel et al., 2009; Pradat et al., 2007; Wojcik et al., 2006). It thus must be very crucial to further elucidate, how deep the connection of RTNs and/or other ER shaping proteins might be in relation to such fatal diseases. This information could pave way for discovery of biological factors as suitable therapeutic candidates in fighting lethal disorders.

1.2.5.3 Multiple sclerosis

Multiple sclerosis (MS) is a progressive degenerative disorder, which is mostly characterized by episodes of demyelination and damage to the central nervous system. Etiology of MS still needs further elucidation, but some factors, like genetic and environmental constituents, may play a role in the disease onset and progression, whereas immunological factors have been widely recognized for the initial trigger in MS (Chiurchiu et al., 2013; Chiurchiu and Maccarrone, 2011; Noseworthy et al., 2000). In the serum and cerebrospinal fluid of patients with MS, autoantibodies against RTN4A have been reported (Reindl et al., 2003). RTN4A antibodies, when administered exogenously, protected autoimmune encephalomyelitis mouse models for MS against demyelination and suppressed inflammatory responses (Karnezis et al., 2004). In agreement with these findings, RTN4 knockout mice portrayed a delay in the onset of autoimmune encephalomyelitis, and passive immunization with anti-RTN4 immunoglobulin showed a reduction in inflammatory responses (Karnezis et al., 2004). With such data available, it could be stated that RTN4 plays an important role in neurite growth in the brain, while it could also be very useful in preserving or restoring the integrity of neurons after demyelination and axonal loss or neuronal damages during MS. Evidences have supported the concept of targeting RTN4 signalling in MS, which could pave a promising way for a therapeutic approach (Lee and Petratos, 2013).

1.2.5.4 Hereditary spastic paraplegia

Hereditary spastic paraplegia (HSP) comprises of a large group of genetic disorders. HSP's characteristic features include progressive spasticity and weakness in the lower limbs caused by the continuous distal axonopathy, which in turn is caused by defects in the transport mechanisms along axons (Blackstone, 2012; Blackstone et al., 2011; Fink, 2013). Mutations in genes (bearing RHD for ER curvature) such as REEP1, RTN2 and atlastin-1, have been reported in HSP (Blackstone, 2012; Orso et al., 2009; Wakana et al., 2005). Atlastin-1 is known to interact with RTN4 and RTN3 (Hu et al., 2009), while spastin has been reported to interact with RTN1 and RTN3 (Mannan et al., 2006a; Mannan et al., 2006b). The involvement of RTN2 mutations in spastic paraplegia 12 in

addition to its interaction with spastin also is in line with previous findings (Montenegro et al., 2012). RTN2's ortholog in *Drosophila melanogaster* (*RTN-like 1 gene*) was shown to be required for proper organization of ER at the distal motor axons (O'Sullivan et al., 2012). Collectively, these results state that a proper ER shape is essential not only for proper ER function but also for maintenance of axonal architecture and that ER morphogenesis plays a role in HSP.

1.3 The need and extension of EM resolution to live cell imaging

Since the invention of the first simple microscope, the level of advancement in the field of microscopy has taken a giant leap. LM and EM currently used for the purpose of biological imaging undergo a continuous development cycle, giving possibilities for new research ventures. Because of the limitations of normal light, higher resolutions could only be achieved by electron microscopy techniques.

EM currently has not only achieved higher resolutions overtime, but the field has made advancements in automation and precision as well. Techniques like correlative LM and EM are rapidly gaining ground to get insights into the ultrastructures of LM signals (de Boer et al., 2015). While techniques like focused ion beam scanning EM (FIB-SEM) has become a very promising tool to achieve high resolution with precise sample milling at a fully automated level (Briggman and Bock, 2012). Additionally, as compared to conventional EM techniques, serial block-face scanning electron microscopy (SB-EM) and FIB-SEM both generate high resolution 3D EM data, giving a more in-depth and informative biological view.

With the current advancements of super resolution techniques like STED microscopy (Klar et al., 2001) and photoactivated localization microscopy (PALM) (Betzig et al., 2006) the LM has come closer to resolutions which only EM could achieve in the past. In addition, with respect to live cell imaging, the techniques like STED are easily able to perform imaging of living biological samples thus capturing events at high resolution. With many different options currently available for both LM and EM, it is of great importance to know which technique suits the end user the most.

Every LM technique compromises on many factors ranging from resolution and speed of imaging to photo-bleaching and depth of light penetration. The challenges faced while achieving either of the three parameters causes the other two to hinder, thus affecting the overall imaging (**Figure 9**). Currently, it is impossible to achieve high values for all the three parameters in any one imaging technique. Hence, such a trade-off has to be taken into account with regards to the aims of any investigation.

A technique called the light sheet microscopy has been very popular in achieving not only depth in the imaging sample, but also a high speed of imaging which is very good for imaging in larger field of views (Chardes et al., 2014; Huisken and Stainier, 2007; Keller et al., 2008, 2011). Additionally, light sheet imaging also reduces significantly the bleaching problem much faced using conventional or even super resolution microscopy because of the excitation of sample in areas where imaging is not taking place, thus bleaching the sample without collecting any data. Recent advancement in light sheet microscopy to achieve higher depth with less sample damage using two-photon scanned light sheet microscopy also has paved way for deep-tissue imaging (Truong et al., 2011). To increase the resolution with acquisition at a high speed, imaging using Bessel beams creating a lattice has also proved very valuable. This technique known as lattice light sheet also has proved to achieve larger data sets with high resolution

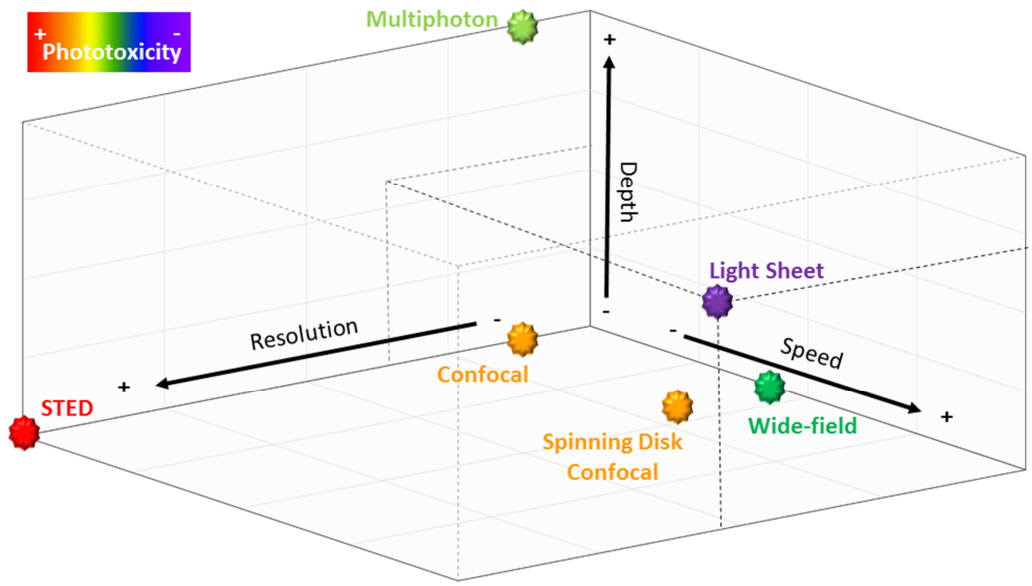

Figure 9. Balance in limiting compensation for super-resolution microscopy. Illustration showing four important aspects of microscopy where for achieving one the others have to be sacrificed (Modified from, thescinder.com/tag/the-eternal-triangle-of-frustration/).

and with less sample damage (Chen et al., 2014).

1.4 Image processing, segmentation and analysis

After the stages of experimentation and imaging, the next challenge faced generally is image processing and analysis. Many software tools have been utilized in the past and further development of those tools have allowed users to process images and conduct analysis on them with great efficiency. Many software tools exists and have been used specifically for LM and EM. Both LM and EM related softwares allow us to process and analyse images in various different ways. Many of these software tools were developed by researchers themselves and because of that are free to use (freeware) and in many cases are also free to modify (open-source). In addition, a number of commercial image processing packages exist. The commercial tools are usually more user friendly but unfortunately fairly expensive. The most popular example of an open-source image analysis tool is perhaps Fiji/ImageJ (Schindelin et al., 2012) with large community of users and multiple plugins; Fiji/ImageJ has been extensively used for LM data processing and analysis. Programs like CellProfiler (Carpenter et al., 2006) and Advanced Cell Classifier (Piccinini et al., 2017) have focused their ability to process LM datasets for high-content screens. In EM, an open-source package, IMOD (Kremer et al., 1996) is a popular choice especially for work with ET datasets. Commercial platforms on the other hand, for image analysis such as Image-Pro (Media Cybernetics, Rockville, MD) and Imaris (Bitplane AG, Zurich, Switzerland) are available for mostly LM datasets. Amira (Thermo Fisher Scientific, Waltham, MA) for both EM and LM have been in the market as well, providing valuable analytical tools for image processing, analysis and visualization of datasets.

In general, most of the open-source software packages have been very extensively

used but the available tools within them have been generally much targeted to special needs and it may be difficult to find a single package that includes all required functions. The freeware tools may also lack a good graphical user interface (GUI) and may have very limited documentation. On the other hand, many commercial software packages have good GUI and extensive documentation but tend to be non-flexible for modifications and tweaks. On the whole, there is a need for a software that would be an open-source package, which is able to easily handle multi-dimensional (2D-5D) datasets from both LM and EM, allows efficient 3D segmentation, performs targeted analysis, visualization and is also flexible for extensions. Additionally, for this research, a tool that could especially assist an easy and robust processing, segmentation and quantification of ER structures was needed.

2 AIMS OF THE STUDY

The aim of this study was to characterise and study membrane-bending proteins belonging to RTN, REEP and FAM134 family, especially in the context of ER morphology. As a shared feature, all these protein families contain RHD. RTN4s (NOGOs) and FAM134C (RETREG3) from the RTN and FAM134 families respectively were studied. Prior to this work, FAM134C had not been studied and lacked basic characterization. REEP3 and REEP4 from the REEP family were studied, focusing on its role in shaping the mitotic ER. Lastly, efforts were put in developing and refining of a software tool for image analysis and processing. This tool was extensively applied in supporting this whole study. The specific aims were

1. To study the expression pattern of reticulon family and pinpoint the localization of RTN4A (NOGO-A), RTN4B and FAM134C using LM and EM techniques

2. To screen for RTN4B binding partners and to elucidate the role of RTN4B and FAM134C in shaping the ER during interphase

3. To dissect the role of REEP3 and REEP4 in shaping ER during mitosis

4. Developing an open source software for improved image processing and analysis

3 MATERIALS AND METHODS

Table 1. Methods that were personally applied by me in this study. The Roman numerals stated here refer to the publication in question.

Method	Publication
Live cell imaging	I, II, III
Electron microscopy	I, II, III, IV
SDS-PAGE and Western blotting	I, II, III
Fluorescence light microscopy	I, II, III
Mammalian cell culture and transfection	I, II, III, IV
Confocal microscopy	I, II, III
Transcriptomics and data analysis	I
Immuno electron microscopy	I, III
Image handling and analysis programs: (MIB, Photoshop, Corel, Imod, Zen, Axioimager, Las af)	I, II, III
Serial block face electron microscopy sample preparation	II, IV
qPCR	I
Gene silencing	I, II, III
Immuno staining for fluorescence microscopy	I, II, III
Electron tomography	I
Cell proliferation assay	I
Mass spectrometry data analysis	III
Amino acid sequence alignment	III
Cloning	I, II, III

4 RESULTS AND DISCUSSION

4.1 Expression profiling of RTNs, REEPs and FAM134C (I, III)

4.1.1 RTN4s are among the most abundantly expressed genes contrary to REEPs and FAM134C

The RTN4s have been extensively studied previously, and many isoforms have been reported (Oertle and Schwab, 2003). We wanted to determine the expression levels of RTNs and a novel ER protein FAM134C, which emerged during this research. For most of this study as a whole, human hepatoma cell line named Huh-7 was used. This cell line was used primarily because we needed a human cell line. Additionally these cells contained abundant ER, especially ER sheets. We first performed a comparative transcriptome analysis of Huh-7 cells using SOLiD sequencing (Sequencing by Oligo/Ligation and Detection). Transcriptome allowed us to analyse and compare the expression levels of all the genes of interest to us. From the RTN family the expression of *RTN4*/NOGO and *RTN3* were the highest with trace amounts of *RTN1* and *RTN2* (I, Fig. 1A). REEPs displayed overall much lower expression levels than RTNs although *REEP3*, *REEP4* and *REEP5* had detectable levels of expression, where *REEP1* was in trace amounts and *REEP2* non-detectable (I, Fig. 1A). FAM134C was also in the detectable range although lower in expression as compared to RTNs or other known abundant ER resident proteins like the *CLIMP63*, *CANX (calnexin)* and *CALR (calreticulin)*. Although the transcriptome showed that RTN4B was the highest expressed from RTN4s, we used qPCR to confirm this finding. Using qPCR on human and mouse cell lines, *RTN4B* was the highest expressed isoform in Huh-7 as well as in NIH/3T3 mouse embryonic fibroblast cells (I, Fig. 1B). On the other hand, in primary mouse superior cervical ganglion (SCG) neurons, we found *Rtn4A/NogoA* to be the highest expressed isoform. In Western blots, an antibody detecting both RTN4A and RTN4B, showed a stronger band of around 55 kDa (corresponding to RTN4B) as compared to a fainter band at 180 kDa (corresponding to RTN4A) (I, Fig. 3C) in Huh-7 cells. It must be noted that the other isoforms of RTN4, namely RTN4C, RTN4D and RTN4E, could also be detected in all the cells that were analysed here (Huh-7, NIH/3T3 and primary mouse neurons), (I, Fig. 1B). FAM134C could be detected clearly from Huh-7 and primary mouse SCG neurons (**Figure 10**). The expression profiles of FAM134 family in neuronal vs non-neuronal cells might help in understanding their functional proximity to RTN4s.

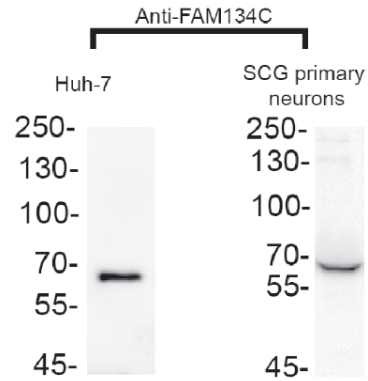

Figure 10. FAM134C is expressed in SCG neurons and Huh-7 cells. Huh-7 (left) and SCG neurons (right) cell lysates analysed by Western blotting with FAM134C antibody showing bands at expected size of ~65 kDa.

4.1.2 Expression of RTNs, REEPs and several ER tubule promoting genes increase during mitosis

It has been shown that a progressive sheet-to-tubule transformation is a general mechanism for ER inheritance in dividing mammalian cells (Puhka et al., 2012; Puhka et al., 2007). While the extent of the

transformation varies between different cell types, the direction of transformation towards more tubular ER form is the same in all the cell types (Huh-7, HeLa, NRK-52E, CHO-K1, Vero) that were analysed. We performed a comparative transcriptome analysis of total mRNA extracts from non-synchronized mitotic Huh-7 cells for SOLiD sequencing and calculated the expression levels of ER related genes. Mitotic Huh-7 cells were isolated using mitotic shake-off method (Terasima and Tolmach, 1963). Due to low counts of the overall mitotic mRNA fraction, this data could not be statistically verified. However, keeping

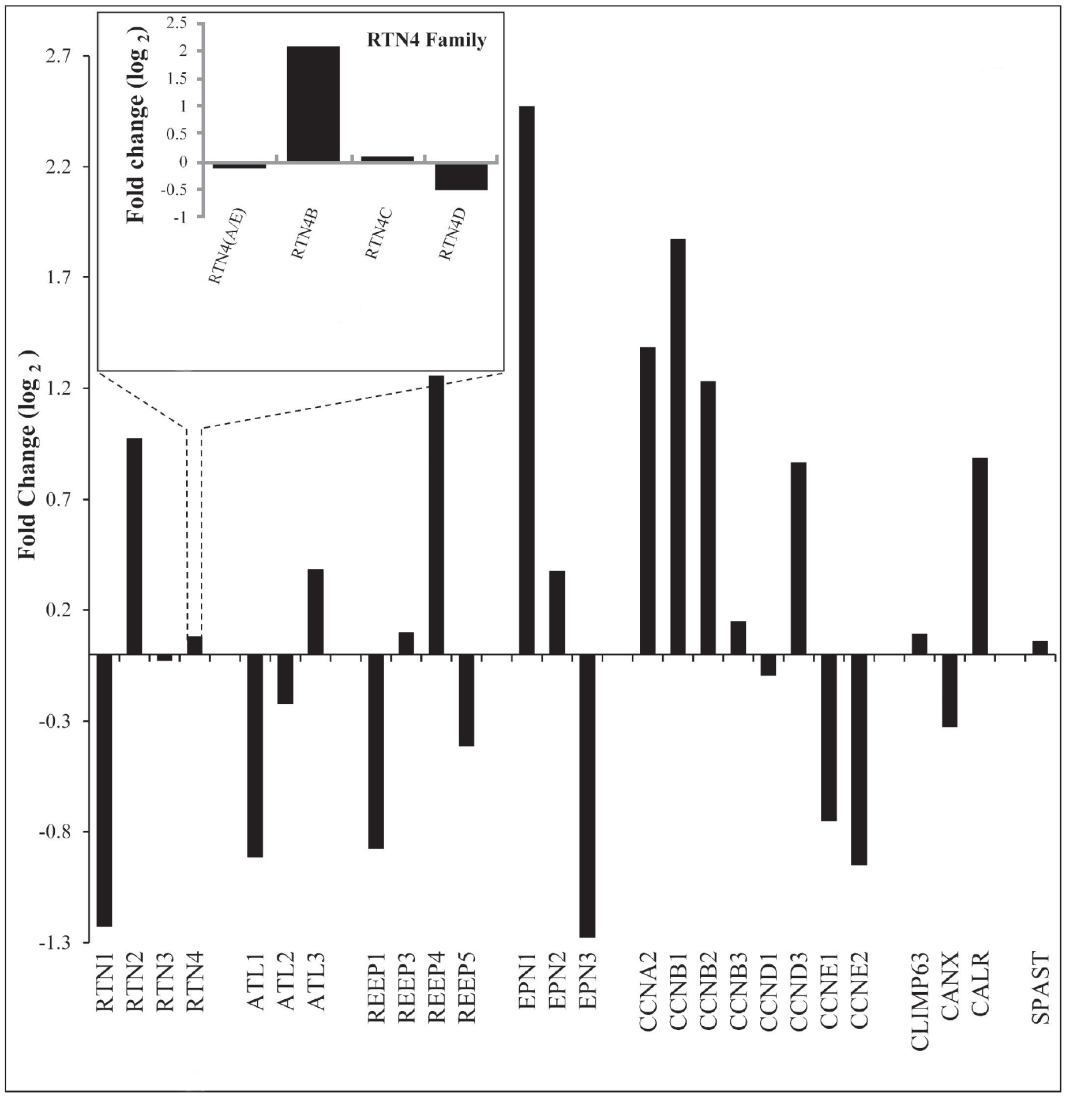

Figure 11. Expression of RTN4B as well as REEP3 and REEP4 increase during mitosis in Huh-7 cells. Relative mRNA level comparison of mitotic and interphase Huh-7 cells. Inset shows comparison of mRNA levels of all RTN4 isoforms. Positive values denote an increase in expression of the respective gene during mitosis and vice-versa. Atlastins (ATL), calnexin (CANX), calreticulin (CALR), cytoskeleton-linking membrane protein (CLIMP), cyclin (CCN), epsin (EPN), receptor expression enhancing protein (REEP), Reticulons (RTN) and spastin (SPAST).

this in mind, interesting profiling data were found on which some conclusions could be made.

Mapping of SOLiD reads revealed that *RTN1-4* genes were all expressed during mitosis (**Figure 11**). When compared to interphase expression profiling, *RTN4* levels increased by 5.7% and *RTN2* levels by 96.5%. In contrast, the level of *RTN1* dropped by 57.3%, whereas the level of *RTN3* remained roughly the same (net change -1.9%). Together, the net change of *RTN1-4* was +2.3%. It might be good to note here, that overall *RTN2* expression level is so low that a 96.5% increase does not have much impact to the total net change of *RTN1-4*. Expression of *RTN4B* was four times higher in mitotic cells than interphase cells, and while the expression of *RTN4D* was slightly decreased, the other splice variants remained roughly at the same level (**Figure 11**). The transcript levels *of NOGO-A/RTN4A* and *RTN4E* are presented in combined category, because SOLiD sequencing cannot reliably discriminate between isoforms that differ only at their very 5' end (**Figure 11**).

Transcriptome analysis identified several other ER-related genes that were expressed differently at interphase vs mitosis (**Figure 11**). The expression of some of the genes involved in the ER tubule and branch point morphogenesis increased (*i.e., RTN2* and *4, ATL3, REEP2-4, EPN1-2*), while some of them decreased (*i.e. RTN1* and *-3, ATL1-2, REEP1* and *EPN3*). The expression of *CLIMP63* increased by 6.6% in the mitotic fraction. The total expression level of atlastins and *REEP* increased during mitosis (13.6% induction of *ATL1-3* and 9% induction of *REEP1-5* in the mitotic fraction). *REEP4* specifically had a nearly 2.4 times higher expression during mitosis while *REEP3* increased only slightly. Spastin (*SPAST*) is a microtubule severing protein that localizes to the ER (Park et al., 2010). The expression of *SPAST* increased slightly (4.2% induction of Spastin transcript variant 1 and 2 in the mitotic fraction). Expression of Epsins (*EPN1-3*), which have previously been shown to regulate mitotic ER membrane morphology and spindle integrity in HeLa cells (Liu and Zheng, 2009), increased by 62.8% in total in the mitotic fraction compared to interphase cells. In the light of our transcriptome analysis, this mitotic transformation of sheets to tubules and the induction of branching (Puhka et al., 2007) might result from the increased expression of RTNs, ATLs, REEPs and SPAST in addition to other unknown factors.

Consistent with previous results showing that protein translation is down-regulated during mitosis (Le Breton et al., 2005), the amount of *CANX*, an ER chaperone which assists in protein folding, was found to decrease by 20.2% for mitosis. The expression of another ER chaperone *CANR* increased by +84.9%. *CANR* has been shown to be needed for the Ca^{2+} regulation, the level of which increase during mitosis (Chen et al., 2011; Jozsef et al., 2014). For comparison, we analyzed the expression level of well-known genes related to cellular events during mitosis. Most of the cyclins which have been associated with cell cycle (Galderisi et al., 2003; Jeffrey et al., 1995) were greatly elevated in the mitotic pool (net change of cyclins was +104.2%), confirming the effectiveness of the isolation of mitotic cells.

As a summary, our results suggest that the *NOGO-B/RTN4B* expression is controlled cell cycle dependently. Our results are consistent with the observed mitotic morphological change of ER from sheets to tubules (Puhka et al., 2012; Puhka et al., 2007), indicating that reticulons, in conjunction with other proteins inducing tubulation and branch

points, might account for the observed morphological change. As REEP3 and REEP4 are needed for ER shaping and clearing during mitosis (Schlaitz et al., 2013), the elevation of both these factors in our current study go hand in hand in context of their specificity during mitosis.

4.2 RTN4B interactome (III, IV)

Protein-protein interactions are studied to gain further insights into protein functions. The interaction or association of a protein with another leading to a cascade of events is one of the nature's most conserved lock and key mechanisms. We wanted to screen interacting partners of RTN4B. For this, we used two human cell lines (Huh-7 and HEK-293), with BioID (Roux et al., 2012) and conventional co-immunoprecipitation approaches. RTN4B-Strep (for co-immunoprecipitation) and RTN4B-BirA (for BioID) tagged constructs were made and expressed either transiently (in Huh-7) or stably (in HEK-293 (Human embryonic kidney)). For the BioID samples, the cells were incubated with biotin and the biotinylated proteins were isolated. In both the approaches, the proteins were digested with trypsin and subjected to mass spectrometry analysis. The data from all these runs gave us many interesting and unique hits (III, Fig. 1). RTN3, which came out as one of the hits had been previously reported as an interacting partner (Dodd et al., 2005). The screen revealed also many already characterised ER resident proteins like atlastins, vesicle-associated membrane protein-associated protein A (VAPA), STIM1 and other RTNs (RTN1 and RTN2) (III, Fig. 1). We also found REEPs (REEP5 and REEP6) to be interacting with RTN4B (III, Fig. 1). Two members of the progesterone receptor membrane component (PGRC1 and PGRC2) also were strong hits (III, Fig. 1). This family is known to be heme-binding proteins (Holman et al., 2006), which co-purify with progesterone binding proteins (Meyer et al., 1996). A study on this interaction would be a completely new angle for RTN4B and may reveal a new function.

FAM134C is a previously uncharacterized protein that came out as a unique hit in these runs (III, Fig. 1). FAM134B, a closely related protein to FAM134C, which had been recently reported to be a receptor for ER-phagy, also came up in the screen (Khaminets et al., 2015). FAM134C, owing to its strong/unique hit (in this screen), in addition to its possible association with ER shaping (due to its transmembrane domains) was further studied. Upon prediction searches, we found multiple hydrophobic sequences that were reminiscent of the RHD domain. Interestingly, the RHD in FAM134C was closer to the N-terminus as compared to C-terminus in case of RTNs. Such a pattern is observed also in REEPs, where the RHD is in proximity to the N-terminus.

The interactions of RTN4B with FAM134C and FAM134B were further validated using a microscopic based method called bimolecular fluorescence complementation (BiFC) (Kaddoum et al., 2010). This method uses the principle where two fragments of GFP (split GFP) reattach and become fluorescent in live cells if they come in close proximity to each other. We used RTN4B as a bait, which was tagged with the major fragment of GFP (GFP1-10) attached to the C-terminus, while the prey was FAM134C/B tagged with the remaining fragment of GFP (GFP-11). FAM134C and FAM134B both were in close proximity to RTN4B, because a positive GFP signal was observed (III, Fig. 2Aa). Myosin 1 isoform C (MYO1C), which has been previously shown to associate with ER-sheets (Joensuu et al., 2014), was used as a negative control (III, Fig. 2Aa). For further confirmation, the bait and prey tags were reversed in FAM134C and RTN4B, and they gave positive signals as well. In addition, we used this method to check if FAM134C interacts with itself. In this case,

bait and prey tags were cloned to FAM134C. This setup also gave a positive BiFC signal (III, Fig. 2Aa). Collectively the experiments suggested that FAM134C has the ability to form homo- and heterodimers. Furthermore, detected fluorescent pattern indicated FAM134C to be an ER resident protein like the RTNs. Quantification of the BiFC signals gave a clear picture of the interaction, confirming our mass spectrometry results (III, Fig. 2Ab).

4.3 RTN4A, RTN4B and FAM134C are ER resident proteins (I, IV)

Although RTN4s had been previously shown to be ER resident proteins, we wanted to analyse the subdomain localization of RTN4A, RTN4B and FAM134C at high resolution.

4.3.1 LM reveals RTN4B, RTN4A and FAM134C to co-localize with general ER marker

We narrowed down to two antibodies specifically recognizing either RTN4B (I, Fig. 2F) or RTN4A (I, Fig. 3C) in neuronal and non-neuronal cells. Confocal LM imaging using co-localization studies of RTN4A and RTN4B with general luminal soluble ER marker Hsp47-GFP showed a very clear overlap (I, Fig. 2A-B and Fig. 3A). Unfortunately, we could not find a working antibody for FAM134C for LM studies. Hence, we over-expressed FAM134C-FLAG construct using very low amounts of DNA and short transfection time for mild expression and saw a very good overlap with another general ER marker, CALR (III, Fig. 4A). Co-localization studies with ER marker Hsp47-eGFP using Pearson's correlation coefficient gave values 0.6 (NIH/3T3) and 0.5 (Huh-7) for RTN4B (I, Supp Fig. S1A); while 0.3 value was observed in NIH/3T3 cells for RTN4A (I, Supp Fig. S1A). For FAM134C, values around 0.65 for CALR and 0.75 for RTN4B were observed (III, Fig. 4B). Pearson's co-efficient was also calculated for FAM134C against other cellular markers like GM130 (Golgi marker) and ERGIC-53 (ERGIC marker). This was done because FAM134C had not been characterised previously at this level, and the closest relative FAM134B had been reported previously to be localised either in ER (Khaminets et al., 2015) or in the Golgi (Kurth et al., 2009).

From the LM analysis, parts of the ER were observed to be devoid of RTN4B/RTN4A. Hence, we could conclude that RTN4B and RTN4A have specific structural domains where they reside. Similarly, in the case with FAM134C, a higher coefficient value for RTN4B than for CALR was observed. After a careful examination of the LM images, it could be seen that various parts possibly representing sheets (marked by Hsp47-GFP or CALR staining) were devoid of RTN4A, RTN4B or FAM134C labelling. Indication for RTN4A and RTN4B to be enriched in ER tubules could be stated by their positive staining at neurite outgrowths (I, Fig. 4B, D), where the ER has been reported to be mostly tubular (Cooney et al., 2002). It is very crucial to note here that a conclusion using LM cannot be made with regards to these proteins being devoid from the ER sheets or any other specific ER subdomains. Hence, we switched to EM for verifying and concluding these findings.

4.3.2 EM and ET reveal RTN4B, RTN4A and FAM134C at high curvature ER

Cells were prepared for pre-embedding immuno-EM using the same primary antibodies that were used for LM studies. As for the analysis of FAM134C, Huh-7 cells mildly over-expressing FAM134C-eGFP construct were prepared for immuno-EM. FAM134C construct was hence detected by

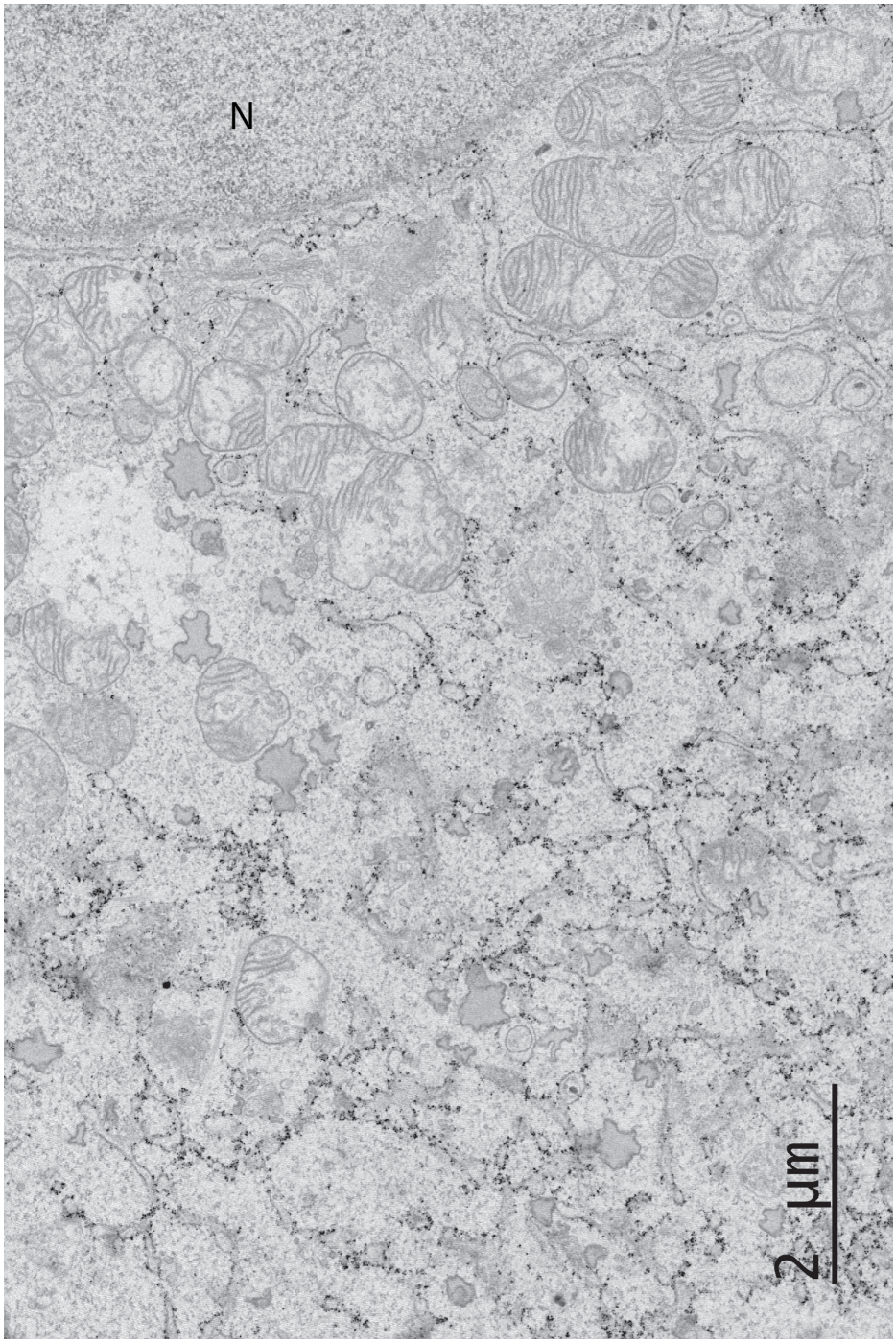

Figure 12. FAM134C localizes to high curvature ER. Pre-embedded immuno-EM micrographs showing silver enhanced gold labels representing the localization of FAM134C-GFP construct in Huh-7 cell. FAM134C can be seen localizing heavily at sheet edges and tubular ER. Tubular ER are more prominent at cell periphery. N (nucleus).

primary antibodies against GFP. Images revealed RTN4B and RTN4A to be clearly devoid from ER sheets while the gold labelling was enriched in the tubular ER, most abundantly at the cell periphery (I, Fig. 2C-D and Fig. 3B). In SCG primary neurons, both RTN4A and RTN4B showed a similar localization, where in addition to a strong labelling at the tubular ER at the neurite outgrowths (I, Fig. 4C and 4E) was observed.

No clear gold labelling was observed at the nuclear envelope or other membrane bound organelles. Upon a careful examination at the PM, no clear labelling for RTN4A nor RTN4B could be observed (I, Fig. 2C-D and Fig. 3B), thus contradicting one previously reported finding (Dodd et al., 2005). In addition, similar results were observed for FAM134C (**Figure 12**), suggesting its close resemblance to RTN4s in its localization. ET was done to get further insights into the localization of RTN4B and RTN4A with respect to ER. ET revealed both these proteins to localize to highly curved ER membranes, while no strong indication of either of the proteins to be in fenestrations was observed (I, Fig. 2E and 3D). It must be noted that our FAM134C localization data contradicts localisation data on its closely related member FAM134B, which has been shown by LM to be in ER sheets (Khaminets et al., 2015). It must be noted that the above mentioned study for localization on FAM134B was done using antibodies while our data is from mild-overexpression of FAM134C.

As the FAM134C has a RHD, its presence on highly curved ER, representing the ER tubules and sheet edges, is in line with our observations. It would be worth to see the localization of FAM134C by using functional antibodies or cell lines stably expressing the protein at endogenous level.

4.4 RTN4B and FAM134C levels affect ER morphology during interphase (I, III)

As both RTN4B and FAM134C contain the RHD, we wanted to investigate the possibility for these proteins to bend membranes.

4.4.1 RTN4B and FAM134C overexpression cause ER tubulation

Huh-7 cells over-expressing either RTN4B or FAM134C were analysed using LM and EM. In both cases, the cells were found to contain globular structures appearing at random locations (I, Fig. 5C) (III, Fig. 5A) throughout the cytoplasm, while it was absent from the nucleus. Live cell imaging revealed that these globular structures were non-dynamic in nature. Additionally these globular structures co-localized with general ER marker CALR (I, Fig. 5C) (III, Fig. 5Aa), thus suggesting that they were ER membrane associated.

To verify that the cell was transfected, we co-transfected our RTN4B or FAM134C constructs with soluble, luminal ER marker Hsp47-APEX. This construct localizes to the ER, and a cytochemical staining during EM sample preparation causes APEX to form an electron dense dark precipitate. This causes the ER lumen to become darker, thus, clearly highlighting transfected cells under EM investigation. We have seen that in co-transfections, over 95% of cells have both constructs expressed in the same cell. EM analysis revealed these globular structures to be heavily tubulated ER membranes, which were highly branched (I, Fig. 5D) (III, Fig. 5C). ET analysis confirmed this finding (I, Fig. 6Cg) (III, Sup Fig. S3B) and clearly showed that these structures were connected to normal ER. Previously, such structures were observed in overexpression of a poxvirus membrane protein called A17 (Erlandson et al., 2016).

For FAM134C, we further confirmed by immuno-EM that these heavily tubulated globular structures were positive for the FAM134C-eGFP construct (**Figure 13**). In the image (**Figure 13**), it can be seen that the outer rim of the heavily tubulated globular structure has a stronger gold labelling, while the inner structures have relatively little labelling. This could be explained by the lack of efficient antibody penetration due to multiple membrane bilayers that the antibodies had to

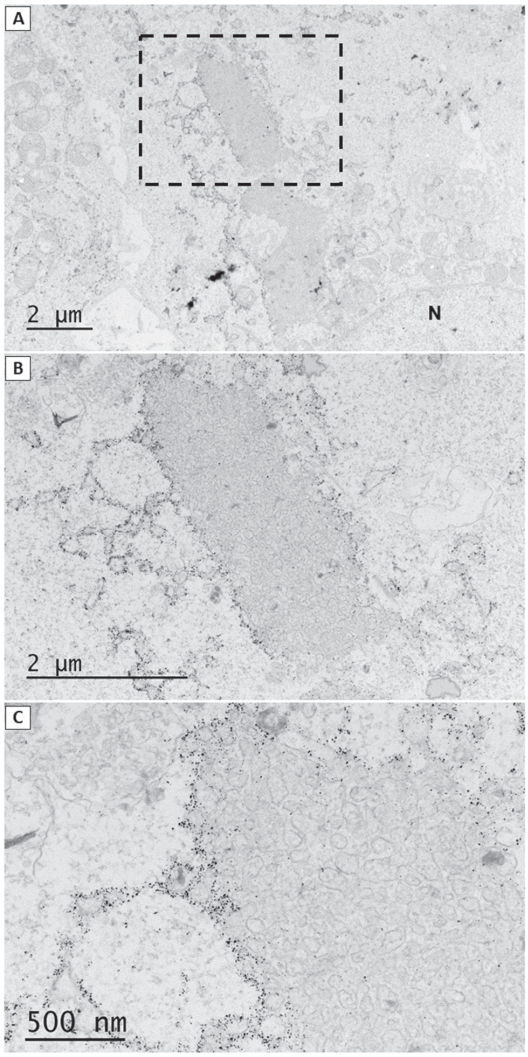

Figure 13. FAM134C overexpression causes ER tubulation. Immuno-EM micrographs showing large globular structures observed at LM to be heavily tubulated and highly branched ER positively gold-labelled for FAM134C construct in Huh-7 cells. Periphery of the globular structures heavily stained with gold than the interior areas. Images showing lower (A) and subsequent higher (B and C) magnifications of the boxed area in A. N (nucleus).

penetrate through. Another explanation could be that most antibodies bind at the surface of the globular structures where they get consumed, thus, not being enough in concentration to reach the inner membranes. The strength of EM here hence can be very clearly commended as the globular structures seen by LM could only be resolved by EM, thus, giving us a clear picture of the phenotype and the functionality of the proteins.

4.4.2 Depletion of RTN4 cause ER sheet enrichment in interphase cells

Role of RTN4, REEP3/4 and FAM134C in shaping ER was studied. For depleting RTN4 and REEP3/4, siRNAs were used while for FAM134C, shRNAs were used. Knockdown efficiency of these proteins were confirmed by Western blotting (I, Sup Fig. S3A, B) (III, Fig. 6B) (II, Fig. 1B). Due to a high sequence similarity between RTN4 isoforms, it would have been very challenging to design siRNAs for depleting any single isoform, and instead siRNAs targeting all RTN4 isoforms were used. Depletion of RTN4 was observed to give rise to large ER sheets (I, Fig. 7).

Depletion of REEP3/4 or FAM134C did not affect interphase ER morphology (II, Fig. 2D) (III, Fig. 6). LM and EM analysis for REEP3/4 or FAM134C knockdown conditions gave similar observations. In case of RTN4 depletion, often these massive ER sheets could be seen stacked to each other (I, Fig. 7). Most of these large sheets were observed at the periphery of the cells. The depletion of RTN4s caused overall cells to look unhealthy and abnormal. One possibility for lack of phenotype (as oppositely seen in case of RTN4) for FAM134C and REEP3/4 depletion condition could be the low levels of expression for the genes in interphase. Knockdown of FAM134C or REEP3/4 might although affect a small subset of ER structure, they could be too small a change to decipher.

4.5 FAM134C elevates in starvation and its N and C-terminus face the cytoplasm (III)

For further characterisation of FAM134C, we first aimed to uncover on how

the FAM134C would be resting on the ER's lipid bilayer. For this, we used a simple and robust microscopy approach. Cells mildly expressing FAM134C tagged with FLAG either at the N-terminus or C-terminus were treated with digitonin or Triton X-100 after fixation. Digitonin permeablizes the PM by dissolving cholesterol thus not affecting the ER much, while Triton X-100 permeablizes all membranes. We observed that both the N- and C-terminal FLAG tags were recognized after both the permeablization treatments (III, Fig. 3). In the control experiment, luminal ER marker CALR could not be detected after digitonin treatment but only with Triton X-100 permeablization. This indicates that both N- and C-terminus of FAM134C face the cytoplasm.

Interestingly, we found a microtubule-associated protein 1A/1B-light chain 3 (LC3) interacting domain at FAM134C's C-terminal end. LC3 has been shown to be a marker for autophagy, where LC3-I and LC3-II levels are supposed to be reduced and elevated, respectively, upon starvation (Kabeya et al., 2000). Upon starvation, we observed FAM134C levels elevated (III, Fig. 7A). This elevation was observed in both Huh-7 and HeLa cells where FAM134C level rose consistently by around 1.3 fold when cells were starved for 1h using amino acid and serum free medium (III, Fig. 7A). In addition, this elevation was specific for starvation conditions, as upon induction of ER-stress using dithiothreitol (DTT), FAM134C remained unchanged (III, Fig. 7B). DTT disrupts disulphide-bond formation thus leading to accumulation of misfolded proteins and eventually ER stress (Braakman et al., 1992). Hence, FAM134C could be complementing the functions performed by proteins like FAM134B, thereby possibly acting as another autophagy receptor for ER-phagy during starvation. It is very interesting to note that FAM134C may have multiple functions that it executes using various domains in its architecture.

4.6 REEP3 and REEP4 specifically determine the ER structure during mitosis (II, IV)

Previous findings of mitotic ER deformations upon REEP3 and REEP4 (REEP3/4) depletion at LM (Schlaitz et al., 2013) encouraged us to follow up on REEP3 and REEP4's specific roles in ER shaping at a higher resolution. Upon simultaneous depletion of REEP3 and REEP4, we observed a very striking phenotype of ER at the vicinity of chromatin in addition to large cisternal ER at the cell periphery (II, Fig 1) using EM. For an in-depth view of these structures, we employed TEM and SB-EM techniques. Measurement of cisternal structures at cell periphery revealed them to be extending as long as 2.5 µm in length (II, Fig 2B), while no major changes in the interphase cells were observed (II, Fig 2C and D). SB-EM data on REEP3/4 depleted mitotic cells revealed that ER associated tightly with chromatin where it was observed to be within the chromatin area as well. This chromatin associated ER was highly tubular in nature nearly reaching out to most of the chromatin material. We modelled all ER at the vicinity of chromatin at a distance of around 320 nm from the chromatin from the SB-EM dataset. Upon a close examination, this tubular ER could be seen all the way embedded inside the chromatin in direct contact with the chromatin material (**Figure 14**).

Looking at these formations it can be stated that multiple tubulating proteins residing on the chromatin associated tubular ER may be not only shaping this highly curved ER, but also might directly be anchoring to chromatin associated proteins thus wrapping around the chromatin. It would be interesting to find out what ER resident proteins are positive at this tubulated chromatin associated ER, and with which set of chromatin associated proteins they may possibly be interacting.

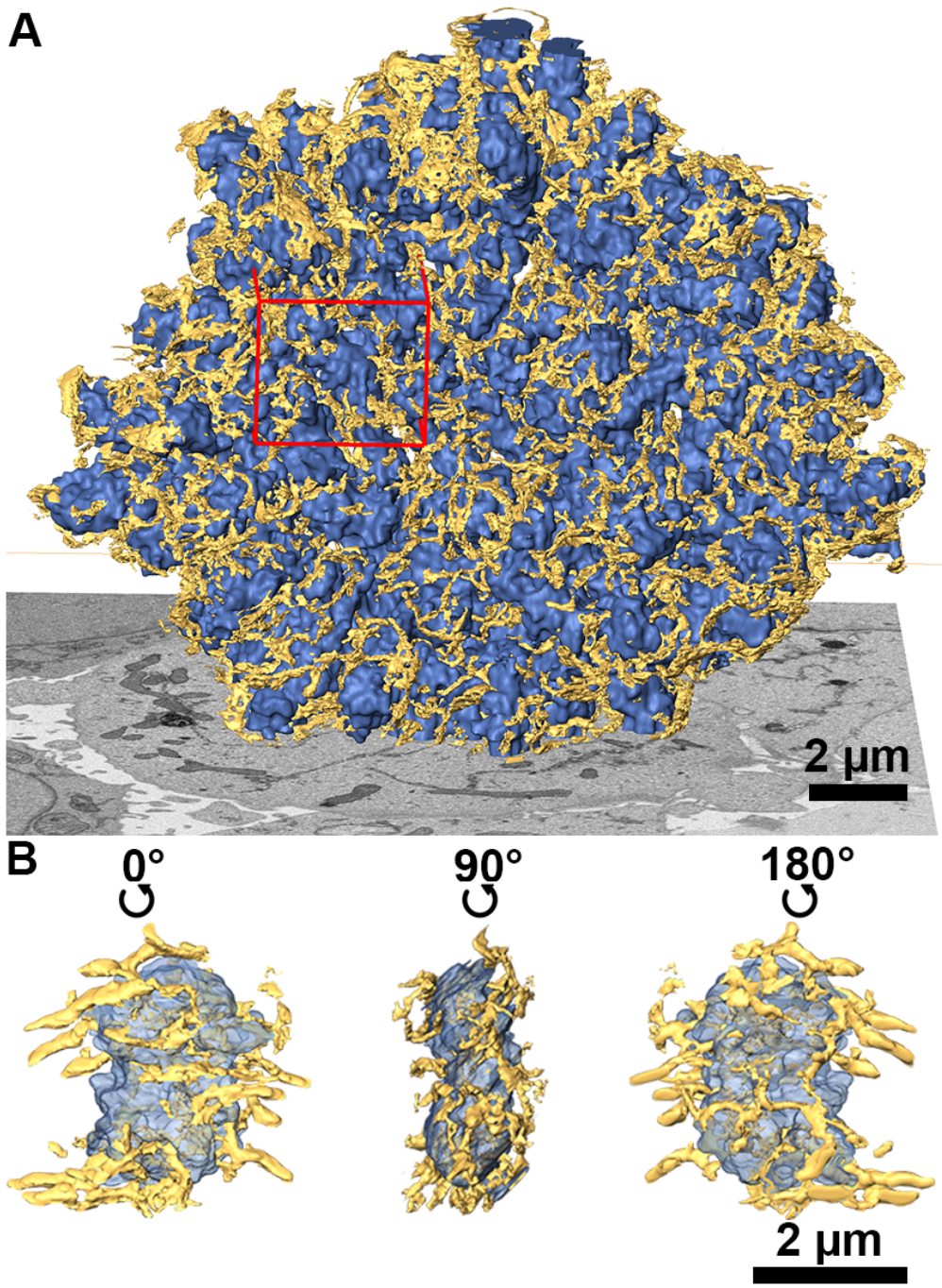

Figure 14. REEP3/4 depletion causes tubular ER to associate with chromatin in HeLa cells. A showing a model generated from segmented SB-EM dataset, showing ER (yellow) (mostly tubular) in close contact with chromatin (blue). B showing a higher mag image of red-boxed region in panel A in three different rotated views.

4.6.1 REEP3/4 have defined domains for membrane shaping and movement

We wanted to understand and pinpoint the specific domains of REEP3/4, which could be responsible for the mitotic ER phenotype. Using LM approach, the peripheral and chromatin-associated phenotypes were observed to be completely rescued using REEP4 construct, but could not be rescued by the REEP4 construct with a RHD mutated domain (II, Fig. 3) lacking membrane bending capabilities (**Figure 15**). With this experiment, we showed that REEP3 and REEP4's RHD domains play a key role in keeping the ER tubular, during mitosis. Defects on ER clearing was also observed in the RHD mutated REEP4, where often expanded ER tubules were observed within the mitotic spindle. The REEP3 and REEP4 both have a similar RHD as compared to the REEP5 and REEP6 . Both REEP3 and REEP4 also contain a positively charged RHD loop (cytoplasmic), which binds microtubules (Schlaitz et al., 2013). During mitosis, the REEP3/4 may get phosphorylated to thereafter get activated by 14-3-3 binding proteins. This activation could be taking place using kinases or phosphatases like the CDC25A/B/C (van Hemert et al., 2001). These cascades of events may allow an active form of REEP3/4 to shape the mitotic ER, eventually transitioning ER to a more tubular conformation using REEP3/4's RHD. Simultaneously, the active protein thus also

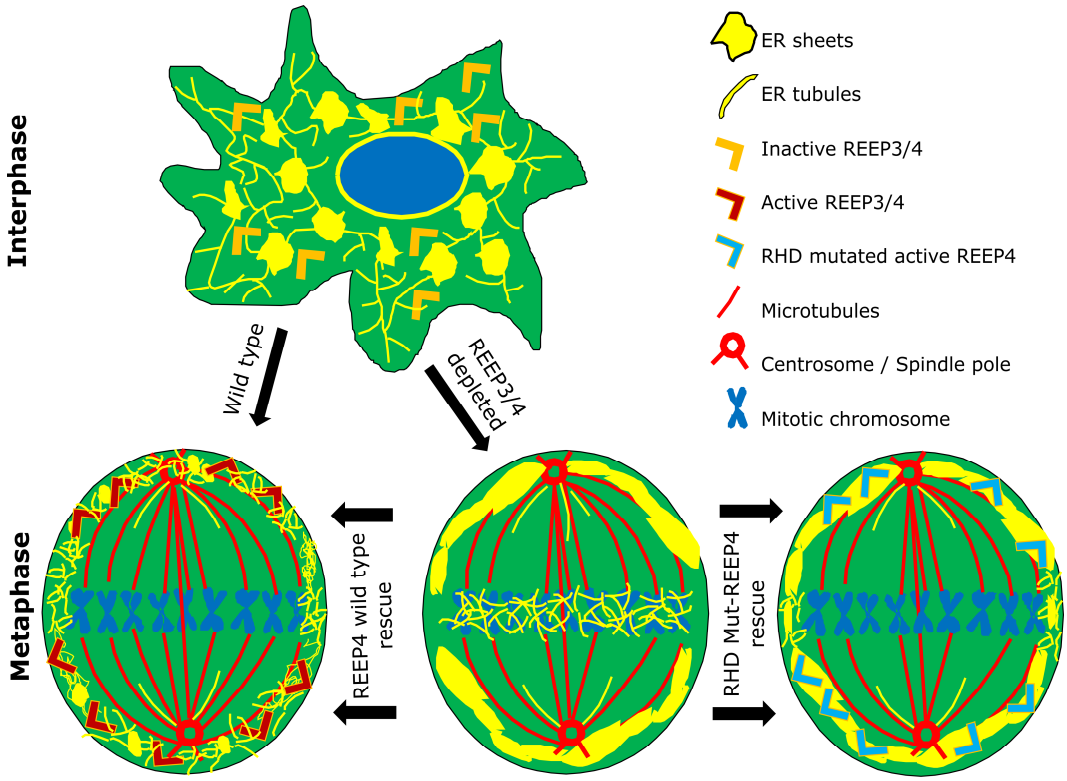

Figure 15. Schematic showing REEP3/4's effect on ER morphology from interphase to mitosis. Model showing ER sheet-tubule ratio shifting to more tubular in wild type where REEP3/4 become active. Knockdown of REEP3/4 causes tubular ER in the vicinity of chromatin with large sheets outside the spindle area. Rescue with wild type REEP4 removes ER defects while rescue with RHD mutated REEP4 (RHD Mut-REEP4) only clears chromatin associated ER but large sheets persist.

clears the ER from the chromatin using the microtubule binding region. It can be envisioned that the REEP3/4's RHD might undergo a conformational change upon activation, while on the other hand it could be staying in a dormant state during interphase not contributing on any membrane shaping activities. It could be possible that REEP3/4s may be interacting with other unknown proteins specifically during interphase for dormancy or during mitosis at its active state.

With these experiments we also confirmed previous finding of ER transitioning more towards tubular form during mitosis (II, Fig 2), which has been a subject of debate (Lu et al., 2009; Puhka et al., 2007).

4.7 Software tool for image segmentation and analysis of multidimensional datasets (IV)

It was crucial to have access to an efficient tool that could be used not only for examining images but also for image processing, segmentation of objects of interest from datasets and making their models for analysis and public presentations. Freely available programs like Fiji/ImageJ (Schindelin et al., 2012), BioimageXD (Kankaanpaa et al., 2012), IMOD (Kremer et al., 1996) and commercial packages like Imaris and Amira have their individual strengths. Some of these programs would be best suited for LM images, while the other for EM, but a platform for performing image analysis of multidimensional datasets from both LM and EM under one package was unavailable at the beginning of this research. In addition, we also needed many targeted algorithms to solve certain specific biological problems and questions. Although some from the aforementioned freeware packages could be utilised, they were all limited in multidimensional dataset handling, analysis and especially in efficient 3D segmentation. Hence, there was a need of a complete software package where we could control and develop all these aspects in conjunction with a good user-friendly graphic user interphase.

We thus developed an open-source platform called MIB (Microscopy Image Browser), which encompasses in itself all components required for us to view, process and analyse our multidimensional image datasets from both LM and EM sources (IV). MIB was written using MATLAB language, which is a popular choice among scientists for computational biology. MIB allows the community to make personalized changes suiting their specific needs and comes with easy to follow tutorials (mib.helsinki.fi). MIB has many special under the hood tweaks to improve its performance and minimize memory consumption. MIB can save datasets in formats compatible with other programs, such as Amira, IMOD or 3D Slicer (Fedorov et al., 2012). From the raw data point of view, every imaging instrument produces data that has its own specific format depending on the proprietor. MIB uses its custom made MATLAB and Bio-Formats (Linkert et al., 2010) readers for reading up to 100 microscopy image and video formats.

A general workflow using MIB would start with importing and assembling the images into multidimensional stacks of up to 5D (width, height, colour, depth and time) followed by their alignment and iterative segmentation by applying multiple semiautomatic and manual tools. Depending on the sample and object, the segmentation can be facilitated by semiautomatic tools followed by tools requiring more manual labour. The segmentation is frequently followed with analysis of the objects (using built-in and custom developed plug-ins) and 3D visualization of the final model.

To answer specific biological questions during this research we used MIB as a

developmental platform for various pipelines and plug-ins.

4.7.1 Measuring of co-localizations between two colour channels in LM datasets

First, a square region of interest (ROI) was drawn. The ROIs including both the channels were cropped from the original datasets and saved as separate images. These cropped images then were analysed using the Pearson's coefficient. As a negative control, one of the colour channels was rotated by 90° and the analysis was performed again. The obtained results were exported to Microsoft Excel (I, Fig. S1A) (III, Fig 4B).

4.7.2 Segmentation of ER

Here we began first by filtering the EM image with BM3D (Chen et al., 2016) filter. The voxels were clustered using SLIC algorithm (clusters voxels, with similar intensities) to form supervoxels. Calculation for adjacency of the supervoxels to each other was performed and the supervoxels were assigned to nodes of a mathematical graph, where each node was represented by respective supervoxel. The nodes were connected based on the calculated adjacency of the supervoxels. The difference in mean intensities between the adjacent supervoxels defined the energy barrier. Thereafter seeds were assigned to ER and background, on which the Min-Cut/Max-Flow algorithm was performed (Boykov and Kolmogorov, 2004) to split the mathematical graph in two partitions, thus segmenting ER from the background (III, Fig. S3B).

4.7.3 Modelling NE and nuclear pores

In this case, the nucleus would first be segmented as a whole semi-automatically using the graph cut approach. In contrast to the SLIC clustering used for ER (section 4.7.2), here we used the watershed algorithm that clusters the pixels based on membrane ridges. The edges of the watershed-based clusters follow the membrane continuity of NE and thus described the nucleus extremely precisely. The segmentation of nucleus was done by using the Min-Cut/Max-Flow algorithms over the generated mathematical graph. The resulting filled shape of the nucleus is then shrunk so that the NE membrane is not included into the shape and thereafter expanded back with a larger step size. A difference of the two would yield a mask in 3D surrounding NE. We used black and white thresholding within this masked area, to threshold the fine shape of the NE membrane including the pores (as they would have a different intensity range) (I, Fig. 7B).

4.7.4 Length of ER profiles

To measure the length of the ER profiles on TEM images we started with manual segmentation of the ER profiles using the brush tool of MIB. The traced out segments were then thinned down to one pixel wide skeleton consisting of end-points and branch points connected with line segments. Thereafter, we analysed the length of each line segment and the numbers of the branch and end-points using a custom made plug-in for MIB. The calculated numbers were exported to Microsoft Excel for interpretation and plotting the results.

Even though MIB was published in 2016, it is still under constant development to accommodate the current needs in our biological research. MIB is constantly improved and extended with new features.

4.8 A novel hypothetical method integrating STED and light sheet microscopy

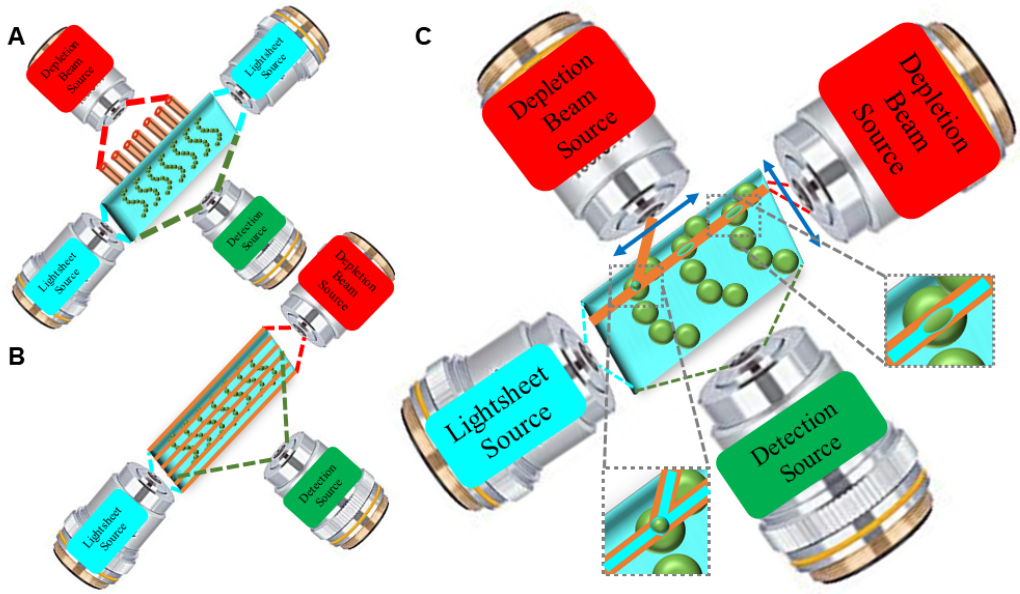

Figure 16. Hypothetical arrangement of an imaging setup combining light sheet microscopy and high-resolution STED microscopy in achieving higher spacial and temporal resolution. (A) Arrangement showing multiple depletion beam perpendicularly hitting the light sheet. (B) Showing an arrangement with multiple depletion beams hitting the light sheet from opposite-end forming a grating like setup and (C) depicting a setup partially combining A and B where single depletion beams perpendicular to each other hitting the light sheet and intercepting at a single 3D point; blue arrows showing direction of respective depletion beam movements. Insets in C showing enlarged view of excitation beam thinning.

As the ER expands throughout the cell, only a subset of the ER can be imaged in live conditions using the current super resolution techniques. Specially, techniques like STED (Klar et al., 2001) is known to also bleach the sample significantly, thus not allowing the cell to be imaged with very great efficiency at x, y and z dimensions. As ER is a very dynamic organelle, the time resolution also plays a crucial role in identifying spacial ER movements such as the previously discussed nanohole or fenestration dynamics (Schroeder et al., 2019). Realizing the advantages of STED and light sheet microscopy (Chardes et al., 2014; Huisken and Stainier, 2007; Keller et al., 2008, 2011), interestingly such challenges could possibly be further eased. It would be novel to combine the two techniques (STED and light sheet microscopy) to reap benefits from both. As described in **Figure 16**, a setup where only the hollow depletion beam of the STED system would cross a sheet of fluorophore exciting laser perpendicularly (**Figure 16A**), to achieve x-y resolution while the sample itself gets unharmed because of the sheet of light exciting only one plane of the sample.

Additionally, instead of having just one depletion beam, multiple depletion beams (already under planning/construction in Prof. Stefan Hell's lab, Max Planck Institute for Biophysical Chemistry, Göttingen) separated from each other using a beam splitter could be used for the de-excitation of the fluorophore to achieve time resolution. During this whole setup, the image acquisition would happen using the detector placed on the opposite side of the STED path. This method could be implemented using either a single or double light sheet excitation, with an offset of maximal focus from the two beams thus, exciting the sample from opposite ends to reduce blurring and keeping the excitation

intensity laterally longer, consistent and thin throughout the sample (Tomer et al., 2012). Additionally, a setup where multiple depletion beams from the opposite side of the light sheet forming a grating can also be setup. Here the hollow depletion beam would only allow a very narrow sheet of light to excite the fluorophore thus giving high resolution in two planes (**Figure 16B**). To improve this setup a third arrangement (**Figure 16C**) could also be envisioned, where two hollow depletion beams would hit the sheet of fluorophore exciting light perpendicular to each other, preferably in the same plane of the light sheet. Such an arrangement would thin the area of excitation even further i.e in x y and z because of small point spread function. As the excitation and depletion in this case would be in the same plane of imaging, only the plane of image acquisition/detection would be excited. The depletion beams in this case would first move in x or y plane (as shown with blue arrows) coordinated with each other for collecting data of the whole area in the respective plane before moving in z to cover the whole sample in 3D. Thus after the imaging on one plane, the light sheet along with the depletion beams could then be directed to the other planes of the sample to collect a 3D stack with a STED resolution. In all these approaches, it would be important to setup the detectors in a way to restrict the detection area, where the detection would be synced to the movement of the depletion beam specifically at the depletion beam intersections throughout the sample.

All these approaches would not only increase lateral and time resolution but also resolution on z direction significantly thus giving a good 4D imaging platform. It must be noted that techniques on thinning the light sheet would also be beneficial which is currently under constant improvement (Friedrich et al., 2011), but still needs further optimisation. Overall, the live sample could be imaged for longer duration while keeping the sample/fluorophore overall more stable as compared to the conventional STED imaging. It must be noted that the spacing between the depletion beams in all cases (**Figure 16A, B and C**) would need to be optimised to a frequency/number that would then move along the x-y plane finally covering the whole sample-set aimed for imaging. Ultimately, this kind of a setup could specifically aid in live ER imaging with higher time and spacial resolution while it spans the whole cell.

5 CONCLUSIONS

With the use of advanced microscopic techniques in addition to general cell biology based assays, we showed RTN4 proteins to be prominently expressed in mammalian cells, where RTN4A and RTN4B are highly expressed in neuronal and non-neuronal cells respectively, showing a cell specific expression pattern (I). RTN4B levels rise during mitosis possibly supporting a proper mitosis by promoting the ER transition from sheets to tubules. Depletion of RTN4 during interphase severely affected ER structure and shifted ER's sheet-tubule balance more towards sheet appearance (I). Using immuno-EM studies, we concluded that RTN4A and RTN4B reside at high-curvature domains of the ER thus shaping it for a proper overall architecture (I).

REEP3/4 specifically shape the ER during mitosis as revealed by our LM and SB-EM data (II). Loss of REEP3/4 in metaphase causes tubular ER to get retained at the chromatin, where it very closely contacts the chromatin, while the peripheral ER remains more sheet like without any proper segregation near the spindle poles (II). Such an observation suggests REEP3/4 to be responsible for clearing tubular ER from chromatin via its cytoplasmic microtubule interacting loop. While subsequently, the RHD domain efficiently carries out mitotic ER shaping (II).

FAM134C is a conserved protein that localizes to the ER where it prefers high curvature ER like the RTNs (III). FAM134C overexpression causes branched ER tubulation at cell soma and long unbranched ER tubules at the cell periphery (III). ER tubulation is caused by FAM134C's RHD domain (III) that possibly forms a wedge, by partially and unsymmetrically inserting into the ER like a typical RHD. This protein interacts with RTN4B and its N- and C-terminus faces the cytoplasm similarly to RTN4 isoforms (III). FAM134C is need in ER-phagy and upon starvation elevates in levels but remain unchanged upon ER stress.

Cellular imaging for answering vital biological questions comes with the challenge of proper image analysis aided by image processing. We developed a tool to combine all vital features needed to process, analyse and handle LM and EM datasets thus robustly channelling our imaging and analysis workflow with high efficiency (IV). This freely available tool can be developed further to cater for other specific needs by end users.

In conclusion, we have further elucidated the roles of RHD containing proteins RTN4A, RTN4B, REEP3, REEP4 and FAM134C. Interestingly, although all these and many other proteins contain the RHD, they vary in their functions. The common feature combining all these proteins is their localization and capability to bend membranes via their RHD. Although the RHD is present in multiple proteins, the exact amino acid sequence varies from one family to the other. This may be a risk management tactics by the cell, over the course of evolution to segregate RHD's function over different protein families, as if/when one family gets affected or targeted by external forces, the other RHD protein families could continue functioning normally or even take over the role of the affected protein families. FAM134C on the other hand is currently poorly understood and so many different aspects of this protein needs to be investigated. Through this work, for the first time, REEP3/4 emerges as a mitosis specific RHD containing protein that plays an important role in proper cell division. It will be valuable for the future to uncover why and how these RHD containing proteins interact amongst each other, thus keeping the whole cell functioning normally. Additionally, also looking into their role in pathogen–host interactions and neurodegenerative diseases may give valuable insights.

6 ACKNOWLEDGEMENTS

This study conducted at the Institute of Biotechnology (BI), University of Helsinki, was made possible by funding from doctoral school Integrative Life Sciences (ILS),DS Health, HiLIFE Fellows program, Sigrid Juselius Foundation and Academy of Finland.

I would like to thank my supervisor Eija Jokitalo for her kind and devoted supervision, this PhD study has been exceptionally enjoyable under your supervision. I not only got to do so many things I wished for under your supervision but also got to learn exponentially in your friendly environment. It was so much fun talking about exciting science and research with you within the field of cell biology, microscopy and beyond. You kept such a beautiful research driven atmosphere in the lab, well balanced with family and cultural values. I cherished every day of my time in your lab and in a lively team of people, you solely are responsible for their nice behaviour and research driven enthusiasm. You have been extremely kind to me and my suggestions and have given me a very positive environment to think and implement science. I hope to keep in touch with you in the future via science and otherwise. Also thanks for the nice food during Easter celebrations !

Dear thesis committee members Varpu Marjomäki and Tero Ahola, I would like to deeply thank you for taking active part in my PhD progress. You both were exceptionally kind and helpful in guiding and also for channelling me from the start till the end. Thank you both so much for taking out time for attending all the annual meetings and giving useful comments.

I would like to thank my pre-examiners Mikko Hiltunen and Aki Manninen for giving their time and comments on my thesis. I also would like to thank the custos Kari Keinänen for discussions and help with planning of my PhD finalization and consultation. I would like to thank the past and current directors of BI for keeping up with the modern facilities at BI making this research possible and keeping the technical quality of instruments at par with international standards.

I would like to thank Mervi Lindman and Arja Strandell for being like a motherly figure to me guiding me so wisely and helping me out so much with big and small things. With so much of help from both of you, I was able to perform much faster. Dear Antti Salminen, it was so amazing to have you around. your help with general protocols and problem solving saved me from making many mistakes. Fun and funny conversations from you kept me going until the end, you might be retired now but certainly not tired. Thank you so much Antti for all the nice moments behind the lab bench and also in-front the bar. I would like to acknowledge Helena Vihinen from the lab for her scientific inputs, long and interesting discussions on electron and light microscopy and the super fun lab environment in additional to immense technical support at EM level and in thesis writing. I would like to acknowledge Ilya Belevich from our lab for all the nice research driven discussions on image analysis and scanning electron microscopy. Dear Ilya, your inputs with regards to helping with imaging at SEM to data analysis and solving big and small issues with software and hardware related concerns is deeply appreciated. It was also much fun to travel with you for scientific conferences and hiking with you while acquiring non-scientific images as well. Dear Olli Ramö, I would like to convey my deepest thanks to you for your supervision in my beginning days at the lab. For the really nice scientific inputs and long conversations about a light microscope and its basics. Most importantly, I also would like to thank you for helping me setup things in the lab while I needed much help. Finally, also for the awesome time over drinks and food which I will never forget. Dear Merja Joensuu, I gained so much scientific knowhow from you while at my beginning days along with Olli. You were a good teacher and a very meticulous mentor to me. I could not have come till the end of my research without your presence. I also wish to thank you for the long hours of scientific and non-scientific discussions ranging from basic cell biology to how to enjoy the Finnish winters over alcoholic and non-alcoholic beverages. Thank you so much for being there MJ. Dear Behnam Lak, ‘the day you came to this lab’, I got another soulmate. Exchange of knowledge from cell to mind biology and talking about

human perception to general life was amazing. You were like my second wife in the lab as Taina stated. Thanks man for your nice company and fun talks over many occasions. Your presence kept me always in a very positive mood. I would like to give a deep vote of thank to dear Taina Suntio. Dear Taina discussing deep cell biology and pathways of many interesting proteins we could think off was just amazing. You have always been a walking talking encyclopaedia of Cell biology. It was so much fun to have shared the same office space with you and to have had conversations ranging from cell to family biology. I feel much wiser after spending all the lab time with your supervision and fun chats. I would like to also thank the recent additions to our lab namely Matias Veikkolainen, Suvi Saarnio, Sreesha Sree and Anni Hyvönen for getting to spend good times with them and nice scientific discussions. I also would like to thank Aki Vartiainen, for a nice and positive time while handling cell mediums and beers, at different time points, along with Mikko Helenius. I wish to deeply thank LMU staff namely, Kimmo Tanhuanpää, Marko Crivaro, Mika Molin and Harri Jäälinoja for their microscopy related help and fruitful microscopy related discussions. I also wish to thank BIU staff namely Antti Isomäki and Jussi Kenkkilä for their inputs and help with the light microscopes in Biomedicum. I would like to acknowledge my collaborators Anne-Lore Schlaitz and Maria Vartiainen for having such a productive collaboration.

I would like to thank my parents Krishna Kumar and Sindhu Kumar and my sister Divya Kumar for giving their immense support and positive advices which helped me a lot to understand my life directions and decision making. I would like to deeply thank my family in Finland my dear Heidi and Maya for their support throughout my PhD research. Dear Heidi you kept me going strongly forward. Thank you and Maya both for all the happiness I needed to complete my research. I also would like to thank my in-laws Ari Jääskelainen, Inga-lill Lönnros-Jääskeläinen for so many nice get-togethers in Haikko over Christmas, and many weekends. You both have been so kind always and I got a lot of the energy from your nice food and wine to complete my experiments efficiently. I also would like to thank Johannas Åbonde (Johannis), Anette Jääskelainen, Annastina Åbonde, Amanda Åbonde and Ida Åbonde for giving me such a nice and homely like environment in Finland over nice food which was always a big support for me to do my work with great efficiency. Dear Juho Honkala, it was nice to have met you at sähly. I always have cherished my friendship with you and every meeting with you gave me more encouragement throughout my research time. A big thanks to my good friend circle Praveen, Jay, Neha, Maitry, Poojitha, Palash, Snehadri, Erika, Sabine, Marianne, Douwe, Ari. R, Aida, Jarno, Vinod, Robbe, Marine, Megha, Ewelina, Sushil, Isabel, Kul, Tuomo, Ilida, Chris, Daniela, Sudarshan and Edu for your friendship, food, music, trips, sports, awesome parties and super fun discussions.

I would also like to deeply thank my Indian-gang with whom I spent so much time and got to enjoy Finland. Dear Durgam, Asha and Apramey, thank you all three for all the nice and fun Hindi conversations, for the awesome food, stories and movies and for the nice trips we took together. I also would like to thank Eeva Sievi who gave me such good advices and so much of support on managing many BiotechClub related activities. I also wish to thank Erkki for all the BiotechClub related support and the really fun get-togethers in and outside Finland. I would like to finally thank all the BiotechClub members and BiotechClub board along with ILS members Geri, Maria, Jurgita, Mridul, Larisa, Liliia, Elina, Sigi and Riikka with whom I learnt a lot and with whom I got to know so much about organization and management. I also thank the field of Biology for being ever so interesting :D.

01.05.2019

7 REFERENCES

Achleitner, G., Gaigg, B., Krasser, A., Kainersdorfer, E., Kohlwein, S.D., Perktold, A., Zellnig, G., and Daum, G. (1999). Association between the endoplasmic reticulum and mitochondria of yeast facilitates interorganelle transport of phospholipids through membrane contact. Eur J Biochem *264*, 545-553.

Agrawal, S.A., Burgoyne, T., Eblimit, A., Bellingham, J., Parfitt, D.A., Lane, A., Nichols, R., Asomugha, C., Hayes, M.J., Munro, P.M., *et al.* (2017). REEP6 deficiency leads to retinal degeneration through disruption of ER homeostasis and protein trafficking. Hum Mol Genet *26*, 2667-2677.

Aimon, S., Callan-Jones, A., Berthaud, A., Pinot, M., Toombes, G.E.S., and Bassereau, P. (2014). Membrane Shape Modulates Transmembrane Protein Distribution. Developmental Cell *28*, 212-218.

Anderson, D.J., and Hetzer, M.W. (2007). Nuclear envelope formation by chromatin-mediated reorganization of the endoplasmic reticulum. Nat Cell Biol *9*, 1160-1166.

Anderson, D.J., and Hetzer, M.W. (2008a). The life cycle of the metazoan nuclear envelope. Curr Opin Cell Biol *20*, 386-392.

Anderson, D.J., and Hetzer, M.W. (2008b). Reshaping of the endoplasmic reticulum limits the rate for nuclear envelope formation. J Cell Biol *182*, 911-924.

Anderson, D.J., and Hetzer, M.W. (2008c). Shaping the endoplasmic reticulum into the nuclear envelope. Journal of Cell Science *121*, 137-142.

Argasinska, J., Rana, A.A., Gilchrist, M.J., Lachani, K., Young, A., and Smith, J.C. (2009). Loss of REEP4 causes paralysis of the Xenopus embryo. Int J Dev Biol *53*, 37-43.

Askanas, V., Wojcik, S., and Engel, W.K. (2007). Expression of Nogo-A in human muscle fibers is not specific for amyotrophic lateral sclerosis. Annals of Neurology *62*, 676-677.

Baumann, N.A., Sullivan, D.P., Ohvo-Rekila, H., Simonot, C., Pottekat, A., Klaassen, Z., Beh, C.T., and Menon, A.K. (2005). Transport of newly synthesized sterol to the sterol-enriched plasma membrane occurs via nonvesicular equilibration. Biochemistry-Us *44*, 5816-5826.

Beck, M., Forster, F., Ecke, M., Plitzko, J.M., Melchior, F., Gerisch, G., Baumeister, W., and Medalia, O. (2004). Nuclear pore complex structure and dynamics revealed by cryoelectron tomography. Science *306*, 1387-1390.

Beck, M., Schmidt, A., Malmstroem, J., Claassen, M., Ori, A., Szymborska, A., Herzog, F., Rinner, O., Ellenberg, J., and Aebersold, R. (2011). The quantitative proteome of a human cell line. Mol Syst Biol *7*, 549.

Benyamini, P., Webster, P., and Meyer, D.I. (2009). Knockdown of p180 eliminates the terminal differentiation of a secretory cell line. Mol Biol Cell *20*, 732-744.

Bernales, S., McDonald, K.L., and Walter, P. (2006). Autophagy counterbalances endoplasmic reticulum expansion during the unfolded protein response. Plos Biology *4*, 2311-2324.

Betzig, E., Patterson, G.H., Sougrat, R., Lindwasser, O.W., Olenych, S., Bonifacino, J.S., Davidson, M.W., Lippincott-Schwartz, J., and Hess, H.F. (2006). Imaging intracellular fluorescent proteins at nanometer resolution. Science *313*, 1642-1645.

Bian, X., Klemm, R.W., Liu, T.Y., Zhang, M., Sun, S., Sui, X.W., Liu, X.Q., Rapoport, T.A.,

and Hu, J.J. (2011). Structures of the atlastin GTPase provide insight into homotypic fusion of endoplasmic reticulum membranes. P Natl Acad Sci USA *108*, 3976-3981.

Bjork, S., Hurt, C.M., Ho, V.K., and Angelotti, T. (2013). REEPs Are Membrane Shaping Adapter Proteins That Modulate Specific G Protein-Coupled Receptor Trafficking by Affecting ER Cargo Capacity. Plos One *8*.

Blackstone, C. (2012). Cellular Pathways of Hereditary Spastic Paraplegia. Annu Rev Neurosci *35*, 25-47.

Blackstone, C., O'Kane, C.J., and Reid, E. (2011). Hereditary spastic paraplegias: membrane traffic and the motor pathway. Nat Rev Neurosci *12*, 31-42.

Block, B.A., Imagawa, T., Campbell, K.P., and Franziniarmstrong, C. (1988). Structural Evidence for Direct Interaction between the Molecular-Components of the Transverse Tubule Sarcoplasmic-Reticulum Junction in Skeletal-Muscle. J Cell Biol *107*, 2587-2600.

Boldogh, I.R., and Pon, L.A. (2007). Mitochondria on the move. Trends Cell Biol *17*, 502-510.

Boucrot, E., Pick, A., Camdere, G., Liska, N., Evergren, E., McMahon, H.T., and Kozlov, M.M. (2012). Membrane Fission Is Promoted by Insertion of Amphipathic Helices and Is Restricted by Crescent BAR Domains. Cell *149*, 124-136.

Boykov, Y., and Kolmogorov, V. (2004). An experimental comparison of min-cut/max-flow algorithms for energy minimization in vision. Ieee T Pattern Anal *26*, 1124-1137.

Braakman, I., Helenius, J., and Helenius, A. (1992). Manipulating Disulfide Bond Formation and Protein Folding in the Endoplasmic-Reticulum. Embo Journal *11*, 1717-1722.

Briggman, K.L., and Bock, D.D. (2012). Volume electron microscopy for neuronal circuit reconstruction. Curr Opin Neurobiol *22*, 154-161.

Burke, B., and Ellenberg, J. (2002). Remodelling the walls of the nucleus. Nat Rev Mol Cell Biol *3*, 487-497.

Byrnes, L.J., and Sondermann, H. (2011). Structural basis for the nucleotide-dependent dimerization of the large G protein atlastin-1/SPG3A. P Natl Acad Sci USA *108*, 2216-2221.

Campelo, F., McMahon, H.T., and Kozlov, M.M. (2008). The hydrophobic insertion mechanism of membrane curvature generation by proteins. Biophys J *95*, 2325-2339.

Carpenter, A.E., Jones, T.R., Lamprecht, M.R., Clarke, C., Kang, I.H., Friman, O., Guertin, D.A., Chang, J.H., Lindquist, R.A., Moffat, J., *et al.* (2006). CellProfiler: image analysis software for identifying and quantifying cell phenotypes. Genome Biology *7*.

Carrasco, S., and Meyer, T. (2011). STIM Proteins and the Endoplasmic Reticulum-Plasma Membrane Junctions. Annu Rev Biochem *80*, 973-1000.

Castermans, D., Vermeesch, J.R., Fryns, J.P., Steyaert, J.G., Van de Ven, W.J.M., Creemers, J.W.M., and Devriendt, K. (2007). Identification and characterization of the TRIP8 and REEP3 genes on chromosome 10q21.3 as novel candidate genes for autism. Eur J Hum Genet *15*, 422-431.

Chardes, C., Melenec, P., Bertrand, V., and Lenne, P.F. (2014). Setting up a simple light sheet microscope for in toto imaging of C. elegans development. J Vis Exp.

Chen, B.C., Legant, W.R., Wang, K., Shao, L., Milkie, D.E., Davidson, M.W., Janetopoulos, C., Wu, X.F.S., Hammer, J.A., Liu, Z., *et al.*

(2014). Lattice light-sheet microscopy: Imaging molecules to embryos at high spatiotemporal resolution. Science *346*, 439-+.

Chen, L.L., Gou, S.P., Yao, Y., Bai, J., Jiao, L.C., and Sheng, K. (2016). Denoising of Low Dose CT Image with Context - Based BM3D. Proceedings of the 2016 Ieee Region 10 Conference (Tencon), 682-685.

Chen, M.S., Huber, A.B., van der Haar, M.E., Frank, M., Schnell, L., Spillmann, A.A., Christ, F., and Schwab, M.E. (2000). Nogo-A is a myelin-associated neurite outgrowth inhibitor and an antigen for monoclonal antibody IN-1. Nature *403*, 434-439.

Chen, R., Jin, R., Wu, L., Ye, X., Yang, Y., Luo, K., Wang, W., Wu, D., Ye, X., Huang, L., *et al.* (2011). Reticulon 3 attenuates the clearance of cytosolic prion aggregates via inhibiting autophagy. Autophagy *7*, 205-216.

Chen, S., Desai, T., McNew, J.A., Gerard, P., and Novick, P.J. (2015). Lunapark stabilizes nascent three-way junctions in the endoplasmic reticulum. P Natl Acad Sci USA *112*, 418-423.

Chen, S.L., Novick, P., and Ferro-Novick, S. (2012). ER network formation requires a balance of the dynamin-like GTPase Sey1p and the Lunapark family member Lnp1p. Nat Cell Biol *14*, 707-716.

Chiurchiu, V., Cencioni, M.T., Bisicchia, E., De Bardi, M., Gasperini, C., Borsellino, G., Centonze, D., Battistini, L., and Maccarrone, M. (2013). Distinct Modulation of Human Myeloid and Plasmacytoid Dendritic Cells by Anandamide in Multiple Sclerosis. Annals of Neurology *73*, 626-636.

Chiurchiu, V., and Maccarrone, M. (2011). Chronic Inflammatory Disorders and Their Redox Control: From Molecular Mechanisms to Therapeutic Opportunities. Antioxid Redox Sign *15*, 2605-2641.

Cooney, J.R., Hurlburt, J.L., Selig, D.K., Harris, K.M., and Fiala, J.C. (2002). Endosomal compartments serve multiple hippocampal dendritic spines from a widespread rather than a local store of recycling membrane. J Neurosci *22*, 2215-2224.

Copic, A., Latham, C.F., Horlbeck, M.A., D'Arcangelo, J.G., and Miller, E.A. (2012). ER Cargo Properties Specify a Requirement for COPII Coat Rigidity Mediated by Sec13p. Science *335*, 1359-1362.

Courvalin, J.C., Segil, N., Blobel, G., and Worman, H.J. (1992). The Lamin-B Receptor of the Inner Nuclear-Membrane Undergoes Mitosis-Specific Phosphorylation and Is a Substrate for P34cdc2-Type Protein-Kinase. J Biol Chem *267*, 19035-19038.

Csordas, G., Renken, C., Varnai, P., Walter, L., Weaver, D., Buttle, K.F., Balla, T., Mannella, C.A., and Hajnoczky, G. (2006). Structural and functional features and significance of the physical linkage between ER and mitochondria. J Cell Biol *174*, 915-921.

de Boer, P., Hoogenboom, J.P., and Giepmans, B.N.G. (2015). Correlated light and electron microscopy: ultrastructure lights up! Nature Methods *12*, 503-513.

Diaz, A., Wang, X.F., and Ahlquist, P. (2010). Membrane-shaping host reticulon proteins play crucial roles in viral RNA replication compartment formation and function. P Natl Acad Sci USA *107*, 16291-16296.

Dodd, D.A., Niederoest, B., Bloechlinger, S., Dupuis, L., Loeffler, J.P., and Schwab, M.E. (2005). Nogo-A, -B, and -C are found on the cell surface and interact together in many different cell types. J Biol Chem *280*, 12494-12502.

Dupuis, L., de Tapia, M., Rene, F., Lutz-Bucher, B., Gordon, J.W., Mercken, L., Pradier, L., and

Loeffler, J.P. (2000). Differential screening of mutated SOD1 transgenic mice reveals early up-regulation of a fast axonal transport component in spinal cord motor neurons. Neurobiol Dis *7*, 274-285.

Dupuis, L., Gonzalez de Aguilar, J.L., di Scala, F., Rene, F., de Tapia, M., Pradat, P.F., Lacomblez, L., Seihlan, D., Prinjha, R., Walsh, F.S., *et al.* (2002). Nogo provides a molecular marker for diagnosis of amyotrophic lateral sclerosis. Neurobiol Dis *10*, 358-365.

Eden, E.R., White, I.J., Tsapara, A., and Futter, C.E. (2010). Membrane contacts between endosomes and ER provide sites for PTP1B-epidermal growth factor receptor interaction. Nat Cell Biol *12*, 267-U264.

Ehrlich, M., Boll, W., Van Oijen, A., Hariharan, R., Chandran, K., Nibert, M.L., and Kirchhausen, T. (2004). Endocytosis by random initiation and stabilization of clathrin-coated pits. Cell *118*, 591-605.

Ellenberg, J., Siggia, E.D., Moreira, J.E., Smith, C.L., Presley, J.F., Worman, H.J., and LippincottSchwartz, J. (1997). Nuclear membrane dynamics and reassembly in living cells: Targeting of an inner nuclear membrane protein in interphase and mitosis. J Cell Biol *138*, 1193-1206.

Erlandson, K.J., Bisht, H., Weisberg, A.S., Hyun, S.I., Hansen, B.T., Fischer, E.R., Hinshaw, J.E., and Moss, B. (2016). Poxviruses Encode a Reticulon-Like Protein that Promotes Membrane Curvature. Cell Rep *14*, 2084-2091.

Fedorov, A., Beichel, R., Kalpathy-Cramer, J., Finet, J., Fillion-Robin, J.C., Pujol, S., Bauer, C., Jennings, D., Fennessy, F., Sonka, M., *et al.* (2012). 3D Slicer as an image computing platform for the Quantitative Imaging Network. Magn Reson Imaging *30*, 1323-1341.

Fink, J.K. (2013). Hereditary spastic paraplegia: clinico-pathologic features and emerging molecular mechanisms. Acta Neuropathol *126*, 307-328.

Foster, L.J., de Hoog, C.L., Zhang, Y., Zhang, Y., Xie, X., Mootha, V.K., and Mann, M. (2006). A mammalian organelle map by protein correlation profiling. Cell *125*, 187-199.

Fournier, A.E., GrandPre, T., and Strittmatter, S.M. (2001). Identification of a receptor mediating Nogo-66 inhibition of axonal regeneration. Nature *409*, 341-346.

Friedman, J.R., Lackner, L.L., West, M., DiBenedetto, J.R., Nunnari, J., and Voeltz, G.K. (2011). ER tubules mark sites of mitochondrial division. Science *334*, 358-362.

Friedman, J.R., and Voeltz, G.K. (2011). The ER in 3D: a multifunctional dynamic membrane network. Trends Cell Biol *21*, 709-717.

Friedman, J.R., Webster, B.M., Mastronarde, D.N., Verhey, K.J., and Voeltz, G.K. (2010). ER sliding dynamics and ER-mitochondrial contacts occur on acetylated microtubules. J Cell Biol *190*, 363-375.

Friedrich, M., Gan, Q., Ermolayev, V., and Harms, G.S. (2011). STED-SPIM: Stimulated emission depletion improves sheet illumination microscopy resolution. Biophys J *100*, L43-45.

Galderisi, U., Jori, F.P., and Giordano, A. (2003). Cell cycle regulation and neural differentiation. Oncogene *22*, 5208-5219.

GrandPre, T., Nakamura, F., Vartanian, T., and Strittmatter, S.M. (2000). Identification of the Nogo inhibitor of axon regeneration as a Reticulon protein. Nature *403*, 439-444.

Grigoriev, I., Gouveia, S.M., van der Vaart, B., Demmers, J., Smyth, J.T., Honnappa, S., Splinter, D., Steinmetz, M.O., Putney, J.W., Jr.,

Hoogenraad, C.C., *et al.* (2008). STIM1 is a MT-plus-end-tracking protein involved in remodeling of the ER. Curr Biol *18*, 177-182.

Grumati, P., Morozzi, G., Holper, S., Mari, M., Harwardt, M.L.I.E., Yan, R.Q., Muller, S., Reggiori, F., Heilemann, M., and Dikic, I. (2017). Full length RTN3 regulates turnover of tubular endoplasmic reticulum via selective autophagy. Elife *6*.

Harel, N.Y., Cudkowicz, M.E., Brown, R.H., and Strittmatter, S.M. (2009). Serum Nogo-A levels are not elevated in amyotrophic lateral sclerosis patients. Biomarkers *14*, 414-417.

Hayashi, T., Rizzuto, R., Hajnoczky, G., and Su, T.P. (2009). MAM: more than just a housekeeper. Trends in Cell Biology *19*, 81-88.

He, W., Lu, Y., Qahwash, I., Hu, X.Y., Chang, A., and Yan, R. (2004). Reticulon family members modulate BACE1 activity and amyloid-beta peptide generation. Nat Med *10*, 959-965.

Hetzer, M.W. (2010). The Nuclear Envelope. Csh Perspect Biol *2*.

Hetzer, M.W., Walther, T.C., and Mattaj, I.W. (2005). Pushing the envelope: Structure, function, and dynamics of the nuclear periphery. Annu Rev Cell Dev Bi *21*, 347-380.

Holman, T., Thompson, A., Ghosh, K., Goldbeck, R., Zhu, Z.W., and Vulpe, C. (2006). INOR 619-Spectroscopic and biochemical characterization of heme binding to yeast Dap1p and mouse PGRMC1p. Abstr Pap Am Chem S *232*.

Houben, F., Ramaekers, F.C.S., Snoeckx, L.H.E.H., and Broers, J.L.V. (2007). Role of nuclear lamina-cytoskeleton interactions in the maintenance of cellular strength. Bba-Mol Cell Res *1773*, 675-686.

Hu, J., Shibata, Y., Zhu, P.P., Voss, C., Rismanchi, N., Prinz, W.A., Rapoport, T.A., and Blackstone, C. (2009). A class of dynamin-like GTPases involved in the generation of the tubular ER network. Cell *138*, 549-561.

Hu, X., Shi, Q., Zhou, X., He, W., Yi, H., Yin, X., Gearing, M., Levey, A., and Yan, R. (2007). Transgenic mice overexpressing reticulon 3 develop neuritic abnormalities. EMBO J *26*, 2755-2767.

Huang, Y., and Mucke, L. (2012). Alzheimer mechanisms and therapeutic strategies. Cell *148*, 1204-1222.

Huisken, J., and Stainier, D.Y. (2007). Even fluorescence excitation by multidirectional selective plane illumination microscopy (mSPIM). Opt Lett *32*, 2608-2610.

Hurt, C.M., Bjork, S., Ho, V.K., Gilsbach, R., Hein, L., and Angelotti, T. (2014). REEP1 and REEP2 proteins are preferentially expressed in neuronal and neuronal-like exocytotic tissues. Brain Res *1545*, 12-22.

Iwahashi, J., Hamada, N., and Watanabe, H. (2007). Two hydrophobic segments of the RTN1 family determine the ER localization and retention. Biochem Bioph Res Co *355*, 508-512.

Jeffrey, P.D., Russo, A.A., Polyak, K., Gibbs, E., Hurwitz, J., Massague, J., and Pavletich, N.P. (1995). Mechanism of CDK activation revealed by the structure of a cyclinA-CDK2 complex. Nature *376*, 313-320.

Joensuu, M., Belevich, I., Ramo, O., Nevzorov, I., Vihinen, H., Puhka, M., Witkos, T.M., Lowe, M., Vartiainen, M.K., and Jokitalo, E. (2014). ER sheet persistence is coupled to myosin 1c-regulated dynamic actin filament arrays. Molecular Biology of the Cell *25*, 1111-1126.

Jokic, N., Gonzalez de Aguilar, J.L., Pradat, P.F., Dupuis, L., Echaniz-Laguna, A., Muller, A., Dubourg, O., Seilhean, D., Hauw, J.J.,

Loeffler, J.P., *et al.* (2005). Nogo expression in muscle correlates with amyotrophic lateral sclerosis severity. Ann Neurol *57*, 553-556.

Jozsef, L., Tashiro, K., Kuo, A., Park, E.J., Skoura, A., Albinsson, S., Rivera-Molina, F., Harrison, K.D., Iwakiri, Y., Toomre, D., *et al.* (2014). Reticulon 4 is necessary for endoplasmic reticulum tubulation, STIM1-Orai1 coupling, and store-operated calcium entry. The Journal of biological chemistry *289*, 9380-9395.

Kabeya, Y., Mizushima, N., Uero, T., Yamamoto, A., Kirisako, T., Noda, T., Kominami, E., Ohsumi, Y., and Yoshimori, T. (2000). LC3, a mammalian homologue of yeast Apg8p, is localized in autophagosome membranes after processing. Embo Journal *19*, 5720-5728.

Kaddoum, L., Magdeleine, E., Waldo, G.S., Joly, E., and Cabantous, S. (2010). One-step split GFP staining for sensitive protein detection and localization in mammalian cells. Biotechniques *49*, 727-+.

Kankaanpaa, P., Paavolainen, L., Tiitta, S., Karjalainen, M., Paivarinne, J., Nieminen, J., Marjomaki, V., Heino, J., and White, D.J. (2012). BioImageXD: an open, general-purpose and high-throughput image-processing platform. Nature Methods *9*, 683-689.

Karnezis, T., Mandemakers, W., McQualter, J.L., Zheng, B.H., Ho, P.P., Jordan, K.A., Murray, B.M., Barres, B., Tessier-Lavigne, M., and Bernard, C.C.A. (2004). The neurite outgrowth inhibitor Nogo A is involved in autoimmune-mediated demyelination. Nat Neurosci *7*, 736-744.

Keller, P.J., Schmidt, A.D., Wittbrodt, J., and Stelzer, E.H. (2008). Reconstruction of zebrafish early embryonic development by scanned light sheet microscopy. Science *322*, 1065-1069.

Keller, P.J., Schmidt, A.D., Wittbrodt, J., and Stelzer, E.H. (2011). Digital scanned laser light-sheet fluorescence microscopy (DSLM) of zebrafish and Drosophila embryonic development. Cold Spring Harb Protoc *2011*, 1235-1243.

Khaminets, A., Heinrich, T., Mari, M., Grumati, P., Huebner, A.K., Akutsu, M., Liebmann, L., Stolz, A., Nietzsche, S., Koch, N., *et al.* (2015). Regulation of endoplasmic reticulum turnover by selective autophagy. Nature *522*, 354-+.

King, M.C., Drivas, T.G., and Blobel, G. (2008). A network of nuclear envelope membrane proteins linking centromeres to microtubules. Cell *134*, 427-438.

Klar, T.A., Engel, E., and Hell, S.W. (2001). Breaking Abbe's diffraction resolution limit in fluorescence microscopy with stimulated emission depletion beams of various shapes. Phys Rev E *64*.

Klopfenstein, D.R., Kappeler, F., and Hauri, H.P. (1998). A novel direct interaction of endoplasmic reticulum with microtubules. EMBO J *17*, 6168-6177.

Klopfenstein, D.R., Klumperman, J., Lustig, A., Kammerer, R.A., Oorschot, V., and Hauri, H.P. (2001). Subdomain-specific localization of CLIMP-63 (p63) in the endoplasmic reticulum is mediated by its luminal alpha-helical segment. J Cell Biol *153*, 1287-1300.

Knoops, K., Kikkert, M., van den Worm, S.H.E., Zevenhoven-Dobbe, J.C., van der Meer, Y., Koster, A.J., Mommaas, A.M., and Snijder, E.J. (2008). SARS-coronavirus replication is supported by a reticulovesicular network of modified endoplasmic reticulum. Plos Biology *6*, 1957-1974.

Kornmann, B., Currie, E., Collins, S.R., Schuldiner, M., Nunnari, J., Weissman, J.S., and Walter, P. (2009). An ER-Mitochondria

Tethering Complex Revealed by a Synthetic Biology Screen. Science *325*, 477-481.

Kremer, J.R., Mastronarde, D.N., and McIntosh, J.R. (1996). Computer visualization of three-dimensional image data using IMOD. J Struct Biol *116*, 71-76.

Kuang, E., Wan, Q.W., Li, X.J., Xu, H., Liu, Q.Z., and Qi, Y.P. (2005). ER Ca2+ depletion triggers apoptotic signals for endoplasmic reticulum (ER) overload response induced by overexpressed reticulon 3 (RTN3/HAP). J Cell Physiol *204*, 549-559.

Kume, H., Konishi, Y., Murayama, K.S., Kametani, F., and Araki, W. (2009a). Expression of reticulon 3 in Alzheimer's disease brain. Neuropath Appl Neuro *35*, 178-188.

Kume, H., Murayama, K.S., and Araki, W. (2009b). The Two-Hydrophobic Domain Tertiary Structure of Reticulon Proteins Is Critical for Modulation of beta-Secretase BACE1. J Neurosci Res *87*, 2963-2972.

Kurth, I., Pamminger, T., Hennings, J.C., Soehendra, D., Huebner, A.K., Rotthier, A., Baets, J., Senderek, J., Topaloglu, H., Farrell, S.A., *et al.* (2009). Mutations in FAM134B, encoding a newly identified Golgi protein, cause severe sensory and autonomic neuropathy. Nat Genet *41*, 1179-1181.

Lauren, J., Hu, F.H., Chin, J., Liao, J., Airaksinen, M.S., and Strittmatter, S.M. (2007). Characterization of myelin ligand complexes with neuronal Nogo-66 receptor family members. J Biol Chem *282*, 5715-5725.

Le Breton, M., Cormier, P., Belle, R., Mulner-Lorillon, O., and Morales, J. (2005). Translational control during mitosis. Biochimie *87*, 805-811.

Lee, C., and Chen, L.B. (1988). Dynamic Behavior of Endoplasmic-Reticulum in Living Cells. Cell *54*, 37-46.

Lee, J.Y., and Petratos, S. (2013). Multiple Sclerosis: Does Nogo Play a Role? Neuroscientist *19*, 394-408.

Lennemann, N.J., and Coyne, C.B. (2017). Dengue and Zika viruses subvert reticulophagy by NS2B3-mediated cleavage of FAM134B. Autophagy *13*, 322-332.

Li, Y.F., and Prinz, W.A. (2004). ATP-binding cassette (ABC) transporters mediate nonvesicular, raft-modulated sterol movement from the plasma membrane to the endoplasmic reticulum. J Biol Chem *279*, 45226-45234.

Limpens, R.W.A.L., van der Schaar, H.M., Kumar, D., Koster, A.J., Snijder, E.J., van Kuppeveld, F.J.M., and Barcena, M. (2011). The Transformation of Enterovirus Replication Structures: a Three-Dimensional Study of Single- and Double-Membrane Compartments. Mbio *2*.

Linkert, M., Rueden, C.T., Allan, C., Burel, J.M., Moore, W., Patterson, A., Loranger, B., Moore, J., Neves, C., Macdonald, D., *et al.* (2010). Metadata matters: access to image data in the real world. J Cell Biol *189*, 777-782.

Liu, Y., Bai, G.Q., Cheng, J., Wu, S.H., Wang, L., Yan, F.M., Zhang, L.X., and Cui, Y.F. (2005). [Screening and cloning of hepatitis C virus non-structural protein 4A interacting protein gene in hepatocytes]. Zhonghua Gan Zang Bing Za Zhi *13*, 738-740.

Liu, Z., and Zheng, Y. (2009). A requirement for epsin in mitotic membrane and spindle organization. The Journal of cell biology *186*, 473-480.

Lu, L., Ladinsky, M.S., and Kirchhausen, T. (2009). Cisternal Organization of the

Endoplasmic Reticulum during Mitosis. Molecular Biology of the Cell *20*, 3471-3480.

Lu, L., Ladinsky, M.S., and Kirchhausen, T. (2011). Formation of the postmitotic nuclear envelope from extended ER cisternae precedes nuclear pore assembly. J Cell Biol *194*, 425-440.

Mannan, A.U., Boehm, J., Sauter, S.M., Rauber, A., Byrne, P.C., Neesen, J., and Engel, W. (2006a). Spastin, the most commonly mutated protein in hereditary spastic paraplegia interacts with reticulon 1 an endoplasmic reticulum protein. Neurogenetics *7*, 93-103.

Mannan, A.U., Krawen, P., Sauter, S.M., Boehm, J., Chronowska, A., Paulus, W., Neesen, J., and Engel, W. (2006b). ZFYVE27 (SPG33), a novel spastin-binding protein, is mutated in hereditary spastic paraplegia. American Journal of Human Genetics *79*, 351-357.

McCullough, S., and Lucocq, J. (2005). Endoplasmic reticulum positioning and partitioning in mitotic HeLa cells. J Anat *206*, 415-425.

McMahon, H.T., and Boucrot, E. (2015). Membrane curvature at a glance. Journal of Cell Science *128*, 1065-1070.

Meyer, C., Schmid, R., Scriba, P.C., and Wehling, M. (1996). Purification and partial sequencing of high-affinity progesterone-binding site(s) from porcine liver membranes. Eur J Biochem *239*, 726-731.

Mitchell, J.D., and Borasio, G.D. (2007). Amyotrophic lateral sclerosis. Lancet *369*, 2031-2041.

Montenegro, G., Rebelo, A.P., Connell, J., Allison, R., Babalini, C., D'Aloia, M., Montieri, P., Schule, R., Ishiura, H., Price, J., *et al.* (2012). Mutations in the ER-shaping protein reticulon 2 cause the axon-degenerative disorder hereditary spastic paraplegia type 12. J Clin Invest *122*, 538-544.

Murphy, S.M., Davidson, G.L., Brandner, S., Houlden, H., and Reilly, M.M. (2012). Mutation in FAM134B causing severe hereditary sensory neuropathy. J Neurol Neurosur Ps *83*, 119-120.

Nagaraj, N., Wisniewski, J.R., Geiger, T., Cox, J., Kircher, M., Kelso, J., Paabo, S., and Mann, M. (2011). Deep proteome and transcriptome mapping of a human cancer cell line. Mol Syst Biol *7*, 548.

Nixon-Abell, J., Obara, C.J., Weigel, A.V., Li, D., Legant, W.R., Xu, C.S., Pasolli, H.A., Harvey, K., Hess, H.F., Betzig, E., *et al.* (2016). Increased spatiotemporal resolution reveals highly dynamic dense tubular matrices in the peripheral ER. Science *354*.

Noseworthy, J.H., Lucchinetti, C., Rodriguez, M., and Weinshenker, B.G. (2000). Medical progress: Multiple sclerosis. New Engl J Med *343*, 938-952.

O'Sullivan, N.C., Jahn, T.R., Reid, E., and O'Kane, C.J. (2012). Reticulon-like-1, the Drosophila orthologue of the Hereditary Spastic Paraplegia gene reticulon 2, is required for organization of endoplasmic reticulum and of distal motor axons. Hum Mol Genet *21*, 3356-3365.

Oertle, T., Merkler, D., and Schwab, M.E. (2003). Do cancer cells die because of Nogo-B? Oncogene *22*, 1390-1399.

Oertle, T., and Schwab, M.E. (2003). Nogo and its paRTNers. Trends Cell Biol *13*, 187-194.

Orso, G., Pendin, D., Liu, S., Tosetto, J., Moss, T.J., Faust, J.E., Micaroni, M., Egorova, A., Martinuzzi, A., McNew, J.A., *et al.* (2009). Homotypic fusion of ER membranes requires the dynamin-like GTPase Atlastin. Nature *460*, 978-U958.

Osman, C., Voelker, D.R., and Langer, T. (2011). Making heads or tails of phospholipids in mitochondria. J Cell Biol *192*, 7-16.

Otsuka, S., Steyer, A.M., Schorb, M., Heriche, J.K., Hossain, M.J., Sethi, S., Kueblbeck, M., Schwab, Y., Beck, M., and Ellenberg, J. (2018). Postmitotic nuclear pore assembly proceeds by radial dilation of small membrane openings. Nat Struct Mol Biol *25*, 21-+.

Park, S.H., Zhu, P.P., Parker, R.L., and Blackstone, C. (2010). Hereditary spastic paraplegia proteins REEP1, spastin, and atlastin-1 coordinate microtubule interactions with the tubular ER network. J Clin Invest *120*, 1097-1110.

Peter, B.J., Kent, H.M., Mills, I.G., Vallis, Y., Butler, P.J.G., Evans, P.R., and McMahon, H.T. (2004). BAR domains as sensors of membrane curvature: The amphiphysin BAR structure. Science *303*, 495-499.

Piccinini, F., Balassa, T., Szkalisity, A., Molnar, C., Paavolainen, L., Kujala, K., Buzas, K., Sarazova, M., Pietiainen, V., Kutay, U., *et al.* (2017). Advanced Cell Classifier: User-Friendly Machine-Learning-Based Software for Discovering Phenotypes in High-Content Imaging Data. Cell Syst *4*, 651-+.

Pradat, P.F., Bruneteau, G., de Aguilar, J.L.G., Dupuis, L., Jokic, N., Salachas, F., Le Forestier, N., Echaniz-Laguna, A., Dubourg, O., Hauw, J.J., *et al.* (2007). Muscle Nogo-A expression is a prognostic marker in lower motor neuron syndromes. Annals of Neurology *62*, 15-20.

Puhka, M., Joensuu, M., Vihinen, H., Belevich, I., and Jokitalo, E. (2012). Progressive sheet-to-tubule transformation is a general mechanism for endoplasmic reticulum partitioning in dividing mammalian cells. Mol Biol Cell *23*, 2424-2432.

Puhka, M., Vihinen, H., Joensuu, M., and Jokitalo, E. (2007). Endoplasmic reticulum remains continuous and undergoes sheet-to-tubule transformation during cell division in mammalian cells. J Cell Biol *179*, 895-909.

Reindl, M., Khantane, S., Ehling, R., Schanda, K., Lutterotti, A., Brinkhoff, C., Oertle, T., Schwab, M.E., Deisenhammer, F., Berger, T., *et al.* (2003). Serum and cerebrospinal fluid antibodies to Nogo-A in patients with multiple sclerosis and acute neurological disorders. J Neuroimmunol *145*, 139-147.

Rizzuto, R., Pinton, P., Carrington, W., Fay, F.S., Fogarty, K.E., Lifshitz, L.M., Tuft, R.A., and Pozzan, T. (1998). Close contacts with the endoplasmic reticulum as determinants of mitochondrial Ca2+ responses. Science *280*, 1763-1766.

Rocha, N., Kuijl, C., van der Kant, R., Janssen, L., Houben, D., Janssen, H., Zwart, W., and Neefjes, J. (2009). Cholesterol sensor ORP1L contacts the ER protein VAP to control Rab7-RILP-p150 Glued and late endosome positioning. J Cell Biol *185*, 1209-1225.

Roos, J., DiGregorio, P.J., Yeromin, A.V., Ohlsen, K., Lioudyno, M., Zhang, S., Safrina, O., Kozak, J.A., Wagner, S.L., Cahalan, M.D., *et al.* (2005). STIM1, an essential and conserved component of store-operated Ca2+ channel function. J Cell Biol *169*, 435-445.

Roux, K.J., Kim, D.I., Raida, M., and Burke, B. (2012). A promiscuous biotin ligase fusion protein identifies proximal and interacting proteins in mammalian cells. J Cell Biol *196*, 801-810.

Rowland, A.A., Chitwood, P.J., Phillips, M.J., and Voeltz, G.K. (2014). ER Contact Sites Define the Position and Timing of Endosome Fission. Cell *159*, 1027-1041.

Saito, H., Kubota, M., Roberts, R.W., Chi, Q.Y., and Matsunami, H. (2004). RTP family members induce functional expression of mammalian odorant receptors. Cell *119*, 679-691.

Schindelin, J., Arganda-Carreras, I., Frise, E., Kaynig, V., Longair, M., Pietzsch, T., Preibisch, S., Rueden, C., Saalfeld, S., Schmid, B., *et al.* (2012). Fiji: an open-source platform for biological-image analysis. Nature Methods *9*, 676-682.

Schirmer, E.C., Florens, L., Guan, T.L., Yates, J.R., and Gerace, L. (2003). Nuclear membrane proteins with potential disease links found by subtractive proteomics. Science *301*, 1380-1382.

Schlaitz, A.L., Thompson, J., Wong, C.C., Yates, J.R., 3rd, and Heald, R. (2013). REEP3/4 ensure endoplasmic reticulum clearance from metaphase chromatin and proper nuclear envelope architecture. Dev Cell *26*, 315-323.

Schroeder, L.K., Barentine, A.E.S., Merta, H., Schweighofer, S., Zhang, Y., Baddeley, D., Bewersdorf, J., and Bahmanyar, S. (2019). Dynamic nanoscale morphology of the ER surveyed by STED microscopy. J Cell Biol *218*, 83-96.

Senda, T., and Yoshinaga-Hirabayashi, T. (1998). Intermembrane bridges within membrane organelles revealed by quick-freeze deep-etch electron microscopy. Anat Rec *251*, 339-345.

Shibata, Y., Hu, J.J., Kozlov, M.M., and Rapoport, T.A. (2009). Mechanisms Shaping the Membranes of Cellular Organelles. Annu Rev Cell Dev Bi *25*, 329-354.

Shibata, Y., Shemesh, T., Prinz, W.A., Palazzo, A.F., Kozlov, M.M., and Rapoport, T.A. (2010). Mechanisms determining the morphology of the peripheral ER. Cell *143*, 774-788.

Shibata, Y., Voss, C., Rist, J.M., Hu, J., Rapoport, T.A., Prinz, W.A., and Voeltz, G.K. (2008). The reticulon and DP1/Yop1p proteins form immobile oligomers in the tubular endoplasmic reticulum. J Biol Chem *283*, 18892-18904.

Shih, S.R., Stollar, V., and Li, M.L. (2011). Host Factors in Enterovirus 71 Replication. J Virol *85*, 9658-9666.

Smyth, J.T., Beg, A.M., Wu, S., Putney, J.W., Jr., and Rusan, N.M. (2012). Phosphoregulation of STIM1 leads to exclusion of the endoplasmic reticulum from the mitotic spindle. Curr Biol *22*, 1487-1493.

Staehelin, L.A. (1997). The plant ER: A dynamic organelle composed of a large number of discrete functional domains. Plant J *11*, 1151-1165.

Starr, D.A., and Han, M. (2002). Role of ANC-1 in tethering nuclei to the actin cytoskeleton. Science *298*, 406-409.

Stefan, C.J., Manford, A.G., Baird, D., Yamada-Hanff, J., Mao, Y.X., and Emr, S.D. (2011). Osh Proteins Regulate Phosphoinositide Metabolism at ER-Plasma Membrane Contact Sites. Cell *144*, 389-401.

Steiner, P., Kulangara, K., Sarria, J.C.F., Glauser, L., Regazzi, R., and Hirling, H. (2004). Reticulon 1-C/neuroendocrine-specific protein-C interacts with SNARE proteins. Journal of Neurochemistry *89*, 569-580.

Stone, S.J., and Vance, J.E. (2000). Phosphatidylserine synthase-1 and-2 are localized to mitochondria-associated membranes. J Biol Chem *275*, 34534-34540.

Suetsugu, S. (2010). The proposed functions of membrane curvatures mediated by the BAR domain superfamily proteins. J Biochem *148*, 1-12.

Suetsugu, S., Toyooka, K., and Senju, Y. (2010). Subcellular membrane curvature mediated by the BAR domain superfamily proteins. Semin Cell Dev Biol *21*, 340-349.

Tagami, S., Eguchi, Y., Kinoshita, M., Takeda, M., and Tsujimoto, Y. (2000). A novel protein, RTN-x(S), interacts with both Bcl-x(L) and Bcl-2 on endoplasmic reticulum and reduces their anti-apoptotic activity. Oncogene *19*, 5736-5746.

Takeshima, H., Komazaki, S., Nishi, M., Iino, M., and Kangawa, K. (2000). Junctophilins: a novel family of junctional membrane complex proteins. Mol Cell *6*, 11-22.

Tang, W.F., Yang, S.Y., Wu, B.W., Jheng, J.R., Chen, Y.L., Shih, C.H., Lin, K.H., Lai, H.C., Tang, P., and Horng, J.T. (2007). Reticulon 3 binds the 2C protein of enterovirus 71 and is required for viral replication. J Biol Chem *282*, 5888-5898.

Terasaki, M. (2018). Axonal endoplasmic reticulum is very narrow. Journal of Cell Science *131*.

Terasaki, M., Shemesh, T., Kasthuri, N., Klemm, R.W., Schalek, R., Hayworth, K.J., Hand, A.R., Yankova, M., Huber, G., Lichtman, J.W., *et al.* (2013). Stacked Endoplasmic Reticulum Sheets Are Connected by Helicoidal Membrane Motifs. Cell *154*, 285-296.

Terasima, T., and Tolmach, L.J. (1963). Growth and nucleic acid synthesis in synchronously dividing populations of HeLa cells. Exp Cell Res *30*, 344-362.

Tomer, R., Khairy, K., Amat, F., and Keller, P.J. (2012). Quantitative high-speed imaging of entire developing embryos with simultaneous multiview light-sheet microscopy. Nat Methods *9*, 755-763.

Toulmay, A., and Prinz, W.A. (2011). Lipid transfer and signaling at organelle contact sites: the tip of the iceberg. Curr Opin Cell Biol *23*, 458-463.

Tran, E.J., and Wente, S.R. (2006). Dynamic nuclear pore complexes: life on the edge. Cell *125*, 1041-1053.

Travers, K.J., Patil, C.K., Wodicka, L., Lockhart, D.J., Weissman, J.S., and Walter, P. (2000). Functional and genomic analyses reveal an essential coordination between the unfolded protein response and ER-associated degradation. Cell *101*, 249-258.

Truong, T.V., Supatto, W., Koos, D.S., Choi, J.M., and Fraser, S.E. (2011). Deep and fast live imaging with two-photon scanned light-sheet microscopy. Nat Methods *8*, 757-760.

van Hemert, M.J., de Steensma, H.Y., and van Heusden, G.P.H. (2001). 14-3-3 proteins: key regulators of cell division, signalling and apoptosis. Bioessays *23*, 936-946.

van Meer, G., Voelker, D.R., and Feigenson, G.W. (2008). Membrane lipids: where they are and how they behave. Nat Rev Mol Cell Bio *9*, 112-124.

Vance, J.E. (1990). Phospholipid-Synthesis in a Membrane-Fraction Associated with Mitochondria. J Biol Chem *265*, 7248-7256.

Vandevelde, H.J.K., Roebroek, A.J.M., Senden, N.H.M., Ramaekers, F.C.S., and Vandeven, W.J.M. (1994). Nsp-Encoded Reticulons, Neuroendocrine Proteins of a Novel Gene Family Associated with Membranes of the Endoplasmic-Reticulum. Journal of Cell Science *107*, 2403-2416.

Voelker, D.R. (2000). Interorganelle transport of aminoglycerophospholipids. Bba-Mol Cell Biol L *1486*, 97-107.

Voeltz, G.K., and Prinz, W.A. (2007). Sheets, ribbons and tubules - how organelles get their shape. Nat Rev Mol Cell Biol *8*, 258-264.

Voeltz, G.K., Prinz, W.A., Shibata, Y., Rist, J.M., and Rapoport, T.A. (2006). A class of membrane proteins shaping the tubular endoplasmic reticulum. Cell *124*, 573-586.

Wakana, Y., Koyama, S., Nakajima, K., Hatsuzawa, K., Nagahama, M., Tani, K., Hauri, H.P., Melancon, P., and Tagaya, M. (2005). Reticulon 3 is involved in membrane trafficking between the endoplasmic reticulum and Golgi. Biochem Bioph Res Co *334*, 1198-1205.

Walter, P., and Ron, D. (2011). The Unfolded Protein Response: From Stress Pathway to Homeostatic Regulation. Science *334*, 1081-1086.

Wan, Q.W., Kuang, E., Dong, W., Zhou, S.M., Xu, H., Qi, Y.P., and Liu, Y.L. (2007). Reticulon 3 mediates Bcl-2 accumulation in mitochondria in response to endoplasmic reticulum stress. Apoptosis *12*, 319-328.

Wang, S., Romano, F.B., Field, C.M., Mitchison, T.J., and Rapoport, T.A. (2013). Multiple mechanisms determine ER network morphology during the cell cycle in Xenopus egg extracts. J Cell Biol *203*, 801-814.

West, M., Zurek, N., Hoenger, A., and Voeltz, G.K. (2011). A 3D analysis of yeast ER structure reveals how ER domains are organized by membrane curvature. J Cell Biol *193*, 333-346.

Wieczorek, D.F., and Hughes, S.R. (1991). Developmentally Regulated Cdna Expressed Exclusively in Neural Tissue. Mol Brain Res *10*, 33-41.

Wojcik, S., Engel, W.K., and Askanas, V. (2006). Increased expression of Noga-A in ALS muscle biopsies is not unique for this disease. Acta Myol *25*, 116-118.

Wu, Y.M., Whiteus, C., Xu, C.S., Hayworth, K.J., Weinberg, R.J., Hess, H.F., and De Camilli, P. (2017). Contacts between the endoplasmic reticulum and other membranes in neurons. P Natl Acad Sci USA *114*, E4859-E4867.

Yang, Y.S., and Strittmatter, S.M. (2007). The reticulons: a family of proteins with diverse functions. Genome Biol *8*, 234.

Yao, L., Xie, D.Y., Geng, L., Shi, D., Huang, J., Wu, Y.F., Lv, F., Liang, D.D., Li, L., Liu, Y., *et al.* (2018). REEP5 (Receptor Accessory Protein 5) Acts as a Sarcoplasmic Reticulum Membrane Sculptor to Modulate Cardiac Function. J Am Heart Assoc *7*.

Yokota, T., Mishra, M., Akatsu, H., Tani, Y., Miyauchi, T., Yamamoto, T., Kosaka, K., Nagai, Y., Sawada, T., and Heese, K. (2006). Brain site-specific gene expression analysis in Alzheimer's disease patients. Eur J Clin Invest *36*, 820-830.

Zhu, L., Xiang, R., Dong, W., Liu, Y.L., and Qi, Y.P. (2007). Anti-apoptotic activity of Bcl-2 is enhanced by its interaction with RTN3. Cell Biol Int *31*, 825-830.

Zimmerberg, J., and Kozlov, M.M. (2006). How proteins produce cellular membrane curvature. Nat Rev Mol Cell Bio *7*, 9-19.

I

SCIENTIFIC REPORTS

OPEN

NOGO-A/RTN4A and NOGO-B/RTN4B are simultaneously expressed in epithelial, fibroblast and neuronal cells and maintain ER morphology

Received: 12 April 2016
Accepted: 07 October 2016
Published: 27 October 2016

Olli Rämö[1,*], Darshan Kumar[1,*], Erika Gucciardo[1], Merja Joensuu[1], Maiju Saarekas[1], Helena Vihinen[1,2], Ilya Belevich[1,2], Olli-Pekka Smolander[3], Kui Qian[3], Petri Auvinen[3] & Eija Jokitalo[1,2]

Reticulons (RTNs) are a large family of membrane associated proteins with various functions. NOGO-A/RTN4A has a well-known function in limiting neurite outgrowth and restricting the plasticity of the mammalian central nervous system. On the other hand, Reticulon 4 proteins were shown to be involved in forming and maintaining endoplasmic reticulum (ER) tubules. Using comparative transcriptome analysis and qPCR, we show here that *NOGO-B/RTN4B* and *NOGO-A/RTN4A* are simultaneously expressed in cultured epithelial, fibroblast and neuronal cells. Electron tomography combined with immunolabelling reveal that both isoforms localize preferably to curved membranes on ER tubules and sheet edges. Morphological analysis of cells with manipulated levels of NOGO-B/RTN4B revealed that it is required for maintenance of normal ER shape; over-expression changes the sheet/tubule balance strongly towards tubules and causes the deformation of the cell shape while depletion of the protein induces formation of large peripheral ER sheets.

Two members of reticulon (RTN) family, NOGO-A/RTN4A and NOGO-B/RTN4B, have recently been the focus of intense investigation due to their functions as an inhibitor of neurite outgrowth and involvement in restricting the plasticity of the central nervous system[1–3] and on the other hand, in generating curvature on ER tubules[4]. The discrepancy between these findings comes from the required localization and topology of membrane insertion needed to support these functions. It is difficult to explain how one protein, or structurally very similar isoforms, can be localized on the cytosolic side of the ER membrane and on extracellular side of the plasma membrane (PM)[5].

Mammals have four reticulon genes (*RTN1*, *RTN2*, *RTN3* and *NOGO/RTN4*), each of which, due to differential splicing and promoter usage, can give rise to a range of alternatively spliced transcript variants that are encoding different isoforms[5]. Most transcripts are enriched in nervous tissues. *NOGO-A/RTN4A* has been regarded as a neuron specific form, whereas NOGO-B/RTN4B has a widespread expression pattern, as in case of housekeeping genes[5]. The *RTN* family is characteristic for its highly conserved C-terminal reticulon homology domain (RHD) of 150–200 amino acids containing two hydrophobic stretches separated by a 66 amino-acid hydrophilic loop and followed by a short C-terminal tail[6]. In comparison to the closely conserved C-terminus that may give rise to overlapping functions within the RTN family, no sequence homology can be observed in the N-terminus of the variants[5].

Rapoport and colleagues demonstrated that *NOGO-A/RTN4A* together with DP1 (deleted in polyposis 1, also known as receptor expression enhancing protein 5, REEP5[7]; yeast homolog *Yop1p*[8]) is responsible for generating

[1]Cell and Molecular Biology Program, Institute of Biotechnology, University of Helsinki, Helsinki, Finland. [2]Electron Microscopy Unit, Institute of Biotechnology, University of Helsinki, Helsinki, Finland. [3]DNA Sequencing and Genomics Laboratory, Institute of Biotechnology, University of Helsinki, Helsinki, Finland. *These authors contributed equally to this work. Correspondence and requests for materials should be addressed to E.J. (email: Eija.Jokitalo@Helsinki.fi)

and maintaining ER tubules[4]. Overexpression of these proteins generates long unbranched tubules, whereas their deletion leads to loss of tubular ER in yeast *Saccharomyces cerevisiae*[4]. Authors suggested that the hydrophobic regions of reticulon homology domain may form two hairpin loops that are wedged into the outer membrane leaflet, creating the necessary increase in local surface area needed for high membrane curvature. Local, one-dimensional curvature is extended and stabilized by the formation of extensive homo- and hetero-oligomers between reticulons and DP1/Yop1p generating a scaffold within the membrane along the tubule's length[9].

The formation of reticular ER network of tubules requires interplay between several other proteins. REEPs, a family of membrane associated proteins, have been shown to affect ER structure[4,7,9,10] along with connecting ER tubules to cytoskeleton. Like other ER related proteins, the mutations in REEP1 were found to be associated with neurodegenerative disorder, hereditary spastic paraplegia (HSP)[11,12]. The atlastin (1–3) proteins (and their yeast homolog Sey1p) belong to a large protein family that interact with the reticulons and DP1/Yop1p and stimulate homotypic fusion, *e.g.*, membrane fusion between ER tubules or sheets, to produce branched reticular ER network[9,13,14]. Mutations in or depletion of atlastins in mammalian cells leads to long unbranched ER tubules, and to network fragmentation in fruit fly *Drosophila melanogaster* neurons, while the over-expression leads to ER membrane expansion[14,15]. Atlastin has been shown to bind to ATPase spastin[16] that interacts with RTN1[17].

In the present study, we have performed a comparative transcriptome analysis and quantitative PCR (qPCR) for expression profiling of the whole reticulon family in cultured human hepatoma and mouse fibroblast cell lines and primary mouse neurons, and show that *NOGO-B/RTN4B* is the main *RTN4* isoform expressed in hepatoma and fibroblast cells and *Nogo-A/Rtn4A* in primary neurons. However, in all cell types studied, several of the other *RTN4* isoforms are expressed at reasonable high levels too, suggesting that none of the isoforms should be regarded as a cell type specific isoform. High resolution imaging and localization studies revealed that both NOGO-A/RTN4A and NOGO-B/RTN4B localized on ER. We have been unable to find evidence for RTN4 plasma membrane localization. Using electron tomography (ET) combined with immunolabelling, we were able to show that both proteins localized preferably to curved membranes on ER tubules and sheet edges. Morphological analysis of cells with manipulated levels of NOGO-A/RTN4A or NOGO-B/RTN4B revealed that these proteins are required for maintenance of normal ER shape; over-expression changes the sheet/tubule balance strongly towards tubules and causes the deformation of the cell shape while depletion induces formation of large peripheral ER sheets.

Results

Several reticulon 4 splice variants are simultaneously expressed in cultured human Huh-7, mouse NIH/3T3 and mouse primary neuronal cells. As a starting point for the present study, we performed a comparative transcriptome analysis to study the expression of all *RTN* family members in human hepatoma cell line (Huh-7). For this, we extracted total mRNA for SOLiD sequencing[18,19] from where the reads were mapped to compare the expression levels of *RTN* family members and other ER-related proteins. The analysis revealed that although all four *RTN* genes were simultaneously expressed, expression levels of *RTN3* and *RTN4* were equal and clearly exceeded those of *RTN1* and *RTN2*. Compared to the genes encoding ER structure related proteins, *RTN3* and *RTN4* levels were only slightly lower than ER sheet promoting *CLIMP63*, and clearly higher than *ATL* (encoding for atlastins) and *REEP*s. On the other hand, compared to the genes encoding ER chaperones *CANX* (encoding for calnexin) and *CALR* (encoding for calreticulin), the levels were about 4- and 2-fold lower, respectively (Fig. 1A).

RTN4 gene gives rise to five isoforms, *RTN4A-E*. We used qPCR to determine the expression levels of the splice variants in Huh-7 cells, cultured mouse embryonic fibroblast (NIH/3T3) cells and in mouse primary neurons. First, all *RTN4* isoforms were expressed in Huh-7 cells; *NOGO-B/RTN4B* was the main isoform expressed, and its level was around 4-fold higher compared to *NOGO-C/RTN4C*, 5-fold to *RTN4D* and 30-fold to *NOGO-A/RTN4A*. In contrast, the expression of *RTN4E* was just at detectable level (Fig. 1B). In NIH/3T3 cells, *Nogo-B/Rtn4B* was also the main isoform expressed, and the ratio between A and B isoforms was similar to Huh-7 cells, whereas *Nogo-C/Rtn4C* levels were 17 times lower in NIH/3T3 cells. In mouse neurons, the expression profile was different; *Nogo-A/Rtn4A* was the main isoform and its level was about 8- and 27-folds higher compared to *Nogo-B/Rtn4B* and *Nogo-C/Rtn4C*, respectively (Fig. 1B). The expression of *Rtn4E* and *Rtn4D* were both very low (Fig. 1B). In summary, qPCR revealed that all reticulon 4 isoforms were expressed in human hepatoma cells as well as in mouse fibroblasts and primary neurons, but at varying levels. Comparison of the three cell types revealed clear difference between neurons and other cell types, whereas similar profile was found from non-neuronal cells of human and mouse origin. *NOGO-B/RTN4B* and *Nogo-A/Rtn4A* are the main isoforms in non-neuronal and neuronal cells, respectively. Since *NOGO-A/RTN4A* has reasonably high expression in non-neuronal cells too, it should not be considered purely as a neuron specific isoform.

Endogenous reticulon 4B and 4A localize on ER membranes and show preference to positively curved membranes. Most of the data concerning the localization of RTN4 isoforms on ER membranes are based on over expression data[4,20–22] although few studies have been done using antibodies against endogenous proteins[23–25]. In our study, we used cell lines with different ER morphology and network organization to analyse the localization of endogenous NOGO-B/RTN4B and NOGO-A/RTN4A. ER in Huh-7 cells consist of highly abundant, large ribosome studded fenestrated sheets along with tubules at cell periphery[26], whereas the ER in NIH/3T3 cells comprises of large but mostly intact ER sheets at the perinuclear region and abundant tubular network covering most of the cytoplasmic space. In short, ER in Huh-7 cells is mainly composed of sheets and in NIH/3T3 of tubules. Light microscopy (LM) analysis revealed clear co-localization of endogenous NOGO-B/RTN4B with soluble luminal ER marker Hsp47-EGFP in both cell lines (Fig. 2A,B). The overall labelling pattern looked similar in both cell lines, although in Huh-7 cells, the Hsp47-EGFP labelling was most distinctive in the perinuclear region, where ER sheets dominate. In both cell types, co-localization was lowest at perinuclear region,

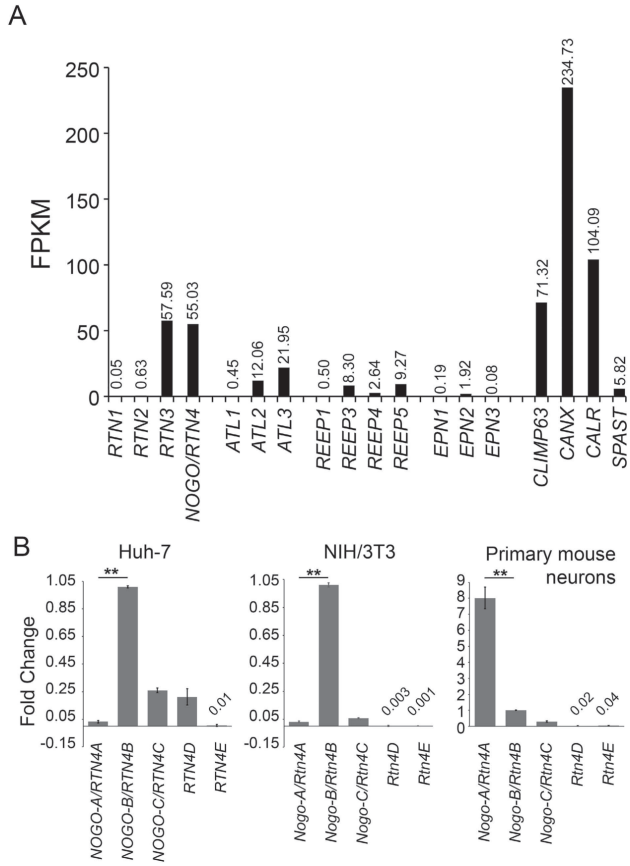

Figure 1. Several reticulon 4 splice variants are simultaneously expressed in cultured human hepatoma (Huh-7), mouse fibroblast (NIH/3T3) and primary mouse neuronal cells. (**A**) Transcriptome showing fragments per kilobase of transcript per million mapped reads (FPKM) values for indicated mRNA levels in Huh-7 cells. (**B**) qPCR data showing relative mRNA levels for indicated *RTN4* isoforms in Huh-7, NIH/3T3 and primary mouse cortical neurons. Species specific β-actin was used as internal controls. Graphs in B were normalized against *NOGO-B/RTN4-B* for all three cell types.

and highest at cell periphery, where ER is mostly in tubular form (insets). Quantitation gave Pearson's correlation coefficient values 0.6 for NIH/3T3 and 0.5 for Huh-7cells (Supplementary Fig. S1A). Western blotting revealed one clear band corresponding to the size of NOGO-B/RTN4B in Huh-7 and NIH/3T3 cell lysates, verifying the specificity of the antibody (Fig. 2F). To test the specificity of the anti-NOGO-B/RTN4B antibody in immunofluorescence, random fields of silenced and control Huh-7 cells were imaged with the same parameters, and relative mean signal intensities were determined (Supplementary Fig. S1B,C). 60% reduction in relative mean signal intensity matches well with the Western blotting results showing 50–60% reduction of NOGO-B/RTN4B after 48 hours silencing (Supplementary Fig. S3A,B).

Pre-embedding immuno electron microscopy (immuno-EM) verified the ER localization in both cell lines (Fig. 2C,D). In this technique, saponin-permeabilized cells were immunolabelled using1.4 nm-gold particle conjugated Fab fragments as secondary detection step and silver enhanced prior plastic embedding. Because of the nature of the silver enhancement reaction, stereological quantitation approaches are not applicable, however, in addition to revealing the localization, some conclusions on quantities can be drawn based on the cluster size and amounts. The labelling was strongest in cell periphery on ER tubules, although punctate labelling on ER sheets could be found too. The labelling pattern in Huh-7 cells was further analysed at 3D using ET, which allowed more reliable identification of sheets and tubules (Fig. 2E). First, labelling localized clearly on tubules and sheet edges. Secondly, flat parts of ER sheets were devoid of labelling. In addition to sheet edges, membrane curvature could

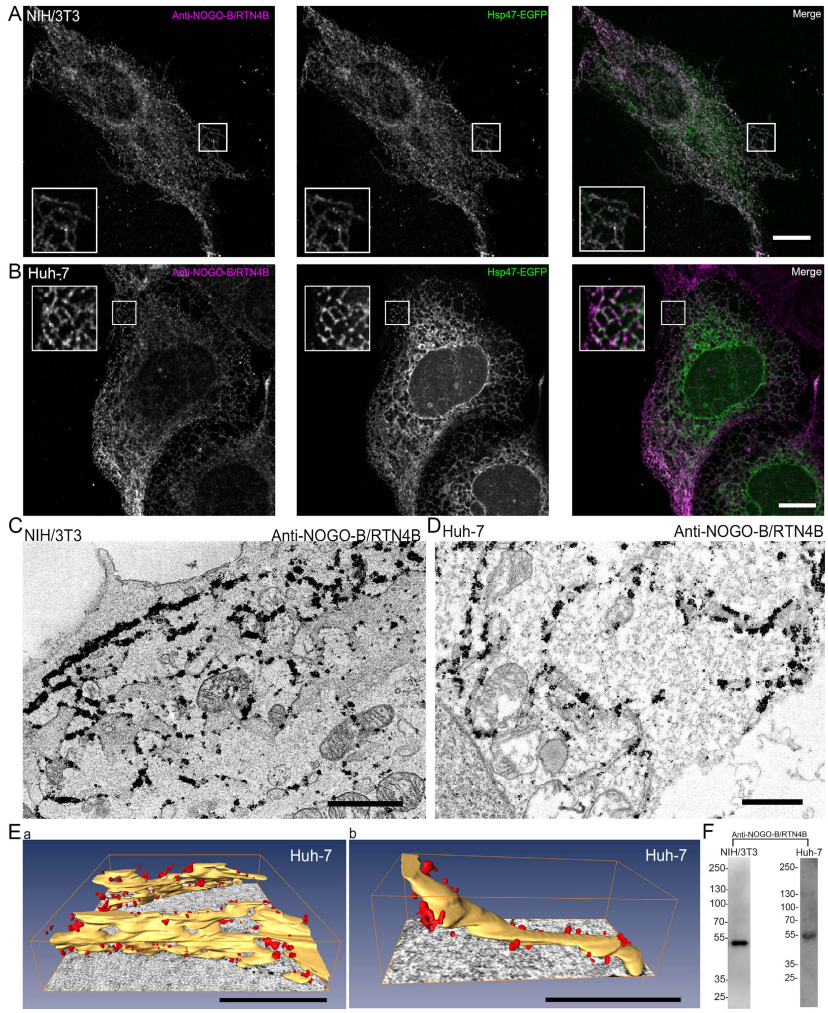

Figure 2. NOGO-B/RTN4B localizes to ER tubules and sheet edges. Confocal LM images of (**A**) NIH/3T3 and (**B**) Huh-7 cells showing localization of immunolabelled endogenous NOGO-B/RTN4B and ER marker Hsp47-EGFP in the ER. Merged images reveal co-localization in ER tubules and sheet edges. Insets show higher magnification of boxed areas. TEM micrographs of (**C**) NIH/3T3 and (**D**) Huh-7 cells showing immunolabelling of endogenous NOGO-B/RTN4B. (**E**) Models of electron tomograms showing immunolabelling (red) of endogenous NOGO-B/RTN4B in Huh-7 cells at sheet edges (Ea) and tubules (Eb) of the ER (yellow). NIH/3T3 (**F**, left) and Huh-7 (**F**, right) cell lysates were analysed by Western blotting with NOGO-B/RTN4B antibody to verify the antibody specificity. Bars, 10 μm (**A**,**B**), 1 μm (**C**,**D**), 500 nm (**E**). Scale bars in E are in the perspective view and apply to the centre of the image.

also be found from fenestrations, which comprise both positive and negative curvature. Interestingly, we found that most of the small and regular shaped fenestrations[26] on ER sheets were devoid of labelling, supporting the suggestion that NOGO-B/RTN4B prefers positively curved membranes. However, occasionally we could find labelling associated to slightly larger and more irregular fenestrations, which were clearly smaller than ER polygons (Supplementary Video S1). We cannot exclude the possibility that these structures might be in a process of forming a polygon opening, or polygon undergoing a closure.

Antibody labelling against endogenous NOGO-A/RTN4A revealed a clear ER network labelling pattern in NIH/3T3 cells (Fig. 3A). Quantitation of endogenous NOGO-A/RTN4A and luminal ER marker labelling gave

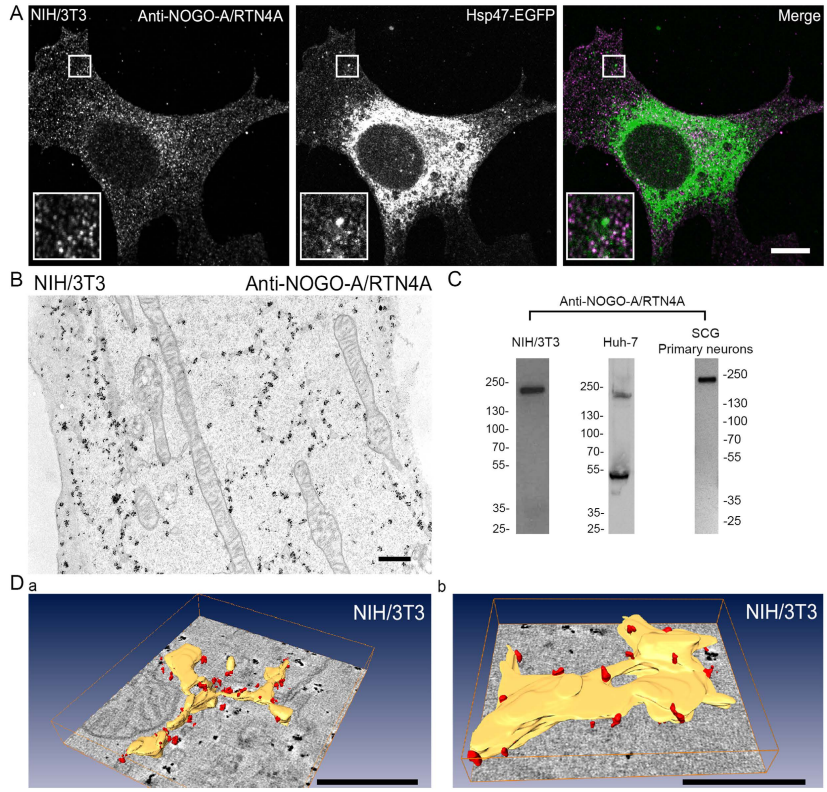

Figure 3. NOGO-A/RTN4A localizes to ER tubules and sheet edges in fibroblast cells. (**A**) Confocal LM images of NIH/3T3 cells showing localization of immunolabelled endogenous NOGO-A/RTN4A and ER marker Hsp47-EGFP. Insets show higher magnification of boxed areas. (**B**) TEM micrograph of NIH/3T3 cell showing immunolabelling of endogenous NOGO-A/RTN4A. NIH/3T3 (**C**, left), Huh-7 (**C**, middle) and primary mouse neuronal (**C**, right) cell lysates were analysed by Western blotting with NOGO-A/RTN4A antibody to verify the antibody specificity. (**D**) Models of electron tomograms showing immunolabelling (red) of endogenous NOGO-A/RTN4A in NIH/3T3 cell at sheet edges and tubules of the ER (yellow). Bars, 10 μm (**A**), 500 nm (**B**,**D**). Scale bars in D are in the perspective view and apply to the centre of the image.

Pearson's correlation coefficient value 0.3, which was about half compared to the value between NOGO-B/RTN4B and ER marker in same cells (Supplementary Fig. S1A). Thin section TEM and ET analysis of immunolabelled NIH/3T3 cells confirmed that NOGO-A/RTN4A associated label was on ER tubules and sheet edges (Fig. 3B,D) reminiscent of NOGO-B/RTN4B labelling. NOGO-A/RTN4A localized heavily in the tubular ER close to PM, and, to some extent, also near the PM where no clear ER-connection could be observed (Fig. 3B). We could not detect staining at the extracellular side of the PM, which is in contrast to earlier study showing that NOGO-A/RTN4A localizes to the extracellular side of the PM in fibroblasts[27]. Western blotting revealed one clear band corresponding to the size of NOGO-A/RTN4A and no band in the area corresponding to the smaller size of NOGO-B/RTN4B in NIH/3T3 cell lysates, verifying the specificity of this antibody, too (Fig. 3C). In Huh-7 cells the same antibody gave two bands corresponding to the size of NOGO-A/RTN4A and NOGO-B/RTN4B, suggesting that although antibody is specific for mouse proteins, it may have some cross-reactivity in human cell types (Fig. 3C). Antibody specificities in NIH/3T3 cells allowed simultaneous immunofluorescence labelling of endogenous NOGO-A/RTN4A and NOGO-B/RTN4B (Supplementary Fig. S2). Results confirmed the localization of these two proteins on ER. However, in the merged image, green and magenta fluorescent signals alternated along the ER profiles rather than showing a homogeneous overlap (in white). Pearson's correlation coefficient value was 0.5.

Next, we studied the localization of endogenous NOGO-B/RTN4B and NOGO-A/RTN4A in mouse superior cervical ganglia (SCG) primary neurons. The morphological analysis revealed distinct ER network organizations in various parts of the cell (Fig. 4A; Supplementary Video S2): Immediately under the PM, a layer of densely

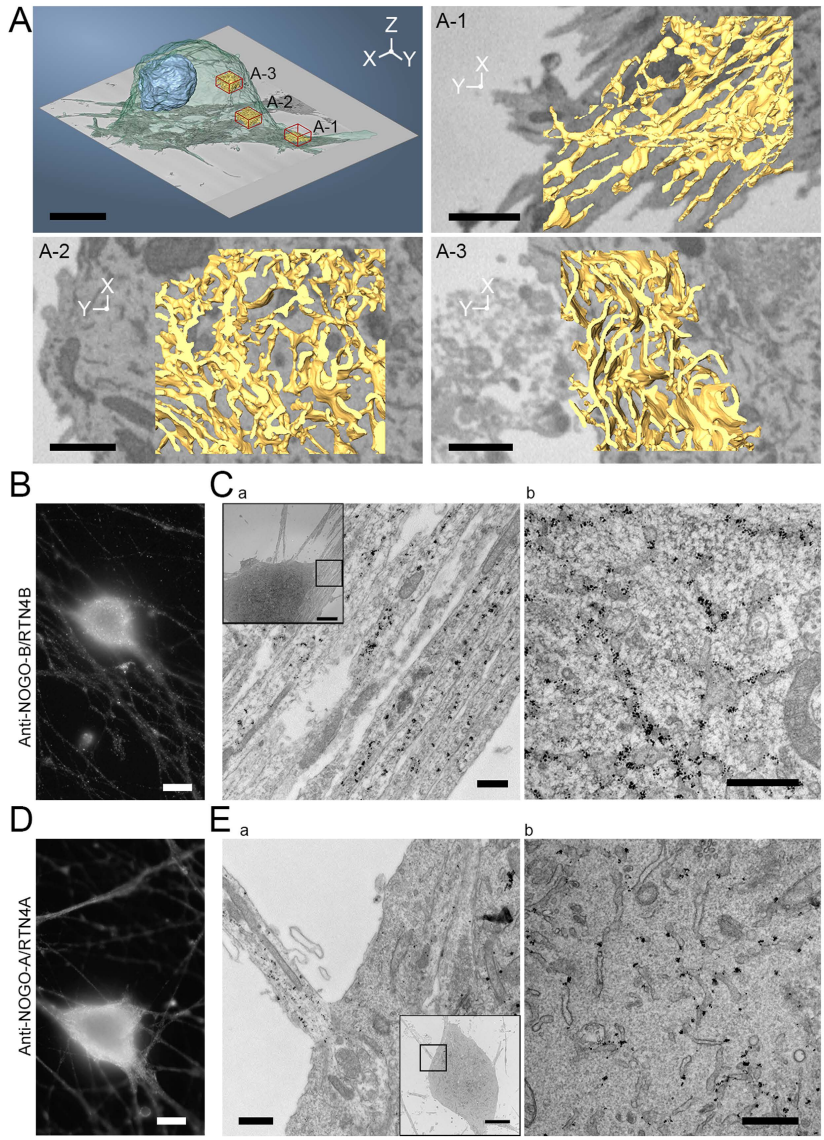

Figure 4. NOGO-B/RTN4B and NOGO-A/RTN4A localize to ER tubules and sheet edges in primary mouse neurons. (**A**) A model of SCG primary mouse neuron segmented from SB-EM data showing outlines of the cell (transparent green), nucleus (blue), and ER (yellow) at three different regions (red cubes). ER at neurite outgrowths (A-1) was mostly in tubular form while in the pericentriolar area (A-2) the ER comprised of a mixture of tubules and smaller sheets and the area immediately under the PM (A-3) had densely packed large ER sheets. Also see Supplementary Video S2. SCG-primary neurons showing endogenous NOGO-B/RTN4B immunolabelling in (**B**) wide field LM image and (**C**) TEM micrograph at neurite outgrowths (Ca) along with tubules and sheet edges at the cell soma (Cb). SCG-primary neurons showing endogenous NOGO-A/RTN4A immunolabelling in (**D**) wide field LM image and (**E**) TEM micrograph, at neurite outgrowths (Ea) along with tubules and sheet edges under the PM (Eb). Bars, 10 μm (**A**,**B**,**D**), 1 μm (A-1, A-2 and A-3), 500 nm (Ca, Cb, Ea and Eb), 5 μm (insets Ca, Cb, Ea and Eb).

packed large intact sheets were found (Fig. 4A-3), and towards the pericentriolar area the ER comprised of tubules and smaller sheets (Fig. 4A-2), whereas in neurite outgrowths ER was mainly tubular (Fig. 4A-1). At LM level, labelling of NOGO-B/RTN4B (Fig. 4B) and NOGO-A/RTN4A (Fig. 4D) looked similar, and were found extending from pericentriolar part of the cell to the cell periphery in cell soma as well as in neurites. Immuno-EM of NOGO-B/RTN4B revealed that endogenous protein localized mainly to ER at cell soma (Fig. 4Cb), as well as on ER tubules within neurites (Fig. 4Ca). Similarly as with fibroblasts, some NOGO-A/RTN4A associated label was found at the cytosolic side of the PM without clear presence of ER (Fig. 4Eb) in addition to prominent labelling pattern on ER tubules in cell soma and neurites (Fig. 4Ea). Previously NOGO-A/RTN4A has been reported to localize on the extracellular side of the PM on Dorsal Root Ganglion neurons and myoblasts[27]. Our immuno-EM studies could not verify these findings as no labelling was observed on the extracellular side of the PM. Together, these results indicate that NOGO-A/RTN4A and NOGO-B/RTN4B both localize prominently on ER tubules and sheet edges.

Manipulation of reticulon 4B levels induces severe morphological changes on ER and overall cell shape. Overexpression of RTN4B-EGFP in Huh-7 cells induced changes on ER morphology as well as in the overall cell morphology. Scanning EM revealed long filopodia-like protrusions and overall rounding of the cells in response to RTN4B-EGFP expression (Fig. 5A). LM analysis revealed formation of long unbranched ER tubules extending through the cell at moderate level of expression (Fig. 5B). Live cell imaging revealed that these long ER tubules were non-motile in comparison to cells expressing Hsp47-EGFP (Supplementary Video S3). At higher expression levels, formation of globular profiles, positive for endogenous ER protein calreticulin, at varying sizes could also be observed (Fig. 5C). TEM analysis showed that the globular structures observed at LM comprised a densely branched network of thin and rather short tubules connected to more typical ER profiles (Fig. 5D).

It has been shown before that NOGO-B/RTN4B forms dimers/oligomers besides interacting with other proteins[10]. We used bimolecular fluorescence complementation assay (BiFC)[28] to lock NOGO-B/RTN4B homo-oligomers to study their impact on ER structure. For this, we constructed NOGO-B/RTN4B tagged with GFP1-10 or GFP11 at the C- terminus of the protein. A clear BiFC signal was obtained in Huh-7 cells co-expressing these truncated GFP constructs (Fig. 6Aa) confirming the close interaction between RTN4Bs. In highly overexpressing cells, the signal came from tubular network and large bright globular structures throughout the network, which colocalized with soluble luminal ER marker Hsp47-mCherry (Fig. 6Ba). In mildly over-expressing cells the BiFC signal originated from the tubules and sheet edges in Huh-7 cells (Fig. 6Bb), verifying that the functional BiFC NOGO-B/RTN4B GFP-constructs localized as the endogenous reticulon 4B protein (Fig. 2). Locking of NOGO-B/RTN4B oligomers induced similar filopodia-like protrusions as the over-expression of NOGO-B/RTN4B-EGFP (see Fig. 5B). Correlative light and 3D- electron microscopy (CLEM) analysis revealed that these globular BiFC-positive structures were composed of a dense network of short ribosome-free tubules that were connected to sheets at the immediate vicinity of the cluster (Fig. 6C; Supplementary Video S4). These structures were reminiscent of tight tubular ER clusters that has been shown to form upon ATP depletion[29]. Similar tubular ER structures could be found also from cells overexpressing NOGO-B/RTN4B-EGFP but mostly after longer expression times indicating that these structures are not specific consequence of locked oligomers but rather that locked oligomers are more prone to induce such structures.

To study the role of NOGO-B/RTN4B on the cell growth rate, we subjected Huh-7 cells over-expressing NOGO-B/RTN4B-EGFP or as a control Hsp47-EGFP, to time-lapse video microscopy (using continuous cell culturing and imaging platform Cell-IQ) and collected images at 1 h intervals between t_{14h}–t_{48h} post transfection. The analysis revealed that cells expressing Hsp47-EGFP or NOGO-B/RTN4B-EGFP showed similar growth pattern for the first 24h post transfection, after which the growth rate of NOGO-B/RTN4B-EGFP overexpressing cells started to decline (Fig. 6D). The control cells continued similar growth pattern for additional 17 h, after which the growth rate reached a plateau, most likely due to reduced nutrients in the growth media.

Because of the sequence similarity between RTN4 isoforms, isoform-specific siRNAs would have been very challenging to design and instead, siRNAs recognizing all *RTN4* isoforms were used (Fig. 7). According to Western blotting a pool of 3 constructs or just one construct lead to 50–60% reduction of NOGO-B/RTN4B after 48 hours (Supplementary Fig. S3A,B). LM analysis of RTN4-depleted cells revealed an increased number of peripheral ER sheets (Fig. 7Aa,b) compared to scrambled siRNA (Fig. 7Ac,d). These findings were supported by 3D-EM (Fig. 7B). ET revealed that RTN4-depleted Huh-7 cells contained extended ER sheets, which in extreme cases were stacked at the cell periphery. The fenestrations typical for ER in these cells[30] could be seen in the stacked ER sheets (Fig. 7Ba). SB-EM revealed large ER sheets through the cytoplasmic space (Fig. 7Bb). Nucleus, mitochondria and Golgi morphology appeared normal. Thin section TEM analysis confirmed that similar morphological changes were produced with each silencing construct separately and with a pool of 3, thus ruling out any off-target effects (Supplementary Fig. S3C).

Discussion

Reticulons have been shown to have a role in many cellular functions ranging from inhibition of neural outgrowth and axonal regeneration in the central nervous system[3] to ER morphogenesis[4] and ER stress-induced apoptosis[31,32]. Recently, additional roles, including involvement in STIM1-Orai1-Coupling and Store-operated Calcium Entry[23], autophagy[33], DNA binding[34], and inflammatory-related functions[35], have been reported for RTNs, and their involvement in neurodegenerative diseases such as Alzheimer's disease, amyotrophic lateral sclerosis, multiple sclerosis, as well as hereditary spastic paraplegia[36], are evident. In addition to conflicting results reported from neurobiology and cell biology regarding the localization and expression of NOGO-A/RTN4A, a clear and detailed description of the expression, localization and functional significance of the other reticulon 4 isoforms has been lacking. Here we report, based on transcriptome analysis, that RTN1-4 are simultaneously

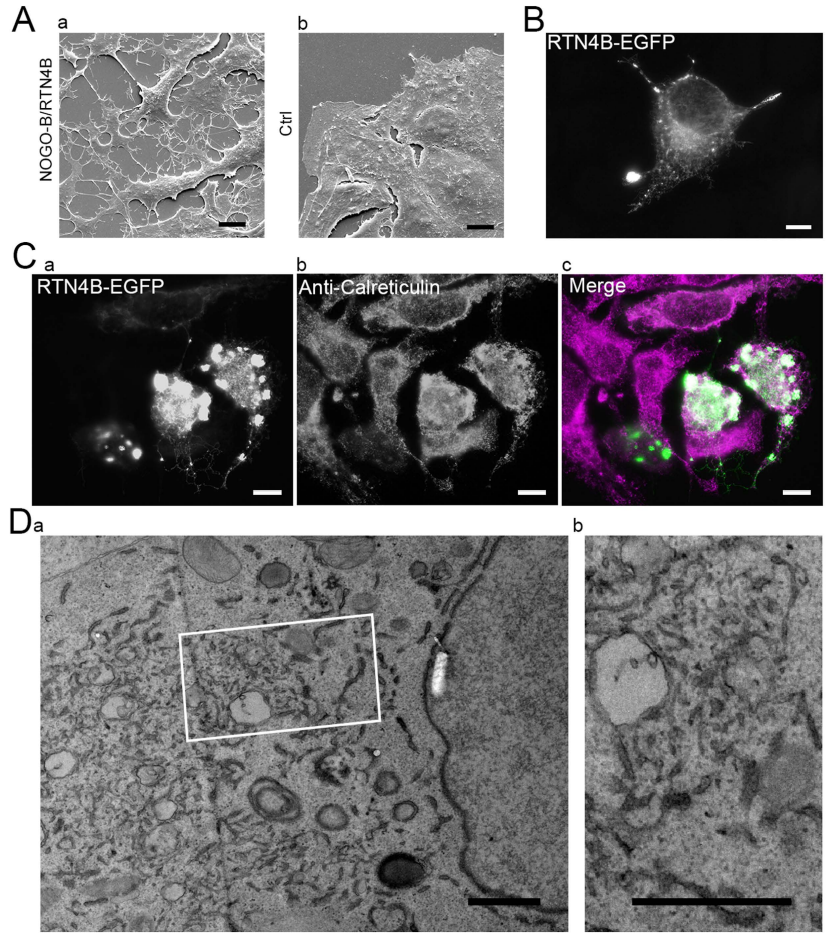

Figure 5. NOGO-B/RTN4B overexpression affects overall cell shape and ER morphology. (**A**) Scanning EM images of Huh-7 cells overexpressing (Aa) pCMV-RTN4B or (Ab) CMVTag1 (control) for 24 hours. (**B**) Wide field LM image of Huh-7 cells overexpressing RTN4B-EGFP for 24 hours showing filopodia like protrusions. Also see Supplementary Video S3. (**C**) Wide field LM image Huh-7 cells overexpressing RTN4B-EGFP (Ca) for 24 hours showing tubular ER network and globular profiles positive for ER marker calreticulin (Cb). (**D**) TEM micrographs of Huh-7 cell co-expressing ssHRP-KDEL and RTN4B-EGFP for 24 hours. (Db) shows a higher magnification of the boxed area in Da revealing a dense network of short ribosome-free tubules connected to ER sheets. Bars, 10 μm (**A**,**B**,**C**), 1 μm (Da and Db).

expressed, at different levels, in cultured hepatoma cells. Consistent with previous results[36], our qPCR expression profiling of *RTN4* isoforms detected 5 isoforms in cultured hepatoma, fibroblast and primary neuronal cells: A-D isoforms were expressed in varying degrees and E was present at relatively low level. While RTNs have been suggested to have general roles on ER, the simultaneous presence of *NOGO-B/RTN4B* and *NOGO-A/RTN4A*, in addition to other isoforms, in all three cell lines suggests distinct cellular roles for these proteins.

It has been suggested that the hydrophilic loop of the NOGO-A/RTN4A localizes to the extracellular side of the PM and binds to its axonal receptor[37]. Controversially, based on several cell biological studies, RTNs localize to the highly curved regions of ER[4]. N-terminus of all RTN4 isoforms lack a specific signal sequence for ER translocation, which might account for their reported presence both in the ER and at the extracellular side of the PM[5,6]. Here we addressed the discrepancy related to the localization of the NOGO-A/RTN4A by detecting endogenous NOGO-A/RTN4A in fibroblasts and neurons. Majority of the labelling was detected on the cytoplasmic side of the cells, at ER tubules and sheet edges, while the extracellular side of the PM was mostly void of the labelling. We

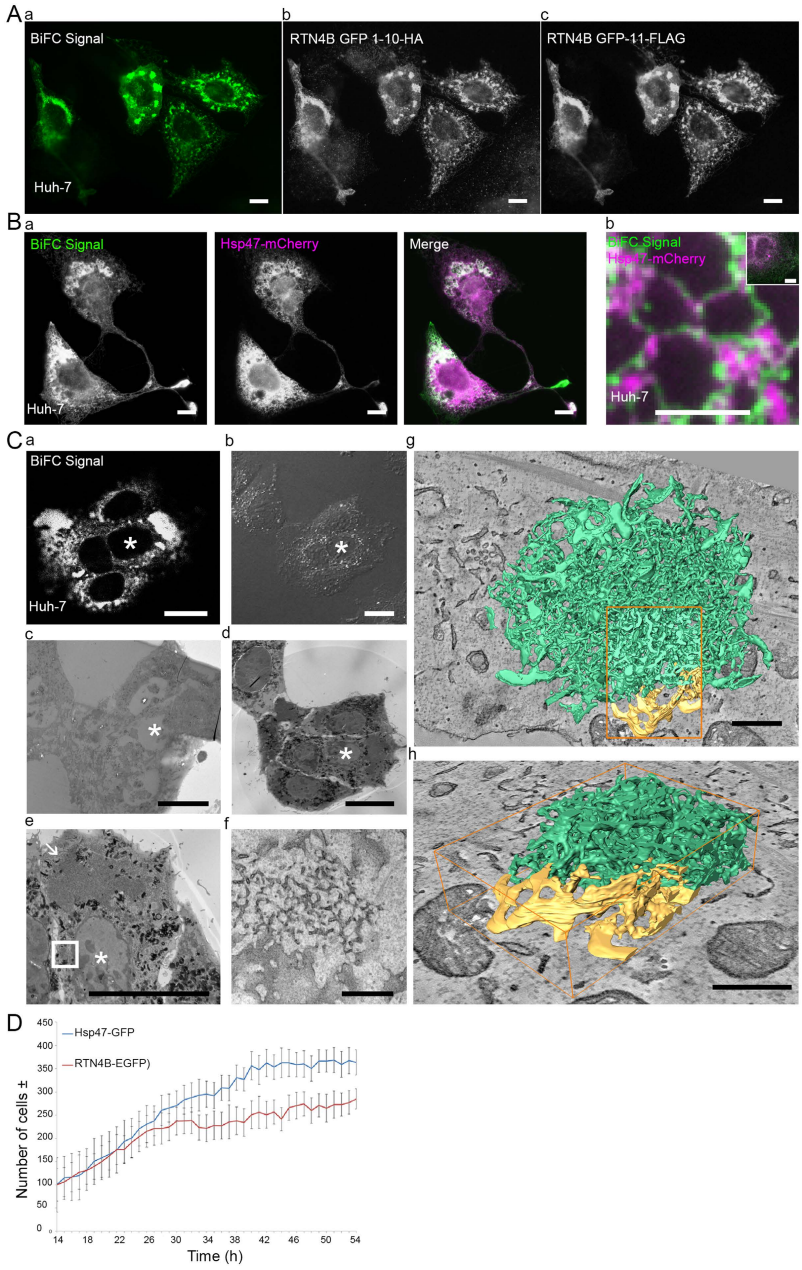

Figure 6. Overexpression of locked NOGO-B/RTN4B dimers induces strong ER tubulation and overexpression NOGO-B/RTN4B hampers cell growth. (Aa) Wide field LM image showing a positive BiFC signal arising from co-expression of RTN4B-GFP1-10-HA and RTN4B-GFP-11-FLAG constructs in Huh-7 cells for 24 hours. Wide field LM images of immunolabelled (Ab) HA and (Ac) FLAG tags verifying the equal expression of both constructs in the cells. BiFC signal (Ba) co-localizes with the ER marker Hsp47-mCherry at tubular ER network and large globular BiFC signal-positive structures in highly over-expressing cells, and

(Bb) shows only partial co-localization in moderately over-expressing cells. Inset in Bb showing the overview of the cell. (**C**) CLEM workflow of Huh-7 cells co-expressing RTN4B-GFP1-10-HA and RTN4B-GFP-11-FLAG. (Ca) Confocal LM image showing the BiFC signal, (Cb) phase contrast LM image and low magnification TEM micrographs from consecutive (Cc) 60 nm and (Cd) 250 nm thin sections from the same cell cluster. (Ce) TEM micrograph of the whole cell depicted with asterisk in Ca-Cd and (Cf) the higher magnification micrograph of a small globular ER cluster depicted by a white box in Ce. Arrow in Ce depicts another, much larger globular ER cluster in the same cell. (Cg,Ch) 3D- models generated from serial TEM tomograms from the same boxed area in Ce revealing that normal fenestrated sheets (yellow) are directly connected to heavily tubular smooth ER (green). Cg shows the whole globular ER cluster, and the magnified part of the model shown in Cf is depicted by an orange box. (**D**) Cell-IQ data showing number of cells overexpressing RTN4B-EGFP (red line) vs control (Hsp47-EGFP) (blue line). Imaging started 14 hours after transfection. Also see Supplementary Video S4. Bars, 10 μm (A,Ba and inset Bb), 2.5 μm (Bb), 20 μm (Ca, Cb, Cc, Cd and Ce), 500 nm (Cf, Cg and Ch).

also observed abundant labelling at cell periphery next to the PM either in conjunction with ER profiles or without an immediate connection to ER. Based on theoretical models, several RHD conformations are possible and the RTNs may be able to insert and flip–flop within PM, giving rise to several alternative orientations of the proteins[4,5,38–40]. The detected labelling at cell periphery might originate from PM or from ER profiles located above or under the thin section. The different membrane topology at highly curved ER areas or under the flat PM suggests that NOGO-A/RTN4A performs divergent functions at different cellular locations, which might be explained by *e.g.* the interacting protein environment, indicating that NOGO-A/RTN4A might have additional roles beyond ER morphogenesis. The controversial results obtained from cell- and neurobiology might be explained by the different functions these cells perform.

RTNs have also been suggested to form arc-shaped oligomers[10], which would generate and stabilize membrane curvature by wedging and scaffolding mechanisms. Structural evidence for the proposal has so far been missing. Here we show by immuno-EM and -ET that the endogenous NOGO-B/RTN4B and NOGO-A/RTN4A localize to curved ER membranes in distinct patterns. NOGO-B/RTN4B and NOGO-A/RTN4A localized to curved ER membranes, *i.e.* tubules and sheets edges and while it was devoid from small sheet fenestrations, labelling was occasionally seen at larger fenestrations. Clusters of label were seen at relatively regular intervals covering the tubule length and sheet edges indicating that endogenous NOGO-B/RTN4B and NOGO-A/RTN4A do not cover the whole tubule length but rather are present at distinct regions along the structure. Interestingly, the labelling pattern at ER tubules, sheet edges and adjacent to PM were slightly different; while the cluster size was relatively large at ER tubules, fewer and smaller silver/gold clusters were seen at sheet edges and under PM. This might indicate that NOGO-B/RTN4B and NOGO-A/RTN4A forms oligomers at distinct spots at ER tubules and through oligomerization bends the ER membranes, whereas smaller oligomers, or singular proteins, could be residing at sheet edges and at PM.

Artificial over-expression of NOGO-B/RTN4B induced proliferation and immobilization of ER tubules along with long filopodia-like protrusions and rounding of the cell. In agreement with previous results showing that manipulation of RTN4C levels inhibit cell growth[41], these events induced by over-expression of NOGO-B/RTN4B were conveyed into a significant drop in the cell growth rate and eventually led to cell apoptosis. The altered ER morphology upon NOGO-B/RTN4B over-expression does not resemble the organized smooth ER structures that have been described after over-expression of several ER membrane proteins[42], but rather the random tubular SER patches induced by a treatment with the drug 1-Phenyl-2-decanoyl-amino-3-morpholino-1-propanol (PDMP)[43]. Finally, in the light of these results, using the NOGO-B/RTN4B overexpression constructs as general markers for ER tubules should be carefully considered as even small changes in protein levels affect sheet-tubule balance and thereby induce clear changes in the ER morphology. Recent development in targeted genome editing technology[44,45] provides solution as this approach can be used to generate stable cell lines expressing epitopically tagged versions of various ER membrane proteins at endogenous levels to avoid changes in sheet-tubule balance or expansion of the membrane.

Methods

Cell culture, constructs, overexpression and silencing. NIH/3T3 (CRL-1658; ATCC, LGC Standards GmbH, Germany) were cultured in DMEM (BioWhittaker, Lonza, Verviers, Belgium) and Huh-7 (JCRB0403; Japanese Collection of Research Bioresources Cell Bank, Osaka, Japan) in EMEM (Lonza), containing 5 or 10% fetal bovine serum (Gibco, Invitrogen, Thermo Fisher Scientific, Waltham, MA) and other supplements (Lonza). Cervical ganglion primary sympathetic neurons from new-born Swiss type NMRI-mouse (SCG primary neurons) were cultivated on polyornitin-laminin (Sigma-Aldrich, St. Louis, MO) coated coverslips in neurobasal-medium containing B27 (Gibco, Invitrogen) and 30 ng/ml mouse 2.5 S nerve growth factor (NGF; Promega, Madison, WI). Mouse E16 (embryo collected 16 days after fertilization) primary cortical neurons were used for the qPCR. pssHRP-KDEL[46] and pHsp47-EGFP[47] were provided by the respective laboratories. Construction of Hsp47-mCherry has been described previously[30]. Reticulon 4B gene was amplified from U-2 OS cDNA produced from extracted total mRNA and then cloned into pCMV-Tag1 (Agilent Technologies, Espoo, Finland). EGFP was subcloned into C-terminus of the pCMV-RTN4B expression vector by PCR from pEGFP-N1 (Clontech, Takara Bio Inc., Tokyo, Japan) resulting in pCMV-RTN4B-EGFP. For the BiFC constructs, RTN4B in pENTR221gateway compatible vector (without stop codon) from Orfeome library, GBU, Helsinki University, was taken through L.R reaction (Gateway® Cloning, Life Technologies, Thermo Fisher Scientific) against pDEST-GFP-1-10-N3 or pDEST-GFP-11- N3 gateway compatible vectors (Gift from Maria Vartiainen's lab, University of Helsinki) creating C-terminal fusion vectors RTN4b-GFP-11 and RTN4B-GFP-1-10. For overexpression studies and all DNA transfections, Fugene HD (Promega) was used according to manufacturer's instructions

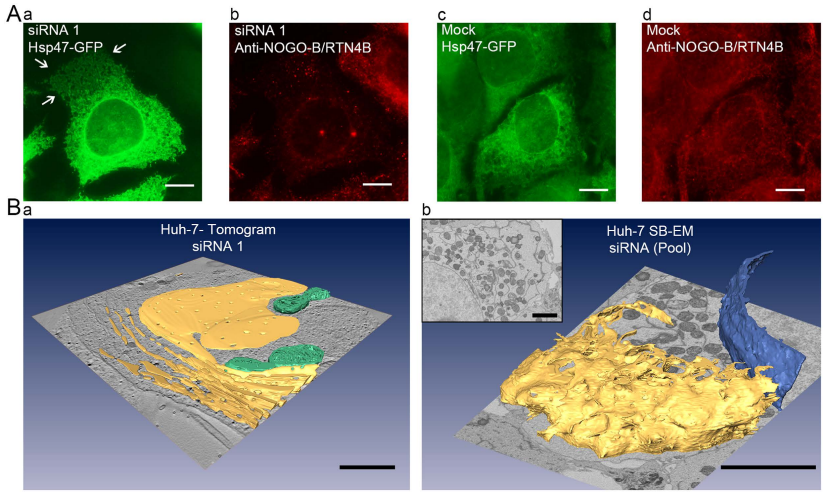

Figure 7. RTN4 depletion causes the loss of ER tubules and generation of large ER sheets that can become stacked in Huh-7 cells. (**A**) Wide field LM images showing RTN4 depleted cell with larger peripheral ER sheets (Aa, Ab; indicated by white arrows) as compared to mock (scrambled siRNA) (Ac, Ad). (**B**) ER (yellow) models from RTN4B depleted Huh-7 cells generated from ET (Ba) and SB-EM (Bb) datasets reveal large stacked sheets. Mitochondria (in Ba) and nuclear envelope (in Bb) are depicted in green and blue, respectively. Also see Supplementary Video S5 (ET) and Supplementary Video S6 (SB-EM). Bars, 10 μm (**A**), 1 μm (Ba and inset of Bb), 5 μm (Bb).

and cells fixed for analysis 24 h or 48 h post-transfection. For co-transfections of two and three plasmids a ratio of 1:2 (wt:wt) and 0.5:0.5:4 (wt:wt:wt) was used. RTN4 silencing was done using INTERFERin (Polyplus-transfection, France) for 48 h according to manufacturer's instruction, and the ER marker was transfected 24 h post silencing for the remaining 24 h. For silencing single or total of pooled target-specific siRNA oligonucleotides from Thermo Scientific Dharmacon (Lafayette, CO) (sequences: 5′-GCGCAAAGCUGAAUGAAAAUU-3′, 5′-GUUCAGAAGUACAGUAAUUUU-3′ and 5′-CGGUAAAGCAGGAAUGACAUU-3′, the 2-nucleotide overhanging uridine is indicated as UU)[48] were used. The silencing efficiency of the siRNAs was quantified using Western blotting.

Antibodies. Antibodies against reticulon 4B (AB-163; Kinasource Ltd, Dundee, UK), reticulon 4A (ab62024; Abcam, Cambridge, UK), HA (MMS-101R-50; Covance, Princeton, NJ), FLAG (F7425; Sigma-Aldrich), calreticulin (2679S; Cell Signalling Technologies, MA) and β-actin (ab8227-50; Abcam) were used as primary antibodies. When indicated, rabbit anti-sheep bridging antibody (313-001-003; Jackson ImmunoResearch Labs Inc., West Grove, PA) was used. Secondary antibodies were Rhodamine Red-X (016-290-084; Jackson ImmunoResearch), Alexa 647 (A31571; Life technologies), Alexa 488 (A-11008; Life Technologies) and 1.4 nm nanogold-conjugated anti-rabbit antibody (Nanoprobes, Stony Brook, NY).

Immunofluorescence staining and Western blotting. For NOGO-B/RTN4B labelling, cells were fixed with −20 °C methanol, blocked with 10% goat serum (Gibco-Life Technologies) and 1% BSA (bovine serum albumin), labelled with indicated antibodies and mounted in Mowiol (Hoechst, Frankfurt, Germany) supplemented with Dabco (Sigma-Aldrich). All the other samples were fixed with 4% formaldehyde (Electron Microscopy Sciences, Hatfield, PA), 0.1 mM $MgCl_2$, and 0.1 mM $CaCl_2$ in phosphate-buffered saline (PBS), quenched with 50 mM NH_4Cl, permeabilized with 0.1% Triton X-100, and then blocked with 0.2% BSA in Dulbecco PBS. When appropriate, the cells were then incubated consecutively with primary and secondary antibodies, diluted in blocking solution. Samples were mounted in Mowiol supplemented with Dabco. Western blotting was done with indicated antibodies according to manufacturer's instructions and by using standard protocols.

Light microscopy and image quantitation. Wide-field images of fixed cells were taken with Zeiss AxioImager M2 482 epifluorescence microscope equipped with 63 × /Plan-Apochromat/1.40 oil/M27 and 483 AxioCam HRm camera (Zeiss, Oberkochen, Germany) (Figs 4,5 and 6A,B), Leica DM6000B upright fluorescence wide field microscope equipped with 40X/1.25-0.75 HCX PL APO CS oil objective, Hamamatsu Orca-Flash4.0 V2 sCMOS camera (Wetzlar, Germany) (Supplementary Figure S1) or with Olympus BX61 wide field microscope (Tokyo, Japan) (Fig. 7). Images were acquired with AxioVision4 (Zeiss), LAS X software (Leica) or Fluoview software (Olympus). Confocal images of fixed cells were taken with LSM880 confocal laser scanning microscope

(Zeiss) with a 63X plan-apochromat (NA = 1.40) oil objective, GaAsP detector and ZEN 2 software (Zeiss) (Figs 2 and 3) or with inverted TCS SP5II HCS A confocal (Leica, Mannheim, Germany) using an HCX PL APO (Leica) lambda blue 63.0 × /1.2 W Corr/0.17 CS objective, HyD 4 detector (Leica) with either standard or BrightR detection mode, Scan DIC and blue (Ar 488 nm/35 mW) laser line, and RSP 500 beam splitter (Fig. 6Ca). Live Huh-7 cells were imaged at 37 °C and 5% CO_2 on glass-bottom dishes (MatTek, Ashland, MA). Videos were acquired using a PLANAPO 60 × 1.45 (oil) objective with additional 1.6× magnification in an IX-71 inverted microscope (Olympus) equipped with a TILL imaging system (TILL Photonics, FEI Company, Hillsboro, OR), iXon camera (Andor, Oxford Instruments, Abingdon, UK). Pearson's correlation coefficiencies were calculated using Microscopy Image Browser (MIB)[49] for square ROIs placed on the cell lamella ($n > 10$). As a negative control, the Pearson's correlation coefficient was also calculated for the same ROIs after rotating one of the two channels by 90°[49]. Cell segmentation and mean intensity measurements of NOGO-B/RTN4B in mock and silenced Huh-7 cells ($n = 20$) were done using MIB.

Electron microscopy. Cells grown on glass coverslips were cytochemically stained and flat embedded as described previously[50]. Cells were fixed with 2% glutaraldehyde (Sigma-Aldrich) and 1.5% formaldehyde in 0.1 M sodium cacodylate buffer, pH 7.4, for 20 min at room temperature (RT). Cytochemical staining with 3,3′-diaminobenzidine (TAAB, Berks, UK) was done for pssHRP-KDEL transfected cells. Cells were then post-fixed with 1% reduced osmium tetroxide in sodium cacodylate buffer for 1 h on ice, dehydrated through series of ethanols and acetone, and infiltrated with Epon (TAAB 812) for 2 h prior 14- h- polymerization at 60 °C. 60-nm or 100-nm thin sections were cut, post-stained with uranyl acetate and lead citrate and imaged with Tecnai 12 (FEI Company, at 80 kV or 120 kV equipped with Orius SC 1000B (Gatan Inc.) CCD camera. For immuno-EM the cells were fixed with paraformaldehyde-lysine-periodate -fixative[51]. Cells were permeabilized with 0.01% saponin (Sigma-Aldrich) and immunolabelled with anti-NOGO-B/RTN4B followed with rabbit anti-sheep bridging antibody or with anti NOGO-A/RTN4A antibody, and 1.4 nm nanogold-conjugated anti-rabbit secondary antibody, silver enhanced with HQ Silver kit (Nanoprobes, Stony Brook, NY) and gold toned with 0.05% gold chloride. Finally cells were processed for osmication, dehydration, Epon embedding, sectioning and imaging as described above.

Scanning electron microscopy and SB-EM. For scanning electron microscopy (SEM), cell monolayers overexpressing pCMV-RTN4B-HA or pCMVTag1 for 24 h were grown on glass coverslips and fixed with 2% glutaraldehyde in 0.1 M sodium cacodylate buffer, pH 7.4 for 30 min at RT and post-fixed with 1% osmium tetroxide in 0.1 M sodium cacodylate buffer for 60 min at RT. The samples were dehydrated through series of ethanols, followed by overnight dehydration with hexamethyldisilazane (Sigma-Aldrich). All the samples were coated with platinum using Agar sputter coater (Agar scientific Ltd, Essex, UK). Imaging was done using Zeiss DSM 962 (Oberkochen, Germany) at 10 kV. SB-EM samples of mouse primary neurons and RTN4 knockdown Huh-7 cells were prepared as described previously[26]. Images were acquired with a FEG-SEM Quanta 250 (FEI Company, Hillsboro, OR) equipped with a microtome (3View; Gatan Inc., Pleasanton, CA), using a backscattered electron detector (Gatan Inc.). The imaging was done using 0.3-Torr pressure, 2.5 kV beam voltage and spot size 3. Image processing and segmentation were done using MIB. Visualization of models and rendering of videos were done in Amira (VSG, FEI Company).

Electron tomography. ET was done on serial 250-nm thick sections as previously described[52], except that the tilt series images between ±62° were acquired with an UltraScan 4000 CCD camera, 4 k × 4 k (Gatan Inc.) at nominal magnification of 6.500×, 7.800× or 9.600×. Dual axis tilt series were acquired using SerialEM software running on a Tecnai FEG 20 microscope (FEI Company, Hillsboro, OR) operating at 200 kV. Gold particles on tomograms were quantified by manually tagging on separately modelled ER structures. Reconstructions were done using IMOD software[53] followed by visualization and modelling using MIB and Amira (VSG, FEI Company). The presented 3D models of ER are shown in perspective view, where the bars apply to the centre point of the image except in Fig. 6Cf.

Expression profiling SOLiD sequencing and qPCR. Three separate total RNAs were extracted from Huh-7 cells with TRIzol (Invitrogen) reagent according to manufacturer's protocol. Messenger RNA was further extracted from the samples using mRNA isolation kit (Roche, Basel, Switzerland). cDNA libraries from 100 ng of isolated mRNAs were produced using Ovation® RNA-Seq System V2 kit (NuGEN, Leek, The Netherlands). Samples were barcoded and thereafter sequenced using a paired end mode with SOLiD 5500XL (Life Techologies). The SOLiD pair-end sequencing reads were mapped to human transcriptome using Tophat[18] with RefSeq gene annotation from UCSC (University of California, Santa Cruz, CA) genome browser. The expression level of transcripts was estimated by Cufflinks[19]. Aligned read data from SOLiD sequencing is stored in European Nucleotide Archive (ENA, accession PRJEB12539). The total mRNA from Huh-7, NIH/3T3 and primary mouse (E16) cortical neuronal cells was extracted as mentioned above and reverse transcribed using Roche Transcriptor First Strand cDNA Synthesis Kit. qPCR was performed using iQ™ SYBR® Green Supermix (Bio-Rad Laboratories, Inc, Hercules, CA) with CFX384 Touch system (Biorad). Four technical replicates were used for every isoform. Primers used for the qPCR were provided by Oligomer Oy (Helsinki, Finland) and are presented in Supplementary Table S1. Results are normalized for NOGO-B/RTN4B and expressed as the mean ± SE, where housekeeping human or mouse genes β-actin were used. Results were assessed using 2 tailed student *t* test. $P < 0.05$ were considered statistically significant.

Cell proliferation. Huh-7 cells were grown on 24-well plates and transfected with either RTN4B-EGFP or with control (ER marker Hsp47-EGFP). The cells were grown on a continuous cell culturing platform with integrated optics for phase contrast imaging and machine vision technology (Cell-IQ, CM Technologies Ltd, Tampere, Finland) in a humidified, 5% CO_2 atmosphere at 37 °C for approximately 72 h post transfection. Four random positions from each of the three replicates were imaged at 1 h intervals. The total cell count was measured from 14 h to 72 h post transfection using MIB. Cells were recognized and automatically counted by segmenting fluorescent images in MIB. Graphs of averaged cell numbers were generated, normalized and statistically analysed in Excel (Microsoft).

Statistical testing. Statistical analysis of cell growth rates of Huh-7/Hsp47-EGFP (control; average n/h = 324 cells) compared to Huh-7/RTN4B-EGFP (NOGO-B/RTN4B overexpression; n/h = 355 cells) were done to data derived from 4 parallel samples and 3 replicates. Degrees of freedom ($d.f._{control} = 14$; $d.f._{NOGO\text{-}B/RTN4B} = 21$) were calculated with Welch-Satterthwaite equation. Statistical significance of normally distributed data was calculated with Student's *t*-test (Excel, Microsoft), assuming unequal variances. The *p*-values were tested for time points 14/24 h ($p > 0.1$) and 42/53 h ($p < 0.025$).

References

1. van de Velde, H. J., Roebroek, A. J., Senden, N. H., Ramaekers, F. C. & Van de Ven, W. J. NSP-encoded reticulons, neuroendocrine proteins of a novel gene family associated with membranes of the endoplasmic reticulum. *J Cell Sci* **107** (Pt 9), 2403–2416 (1994).
2. Chen, M. S. *et al.* Nogo-A is a myelin-associated neurite outgrowth inhibitor and an antigen for monoclonal antibody IN-1. *Nature* **403,** 434–439 (2000).
3. GrandPre, T., Nakamura, F., Vartanian, T. & Strittmatter, S. M. Identification of the Nogo inhibitor of axon regeneration as a Reticulon protein. *Nature* **403,** 439–444 (2000).
4. Voeltz, G. K., Prinz, W. A., Shibata, Y., Rist, J. M. & Rapoport, T. A. A class of membrane proteins shaping the tubular endoplasmic reticulum. *Cell* **124,** 573–586 (2006).
5. Oertle, T. & Schwab, M. E. Nogo and its paRTNers. *Trends Cell Biol* **13,** 187–194 (2003).
6. Yang, Y. S. & Strittmatter, S. M. The reticulons: a family of proteins with diverse functions. *Genome Biol* **8,** 234 (2007).
7. Park, S. H., Zhu, P. P., Parker, R. L. & Blackstone, C. Hereditary spastic paraplegia proteins REEP1, spastin, and atlastin-1 coordinate microtubule interactions with the tubular ER network. *J Clin Invest* **120,** 1097–1110 (2010).
8. Calero, M., Whittaker, G. R. & Collins, R. N. Yop1p, the yeast homolog of the polyposis locus protein 1, interacts with Yip1p and negatively regulates cell growth. *J Biol Chem* **276,** 12100–12112 (2001).
9. Hu, J. *et al.* Membrane proteins of the endoplasmic reticulum induce high-curvature tubules. *Science* **319,** 1247–1250 (2008).
10. Shibata, Y. *et al.* The reticulon and DP1/Yop1p proteins form immobile oligomers in the tubular endoplasmic reticulum. *J Biol Chem* **283,** 18892–18904 (2008).
11. Zuchner, S. *et al.* Mutations in the novel mitochondrial protein REEP1 cause hereditary spastic paraplegia type 31. *Am J Hum Genet* **79,** 365–369 (2006).
12. Beetz, C. *et al.* REEP1 mutation spectrum and genotype/phenotype correlation in hereditary spastic paraplegia type 31. *Brain* **131,** 1078–1086 (2008).
13. Orso, G. *et al.* Homotypic fusion of ER membranes requires the dynamin-like GTPase atlastin. *Nature* **460,** 978–983 (2009).
14. Rismanchi, N., Soderblom, C., Stadler, J., Zhu, P. P. & Blackstone, C. Atlastin GTPases are required for Golgi apparatus and ER morphogenesis. *Hum Mol Genet* **17,** 1591–1604 (2008).
15. Hu, J. *et al.* A class of dynamin-like GTPases involved in the generation of the tubular ER network. *Cell* **138,** 549–561 (2009).
16. Sanderson, C. M. *et al.* Spastin and atlastin, two proteins mutated in autosomal-dominant hereditary spastic paraplegia, are binding partners. *Hum Mol Genet* **15,** 307–318 (2006).
17. Mannan, A. U. *et al.* Spastin, the most commonly mutated protein in hereditary spastic paraplegia interacts with Reticulon 1 an endoplasmic reticulum protein. *Neurogenetics* **7,** 93–103 (2006).
18. Trapnell, C. *et al.* Differential gene and transcript expression analysis of RNA-seq experiments with TopHat and Cufflinks. *Nat Protoc* **7,** 562–578 (2012).
19. Trapnell, C. *et al.* Differential analysis of gene regulation at transcript resolution with RNA-seq. *Nat Biotechnol* **31,** 46–53 (2013).
20. Zurek, N., Sparks, L. & Voeltz, G. Reticulon short hairpin transmembrane domains are used to shape ER tubules. *Traffic* **12,** 28–41 (2011).
21. Kimura, T. *et al.* Endoplasmic Protein Nogo-B (RTN4-B) Interacts with GRAMD4 and Regulates TLR9-Mediated Innate Immune Responses. *J Immunol* **194,** 5426–5436 (2015).
22. Khaminets, A. *et al.* Regulation of endoplasmic reticulum turnover by selective autophagy. *Nature* **522,** 354–358 (2015).
23. Jozsef, L. *et al.* Reticulon 4 is necessary for endoplasmic reticulum tubulation, STIM1-Orai1 coupling, and store-operated calcium entry. *J Biol Chem* **289,** 9380–9395 (2014).
24. Schanda, K. *et al.* Nogo-B is associated with cytoskeletal structures in human monocyte-derived macrophages. *BMC Res Notes* **4,** 6 (2011).
25. Gerondopoulos, A. *et al.* Rab18 and a Rab18 GEF complex are required for normal ER structure. *Journal of Cell Biology* **205,** 707–720 (2014).
26. Puhka, M., Joensuu, M., Vihinen, H., Belevich, I. & Jokitalo, E. Progressive sheet-to-tubule transformation is a general mechanism for endoplasmic reticulum partitioning in dividing mammalian cells. *Mol Biol Cell* **23,** 2424–2432 (2012).
27. Dodd, D. A. *et al.* Nogo-A, -B, and -C are found on the cell surface and interact together in many different cell types. *J Biol Chem* **280,** 12494–12502 (2005).
28. Kaddoum, L., Magdeleine, E., Waldo, G. S., Joly, E. & Cabantous, S. One-step split GFP staining for sensitive protein detection and localization in mammalian cells. *Biotechniques* **49,** 727–728, 730, 732 passim (2010).
29. Lingwood, D., Schuck, S., Ferguson, C., Gerl, M. J. & Simons, K. Generation of cubic membranes by controlled homotypic interaction of membrane proteins in the endoplasmic reticulum. *J Biol Chem* **284,** 12041–12048 (2009).
30. Joensuu, M. *et al.* ER sheet persistence is coupled to myosin 1c-regulated dynamic actin filament arrays. *Mol Biol Cell* **25,** 1111–1126 (2014).
31. Kuang, E. *et al.* ER stress triggers apoptosis induced by Nogo-B/ASY overexpression. *Exp Cell Res* **312,** 1983–1988 (2006).
32. Tagami, S., Eguchi, Y., Kinoshita, M., Takeda, M. & Tsujimoto, Y. A novel protein, RTN-XS, interacts with both Bcl-XL and Bcl-2 on endoplasmic reticulum and reduces their anti-apoptotic activity. *Oncogene* **19,** 5736–5746 (2000).
33. Chen, R. *et al.* Reticulon 3 attenuates the clearance of cytosolic prion aggregates via inhibiting autophagy. *Autophagy* **7,** 205–216 (2011).
34. Melino, S., Nepravishta, R., Bellomaria, A., Di Marco, S. & Paci, M. Nucleic acid binding of the RTN1-C C-terminal region: toward the functional role of a reticulon protein. *Biochemistry* **48,** 242–253 (2009).

35. Yu, J. *et al.* Reticulon 4B (Nogo-B) is necessary for macrophage infiltration and tissue repair. *Proc Natl Acad Sci USA* **106,** 17511–17516 (2009).
36. Chiurchiu, V., Maccarrone, M. & Orlacchio, A. The role of reticulons in neurodegenerative diseases. *Neuromolecular Med* **16,** 3–15 (2014).
37. O'Neill, P., Whalley, K. & Ferretti, P. Nogo and Nogo-66 receptor in human and chick: implications for development and regeneration. *Dev Dyn* **231,** 109–121 (2004).
38. Oertle, T. *et al.* Nogo-A inhibits neurite outgrowth and cell spreading with three discrete regions. *J Neurosci* **23,** 5393–5406 (2003).
39. Oertle, T., Merkler, D. & Schwab, M. E. Do cancer cells die because of Nogo-B? *Oncogene* **22,** 1390–1399 (2003).
40. He, W., Shi, Q., Hu, X. & Yan, R. The membrane topology of RTN3 and its effect on binding of RTN3 to BACE1. *J Biol Chem* **282,** 29144–29151 (2007).
41. Xue, H., Wang, Z., Chen, J., Yang, Z. & Tang, J. Knockdown of reticulon 4C by lentivirus inhibits human colorectal cancer cell growth. *Mol Med Rep* **12,** 2063–2067 (2015).
42. Borgese, N., Francolini, M. & Snapp, E. Endoplasmic reticulum architecture: structures in flux. *Current opinion in cell biology* **18,** 358–364 (2006).
43. Sprocati, T., Ronchi, P., Raimondi, A., Francolini, M. & Borgese, N. Dynamic and reversible restructuring of the ER induced by PDMP in cultured cells. *J Cell Sci* **119,** 3249–3260 (2006).
44. Lin, S., Staahl, B. T., Alla, R. K. & Doudna, J. A. Enhanced homology-directed human genome engineering by controlled timing of CRISPR/Cas9 delivery. *Elife* **3,** e04766 (2014).
45. Rong, Z., Zhu, S., Xu, Y. & Fu, X. Homologous recombination in human embryonic stem cells using CRISPR/Cas9 nickase and a long DNA donor template. *Protein Cell* **5,** 258–260 (2014).
46. Connolly, C. N., Futter, C. E., Gibson, A., Hopkins, C. R. & Cutler, D. F. Transport into and out of the Golgi complex studied by transfecting cells with cDNAs encoding horseradish peroxidase. *J Cell Biol* **127,** 641–652 (1994).
47. Kano, F. *et al.* NSF/SNAPs and p97/p47/VCIP135 are sequentially required for cell cycle-dependent reformation of the ER network. *Genes Cells* **10,** 989–999 (2005).
48. Elbashir, S. M. *et al.* Duplexes of 21-nucleotide RNAs mediate RNA interference in cultured mammalian cells. *Nature* **411,** 494–498 (2001).
49. Belevich, I., Joensuu, M., Kumar, D., Vihinen, H. & Jokitalo, E. Microscopy Image Browser: A Platform for Segmentation and Analysis of Multidimensional Datasets. *PLoS Biol* **14,** e1002340 (2016).
50. Jokitalo, E., Cabrera-Poch, N., Warren, G. & Shima, D. T. Golgi clusters and vesicles mediate mitotic inheritance independently of the endoplasmic reticulum. *J Cell Biol* **154,** 317–330 (2001).
51. Mclean, I. W. & Nakane, P. K. Periodate-Lysine-Paraformaldehyde Fixative - New Fixative for Immunoelectron Microscopy. *Journal of Histochemistry & Cytochemistry* **22,** 1077–1083 (1974).
52. Puhka, M., Vihinen, H., Joensuu, M. & Jokitalo, E. Endoplasmic reticulum remains continuous and undergoes sheet-to-tubule transformation during cell division in mammalian cells. *J Cell Biol* **179,** 895–909 (2007).
53. Kremer, J. R., Mastronarde, D. N. & McIntosh, J. R. Computer visualization of three-dimensional image data using IMOD. *J Struct Biol* **116,** 71–76 (1996).

Acknowledgements

We thank Tiina Viita and Maria Vartiainen (Institute of Biotechnology, University of Helsinki) for the BiFC constructs; Urmas Arumäe and Mikko Airavaara (Institute of Biotechnology, University of Helsinki) for SCG primary neurons; Mikhail Paveliev (Neuroscience Centre, University of Helsinki) for mouse cortical primary neurons; Suvi Saarnio and Iiris Hovatta (University of Helsinki) for help with qPCR; Mervi Lindman and Antti Salminen (Electron Microscopy Unit, Institute of Biotechnology, University of Helsinki) for assistance in EM; and Marko Crivaro, Mika Molin and Kimmo Tanhuanpää (Light Microscopy Unit, Institute of Biotechnology, University of Helsinki) for assistance with the statistical analysis and live cell imaging. This study was supported by the Academy of Finland (projects 131650 and 1287975, to E.J.) and Biocenter Finland. O.R., D.K. and M.J. were students of the Viikki Graduate School in Molecular Biosciences, University of Helsinki.

Author Contributions

O.R., P.A. and E.J. designed the study. O.R., D.K., E.G., M.J., M.S., H.V. and I.B. performed the experiments. O.R., D.K., H.V., I.B., O.-P.S., K.Q., P.A. and E.J. interpreted the data and M.J., D.K. and E.J. wrote the manuscript. All authors discussed the results and reviewed the manuscript.

Additional Information

Supplementary information accompanies this paper at http://www.nature.com/srep

Competing financial interests: The authors declare no competing financial interests.

How to cite this article: Rämö, O. *et al.* NOGO-A/RTN4A and NOGO-B/RTN4B are simultaneously expressed in epithelial, fibroblast and neuronal cells and maintain ER morphology. *Sci. Rep.* **6**, 35969; doi: 10.1038/srep35969 (2016).

Publisher's note: Springer Nature remains neutral with regard to jurisdictional claims in published maps and institutional affiliations.

II

REEP3 and REEP4 Determine the Tubular Morphology of the Endoplasmic Reticulum during Mitosis

Darshan Kumar[a,#], Banafsheh Golchoubian[b,#], Ilya Belevich[a,c], Eija Jokitalo*[,a,c], Anne-Lore Schlaitz*[,b]

[a]Cell and Molecular Biology Program, Institute of Biotechnology, University of Helsinki, Helsinki, Finland

[b]Center for Molecular Biology of Heidelberg University (ZMBH), Heidelberg, Germany

[c]Electron Microscopy Unit, Institute of Biotechnology, University of Helsinki, Helsinki, Finland

[#]These authors contributed equally to this work.

* Co-corresponding authors

Correspondence:

Anne-Lore Schlaitz

phone: (+49)6221 546889

email: a.schlaitz@zmbh.uni-heidelberg.de

Eija Jokitalo

phone: (+358)50 4696799

email: Eija.Jokitalo@Helsinki.fi

Running title: REEP3/4 shape mitotic ER

keywords: endoplasmic reticulum morphology, mitosis, reticulon-homology domain, REEP

Abstract

The endoplasmic reticulum (ER) is extensively remodeled during metazoan open mitosis. However, whether the ER becomes more tubular or more cisternal during mitosis is controversial, and dedicated factors governing the morphology of the mitotic ER have remained elusive. Here, we describe the ER membrane proteins REEP3 and REEP4 as major determinants of ER morphology in metaphase cells. REEP3/4 are specifically required for generating the high-curvature morphology of mitotic ER and promote ER tubulation through their reticulon homology domains. This ER shaping activity of REEP3/4 is distinct from their previously described function to clear ER from metaphase chromatin. We further show that related REEP proteins do not contribute to mitotic ER shaping and provide evidence that the REEP3/4 carboxyterminus mediates regulation of the proteins. These findings confirm that ER converts to higher curvature during mitosis, identify REEP3/4 as specific and crucial morphogenic factors mediating ER tubulation during mitosis and define the first cell cycle-specific role for reticulon homology domain proteins.

Introduction

The endoplasmic reticulum (ER) is a single membrane network of high curvature tubules and flat cisternae with highly curved edges, called ER sheets (Shibata et al., 2006; Goyal and Blackstone, 2013). A major structural determinant of ER tubules and the curved edges of ER sheets are morphogenic proteins containing reticulon homology domains (RHDs), in particular Reticulons (RTN1-4 in mammals) and REEP proteins (REEP1-6 in mammals). RHDs consist of paired hydrophobic hairpin structures that are believed to stabilize high membrane curvature by acting as wedges in the cytoplasmic leaflet of the ER membrane and by oligomerizing into scaffolds (Voeltz et al., 2006; Shibata et al., 2010; Westrate et al., 2015). During interphase, the peripheral ER and the nuclear envelope (NE) are two connected subdomains of the organelle. As cells enter mitosis, the NE disassembles and its membrane-associated components disperse across the peripheral ER. Throughout mitosis, the peripheral ER remains a single network and retracts from chromatin (Ellenberg et al., 1997). After chromosome segregation, ER contacts daughter cell chromatin to initiate the formation of a new NE (Güttinger et al., 2009; Schellhaus et al., 2016). Thus, ER morphology and dynamics are tightly coupled to NE dynamics during mitosis. In addition, the ER has been proposed to contribute to cytokinesis and may serve as a “spindle envelope” that promotes mitotic spindle assembly (Prekeris and Gould, 2008; Zhang et al., 2010; Schweizer et al., 2015). Hence, it is likely that the ER is remodelled at the onset of mitosis to fulfill a variety of cell cycle-specific functions. However, whether ER overall becomes more tubular or more sheet-like during mitosis is debated. Our earlier work demonstrated that ER undergoes a morphological transition to higher curvature, i.e. towards tubules and highly fenestrated sheet remnants, upon entry into mitosis (Puhka et al., 2007, 2012). However, others have reported a transition to more cisternal ER during mitosis (Lu et al., 2009; Wang et al., 2013). Importantly, specific factors determining mitotic ER morphology are currently unknown. We previously described REEP3 and REEP4 as RHD proteins that clear ER from metaphase chromosomes in a microtubule-dependent manner (Schlaitz et al., 2013). We now uncover that, REEP3/4 induce high curvature ER specifically during mitosis through their RHDs. REEP3/4 may thus molecularly couple membrane shaping and positioning to organize the ER during mitosis. Our findings lend further support to our

earlier observations that ER exhibits higher curvature during mitosis than during interphase, assign for the first time a cell cycle specific function to distinct RHD proteins and provide a framework for understanding organelle restructuring during mitosis.

Results

REEP3 and REEP4 are required for high ER membrane curvature in mitosis

To identify determinants of mitotic ER morphology, we depleted HeLa cells of selected RHD proteins by RNAi and analyzed ER structure by confocal light and serial block-face scanning electron microscopy (SB-EM). We chose REEP5 because it is the most abundant RHD protein in HeLa cells (Itzhak et al., 2016; Bekker-Jensen et al., 2017) and REEP3 and REEP4 because of their previously described role in mitotic ER organization (Schlaitz et al., 2013). In control cells, confocal light microscopy showed a diffuse distribution of ER during metaphase. Due to the high density of ER in mitotic cells and the limited resolution of light microscopy, most of the ER signal could not be resolved into individual structures (Figure 1A). Single depletions of REEP3, REEP4, or REEP5 efficiently reduced their respective protein levels but resulted in the same diffuse ER pattern that was observed in control cells (Figure 1A, B; quantifications in Figure S1). REEP3 and REEP4 function redundantly to remove ER from mitotic chromosomes (Schlaitz et al., 2013). We therefore also analyzed REEP3/4 double depleted cells for ER morphology defects using either a combination of the two single-targeting siRNAs or one double-targeting siRNA. Upon REEP3/4 double depletion, metaphase ER morphology changed profoundly. Discrete, long curvilinear ER profiles, separated by clearly ER-less regions were predominant in more than 80% of the cells treated with the double targeting siRNA (Figures 1A, B and S1). SB-EM analysis revealed that the ER network in control cells was excluded from chromatin and the spindle area. It consisted of many short ER tubules and only a few small or highly fenestrated sheets (Figure 1C, D, E, Supplemental Video 1). As these ER structures are small and densely packed (Figure 1E), they appear as diffuse haze by light microscopy (Figure 1A). After REEP3/4 RNAi, large sheets appeared, which were fenestrated to a similar degree as the remaining sheet-like regions in control cells. ER profiles were distributed throughout the entire cell and extended into the spindle area (Figure 1C, D, E, Supplemental Video 2). The large and discrete peripheral ER sheets after REEP3/4 RNAi manifest as individual long profiles in cross-section in the confocal light microscopy images (Figure 1A).

For a quantitative analysis of changes in ER morphology, we imaged control, REEP5 RNAi and REEP3/4 RNAi cells by transmission electron microscopy (TEM) and measured the lengths of peripheral ER profiles in both metaphase and interphase cells. High curvature ER regions such as tubules or small sheets are seen as short profiles whereas large sheets result in long continuous ER profiles in 60-nm TEM sections. Therefore, the shorter the observed profiles in these analyses, the higher the curvature of the underlying ER morphology (Puhka et al., 2012). In control metaphase cells, 76% of ER profiles had a length between 40 nm (the shortest expected profile length corresponding to a tubule in cross section) and 399 nm. Fewer than 4% of the profiles were longer than 1 µm. Upon REEP3/4 RNAi, the length distribution of metaphase ER profiles changed dramatically. Only 29% of REEP3/4 RNAi profiles were between 40 and 399 nm long and more than 40% were longer than 1 µm (Figure 2A, B). In contrast, ER profile length distributions in interphase were nearly identical for control or REEP3/4-depleted cells (Figure 2C,D), suggesting that REEP3/4 mediate high curvature of ER specifically during mitosis. Depletion of REEP5 caused no changes in metaphase ER profile lengths (Figure 2E, F), implying that the total amount of RHD protein was not critical for the observed high curvature ER morphology during mitosis. REEP5 knockdown did not lead to major changes to interphase ER profile lengths either (Figure 2G, H), in agreement with previous observations that multiple RHD proteins contribute redundantly to ER morphology in interphase cells (Voeltz et al., 2006; Anderson and Hetzer, 2008). In summary, these results show that REEP3/4 are essential for the normal, high curvature ER morphology during mitosis but are not required for normal interphase ER morphology.

REEP3/4 shape the mitotic ER through their reticulon homology domain

Next, we tested whether REEP3/4 promote the formation of high curvature ER during mitosis through their RHDs. Since REEP3/4 function redundantly, both in the clearance of ER from chromosomes and in mitotic ER shaping (Schlaitz et al., 2013; Figure 1A), we analyzed REEP4 as a representative for both proteins. We aimed to convert the second hydrophobic hairpin of the REEP4 RHD into a double-spanning transmembrane region by inserting additional hydrophobic residues and replacing two charged amino acids by hydrophobic ones (Figure 3A). Analogous

mutations have been shown to abolish the curvature-promoting properties of the RHD of Reticulon 4 (Zurek et al., 2011). We refer to the resulting REEP4 mutant as REEP4(mutRHD) for “REEP4 with mutated reticulon homology domain”. Importantly, REEP4(mutRHD)-HA retained the correct topology because like wild-type REEP4 it localized to the ER and its C-terminus faced the cytoplasm (Figure S2). To examine whether REEP4 and REEP4(mutRHD) could rescue the ER morphology defects after REEP3/4 depletion, we expressed RNAi-resistant versions of the proteins in control and REEP3/4 knockdown cells containing the general ER marker GFP-Sec61β. Mitotic ER morphology was analyzed in live cells because standard fixation protocols compatible with immunofluorescence staining perturbed mitotic ER morphology. mCherry-tagged Histone 2B (H2B-mCherry) was co-transfected together with the rescue constructs in order to identify transfected cells that expressed the rescue constructs and to label chromatin. In 84% of cells depleted of REEP3/4 and not expressing a rescue construct the ER was present predominantly in the form of clearly distinguishable long cytoplasmic ER profiles corresponding to large sheets. Wild-type REEP4 largely restored the diffuse ER appearance seen in control cells and corresponding to high curvature ER whereas REEP4(mutRHD) did not (Figure 3B, C). Hence, the REEP4 RHD is required to promote tubulation of mitotic ER. REEP4(mutRHD)-HA was present at similar or higher levels than REEP4-HA in the rescue experiments (Figure 3D), excluding the possibility that REEP4(mutRHD) failed to restore ER morphology due to low protein expression. Microtubule-dependent clearance of ER from mitotic chromatin requires the cytoplasmic loop of the REEP4 RHD (red in Figure 3A; Schlaitz et al., 2013), which remains intact in REEP4(mutRHD). Accordingly, REEP4 and REEP4(mutRHD) associated with microtubules to a similar extent in a co-pelleting assay (Figure 4A). To ask whether REEP4(mutRHD) can mediate clearance of ER from mitotic chromosomes, we analyzed fixed cells with recently segregated chromosomes. GFP-Sec61β expressing HeLa cells were co-transfected with control or REEP3/4 siRNA and either a plasmid encoding H2B-mCherry as a control treatment, or with plasmids encoding RNAi-resistant REEP4 or REEP4(mutRHD). ER was excluded from chromatin in cells transfected with control siRNA. In contrast, REEP3/4 depletion caused a strong accumulation of ER on chromatin as expected. Both REEP4 and REEP4(mutRHD) restored clearance of ER from chromatin in

REEP3/4 RNAi cells (Figure 4B, C). REEP4(mutRHD) rescued ER clearance less efficiently than REEP4, possibly because the highly cisternal morphology of the ER in REEP3/4 RNAi cells expressing REEP4(mutRHD) impaired microtubule-based transport of the organelle. Collectively, these results demonstrate that the REEP4 RHD is required for generating high-curvature ER in mitosis but is dispensable for clearing ER from chromatin. Given their high similarity, we assume that the same is true for the REEP3 RHD. Hence, the two functions of REEP3/4 in ER positioning and ER shaping can be uncoupled and the appearance of lower curvature ER after REEP3/4 RNAi is not a consequence of reduced microtubule association of the ER.

The REEP4 C-terminus is required for mitotic ER shaping in addition to the RHD

We next asked how REEP3 and REEP4 are able to shape the ER specifically during mitosis. REEP4 mRNA levels increase during mitosis in Huh-7 cells according to high-throughput data (Palozola et al., 2017). To determine whether REEP3/4 protein levels change during the cell cycle, we collected mitotic cells by shake-off (Schorl and Sedivy, 2007) and compared this mitotically enriched cell population to an interphase-arrested population of cells. REEP4 protein levels were increased by about 50% in the mitotic population whereas REEP3 protein levels remained nearly unchanged (Figure S3). This small difference implied that an adjustment of protein amounts may not be the principal mechanism conferring the mitosis-specific functions of REEP3/4. To ask which regulatory regions of REEP3/4 could be important for their role in mitotic ER shaping we considered the related REEP1 and REEP2. These two additional members of the REEP1-REEP4 protein family have been shown (for REEP1) or predicted (for REEP2) to associate with microtubules in contrast to the more divergent REEP5/6 proteins (Park et al., 2010; Schlaitz et al., 2013). Both REEP1 and REEP2 are expressed at very low levels in HeLa cells (Bekker-Jensen et al., 2017), consistent with the finding that REEP1 and REEP2 expression cannot be readily detected in non-neuronal tissues (Hurt et al., 2014). REEP1-4 are highly similar in their RHD-containing N-terminal regions but divergent in their C-termini (Park et al., 2010; Figure S4). We further investigated REEP2 because REEP1 has a markedly shorter C-terminal region than REEP2, REEP3 or REEP4 (Park et al., 2010; Figure S4). Endogenous amounts of REEP2

correspond to approximately 1% of the combined amounts of endogenous REEP3 and REEP4 based on recent high-throughput proteomics data (Bekker-Jensen et al., 2017). We were not able to detect the REEP2 protein or mRNA in HeLa cells and assumed that any functions of REEP2 in organizing the mitotic ER would likely be compensated for by the much more abundant REEP3/4. We therefore did not attempt to deplete REEP2 from HeLa cells. Instead, we tested whether exogenous expression of REEP2 could rescue the defects of REEP3/4-depletion. REEP2 localized to the ER in interphase and mitotic cells (Figure S5) and its overexpression did not perturb ER morphology in control metaphase cells (Figure S6). The REEP2 rescue construct was expressed at similar levels as the REEP4 rescue construct in REEP3/4-depleted cells (Figure 5A) but failed to restore high curvature ER morphology during mitosis (Figure 5B, C). However, REEP2 restored ER clearing from chromosomes in mitotic cells lacking REEP3/4 (Figure 5B). Consistently, REEP2 associated efficiently with microtubules (Figure S7). REEP2 thus displays a behavior that is similar to REEP4(mutRHD), despite the fact that the REEP2 N-terminal RHD and surrounding sequences are nearly identical to REEP3/4's (Figure S4). These observations suggest that REEP3/4 contain residues in their C-terminal regions that promote mitosis-specific ER shaping and may be targets of regulatory inputs. To further test this idea, we created a mutant of REEP4 containing the RHD but lacking the entire C-terminus. We call this N-terminal REEP4 fragment REEP4N (Figure 6A). Additionally, we generated a chimera of REEP2 and REEP4, in which the RHD-containing N-terminus of REEP2 was fused to the C-terminus of REEP4 (REEP2N4C; Figure 6A). REEP4N-HA and REEP2N4C localized to the ER with the predicted topologies (Figure S8), were expressed at similar levels as REEP4-HA (Figure 6B) and their exogenous expression did not cause ER morphology defects in control cells (Figure S6). Similar to REEP2, REEP4N did not rescue mitotic ER morphology after REEP3/4 depletion (Figure 6C, D). However, REEP2N4C efficiently restored proper ER morphology in mitotic cells (Figure 6C, D), suggesting that the putative regulatory sequences derived from REEP4 could now work together with the REEP2 RHD to promote formation of high curvature ER during mitosis.

Thus, the C-terminus of REEP4 harbors residues that are critical for the mitosis-specific functions of the protein. The identification of the signaling mechanisms that govern cell-cycle regulation of REEP3/4 activity will be important tasks for future research.

Discussion

Here we provide new support for our earlier proposal that the ER has a high curvature morphology during mitosis (Puhka et al., 2007 and 2012), which had been called into question by Lu et al. (2009). We now demonstrate that the reticulon homology domain proteins REEP3 and REEP4 are important determinants of mitotic ER morphology. We can clearly visualize and distinguish the high curvature morphology of wild type cells as well as the sheet-like morphology of REEP3/4 RNAi cells, excluding any technical bias in EM sample preparation. REEP3/4 are critical to generate high curvature ER and at the same time position ER away from chromatin during mitosis. REEP3/4 therefore combine distinct molecular activities to create the characteristic organization of the ER during mitosis.

Remarkably, an active RHD within REEP4 and the generation of high curvature peripheral ER are not strictly necessary for the clearing of ER from chromatin. On the other hand, ER morphology during mitosis is not controlled by accumulation of the organelle at the spindle poles as ER morphology remained in an aberrant low curvature state even when positioning was largely normal after rescue with REEP4(mutRHD), REEP2 or the REEP4 truncation mutant REEP4N.

Mitotic ER remodeling is essential in the context of an open mitosis as the nuclear envelope merges with the peripheral ER upon mitotic entry and is reformed from the ER after chromosome segregation. Mitotic nuclear envelope dynamics and its links to ER organization are still incompletely understood. REEP3/4 as critical ER remodelers will enable the study of how mitotic ER organization impacts nuclear envelope dynamics. Moreover, the contributions of ER remodeling to the organelle's roles in spindle assembly, chromosome segregation and cytokinesis can now be addressed.

An important question emerging from our study concerns the mitosis-specific regulation of REEP3/4. REEP3/4 protein levels in mitotic versus interphase cells were quite similar. Thus,

REEP3/4 activity may be modulated in a cell cycle-specific manner. The observation that the REEP4 C-terminus is required to promote normal high curvature ER morphology during metaphase provides a starting point to identify the signaling pathways that control REEP3/4 functions during mitosis. Insight into the regulation of REEP3/4 may eventually provide a framework to understand the regulation of further ER morphogenic proteins and the mitotic remodeling of other membrane-bound organelles.

In summary, we show that REEP3/4 create high curvature ER during mitosis and have separable functions in mitotic ER shaping and positioning. REEP3/4 provide the first examples of RHD proteins with distinct functions during the cell cycle. Other Reticulon/REEP proteins may similarly have specialized functions, which would begin to explain the puzzling complexity in this group of crucial ER morphogenic proteins.

Materials and methods

Cell culture, siRNAs, plasmids and transfections

HeLa cells (ATCC CCL-2, authenticated by UC Berkeley tissue culture facility) were cultured in DMEM supplemented with 10% fetal bovine serum (FBS) at 37°C in a humidified 5% CO_2 incubator. HeLa cells stably expressing AcGFP-Sec61β have been described previously (Schlaitz et al., 2013) and were maintained in DMEM/10%FBS supplemented with 400 µg/ml Geneticin (Sigma). Cells were checked for mycoplasma contamination every six months and were always negative. For plasmid transfections or siRNA/plasmid co-transfections, $1.8x10^5$ cells were seeded in one well of a 24-well plate and transfected the next day with 0.4 µg plasmid DNA using Lipofectamine 2000 (Invitrogen) according to the manufacturer's instructions. siRNAs were transfected using Lipofectamine RNAiMax (Invitrogen) according to the manufacturer's instructions. Three to six hours after transfection, cells were split onto coverslips or into µ-slide wells (ibidi).

For all rescue experiments, the HA-tagged rescue constructs were co-transfected with H2B-mCherry. All H2B-mCherry-expressing cells were imaged live and considered for analysis. Live cell

microscopy had to be performed in order to best preserve ER morphology for assessment of phenotypes. We were not able to express functional fluorescent-protein tagged REEP4 in HeLa cells and therefore had to use the HA-tagged constructs which are invisible in our live imaging experiments. However, transfected cells are highly likely to have received both plasmids, H2B-mCherry and the HA-tagged rescue construct, (Susa et al., 2008; Xie et al., 2011) and a rescue of ER clearance was observed in the large majority of H2B-mCherry-expressing cells, indicating that they also expressed the rescue constructs. Transfection efficiencies in our experiments were approximately 25%. With this mean transfection efficiency and quantifications of Western blot signal from the lysates of the entire cell populations we can derive that the rescue constructs in the transfected cells were on average 1.2- to five-fold overexpressed in comparison to endogenous REEP4.

siRNAs used in this study:

name/catalogue number	**description/reference**	**sequence**
4392420, s37271 (ThermoFisher)	REEP3/4 double targeting siRNA (Schlaitz et al., 2013)	GGAUUGUUUUUGCACUCUUtt
4392420, s47939 (ThermoFisher)	REEP3 single depletion siRNA (Schlaitz et al., 2013)	CAGUAUGCAUGAUUUAACAtt
AM16708, #32438 (ThermoFisher)	REEP4 single depletion siRNA (Schlaitz et al., 2013)	GGCUGUGAAGACCAAGAACtt
4392420, s15454 (ThermoFisher)	REEP5 siRNA	CGAAGAAAGCUACCGUGAAtt
Ambion negative control, AM4611 siRNA	non-targeting control siRNA	

Plasmids used in this study:

plasmid name	**description**	**source/reference**
REEP4(WT)-HA	human full length wild type REEP4, resistant to Ambion siRNA s37271, C-terminally HA-tagged	Schlaitz et al., 2013
REEP4(mut RHD)-HA	human full length REEP4 with mutRHD mutation, resistant to Ambion siRNA s37271, C-terminally HA-tagged	This study: REEP4-HA was amplified with primers including overhangs coding for the inserted and mutated residues, plasmid was assembled using Gibson assembly (NEB).
H2B-mCherry	human Histone H2B, C-terminally mCherry-tagged	Neumann et al., 2010; provided by Dr. Elisa Dultz (ETH Zurich)
Hsp47-APEX-RDEL	mouse Hsp47 C-terminally tagged with APEX2 and RDEL ER retention signal	Dr. Maria Vartiainen (University of Helsinki)
REEP2-HA	human full length wild type REEP2, C-terminally HA-tagged	This study: REEP2 sequence was PCR amplified from cDNA clone MHS1011-61419 (Open Biosystems) and cloned over SacI/SacII restriction sites into a modified version of pEGFP-N1 (Clontech) in which the pEGFP sequence was replaced by the HA-sequence.
REEP4N-HA	human REEP4 amino acids 1 to 123, resistant to Ambion siRNA s37271, C-terminally HA-tagged	This study: The sequence coding for REEP4 aa 1 to 123 was PCR amplified from REEP4-HA and cloned over SacI/SacII restriction sites into a modified version of pEGFP-N1 (Clontech) in which the pEGFP sequence was replaced by the HA-sequence.

REEP2N4C-HA	plasmid expressing a chimeric construct consisting of REEP2(aa1-127) fused to REEP4(aa128 to 257).	This study: The REEP2-HA plasmid was PCR-linearized excluding the sequence coding for REEP2 aa 128 to 252. The REEP4 sequence coding for aa 128 to 257 was amplified from REEP4-HA including overhangs corresponding to the ends of the REEP2-HA PCR product. Both fragments were joined using Gibson assembly (NEB).

Rationale for generation of REEP4(mutRHD)-HA. Precise structural information of RHDs is not available but stretches of hydrophobic amino acids within this motif are believed to insert as paired hairpins into the outer leaflet of the ER membrane lipid bilayer, displacing membrane lipids in this leaflet and thus generating or stabilizing high membrane curvature (Voeltz et al., 2006; Hu et al., 2008). An unusual orientation of the membrane-associated segments as well as an amphipathic helix following the RHD have been proposed to contribute to RHD protein function but the presence of the two hydrophobic RHD hairpins is essential for curvature formation (Brady et al., 2015). Elongation of one or both of the putative RHD hydrophobic hairpins to convert them into double-spanning transmembrane domains has been shown to abolish RHD curvature promoting properties (Zurek et al., 2011). We targeted the second hairpin of REEP4's RHD to preserve the cytoplasmic loop between the hairpins, which is required for microtubule binding. We followed the approach taken by Zurek et al. (2011) and inserted five additional hydrophobic amino acids into the first part of the second hairpin to extend this stretch to nineteen hydrophobic amino acids, the length of a regular transmembrane span. Immediately following this new transmembrane span we added two charged glutamate residues. Together with a third glutamate residue already present in the REEP4 sequence this charged sequence stretch should be forced into the ER lumen. The second part of the predicted hairpin contained many hydrophobic but also polar and charged amino acids. The polar and charged amino acids may affect orientation within the lipid bilayer and thus the functionality of the RHD. To create a morphogenically inert transmembrane span we

mutated two of the charged residues in the second part of the hydrophobic hairpin, generating a second 21 amino acids long transmembrane segement. According to the transmembrane helices prediction tools TMHMM and TMpred (Sonnhammer et al., 1998; Hofmann and Stoffel, 1993), the mutRHD stretch is highly likely to be a double-spanning transmembrane domain.

Antibodies, immunofluorescence, and light microscopy

For immunofluorescence, cells grown on coverslips were fixed with 3% formaldehyde/0.02 % glutaraldehyde (Electron Microscopy Sciences), quenched with 0.5 mg/ml $NaBH_4$ (Sigma), permeabilized with 0.1% Triton X-100 (Merck) in PBS and blocked with 5% normal donkey serum (Abcam). Primary antibodies were diluted in PBS/0.1% Tween to the concentrations specified in the table below. Secondary antibodies were raised in donkey, coupled to Alexa 568, Alexa 488 or Alexa 647 dyes (ThermoFisher) and used at a dilution of 1/500. For selective permeabilization of the plasma membrane, coverslips were treated with 40 µg/ml digitonin (Merck) in PBS for 5 minutes on ice and antibody dilutions were prepared in PBS. DNA was labeled with Hoechst 33342 (Merck). Coverslips were mounted with ProLong Diamond (ThermoFisher) and imaged on a Zeiss LSM780 microscope with a 63x obejective using the ZEN software. Live cell imaging was performed on a Leica DMi8 spinning disk microscope using a 63x objective equipped with a Hamamatsu EMCCD camera, Yokogawa spinning disk head and diode lasers with 488 nm and 561 nm laser lines. Image acquisition was performed using Metamorph software (Molecular Devices). The microscope was equipped with an environmental chamber. The temperature during live cell imaging was set to 34°C and cells were kept in µ-slides (ibidi) in CO_2-independent L15 medium supplemented with 20% FBS (ThermoFisher).

The following antibodies were used in this study:

name	**source/reference**	**use**
anti HA-tag 6E2	CST, #2367	immunofluorescence (IF): 1/100
anti HA-tag 3F10	Sigma, # 11867423001	Western blotting (WB): 1/5000
anti REEP5	Proteintech, 14643-1-AP	WB: 1/5000
anti REEP4(7-1)	this study; raised against REEP4 peptide NH2-CDTEAVPRAPARPREKPLIR-CONH2, position 203-221 of the human REEP4 protein (Pineda Antibody Service)	WB: 1/1000
anti REEP3	Abcam, ab106463 (note: major detected band at 35 kDa is background, minor band at around 26 kDa corresponds to REEP3)	WB: 1/1000
anti β-actin	Abcam, ab8224	WB: 1/5000
anti phospho-H3 D2C8	CST, #3377T	WB: 1/1000
anti GAPDH 14C10	CST, #2118S	WB: 1/1000
anti Lamin B1	Abcam, ab 16048	IF: 1/500

Light microscopy image analysis and quantifications

1. Live microscopy to assess ER morphology under different depletion and rescue conditions

To quantify the ocurrence of ER morphology defects we manually classified the images obtained during live cell microscopy according to the following criteria: ER morphology was considered normal if the majority of peripheral ER displayed a diffuse distribution with at most a few ER-less regions and if only a minor portion of ER was present as curvilinear profiles. ER morphology was considered abnormal (cisternal) if the majority of ER in the periphery was present in the form of long curvilinear profiles with extensive ER-less gaps and if only a minority of ER appeared as a

diffuse “haze”. Across all experiments and different researchers examining the phenotypes, roughly 80% of cells depleted of REEP3/4 and not expressing a rescue construct displayed abnormal cisternal ER morphology during metaphase.

For the rescue experiements (Figures 3, 5 and 6) we asked whether the fraction of REEP3/4-depleted cells exhibiting abnormal cisternal ER morphology changed upon transfection with the respective rescue constructs (REEP4(WT), REEP4(mutRHD), REEP2, REEP4N or REEP2N4C) compared to transfection with the empty pHA-vector (non-rescued condition). To exclude a personal bias in the analysis of light microscopy images we performed a blind classification as follows: Individual cells were cropped out from every raw image and saved in the TIF format. Intensities for all color channels across all cropped images were normalized and the resulting images were shuffled and renamed with the experiment date and a randomly assigned number. The shuffled images were independently classified by three authors (DK, BG, AS) based on the abovementioned criteria for normal or abnormal ER morphology. Cells for which either of the two phenotypes could not be clearly assigned, usually due to low image quality, were excluded from the analysis. After assigning scoring outcomes back to the individual experimental conditions, the fraction of cells exhibiting abnormal cisternal ER morphology was determined for every experiment and every condition. The obtained fractional values were normalized to the non-rescue condition, i.e. REEP3/4 RNAi + pHA. The normalized values were then averaged across the three different scorers and over the different experiments for the respective condition (three to five experiments for every condition, n specified in the figure legends) and in the final graphs the mean of the means of all experiments is shown. The whole workflow was performed using Microscopy Image Browser (MIB) and Matlab (Mathworks Inc, MA). Plot generation and statistics were done with Microsoft Excel.

Sample size was determined by experimental constraints – we acquired as many images of live cells as possible during the eight to nine hour imaging sessions. All H2B-mCherry-positive metaphase cells were considered and no cells excluded at the acquisition stage.

2. Quantification of ER clearing from chromosomes of fixed telophase cells (Figure 4)

Quantification of ER clearing was done using Fiji (Schindelin et al., 2012). Background subtraction was performed using a rolling ball algorithm with a diameter of 150 pixels (corresponding to the average cell size). One mask for chromatin based on Hoechst staining and one mask for the entire cell based on GFP-Sec61β signal were generated, mean intensites of ER signal (GFP-Sec61β) in these two regions were measured and the ratio between the two values was calculated. Average values obtained for ER mean intensity fraction for control cells were subtracted from the average values obtained for REEP3/4 RNAi cells to visualize the absolute changes in ER accumulation on chromatin.

Microtubule co-pelleting assays

For microtubule co-pelleting assays, HEK293T cells were transfected with the respective constructs 48 hours before the experiment and lysed by detergent treatment. Lysates were cleared by centrifugation at 10,000 x g and 100,000 x g. The supernatant was supplemented with 1 mM GTP, split in two and incubated with either buffer or with taxol-stabilized microtubules for 30 minutes at room temperature. Samples were centrifuged through a sucrose cushion for 30 minutes at 55,000 x g at 25 ºC. Supernatants and pellets were adjusted to equal volumes and equivalent amounts were analyzed by immunoblotting and detection of tubulin, the HA-tag or endogenous REEP5.

Electron microscopy and ER profile lengths measurements

For transfections, jetPRIME (Polyplus-transfection, France) or Lipofectamine RNAiMAX (ThermoFisher) were used according to manufacturer's instructions and cells were fixed for analysis 48 hours post-transfection (for REEP3/4 depletion) or 72 hours post-transfection (REEP5 depletion). For electron microscopy, cells grown on glass coverslips were cytochemically stained and flat embedded as described previously (Jokitalo et al., 2001; Rämö et al., 2016). TEM images were acquired using Jeol JEM-1400 (Jeol Ltd., Tokyo, Japan) operating at 80kV equipped with Gatan Orius SC 1000B bottom mounted CCD-camera (Gatan Inc., USA).

Samples for SB-EM were prepared as described previously (Puhka et al., 2012). SB-EM data sets were acquired with an FEG-SEM Quanta 250 (Thermo Fisher/FEI, Hillsboro, OR), using a backscattered electron detector (Gatan Inc., Pleasanton, CA) with 2.5-kV beam voltage, a spot size of 3, and a pressure of 0.3 Torr. The block faces were cut with 30-nm increments and imaged with XY resolution of 15 nm per pixel. Image processing and segmentation were done using MIB (Belevich et al., 2016). Visualization of models and rendering of videos were done using Amira (VSG, ThermoFisher/FEI Company).

To measure ER profile lengths in interphase, TEM images from four opposing sides of the nucleus per cell were collected, whereas for the mitotic condition the whole cell was imaged at 2500x magnification. Images from 3 consecutive sections per cell (n= 8 mitotic or 10 interphase control and REEP3/4 RNAi cells; n= 8 mitotic or 20 interphase control cells for REEP5) were collected. For quantification, a skeleton model of the ER network excluding chromatin associated ER was generated and analysed using a specially designed plugin in the MIB software.

Statistical analysis of ER profile lengths measurements

The ER profile length analysis (Figure 2) compares the distribution of ER profile lengths over specified categories. A comparative analysis using dice similarity coefficient (DSC) derived from Sørensen's formula was implemented for a statistical evaluation of the profile length distributions in the different knockdown conditions. A DSC value closer to 1 states a very high overlap or less difference between the two distributions and a DSC value close to zero relates to a very small overlap between the distributions.

Acknowledgements

We thank Mervi Lindman (University of Helsinki) for assistance with EM sample preparation, Holger Lorenz (ZMBH) for expert light microscopy support, Helena Bragulat Teixidor (Heidelberg University) for help with mitotic shake-off experiments, and Rebecca Heald (UC Berkeley) and Sebastian Schuck (ZMBH) for discussions and comments on the manuscript. We acknowledge Maria Vartiainen (University of Helsinki) for her kind gift of Hsp47-APEX-RDEL-plasmid.
This work was funded by the German Research Foundation (DFG, project no SCHL1876/2-1, A.S.), the Academy of Finland (project no 1287975, E.J.), the Sigrid Jusélius Foundation (E.J.), the Biocenter Finland (E.J, and I.B.) and the Helsinki Institute of Life Science Fellow's program (E.J.). D.K. is a graduate student in the program in Integrative Life Science, University of Helsinki. B.G. is a graduate student of the HBIGS Graduate School of Molecular and Cellular Biology of Heidelberg University.

Author contributions

A.S. and E.J. designed the study and acquired funding. D.K., B.G., I.B. and A.S. performed experiments. A.S. wrote the paper. All authors contributed to data analysis and data interpretation, and provided input on the manuscript.

Conflict of interest

The authors declare that they have no conflict of interest.

References

Anderson, D. J., and Hetzer, M. W. (2008). Reshaping of the endoplasmic reticulum limits the rate for nuclear envelope formation. The Journal of Cell Biology *182*, 911–924.

Bekker-Jensen, D. B. *et al.* (2017). An Optimized Shotgun Strategy for the Rapid Generation of Comprehensive Human Proteomes. Cell Systems *4*, 587–599.e4.

Belevich, I., Joensuu, M., Kumar, D., Vihinen, H., and Jokitalo, E. (2016). Microscopy Image Browser: A Platform for Segmentation and Analysis of Multidimensional Datasets. Plos Biol *14*, e1002340–13.

Brady, J. P., Claridge, J. K., Smith, P. G., and Schnell, J. R. (2015). A conserved amphipathic helix is required for membrane tubule formation by Yop1p. Proc Natl Acad Sci USA *112*, E639–E648.

Ellenberg, J., Siggia, E. D., Moreira, J. E., Smith, C. L., Presley, J. F., Worman, H. J., and Lippincott-Schwartz, J. (1997). Nuclear membrane dynamics and reassembly in living cells: targeting of an inner nuclear membrane protein in interphase and mitosis. The Journal of Cell Biology *138*, 1193–1206.

Goyal, U., and Blackstone, C. (2013). Untangling the web: Mechanisms underlying ER network formation. BBA - Molecular Cell Research *1833*, 2492–2498.

Güttinger, S., Laurell, E., and Kutay, U. (2009). Orchestrating nuclear envelope disassembly and reassembly during mitosis. Nature Reviews Molecular Cell Biology *10*, 178–191.

Hofmann, K., and Stoffel, W. (1993). TMBASE - A database of membrane spanning protein segments. Biol. Chem. Hoppe-Seyler *374*, 166.

Hu, J., Shibata, Y., Voss, C., Shemesh, T., Li, Z., Coughlin, M., Kozlov, M. M., Rapoport, T. A., and Prinz, W. A. (2008). Membrane Proteins of the Endoplasmic Reticulum Induce High-Curvature Tubules. Science *319*, 1247–1250.

Hurt, C. M., Björk, S., Ho, V. K., Gilsbach, R., Hein, L., and Angelotti, T. (2014). REEP1 and REEP2 proteins are preferentially expressed in neuronal and neuronal-like exocytotic tissues. Brain Research *1545*, 12–22.

Itzhak, D. N., Tyanova, S., Cox, J., and Borner, G. H. (2016). Global, quantitative and dynamic mapping of protein subcellular localization. Elife *5*, 570.

Jokitalo, E., Cabrera-Poch, N., Warren, G., and Shima, D. T. (2001). Golgi clusters and vesicles mediate mitotic inheritance independently of the endoplasmic reticulum. The Journal of Cell Biology *154*, 317–330.

Lu, L., Ladinsky, M. S., and Kirchhausen, T. (2009). Cisternal organization of the endoplasmic reticulum during mitosis. Molecular Biology of the Cell *20*, 3471–3480.

Neumann, B. *et al.* (2010). Phenotypic profiling of the human genome by time-lapse microscopy reveals cell division genes. Nature *464*, 721–727.

Palozola, K. C., Donahue, G., Liu, H., Grant, G. R., Becker, J. S., Cote, A., Yu, H., Raj, A., and Zaret, K. S. (2017). Mitotic transcription and waves of gene reactivation during mitotic exit. Science *358*, 119–122.

Park, S. H., Zhu, P.-P., Parker, R. L., and Blackstone, C. (2010). Hereditary spastic paraplegia proteins REEP1, spastin, and atlastin-1 coordinate microtubule interactions with the tubular ER

network. J. Clin. Invest. *120*, 1097–1110.

Prekeris, R., and Gould, G. W. (2008). Breaking up is hard to do - membrane traffic in cytokinesis. Journal of Cell Science *121*, 1569–1576.

Puhka, M., Joensuu, M., Vihinen, H., Belevich, I., and Jokitalo, E. (2012). Progressive sheet-to-tubule transformation is a general mechanism for endoplasmic reticulum partitioning in dividing mammalian cells. Molecular Biology of the Cell *23*, 2424–2432.

Puhka, M., Vihinen, H., Joensuu, M., and Jokitalo, E. (2007). Endoplasmic reticulum remains continuous and undergoes sheet-to-tubule transformation during cell division in mammalian cells. The Journal of Cell Biology *179*, 895–909.

Rämö, O. *et al.* (2016). NOGO-A/RTN4A and NOGO-B/RTN4B are simultaneously expressed in epithelial, fibroblast and neuronal cells and maintain ER morphology. Sci Rep *6*, 1–14.

Schellhaus, A. K., De Magistris, P., and Antonin, W. (2016). Nuclear Reformation at the End of Mitosis. Journal of Molecular Biology *428*, 1962–1985.

Schindelin, J. *et al.* (2012). Fiji: an open-source platform for biological-image analysis. Nature Methods *9*, 676–682.

Schlaitz, A.-L., Thompson, J., Wong, C. C. L., Yates, J. R., III, and Heald, R. (2013). REEP3/4 Ensure Endoplasmic Reticulum Clearance from Metaphase Chromatin and Proper Nuclear Envelope Architecture. Developmental Cell *26*, 315–323.

Schorl, C., and Sedivy, J. M. (2007). Analysis of cell cycle phases and progression in cultured mammalian cells. Methods *41*, 143–150.

Schweizer, N., Pawar, N., Weiss, M., and Maiato, H. (2015). An organelle-exclusion envelope assists mitosis and underlies distinct molecular crowding in the spindle region. The Journal of Cell Biology *108*, 17343–10.

Shibata, Y., Shemesh, T., Prinz, W. A., Palazzo, A. F., Kozlov, M. M., and Rapoport, T. A. (2010). Mechanisms Determining the Morphology of the Peripheral ER. Cell *143*, 774–788.

Shibata, Y., Voeltz, G. K., and Rapoport, T. A. (2006). Rough Sheets and Smooth Tubules. Cell *126*, 435–439.

Sonnhammer, E.L., von Heijne, G., and Krogh A. (1998). A hidden Markov model for predicting transmembrane helices in protein sequences. Proc Int Conf Intell Syst Mol Biol. *6*, 175-82.

Susa, T., Kato, T., and Kato, Y. (2007). Reproducible transfection in the presence of carrier DNA using FuGENE6 and Lipofectamine2000. Mol Biol Rep *35*, 313–319.

Voeltz, G. K., Prinz, W. A., Shibata, Y., Rist, J. M., and Rapoport, T. A. (2006). A Class of Membrane Proteins Shaping the Tubular Endoplasmic Reticulum. Cell *124*, 573–586.

Wang, S., Romano, F. B., Field, C. M., Mitchison, T. J., and Rapoport, T. A. (2013). Multiple mechanisms determine ER network morphology during the cell cycle in Xenopus egg extracts. The Journal of Cell Biology *203*, 801–814.

Westrate, L. M., Lee, J. E., Prinz, W. A., and Voeltz, G. K. (2015). Form Follows Function: The Importance of Endoplasmic Reticulum Shape. Annu. Rev. Biochem. *84*, 791–811.

Xie, Z. L., Shao, S. L., Lv, J. W., Wang, C. H., Yuan, C. Z., Zhang, W. W., and Xu, X. J. (2011). Co-transfection and tandem transfection of HEK293A cells for overexpression and RNAi experiments. Cell. Biol. Int. *35*, 187–192.

Zhang, D., Vjestica, A., and Oliferenko, S. (2010). The Cortical ER Network Limits the Permissive Zone for Actomyosin Ring Assembly. Current Biology *20*, 1029–1034.

Zurek, N., Sparks, L., and Voeltz, G. (2010). Reticulon Short Hairpin Transmembrane Domains Are Used to Shape ER Tubules. Traffic *12*, 28–41.

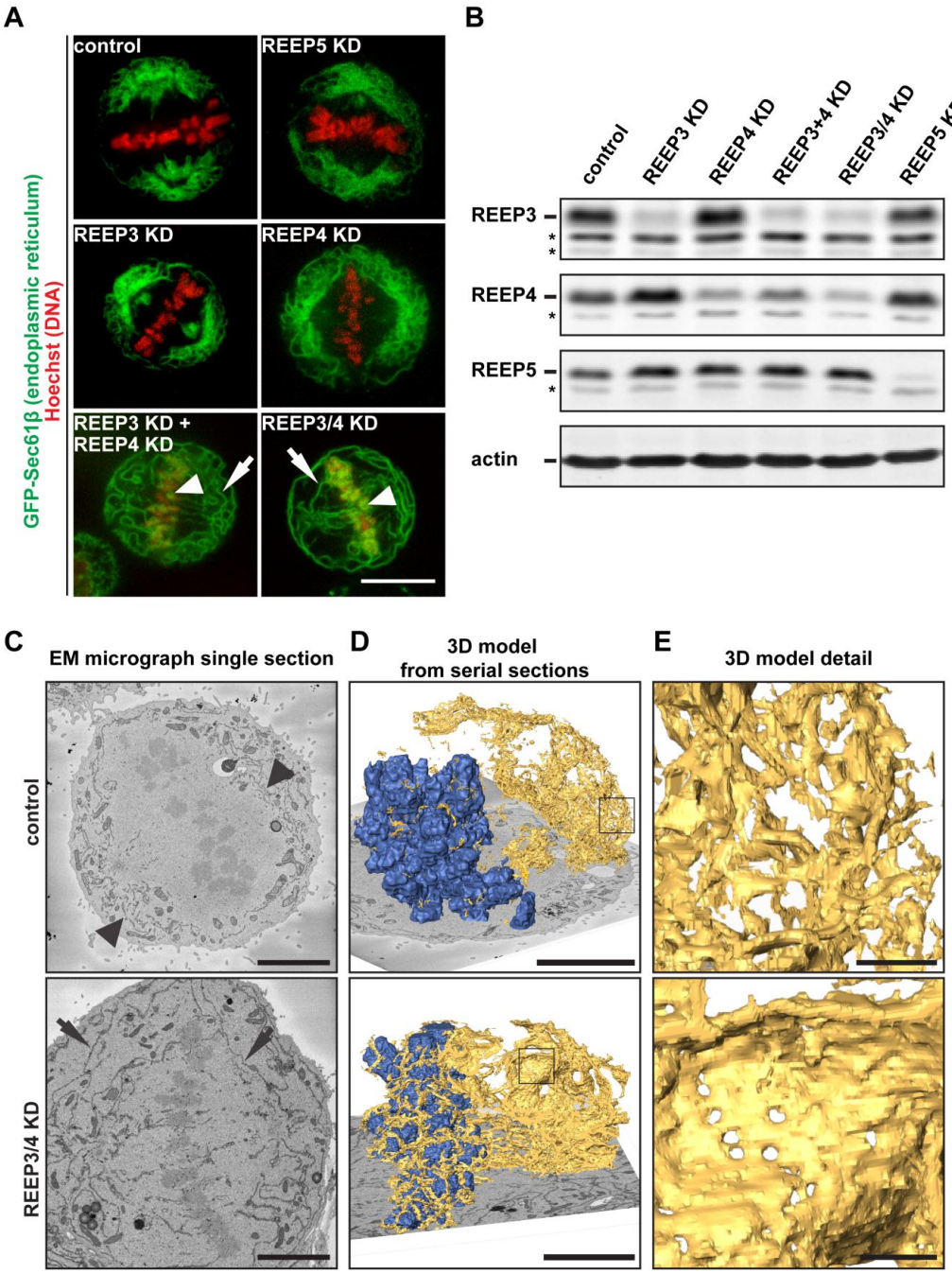

Figure 1. *Generation of high-curvature ER membranes during mitosis depends on REEP3 and REEP4.*

A) HeLa cells stably expressing GFP-Sec61β were transfected with control siRNA, siRNA targeting REEP5, REEP3 or REEP4 individually, a mix of one REEP3- and one REEP4-targeting siRNA or one single REEP3/4-double targeting siRNA. Cells were imaged live at metaphase. In controls and single depletions, ER had a diffuse overall appearance and remained excluded from chromatin. After REEP3/4 double knockdown (KD), ER showed long distinct profiles in the cell periphery (arrows) and accumulated on metaphase chromatin (arrowheads). For quantifications see Figure S1. Scale bar is 10 µm. **B)** Western blot analysis of knockdown experiments as shown in panel (A) confirming efficient depletion of REEP5, REEP3 and REEP4 under the respective conditions. Asterisks indicate non-specific bands. **C)** Single SB-EM images of control and REEP3/4 RNAi cells in metaphase. Control cells show short peripheral ER profiles (arrowheads). In REEP3/4 RNAi cells, ER is present as long profiles in the cell periphery (arrows). Scale bars are 5 µm. **D)** A model for chromatin (blue) and ER (yellow) of control and REEP3/4 RNAi cells generated from the SB-EM data set consisting of 550 and 471 block face images, respectively, taken at 30 nm intervals. For clarity, the model displays the ER around chromosomes (ER in up to 320 nm proximity to chromatin) and all ER in a 1.5 µm wide section across the cell. In control cells, ER exhibits high curvature with tubular and few small sheet regions. In the REEP3/4 RNAi cell, peripheral ER primarily consists of large sheets. For complete models see supplemental videos 1 and 2. Scale Bars are 5 µm. **E)** Details from the models shown in panel D corresponding to the boxed regions. Scale bars are 500 nm.

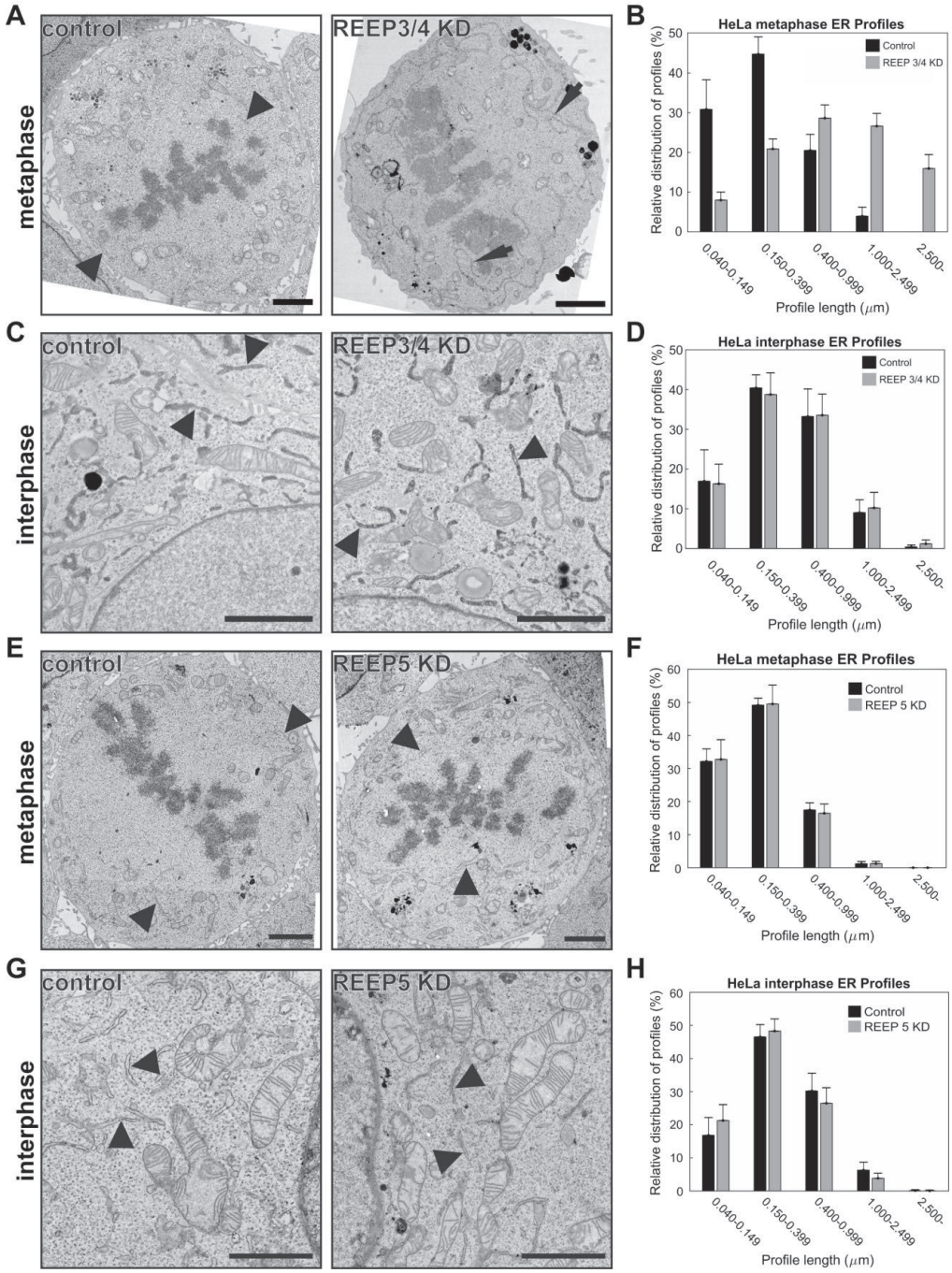

Figure 2. *Metaphase ER curvature decreases upon depletion of REEP3/4.*

A) Representative TEM images from metaphase control and REEP3/4 knockdown (KD) cells. **B)** Relative distribution of ER profile lengths measured from TEM images of control and REEP3/4

RNAi metaphase cells. Number of cells analyzed (n) = 8. For a statistical analysis of the difference between the profile lengths distributions we determined the dice similarity coefficient (DSC), which compares the distribution overlap between two conditions. If the DSC is close to 1, there is a very high overlap between the two distributions, a value of smaller than 1 describes the extent of non-overlap of the two distributions. For details see materials and methods. For metaphase control versus REEP3/4 KD conditions shown in the graph, the DSC is 0.53. **C)** As in panel A but interphase cells. REEP3/4 siRNA and Hsp47-APEX-RDEL were co-transfected. Darker ER staining mediated by Hsp47-APEX-RDEL therefore indicates transfected cells. **D)** As in panel B but interphase cells. n = 10. The DSC is 0.98. **E)** Representative TEM images from metaphase control and REEP5 KD cells. **F)** Relative distribution of ER profile lengths measured from TEM images of control and REEP5 KD metaphase cells. n = 8. The DSC is 0.99. **G)** As in panel E but interphase cells. **H)** As in panel F but interphase cells. n = 20. The DSC is 0.94.
A), C), E), G) Arrowheads and arrows indicate normal and extended profiles, respectively. Scale bars are 2 µm. **B), D), F), H)** Data are mean ± standard deviation.

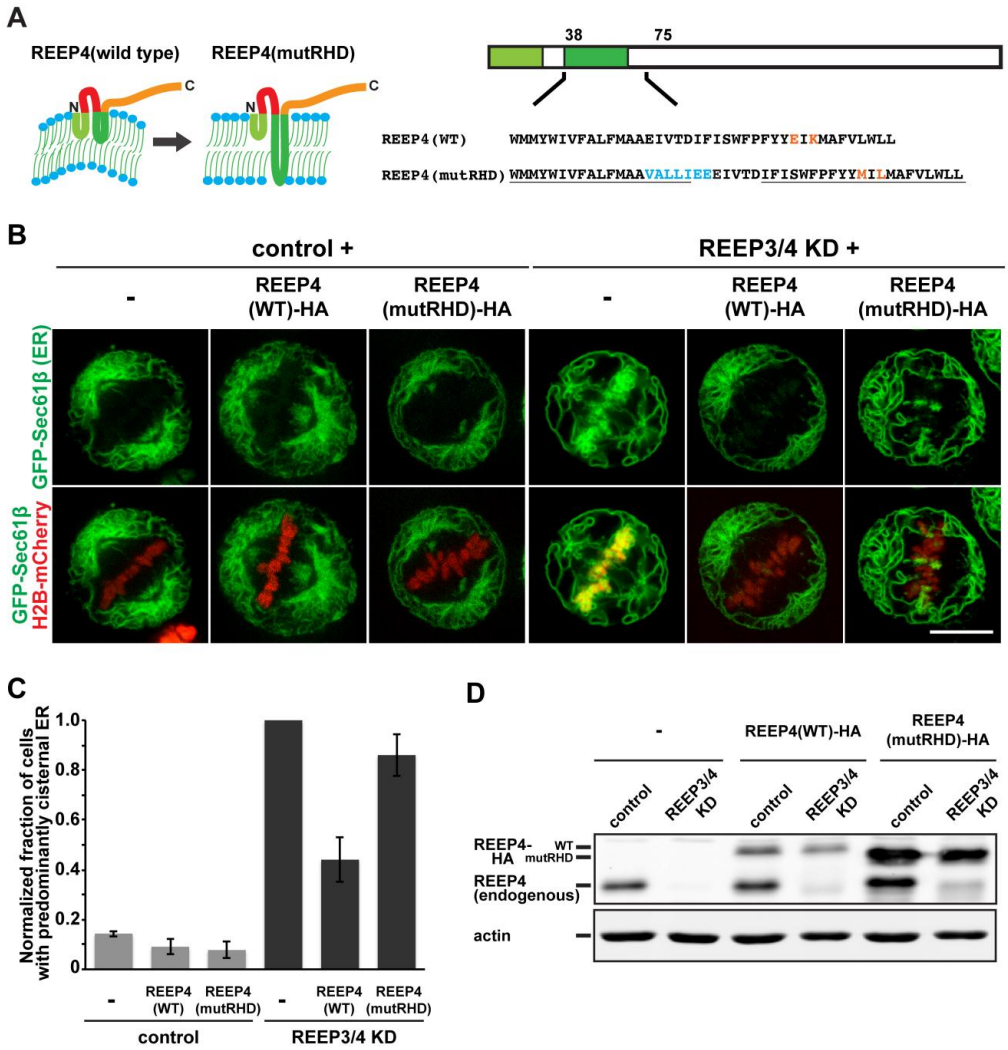

Figure 3. *Mitotic ER shaping by REEP4 depends on its reticulon homology domain.*

A) Design of a REEP4 RHD mutant. The two putative hairpin regions of the RHD are marked in green. Hypothetical topological models of wild type REEP4 and REEP4(mutRHD) are on the left, the mutated sequence region is shown on the right. The second hairpin was converted into a double-spanning transmembrane domain in REEP4(mutRHD). Added amino acids are marked in blue, residues mutated from charged to hydrophobic are marked in orange and the resulting

predicted transmembrane segments with lengths of 19 and 21 amino acids are underlined in the displayed sequence. See materials and methods for details on how the mutant was designed. **B)** ER morphology in GFP-Sec61β-expressing control and REEP3/4 knockdown (KD) cells. Cells were co-transfected with H2B-mCherry and either empty HA-tagging plasmid or RNAi-resistant REEP4-HA or REEP4(mutRHD)-HA and imaged live by spinning disk microscopy. Expression of either rescue construct did not affect ER morphology in control cells. REEP4-HA but not REEP4(mutRHD)-HA restored normal ER morphology in metaphase REEP3/4 KD cells. Scale bar is 10 µm. **C)** Quantification of mitotic ER morphology phenotypes from data as shown in panel B. Cells with predominantly distinct ER profiles were classified as having abnormal cisternal ER morphology. At least twenty cells were analyzed per condition in each of three independent experiments in a blind way. Results were normalized to the value obtained for non-rescued REEP3/4 KD. REEP3/4RNAi cells expressing either REEP4-HA or REEP4(mutRHD)-HA are significantly different ($p=0.03$). Statistical testing was done using Welch's t-test. Error bars are standard error of the mean (SEM). **D)** REEP4(mutRHD)-HA migrates at the expected size in SDS-PAGE and is expressed at higher levels than REEP4-HA in rescue experiments. Cell lysates were generated for the rescue experiment shown in panel (B) and analyzed by SDS-PAGE and immunoblotting. Endogenous REEP4 as well as REEP4-HA and REEP4(mutRHD)-HA were detected with anti-REEP4 antibody, the same blot was probed for actin as loading control. REEP4(mutRHD)-HA ist slightly larger than REEP4-HA but migrates faster in SDS-PAGE, possibly due to a change in hydrophobicity.

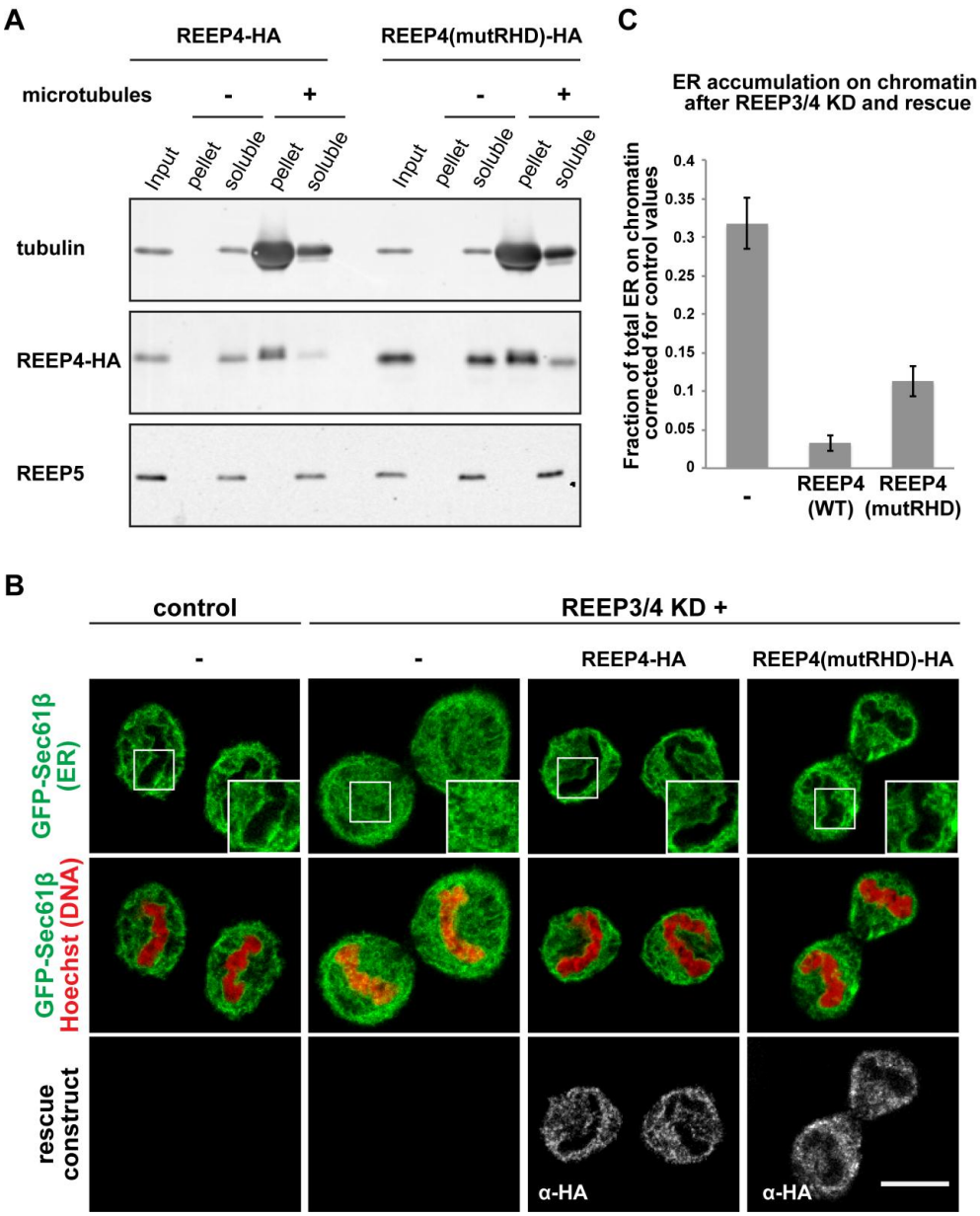

Figure 4. *ER clearing from chromatin does not require the REEP4 reticulon homology domain.*

A) REEP4-HA and REEP4(mutRHD)-HA were subjected to a microtubule co-sedimentation assay. Samples for input, microtubule-bound fraction (pellet) and non microtubule-bound fraction (soluble) were analyzed by SDS-PAGE and Immunoblotting. Both REEP4-HA and REEP4(mutRHD)-HA remain soluble in the absence of microtubules but co-sediment with taxol-stabilized microtubules.

As a negative control, the membrane was probed for REEP5, which remains soluble in the presence of microtubules as previously reported (Schlaitz et al., 2013).

B) Representative confocal images for ER clearing from chromatin in GFP-Sec61β-expressing control or REEP3/4 RNAi cells transfected with plasmids for expression of either H2B-mCherry, REEP4-HA or REEP4(mutRHD)-HA. Immunolabeled HA-tag shown in grey. Both, REEP4 and REEP4(mutRHD) can restore clearing of ER from chromatin in REEP3/4 RNAi cells. Scale bar is 10 µm. **C)** Quantification of ER clearing from data as shown in panel (B). At least fifteen cells undergoing division were analyzed per condition in each of five independent experiments. Shown is the fraction of total ER that associates with chromosomes after REEP3/4 depletion and expression of the different rescue constructs. For each construct, the mean value obtained for ER signal on chromatin after control siRNA treatment (background) was subtracted from the mean value obtained after REEP3/4 siRNA treatment. Values for expression of REEP4-HA or REEP4(mutRHD)-HA are significantly different from H2B-mCherry expression with $p=0.00056$ and $p=0.0014$, respectively. Error bars are SEM. Statistical testing was done using Welch's t-test.

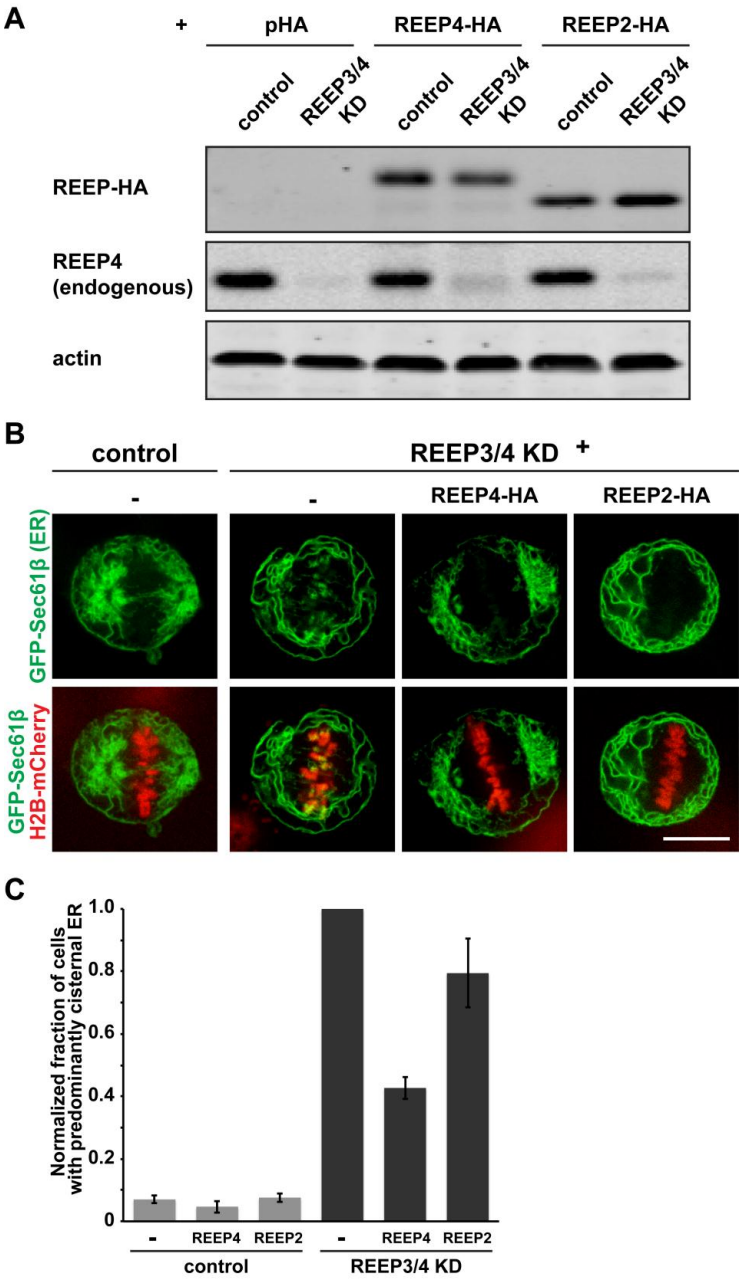

Figure 5. *Expression of REEP2 does not rescue metaphase ER morphology after REEP3/4 depletion*.

A) Cell lysates were generated for the rescue experiments shown in panels B, C and analyzed by SDS-PAGE and immunoblotting. Endogenous REEP4 was detected with anti-REEP4 antibody,

HA-tagged constructs were detected with anti-HA antibody, the same membrane was re-probed for actin as loading control. REEP2-HA migrates at the expected size in SDS-PAGE and is expressed at levels comparable to REEP4-HA in rescue experiments. **B)** ER morphology in GFP-Sec61β-expressing control and REEP3/4 knockdown (KD) cells. Cells were co-transfected with H2B-mCherry and either empty HA-tagging plasmid or RNAi-resistant REEP4-HA or REEP2-HA and imaged live by spinning disk microscopy. REEP4-HA but not REEP2-HA restored normal ER morphology in metaphase REEP3/4 RNAi cells. Scale bar is 10 μm. **C)** Quantification of mitotic ER morphologies from data as shown in panel (B). Cells with predominantly distinct ER profiles were classified as having abnormal cisternal ER morphology. At least twenty cells were analyzed per condition in each of four independent experiments. Error bars are SEM. Values for REEP3/4 KD with expression of REEP4-HA versus REEP2-HA are significantly different with $p=0.04$. Statistical testing was done using Welch's t-test.

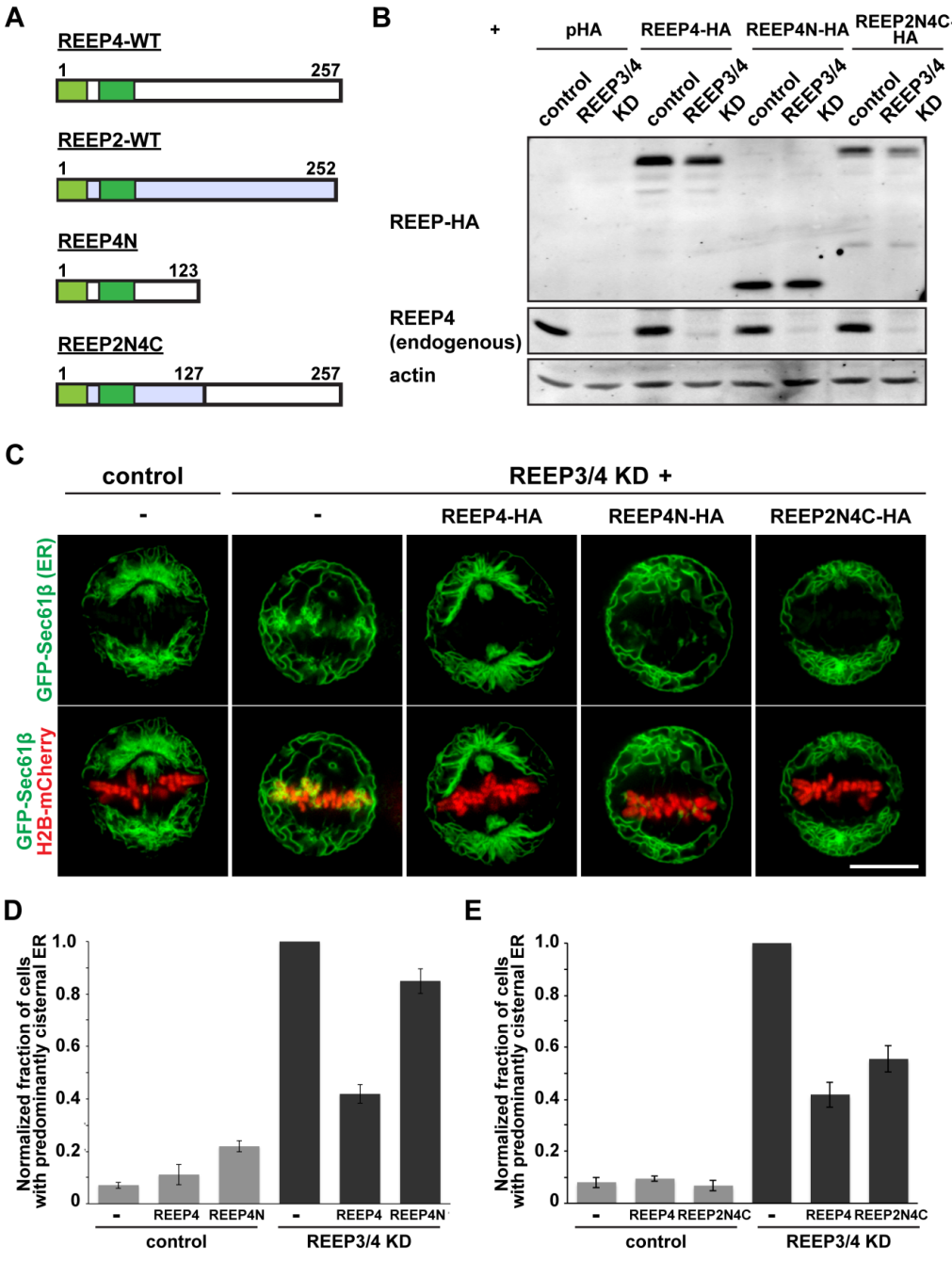

Figure 6. *Expression of a C-terminal truncation of REEP4 does not rescue metaphase ER morphology after REEP3/4 depletion but REEP2(aa1-127) fused to a REEP4 C-terminus does*.

A) Schematic representation of mutants generated. REEP4N: REEP4 N-terminus (REEP4 aa 1-123); REEP2N4C: chimera consisting of REEP2 aa 1-127 fused to REEP4 aa 128-257. **B)** REEP4N-HA and REEP2N4C migrate at the expected size in SDS-PAGE and are expressed at levels comparable to or higher than REEP4-HA in rescue experiments. Cell lysates were generated for the rescue experiments shown in panel C and analyzed by SDS-PAGE and immunoblotting. Endogenous REEP4 was detected with anti-REEP4 antibody, HA-tagged constructs were detected with anti-HA antibody, the same membrane was probed for actin as loading control. **C)** ER morphology in GFP-Sec61β-expressing control and REEP3/4 knockdown (KD) cells. Cells were co-transfected with H2B-mCherry and either empty HA-tagging plasmid or RNAi-resistant REEP4-HA or REEP4N-HA or REEP2N4C-HA and imaged live by spinning disk microscopy. REEP4-HA and REEP2N4C-HA but not REEP4-N-HA restored normal ER morphology in metaphase REEP3/4 RNAi cells. Scale bar is 10 µm. **D)** Quantification of mitotic ER morphologies from data as shown in panel C for rescue with REEP4N. Cells with predominantly distinct ER profiles were classified as having abnormal cisternal ER morphology. At least twenty cells were analyzed per condition in each of five independent experiments. Error bars are SEM. Values for REEP3/4 KD with expression of REEP4-HA versus REEP4N are significantly different with p=0.0001. Statistical testing was done using a Welch's t-test **E)** As in D) but for rescue with REEP2N4C. At least twenty cells were analyzed per condition in each of five independent experiments. Error bars are SEM. Values for REEP3/4 KD with expression of REEP4-HA versus REEP2N4C are not significantly different with p=0.1.

III

RTN4B interacting protein FAM134C promotes ER membrane curvature, elevates upon starvation and is required for ER-phagy

Darshan Kumar[a], Behnam Lak[a], , Taina Suntio[a], Helena Vihinen[a,b], Ilya Belevich[a,b], Tiina Viita[a], Liu Xiaonan[c], Aki Vartiainen[a], Maria Vartiainen[a], Markku Varjosalo[c] and Eija Jokitalo[a,b]

[a]Research Program in Cell and Molecular Biology, [b]Electron Microscopy Unit, [c]Molecular Systems Biology Research Group and Proteomics Unit, Institute of Biotechnology, University of Helsinki, Helsinki, Finland

Address correspondence to: Eija Jokitalo (Eija.Jokitalo@Helsinki.fi)

Abstract

The endoplasmic reticulum (ER) is comprised of a controlled ratio of sheets and tubules. The mechanisms governing this balance keeping the ER intact for normal functioning is not well understood. ER sheet and tubule shapes are maintained by several proteins that have multiple functions. Reticulons (RTNs), especially RTN4, and DP1/Yop1p family members are known to induce ER membrane curvature. RTN4B is the main RTN4 isoform expressed in non-neuronal cells. In this study, we identified FAM134C as RTN4B interacting protein in mammalian, non-neuronal, cells. FAM134C in Huh-7 cells localized specifically to the ER sheet edges and tubules and was not found from the flat parts of the sheets. Ultrastructural analysis revealed that overexpression of FAM134C induced tubulation of ER in form of non-motile unbranched long tubules or dense globular structures of heavily branched tubules. Tubulation of FAM134C is dependent on the reticulon homology domain close to the N-terminus. Upon amino acid starvation, FAM134C level was 1.35-fold, while remaining unchanged upon ER stress. Lack of FAM134C was unable to induce ER-phagy upon amino acid starvation.

Introduction

The endoplasmic reticulum (ER) consists of a continuous membrane system comprising of the peripheral ER and the nuclear envelope. The peripheral ER consists of a network of flat sheets and tubules (Baumann and Walz, 2001; Lynes and Simmen, 2011). Every domain of the ER has its distinct morphology that carry out specific processes (Baumann and Walz, 2001; Goyal and Blackstone, 2013;

Hu et al., 2011; Shibata et al., 2006). The formation and the maintenance of these structures are still under active investigation.

Multiple factors are responsible for maintaining the ER shape and size. It is not known how all these factors complement or compete with each other in their functioning. Reticulons (RTN) and DP1/Yop1p family members regulate the morphology of the tubular ER. Mammals have four reticulon genes (*RTN1*, *RTN2*, *RTN3* and *NOGO-A/RTN4*), each of which can give rise to a range of alternatively spliced transcript variants that encode different isoforms due to differential splicing and promoter usage (Oertle and Schwab, 2003). The RTN family is characteristic for its highly conserved C-terminal reticulon homology domain (RHD) of 150-200 amino acids containing two hydrophobic stretches separated by a 66 amino-acid hydrophilic loop and followed by a short C-terminal tail (Yang and Strittmatter, 2007). No sequence homology can be observed in the N-terminus of the variants. NOGO-A/RTN4A together with DP1 is responsible for generating and maintaining ER tubules (Voeltz et al., 2006). Similar results were reported for NOGO-B/RTN4B (called hereafter RTN4B) (Rämö et al., 2016). Overexpression of NOGO-A/RTN4A and RTN4B generates long unbranched tubules in yeast *Saccharomyces cerevisiae* (Voeltz et al., 2006) and human hepatoma cells (Huh-7) (Rämö et al., 2016) respectively, whereas their deletion leads to loss of tubular ER. RTNs are reported to induce such structural conformations by forming homo and hetero-oligomers that form arc-like scaffolds on and around membranes to give rise to a stable ER tubule (Shibata et al., 2008). Interaction of RTNs with other proteins also is known to complement RTNs function in a sound maintenance of ER structure (Christodoulou et al., 2016). The formation of reticular ER network of tubules requires interplay between several other proteins. REEPs belong to such protein family of membrane associated proteins, which have been shown to affect ER structure (Park et al., 2010b).

ER sheets on the other hand are stabilized by membrane bound polyriosomes and some specific factors like kinectin, CLIMP-63 and p180 that (Puhka et al., 2007; Shibata et al., 2006). The consistent thickness of the ER sheets are maintained by the coiled-coil domain of CLIMP-63 which forms intraluminal bridges (Shibata et al., 2010). The RTNs are known to localise to ER sheet edges thereby maintaining ER morphology (Shibata et al., 2010) as well. FAM134B, a newly identified ER protein, has been reported to localize to the ER sheets and play a role in ER structural maintenance in addition to being associated with ER-phagy (Khaminets et al., 2015).

In this study, we show that FAM134C is a newly identified ER protein that interacts with RTN4B and localizes exclusively to ER tubules and sheet edges. FAM134C is a tubule promoting protein,

which maintains ER structure by residing in positively curved areas of the ER. Overexpression of FAM134C induces massive sheet to tubule transition and dramatically hampers ER dynamics. FAM134C also plays a role in the ER-phagy pathway as it rises, specifically in amino acid starvation but not upon ER stress.

Results

FAM134C and FAM134B interact with RTN4B in mammalian cells

Although several RTN4B interacting partners, such as RTN3, have already been identified (Dodd et al., 2005; Qi et al., 2003; Voeltz et al., 2006), we aimed to complement those studies and find novel partners for RTN4B, which we identified as the major RTN4 isoform in Huh-7 cells (Rämö et al., 2016). For this, we used Huh-7 and human embryonic kidney (HEK-293) cell lines. Both cell lines expressing RTN4B constructs transiently (in Huh-7) or stably (in HEK-293) were tagged either with streptavidin (strep) for pull down or with BirA for pull down using biotin (BioID technique)(Roux et al., 2012). BioID is suitable for identifying dynamic interactions, whereas conventional immunoprecipitation requires more stable interactions. The pull downs were subjected to liquid chromatography - mass spectrometry for proteomic analysis. The analysis disclosed many novel interacting partners from the two cell lines (Fig. 1 and Table. 1). Analysis (post refinement) gave 68 hits, which ranged from proteins belonging to metabolic processes (17 hits) to catalytic activity ranging from hydrolase to transferase activity (17 hits). Around 35 hits were ER membrane associated proteins. Hits also comprised of membrane traffic proteins (12 hits), transporter proteins (10 hits), calcium ion and calcium dependent phospholipid binding functions (5 hits). The runs revealed FAM134C in Huh-7 (streptavidin run) and FAM134B in HEK293 cells (BioID run) as significant and novel interactors.

We used bimolecular fluorescence complementation assay (BiFC) (Kaddoum et al., 2010) to confirm the interaction of FAM134C and FAM134B with RTN4B (Fig. 2). RTN4B has been shown to form homo-oligomers (Shibata et al., 2008) and was used as a positive control. We have shown earlier that myosin 1C associates with ER sheets and has not effect on ER tubules (Joensuu et al., 2014). Myosin 1C was absent from the mass spectrometry hits, and, thus, served as a negative control. FAM134C and FAM134B both gave positive BiFC signals in addition to the positive control RTN4B, while myosin 1C gave a negative signal. These results confirmed our mass spectrometry findings that FAM134C and FAM134B are interacting partners of RTN4B.

FAM134C membrane insertion and topology

FAM134 family contains three known proteins, namely FAM134A (Q8NC44, UniProtKB), FAM134B (Q9H6L5) and FAM134C (Q86VR2). FAM134C is a conserved protein found in many eukaryotes (Fig. S1) but it has not been functionally characterised yet. Currently, two alternatively spliced isoforms of human FAM134C, Q86VR2-1 and Q86VR2-2 (UniProtKB**)** corresponding to 466 aa (amino acid) and 271 aa, respectively, have been described. Western blotting revealed the FAM134C isoform 1 (Q86VR2-1) to correspond to ~65 kDa in Huh-7 (Fig. 6B).

The FAM134C protein sequence lacks conventional signal sequence, but has been predicted to have several transmembrane (TM) domains according to UniProtKB, Protter (Omasits et al., 2014) and TMHMM (Krogh et al., 2001). Both NCBI's conserved domains tool and HHpred (Soding et al., 2005) predict that FAM134C possess a RHD. The RHD corresponded between 60 aa – 210 aa of the FAM134C protein sequence, where all the predicted transmembrane domains of FAM134C fall as well (Fig. S1). A BLAST (basic local alignment search tool) between FAM134C and RTN4B gave an overall sequence similarity of around 26%, where the RHD domain of RTN4B and some of TM domains of FAM134C showed clear overlap.

Protter and TMHMM software predicted only the N-terminus of FAM134C to be cytosolic. To test this prediction and to uncover the FAM134C topology, HeLa cells mildly over-expressing N- or C-terminally tagged FAM134C (FLAG-FAM134C and FAM134C-FLAG, respectively) were fixed and permeabilized with Triton X-100 or digitonin. Cells were then immunostained with antibodies against FLAG and ER luminal protein calreticulin. Wide field imaging revealed that both N- and C-terminal FLAG-tag gave a significant signal, while calreticulin gave a signal only in Triton X-100 permeablized cells (Fig. 3A,B). Collectively we conclude that both N and C-terminus of FAM134C faces the cytoplasm.

FAM134C localizes to the ER and its over-expression induces extensive ER tubulation via RHD

Due to lack of specific antibody working in light microscopy (LM), we used Huh-7 cells over-expressing FAM134C-FLAG for localization studies. Confocal microscopy revealed clear co-localization of FAM134C-FLAG with ER markers calreticulin and RTN4B (Fig. 4Aa, b). RTN4B is shown to localize exclusively to ER tubules and sheet edges (Rämö et al., 2016). FAM134C gave a higher co-localization with RTN4B as compared to calreticulin, which is a general luminal ER marker (Fig. 4Ab, B). Compared to calreticulin staining, FAM134C seemed to localize preferably to ER

tubules and sheet edges (insets Fig. 4Aa). Pearson's coefficient analysis clearly showed no significant co-localization of FAM134C with ERGIC marker ERGIC53 (Hauri and Schweizer, 1992; Kappeler et al., 1997) or Golgi marker GM130 (Nakamura et al., 1995) (Fig. 4B). Huh-7 cell transiently expressing FAM134C-GFP were subjected to immuno electron microscopy. Electron micrograph revealed gold labels detecting the GFP of the fusion protein to be localized to tubules and edges of the sheets (Fig. S2). Heavier labelling was observed at the periphery of the cells which are more prominent for ER tubules (Fig. S2Aa). Occasionally, the labelling was observed at ER sheet fenestrations (Fig. S2B). In addition, labelling was also frequently observed at high curvature ER-mitochondrial contact sites (Fig. S2C).

Cells with higher FAM134C-FLAG expression showed clear morphological changes on ER structure, as large globular structures randomly distributed throughout the cell could be detected (Fig. 5A, Ba). The size of the globules varied greatly from cell to cell ranging from 3 to 7µm in diameter all the way up to 17µm (Fig. 5Ab). The globules were positive for calreticulin, confirming their ER origin (Fig. 5Aa). Cells overexpressing FAM134C also displayed long protrusions extending from the plasma membrane (Fig. 5Bb) (Fig. S3A). Some of the protrusions contained globules, which had similar size distribution than those found from cell cytoplasm, whereas some protrusions comprised of long and unbranched tubules without globules (Fig. 5Bc). Confocal live cell imaging revealed that the ER globules in the cell cytoplasm and in protrusions as well as the unbranched long tubules to be non-dynamic (Movie 1-3). Correlative light and electron microscopy on FAM134C-eGFP overexpressed cells revealed cells to be rounded with long filopodia-like projections. These projections were positive for FAM134C-eGFP signal (Fig S3A).

Transmission electron microscopy (TEM) was used to analyse the ER globules in more details. For this, Huh-7 cells were co-transfected with FAM134C-FLAG and ER marker pssHRP-KDEL (Connolly et al., 1994b). FAM134C over-expressing cells revealed large clusters of highly branched ER tubules (Fig. 5Ca, b). The size of these profiles matched the size of globules seen at LM. These structures were only found in over-expressing cells, and they were composed of a dense network of short ribosome-free tubules that were connected to normal sheets at the immediate vicinity of the cluster. Diameter of the tubules ranged between 40 to 50 nm. Tomography on these tubular clusters revealed the extent of membrane tubulation and branching confirming the regular TEM micrograph observations (Fig. S3B). FAM134C overexpression did not cause any ER fragmentation as previously stated for FAM134B (Khaminets et al., 2015). TEM micrographs showed cellular components like the lipid droplets, mitochondria and Golgi (Fig. 5Ca-c) (Fig. S3B) having normal morphology,

dispersed in and around the tubular ER globules. Immuno-EM (immuno electron microscopy) studies on FAM134C-GFP overexpressing Huh-7 cells showed heavily tabulated structures positive for gold label detecting GFP of the fusion protein. A gradient of gold particle density with a heavy labelling at the periphery of the globular cluster and mild labelling at the centre was observed (Fig. 5d, e).

To elucidate the role of FAM134C's RHD in membrane curvature, we created a FAM134C construct where the FAM134C's RHD was extended (MutFAM134C-GFP) (Fig. S4A). This extension was done to convert the typical RHD of FAM134C to not form a predicted wedge shape into the phospholipid bilayer but to behave like a typical transmembrane domain going all the way through the bilayer of the ER as described previously for RTNs (Zurek et al., 2011). Overexpression with this construct did not induce any ER tubulation. The mutFAM134C's C-terminus was facing the cytoplasm thus orientating similar to wild type FAM134C (Fig. S4C). FAM134C thus brings about ER tubulation via its RHD domain upon overexpression.

FAM134C depletion does not affect ER morphology

ShRNA- mediated knock down was used to deplete FAM134C in Huh-7 cells. According to Western blotting, 48h knockdown with all shRNA construct resulted in around 75% FAM134C silencing (Fig. 6B). Downregulation of FAM134C in Huh-7 cells did not induced any structural ER confirmations. Confocal microscopy revealed that both control and knock down conditions gave similar observations (Fig. 6Aa,b).

This study of FAM134C depletion on ER morphology and organization was subsequently studied at a higher resolution by employing EM. FAM134C shRNAs were co-transfected with pssHRP-KDEL to identify depleted cells. EM observations also revealed ER to be relatively normal with no striking phenotype. The fenestrations (Palade, 1956) which are typical for ER in these cells (Joensuu et al., 2014; Puhka et al., 2012) were seen to appear normally as well. Mitochondrial and ER contacts appeared normal in addition to mitochondrial, nuclear and Golgi morphology. Our EM data hence confirmed our LM findings in addition to giving higher resolution information.

FAM134C elevates upon amino acid starvation

FAM134C is predicted to have a LIR (LC3-interacting region) motif at 445 aa to 450 aa (Q86VR2, UniProtKB) within the protein's intrinsically unstructured region (220 aa – 466 aa) (Fig. S1). Huh-7 and HeLa cells upon 1h amino acid and serum starvation (using EBSS medium) were observed to

have elevated FAM134C levels (Fig. 7Aa, b). The elevation of FAM134C was about 30 % in Huh-7 cells (Fig. Aa). Structural protein RTN4A did not go up in levels as compared to FAM134C upon starvation. Induction of autophagy upon EBSS starvation was confirmed using autophagy marker LC3 (Microtubule-associated protein 1A/1B-light chain 3) (Kabeya et al., 2000) (Fig. 7A). FAM134C elevation was not observed for Huh-7 cells upon induction of ER stress (Fig. 7B). ER stress was induced using DTT (dithiothreitol) and the confirmation of the same was done using ER stress marker Phospho-eIF2α (Fig. 7B) (Kaufman, 1999). LC3 protein levels (LC3I and LC3II) did not change upon knockdown of FAM134C (Fig. 7C). Collectively the data suggested FAM134C to be playing a role by elevating its level specifically upon induction of autophagy via amino acid deprivation and not during ER stress.

ER-phagy is dependent on FAM134C

To test the role of FAM134C in ER-phagy (autophagy of ER) we used the EATR assay (Liang et al., 2018). U2-OS cells were transiently co-transfected with mock, shFAM134C or siRTN4 and general ER translocon complex subunit RAMP4 cloned in TET-On-mCherry-GFP-RAMP4 construct. Upon starvation with EBSS for 1h, cells in FAM134C knockdown condition failed to efficiently bring about ER-phagy (Fig. 8Aa). In starved condition, the percentage of cells with acidified ER (ER positive only for mCherry) reduced to 25% as compared to mock (50%) (box plot Fig. 8Ab), while the non-starved condition had no difference. The extent of ER-phagy per cell also reduced on a per cell basis in starvation condition (violin plot Fig. 8Ab) On the other hand, RTN4 depleted cells pertaining large peripheral ER sheets were able to bring about ER-phagy similar to mock conditions in EBSS treatment (Fig. 8B), with minor defects in the extent of ER-phagy per cell. The following results state FAM134C to be an important determinant for ER-phagy upon amino acid starvation.

Discussion

The reticulon family of proteins have long been the hallmarks of being an ER marker (Voeltz et al., 2006) besides many other ER anchoring proteins. Use of reticulons as an ER marker has been extensively utilized specially for tracking ER's positively curved membranes. It is also known that reticulons interact with other membrane and non-membrane bound proteins. In this study we reveal FAM134C as a novel ER protein that interacts with RTN4B in mammalian cells.

Proteomics done for RTN4B as bait using human cell lines revealed a list of hits belonging to many ER associated proteins. In addition to RTNs, ER shaping proteins like REEP 5/DP1 (receptor expression enhancing protein) (Voeltz et al., 2006) and ATLs (Atlastins) (Hu et al., 2009) were also

observed. Hits also revealed proteins involved in membrane traffic, vesicle formation/movement and fusion namely RAB and VAP family respectively, thus showing the extent of the possible functions of RTN4B. FAM134C, a not well characterised protein came out as one of the strong hits from this screen. As previously reported, a reverse run with FAM134C as bait gave RTN4 as a hit (Huttlin et al., 2017) confirming our findings. FAM134C is a very conserved protein (Fig. S1) where the predicted transmembrane regions of FAM134C including the LIR motif fall within these conserved regions. The FAM134C was seen to have a reticulon domain that also overlapped greatly with the conserved transmembrane region of the protein.

Previously FAM134B, a closely related protein to FAM134C, was reported to localize to Golgi using antibodies against FAM134B (Kurth et al., 2009). The localization experiments in our research showed FAM134C to be clearly an ER protein using a general ER marker calreticulin (Fig. 4A). FAM134B was reported to localize to the ER as well, with more preference to ER sheets than tubules (Khaminets et al., 2015). A higher co-localization (as compared to calreticulin) (Fig. 4) and a positive interaction with RTN4B in our experiments states FAM134C to not only be an ER protein but a protein favouring positively curved membranes instead of the flat sheets. Immuno-EM of FAM134C also revealed its presence at high curvature ER (Fig. S2. A) in addition to partial localizations to other interesting sub domains like ER fenestrations and mitochondrial-ER contacts (Fig. S2B, C). To further support our findings, we tested FAM134C's localization with Golgi and ERGIC markers where a very low co-localization was observed (Fig. 4).

FAM134C's localization to tubular ER including sheet edges pointed towards the observation of heavy tubulation of ER upon FAM134C overexpression (Fig. 5). FAM134C overexpression formed globular clusters at LM that were reminiscent of tightly packed tubular ER structures unorganized in orientation similarly observed for RTN4B overexpression (Rämö et al., 2016) and ATP depletion (Lingwood et al., 2009) conditions. It must be noted that although the globular structures as such were non-dynamic, the dynamics of the highly branched tubules within these globular structures could not be resolved using light microscopy. In light of these data it can be concluded that FAM134C has the capacity to bend membranes towards a positive curvature.

Knockdown of FAM134C revealed no striking phenotype for ER morphology. With the absence of FAM134C, the ER looked relatively normal with sheets and tubules clearly visible. FAM134C is not as highly expressed as other structural proteins like RTN4B in Huh-7 cells (Rämö et al., 2016), it could thus be speculated that although FAM134C has the capacity to induce tubulation, there are

other abundant proteins like RTNs and REEPs keeping the sheet-tubule in balance. The RHD present within the FAM134C close to its N' terminus is responsible for the membrane curvature by partial membrane insertion (Fig. S4), a concept previously described for RTN4 (Voeltz et al., 2006). This reticulon domain within the FAM134C could also be responsible for binding with RTN4B and other unknown membrane bound proteins of the ER. The FAM134C was observed to have both its N' and C' terminus facing the cytoplasm (Fig. 3), a similar result previously observed for FAM134B (Khaminets et al., 2015). Unlike RTN4s the FAM134C's RHD domain sits closer to the N-terminus rather than the C-terminus, an arrangement similarly found in REEP family of proteins (Park et al., 2010a).

Elevation of FAM134C upon starvation was specific for amino acid deprivation induced autophagy. The protein is possibly recruited by the cell for the initial steps of autophagy; where FAM134C with its ability to shape membranes might aid in membrane formation for the autophagosome architecture. Additionally, the FAM134C's LIR domain close to the C' terminus presumably exposed to the cytoplasm, maybe responsible in the autophagy pathway (specifically in ER-phagy). As the depletion of FAM134C hampers the extent of ER-phagy, the LIR domain could be serving as the anchor for selective ER-phagy thus directing selected ER domains for degradation under starvation conditions.

In light of the observations made through this research we see FAM134C as a novel ER residing protein. Although it will be best to do studies on localization for FAM134C using antibodies (currently unavailable) that are trustworthy on LM and EM levels. This could also pave the way for FAM134C to be considered a new marker for ER tubules and sheet edges. FAM134C as a novel tubule promoting protein within the cell, having interaction with key tubule promoting protein like RTN4B, state all these positively curved localizing proteins to be talking to each other thus giving rise to a mesh of interconnected family of curvature promoting proteins functioning hand in hand. The simultaneous presence and interaction of all or many of these proteins are possibly needed to keep the shape, function and dynamics of the ER sound.

FAM134C could also be complementing other functions of RTN4 namely in apoptosis (Tagami et al., 2000), neuronal regeneration (Chen et al., 2000; GrandPre et al., 2000; Prinjha et al., 2000) and tumour suppression (Li et al., 2001). Knock down of FAM134C was shown to have reduced axonal length and number of axonal collaterals and dendrites (Wang et al., 2013). The same study also claimed FAM134C's overexpression to increase neurite outgrowth. Neurite outgrowths mainly contain ER in tubular form (Wu et al., 2017). Our experiments on FAM134C overexpression also

gives long unbranched tubules at the cell periphery of Huh-7 cells suggesting an overlap of function for this protein between different cell types. Plus stranded RNA viruses form membrane modifications in many cases using the membranes from ER (Limpens et al., 2011). Reticulons have been shown to play a crucial role in viral RNA replication (Diaz et al., 2010). With our findings, it could be postulated that FAM134C could also be acting as a host factor for viral progress within a cell, thus also opening therapeutic angles for this protein.

Materials and Methods

Cell culture, constructs, overexpression and silencing

HeLa (CCL-2; ATCC, LGC Standards GmbH, Germany), Flp-In™ T-REx 293 (Thermo Fisher Scientific, Waltham, MA) and U2-OS (ATCC, Manassas, VA) were cultured in DMEM (BioWhittaker, Lonza, Verviers, Belgium) and Huh-7 (JCRB0403; Japanese Collection of Research Bioresources Cell Bank, Osaka, Japan) in EMEM (Lonza), containing 5 or 10% fetal bovine serum (Gibco, Invitrogen, Thermo Fisher Scientific, Waltham, MA) and other supplements (Lonza). FAM134C, FAM134B, MYO1C and RTN4B, in pENTR221gateway compatible vector (with/without stop codon) from Orfeome library, GBU, Helsinki University, were taken through L.R reaction (Gateway® Cloning, Life Technologies, Thermo Fisher Scientific) against pDEST-GFP-1-10-N3, pDEST-GFP-11- N3, pDEST-GFP-1-10-C1, pDEST-GFP-11- C1 (Gift from Maria Vartiainen's lab, University of Helsinki) or pcDNA6.2/C-EmGFP-DEST (Orfeome library, GBU, Helsinki University) gateway compatible vectors creating C or N terminal fusion vectors. TetOn-mCherry-eGFP-RAMP4 was ordered from Addgene (Watertown, MA). DNA transfections were done using Fugene HD (NGF; Promega, Madison, WI) according to manufacturer's instructions. For DNA and siRNA co-transfections jetPRIME (Polyplus, New York, NY) was used according to manufacturer's instructions. For mild overexpression of FAM134C, lower DNA amount was transfected for 16 h as compared to higher DNA amount for 24 h in overexpression conditions. For co-transfections, a ratio of 1:3 (wt:wt) or 0.5:0.5:4 (wt:wt:wt) were used for two or three plasmids respectively. FAM134C silencing was done for 48 h using single or total of pooled short hairpin RNA (shRNA) from FuGu, Helsinki University, shRNA was cloned into pGEM vector backbone. The following sequence for knocking down FAM134C shRNA was used: (CCGGCCTGACATCTCTTCGTCTTGTCTCGAGACAAGACGAAGAGATGTCAGGTTTTTT G). The silencing efficiency of the shRNA was quantified using western blotting. pCMV-Tag1 (Agilent Technologies, Espoo, Finland) was used in transfection as buffer, while pssHRP-KDEL (Connolly et al., 1994a) in transfections for marking ER in EM studies.

Antibodies

Antibodies against FAM134C (A304-684A; Bethyl Laboratories, Inc., Montgomery, TX) reticulon 4B (AB-163; Kinasource Ltd, Dundee, UK), reticulon 4A (ab62024; Abcam, Cambridge, UK), GM130 (610823; BD Biosciences, Franklin Lakes, NJ), ERGIC-53 (ALX-804-602; Enzo Life Sciences, Farmingdale, NY), HA (MMS-101R-50; Covance, Princeton, NJ), FLAG (F7425; Sigma-Aldrich), calreticulin (2679S; Cell Signalling Technologies, MA), anti-GFP (ab290; abcam, Cambridge, UK) and GAPDH (MAB374, Merck Millipore, Billerica, MA) were used as primary antibodies. When indicated, rabbit anti-sheep bridging antibody (313-001-003; Jackson

ImmunoResearch Labs Inc., West Grove, PA) was used. Secondary antibodies were Rhodamine Red-X (016-290-084; Jackson ImmunoResearch), Alexa 647 (A31571; Life technologies) and Alexa 488 (A-11008; Life Technologies).

Purification, Mass Spectrometry and Data processing

LR recombination was performed between the RTN4B in pENTR221gateway compatible vector and the in-house–designed destination vector; the C-terminal tagging vector pcDNA5/FRT/TO/BirA*/Myc/GW or pcDNA5/FRT/TO/StrepII/HA/GW was used for all the experiments. Huh-7 cells were made to mildly express RTN4B or GFP using the above mentioned destination vectors and harvested 16 h post transfection for lysis and affinity purification. For affinity purification, tetracycline-inducible Flp-In™ T-REx 293 cell lines expressing RTN4B or GFP were generated as described in (Varjosalo et al., 2013). Affinity purification for Strep/HA tagged proteins were performed as described earlier (Varjosalo et al., 2013). For BioID purification, approximately 5×10^7 cells in two biological replicates were induced with 2 µg/ml doxycycline and 50 µM biotin 24 h before harvesting. Cells were washed with 0.1 mM MgCl2, 0.1 mM CaCl2 in PBS and harvested in 1 mM EDTA-PBS. Purification of the in vivo biotinylated proteins and mass spectrometry were performed as explained in (Heikkinen et al., 2017). For protein identification, Thermo .RAW files were uploaded into Proteome Discoverer 1.4 (Thermo Scientific) and searched against Sequest search engine of the selected human part of UniProtKB/SwissProt database (http://www.uniprot.org/, version 2015-01). The following parameters were applied: Trypsin was selected as the enzyme and a maximum of 2 miss cleavages were permitted, precursor mass tolerance at ±15 ppm and fragment mass tolerance at 0.05 Da. Carbamidomethylation of cysteine, were defined as static modifications, oxidation of methionine and biotinylation of lysine was specified as variable modifications. All reported data were based on high confidence peptides assigned in Proteome Discoverer with a 0.05 % FDR by Percolator. The high confidence protein-protein interactions were identified using stringent filtering against control contaminant database. The high confidence protein-protein interactions data were imported into Cytoscape 3.2.1 (Shannon et al., 2003) for the visualization. Known protein-protein interactions were derived protein interaction network analysis (PINA2.0) platform (Cowley et al., 2012).

Immunofluorescence staining and Western blotting

For RTN4B labelling, cells were fixed with -20°C methanol, blocked with 10% Goat serum (Gibco-Life Technologies) and 1% BSA (bovine serum albumin), labelled with indicated antibodies and mounted in Mowiol (Hoechst, Frankfurt, Germany) supplemented with Dabco (Sigma-Aldrich). All the other samples were fixed with 4% formaldehyde (Electron Microscopy Sciences, Hatfield, PA), 0.1 mM MgCl2, and 0.1 mM CaCl2 in phosphate-buffered saline (PBS), quenched with 50 mM NH4Cl, permeabilized with 0.1% Triton X-100, and then blocked with 0.2% BSA in Dulbecco PBS. When appropriate, the cells were then incubated consecutively with primary and secondary antibodies, diluted in blocking solution. Samples were mounted in Mowiol supplemented with Dabco. For topology experiments in Fig. 3B, HeLa cells expressing FAM134C–N Term-FLAG and FAM134C-C Term-FLAG were fixed with 4% paraformaldehyde, permeabilized with 30 µg/ml digitonin in PBS on ice for 5 min or 0.1% Triton-X 100 Triton X-100 in PBS on ice (5 min), washed with PBS and processed for immunofluorescence. Western blotting was done with indicated antibodies according to manufacturer's instructions and by using standard protocols.

Light microscopy and image quantitation

Wide-field images of fixed cells were taken with Zeiss AxioImager M2 482 epifluorescence microscope equipped with 63×/Plan-Apochromat/1.40 oil/M27 and 483 AxioCam HRm camera (Zeiss, Oberkochen, Germany) (Fig. 2 and Fig. 5Aa) or with Leica DM6000B upright fluorescence wide field microscope equipped with 40X/1.25-0.75 HCX PL APO CS oil objective, Hamamatsu Orca-Flash4.0 V2 sCMOS camera (Wetzlar, Germany) (Fig. 3A). Images were acquired with AxioVision4 (Zeiss) or LAS X software (Leica). Confocal images of fixed cells were taken with LSM880 confocal laser scanning microscope (Zeiss) with a 63X plan-apochromat (NA=1.40) oil objective, GaAsP detector and ZEN 2 software (Zeiss) (Fig. 4A and Fig. 7A). Live Huh-7 cells were imaged at 37°C and 5% CO2 on glass-bottom dishes (MatTek, Ashland, MA). Live cell imaging was done using either a 3I Marianas (3I intelligent Imaging Innovations, Denver, CO) on a Zeiss Axio Observer Z1 microscope equipped with 63x/1.2 W C-Apochromat Corr (WD=0.28 M27) objective, spinning disk confocal, LED lazers and Andor Neo sCMOS camera (Andor, Oxford Instruments, Abingdon, UK) or with Leica TCS SP5 II HCS-A equipped with HCX PL APO 63x/1,2 W Corr/0,17 CS (water) objective, HeNe 633 nm/12mW and DPSS 561 nm/20mW laser, 3 PMT and 2HyD detectors for fluorescence with adjustable detection range and LAS AF 2.7.7 12.4.2018 software.

Pearson's correlation coefficiencies were calculated using Microscopy Image Browser (MIB) (Belevich et al., 2016) for square ROIs placed with the cell area (n>20). As a negative control, the Pearson's correlation coefficient was also calculated for the same ROIs after rotating one of the two channels by 90°. Cell segmentation and mean intensity measurements of cells (n = 20) were done using MIB. For ER-Phagy study (Fig. 8), U2-OS cells were transiently co-transfected with TetOn-mCherry-eGFP-RAMP4 and mock/siRNA/shFAM134C for 48h. Doxycycline hyclate (D9891, Sigma-Aldrich, Saint Louis, MO) to a final concentration of 4 µg/ml was added 16 h before imaging. Three experimental replicates representing 20 cells per condition with 2 confocal images per cell representing two different heights of a cell more than 1 µm apart were taken. The cell outlines were segmented based on GFP signal from TetOn-mCherry-eGFP-RAMP4 localizing to a subunit of ER translocon complex, giving good estimation of cell area. The segmented cells were further cropped from original images using MIB. Intensity for both colour channels (mCherry and eGFP) for all cropped cells were normalized and the GFP channel multiplied by 2 was subtracted from the mCherry channel to generate an intensity difference map for each cell. The difference map representing the remaining mCherry signals was taken through black and white thresholding (10-255). The thresholded areas were subjected to a step of erosion and dilation to remove noise signal and to obtain the final area of acidified ER (ER-Phagy structures positive only for mCherry signal). The ratio of acidified ER to the cell outline area for each cell was calculated and shown as percentage using violin plots (Fig. 8Ab and Fig. 8Bb).

Electron microscopy and image quantitation

Cells grown on glass coverslips were cytochemically stained and flat embedded as described previously (Jokitalo et al., 2001). Cells were fixed with 2% glutaraldehyde (Sigma-Aldrich) and 1.5% formaldehyde in 0.1 M sodium cacodylate buffer, pH 7.4, for 20 min at room temperature (RT). Cytochemical staining with 3,3'-diaminobenzidine (TAAB, Berks, UK) was done for pssHRP-KDEL or pssHSP47-APEX-KDEL transfected cells. Cells were then postfixed with 1% reduced osmium tetroxide in sodium cacodylate buffer for 1 h on ice, dehydrated through series of ethanols and acetone, and infiltrated with Epon (TAAB 812) for 2 h prior 14- h- polymerization at 60°C. 60-nm or 100-nm thin sections were cut, post-stained with uranyl acetate and lead citrate. For immuno-EM the cells were fixed with paraformaldehyde-lysine-periodate –fixative (Mclean and Nakane, 1974). Cells were permeabilized with 0.01% saponin (Sigma-Aldrich) and immunolabelled with anti-NOGO-

B/RTN4B followed with rabbit anti-sheep bridging antibody or with anti NOGO-A/RTN4A antibody, and 1.4 nm nanogold-conjugated anti-rabbit secondary antibody, silver enhanced with HQ Silver kit (Nanoprobes, Stony Brook, NY) and gold toned with 0.05% gold chloride. Finally cells were processed for osmication, dehydration, Epon embedding and sectioning as described above. Imaging for tomography was done with Tecnai 12 (FEI Company, Hillsboro, OR) at 80 kV or 120 kV equipped with Orius SC 1000B (Gatan Inc., Pleasanton, CA) CCD camera all other EM imaging was done with Jeol JEM-1400 equipped with Gatan Orius SC 1000B bottom mounted CCD-camera (Gatan Inc., USA). Image quantitation on micrographs for determining ER-mitochondria proximity (Fig. 5Ce) was done using MIB (Belevich et al., 2016).

ET was done on serial 230-nm thick sections as previously described (Puhka et al., 2007), except that the tilt series images between ±60° were acquired with an UltraScan 4000 CCD camera, 4 k × 4 k (Gatan Inc.) at nominal magnification of 9.600×. Dual axis tilt series were acquired using SerialEM software running on a Tecnai FEG 20 microscope (FEI Company, Hillsboro, OR) operating at 200 kV. Gold particles on tomograms were quantified by manually tagging on separately modelled ER structures. Reconstructions were done using IMOD software(Kremer et al., 1996) followed by visualization and modelling using MIB and Amira (VSG, FEI Company).

Scanning electron microscopy

For scanning electron microscopy (SEM) (Fig. S3A), cell monolayers overexpressing Hsp47-GFP or FAM134C-GFP for 24 h were grown on glass coverslips and fixed with 2% glutaraldehyde in 0.1 M sodium cacodylate buffer, pH 7.4 for 30 min at RT and post-fixed with 1% osmium tetroxide in 0.1 M sodium cacodylate buffer for 60 min at RT. The samples were dehydrated through series of ethanol, followed by overnight dehydration with hexamethyldisilazane (Sigma-Aldrich). All the samples were coated with platinum using Agar sputter coater (Agar scientific Ltd, Essex, UK). Images were acquired with a FEG-SEM Quanta 250 (FEI Company, Hillsboro, OR) equipped with a microtome (3View; Gatan Inc., Pleasanton, CA), using a backscattered electron detector (Gatan Inc.)

References

Baumann, O., and Walz, B. (2001). Endoplasmic reticulum of animal cells and its organization into structural and functional domains. Int Rev Cytol *205*, 149-214.

Belevich, I., Joensuu, M., Kumar, D., Vihinen, H., and Jokitalo, E. (2016). Microscopy Image Browser: A Platform for Segmentation and Analysis of Multidimensional Datasets. Plos Biol *14*.

Chen, M.S., Huber, A.B., van der Haar, M.E., Frank, M., Schnell, L., Spillmann, A.A., Christ, F., and Schwab, M.E. (2000). Nogo-A is a myelin-associated neurite outgrowth inhibitor and an antigen for monoclonal antibody IN-1. Nature *403*, 434-439.

Christodoulou, A., Santarella-Mellwig, R., Santama, N., and Mattaj, I.W. (2016). Transmembrane protein TMEM170A is a newly discovered regulator of ER and nuclear envelope morphogenesis in human cells. J Cell Sci *129*, 1552-1565.

Connolly, C.N., Futter, C.E., Gibson, A., Hopkins, C.R., and Cutler, D.F. (1994a). Transport into and out of the Golgi-Complex Studied by Transfecting Cells with Cdnas Encoding Horseradish-Peroxidase. Journal of Cell Biology *127*, 641-652.

Connolly, C.N., Futter, C.E., Gibson, A., Hopkins, C.R., and Cutler, D.F. (1994b). Transport into and out of the Golgi complex studied by transfecting cells with cDNAs encoding horseradish peroxidase. J Cell Biol *127*, 641-652.

Cowley, M.J., Pinese, M., Kassahn, K.S., Waddell, N., Pearson, J.V., Grimmond, S.M., Biankin, A.V., Hautaniemi, S., and Wu, J. (2012). PINA v2.0: mining interactome modules. Nucleic Acids Res *40*, D862-865.

Diaz, A., Wang, X., and Ahlquist, P. (2010). Membrane-shaping host reticulon proteins play crucial roles in viral RNA replication compartment formation and function. Proc Natl Acad Sci U S A *107*, 16291-16296.

Dodd, D.A., Niederoest, B., Bloechlinger, S., Dupuis, L., Loeffler, J.P., and Schwab, M.E. (2005). Nogo-A, -B, and -C are found on the cell surface and interact together in many different cell types. J Biol Chem *280*, 12494-12502.

Goyal, U., and Blackstone, C. (2013). Untangling the web: mechanisms underlying ER network formation. Biochim Biophys Acta *1833*, 2492-2498.

GrandPre, T., Nakamura, F., Vartanian, T., and Strittmatter, S.M. (2000). Identification of the Nogo inhibitor of axon regeneration as a Reticulon protein. Nature *403*, 439-444.

Hauri, H.P., and Schweizer, A. (1992). The endoplasmic reticulum-Golgi intermediate compartment. Curr Opin Cell Biol *4*, 600-608.

Heikkinen, T., Kampjarvi, K., Keskitalo, S., von Nandelstadh, P., Liu, X., Rantanen, V., Pitkanen, E., Kinnunen, M., Kuusanmaki, H., Kontro, M., *et al.* (2017). Somatic MED12 Nonsense Mutation Escapes mRNA Decay and Reveals a Motif Required for Nuclear Entry. Hum Mutat *38*, 269-274.

Hu, J., Prinz, W.A., and Rapoport, T.A. (2011). Weaving the web of ER tubules. Cell *147*, 1226-1231.

Hu, J., Shibata, Y., Zhu, P.P., Voss, C., Rismanchi, N., Prinz, W.A., Rapoport, T.A., and Blackstone, C. (2009). A class of dynamin-like GTPases involved in the generation of the tubular ER network. Cell *138*, 549-561.

Huttlin, E.L., Bruckner, R.J., Paulo, J.A., Cannon, J.R., Ting, L., Baltier, K., Colby, G., Gebreab, F., Gygi, M.P., Parzen, H., *et al.* (2017). Architecture of the human interactome defines protein communities and disease networks. Nature *545*, 505-509.

Joensuu, M., Belevich, I., Rämö, O., Nevzorov, I., Vihinen, H., Puhka, M., Witkos, T.M., Lowe, M., Vartiainen, M.K., and Jokitalo, E. (2014). ER sheet persistence is coupled to myosin 1c-regulated dynamic actin filament arrays. Mol Biol Cell *25*, 1111-1126.

Jokitalo, E., Cabrera-Poch, N., Warren, G., and Shima, D.T. (2001). Golgi clusters and vesicles mediate mitotic inheritance independently of the endoplasmic reticulum. J Cell Biol *154*, 317-330.

Kabeya, Y., Mizushima, N., Ueno, T., Yamamoto, A., Kirisako, T., Noda, T., Kominami, E., Ohsumi, Y., and Yoshimori, T. (2000). LC3, a mammalian homologue of yeast Apg8p, is localized in autophagosome membranes after processing. EMBO J *19*, 5720-5728.

Kaddoum, L., Magdeleine, E., Waldo, G.S., Joly, E., and Cabantous, S. (2010). One-step split GFP staining for sensitive protein detection and localization in mammalian cells. Biotechniques *49*, 727-+.

Kappeler, F., Klopfenstein, D.R., Foguet, M., Paccaud, J.P., and Hauri, H.P. (1997). The recycling of ERGIC-53 in the early secretory pathway. ERGIC-53 carries a cytosolic endoplasmic reticulum-exit determinant interacting with COPII. J Biol Chem *272*, 31801-31808.

Kaufman, R.J. (1999). Stress signaling from the lumen of the endoplasmic reticulum: coordination of gene transcriptional and translational controls (vol 13, pg 1211, 1999). Gene Dev *13*, 1898-1898.

Khaminets, A., Heinrich, T., Mari, M., Grumati, P., Huebner, A.K., Akutsu, M., Liebmann, L., Stolz, A., Nietzsche, S., Koch, N., *et al.* (2015). Regulation of endoplasmic reticulum turnover by selective autophagy. Nature *522*, 354-+.

Kremer, J.R., Mastronarde, D.N., and McIntosh, J.R. (1996). Computer visualization of three-dimensional image data using IMOD. J Struct Biol *116*, 71-76.

Krogh, A., Larsson, B., von Heijne, G., and Sonnhammer, E.L. (2001). Predicting transmembrane protein topology with a hidden Markov model: application to complete genomes. J Mol Biol *305*, 567-580.

Kurth, I., Pamminger, T., Hennings, J.C., Soehendra, D., Huebner, A.K., Rotthier, A., Baets, J., Senderek, J., Topaloglu, H., Farrell, S.A., *et al.* (2009). Mutations in FAM134B, encoding a newly identified Golgi protein, cause severe sensory and autonomic neuropathy. Nat Genet *41*, 1179-1181.

Li, Q., Qi, B., Oka, K., Shimakage, M., Yoshioka, N., Inoue, H., Hakura, A., Kodama, K., Stanbridge, E.J., and Yutsudo, M. (2001). Link of a new type of apoptosis-inducing gene ASY/Nogo-B to human cancer. Oncogene *20*, 3929-3936.

Liang, J.R., Lingeman, E., Ahmed, S., and Corn, J.E. (2018). Atlastins remodel the endoplasmic reticulum for selective autophagy. J Cell Biol *217*, 3354-3367.

Limpens, R.W., van der Schaar, H.M., Kumar, D., Koster, A.J., Snijder, E.J., van Kuppeveld, F.J., and Barcena, M. (2011). The transformation of enterovirus replication structures: a three-dimensional study of single- and double-membrane compartments. MBio *2*.

Lingwood, D., Schuck, S., Ferguson, C., Gerl, M.J., and Simons, K. (2009). Generation of cubic membranes by controlled homotypic interaction of membrane proteins in the endoplasmic reticulum. J Biol Chem *284*, 12041-12048.

Lynes, E.M., and Simmen, T. (2011). Urban planning of the endoplasmic reticulum (ER): how diverse mechanisms segregate the many functions of the ER. Biochim Biophys Acta *1813*, 1893-1905.

Mclean, I.W., and Nakane, P.K. (1974). Periodate-Lysine-Paraformaldehyde Fixative - New Fixative for Immunoelectron Microscopy. J Histochem Cytochem *22*, 1077-1083.

Nakamura, N., Rabouille, C., Watson, R., Nilsson, T., Hui, N., Slusarewicz, P., Kreis, T.E., and Warren, G. (1995). Characterization of a cis-Golgi matrix protein, GM130. J Cell Biol *131*, 1715-1726.

Oertle, T., and Schwab, M.E. (2003). Nogo and its paRTNers. Trends Cell Biol *13*, 187-194.

Omasits, U., Ahrens, C.H., Muller, S., and Wollscheid, B. (2014). Protter: interactive protein feature visualization and integration with experimental proteomic data. Bioinformatics *30*, 884-886.

Palade, G.E. (1956). The endoplasmic reticulum. J Biophys Biochem Cytol *2*, 85-98.

Park, S.H., Zhu, P.P., Parker, R.L., and Blackstone, C. (2010a). Hereditary spastic paraplegia proteins REEP1, spastin, and atlastin-1 coordinate microtubule interactions with the tubular ER network. J Clin Invest *120*, 1097-1110.

Park, S.H., Zhu, P.P., Parker, R.L., and Blackstone, C. (2010b). Hereditary spastic paraplegia proteins REEP1, spastin, and atlastin-1 coordinate microtubule interactions with the tubular ER network. J Clin Invest *120*, 1097-1110.

Prinjha, R., Moore, S.E., Vinson, M., Blake, S., Morrow, R., Christie, G., Michlovich, D., Simmons, D.L., and Walsh, F.S. (2000). Neurobiology - Inhibitor of neurite outgrowth in humans. Nature *403*, 383-384.

Puhka, M., Joensuu, M., Vihinen, H., Belevich, I., and Jokitalo, E. (2012). Progressive sheet-to-tubule transformation is a general mechanism for endoplasmic reticulum partitioning in dividing mammalian cells. Mol Biol Cell *23*, 2424-2432.

Puhka, M., Vihinen, H., Joensuu, M., and Jokitalo, E. (2007). Endoplasmic reticulum remains continuous and undergoes sheet-to-tubule transformation during cell division in mammalian cells. J Cell Biol *179*, 895-909.

Qi, B., Qi, Y., Watari, A., Yoshioka, N., Inoue, H., Minemoto, Y., Yamashita, K., Sasagawa, T., and Yutsudo, M. (2003). Pro-apoptotic ASY/Nogo-B protein associates with ASYIP. J Cell Physiol *196*, 312-318.

Rämö, O., Kumar, D., Gucciardo, E., Joensuu, M., Saarekas, M., Vihinen, H., Belevich, I., Smolander, O.P., Qian, K., Auvinen, P., *et al.* (2016). NOGO-A/RTN4A and NOGO-B/RTN4B are simultaneously expressed in epithelial, fibroblast and neuronal cells and maintain ER morphology. Sci Rep *6*, 35969.

Roux, K.J., Kim, D.I., Raida, M., and Burke, B. (2012). A promiscuous biotin ligase fusion protein identifies proximal and interacting proteins in mammalian cells. J Cell Biol *196*, 801-810.

Shannon, P., Markiel, A., Ozier, O., Baliga, N.S., Wang, J.T., Ramage, D., Amin, N., Schwikowski, B., and Ideker, T. (2003). Cytoscape: a software environment for integrated models of biomolecular interaction networks. Genome Res *13*, 2498-2504.

Shibata, Y., Shemesh, T., Prinz, W.A., Palazzo, A.F., Kozlov, M.M., and Rapoport, T.A. (2010). Mechanisms determining the morphology of the peripheral ER. Cell *143*, 774-788.

Shibata, Y., Voeltz, G.K., and Rapoport, T.A. (2006). Rough sheets and smooth tubules. Cell *126*, 435-439.

Shibata, Y., Voss, C., Rist, J.M., Hu, J., Rapoport, T.A., Prinz, W.A., and Voeltz, G.K. (2008). The reticulon and DP1/Yop1p proteins form immobile oligomers in the tubular endoplasmic reticulum. J Biol Chem *283*, 18892-18904.

Soding, J., Biegert, A., and Lupas, A.N. (2005). The HHpred interactive server for protein homology detection and structure prediction. Nucleic Acids Res *33*, W244-248.

Tagami, S., Eguchi, Y., Kinoshita, M., Takeda, M., and Tsujimoto, Y. (2000). A novel protein, RTN-XS, interacts with both Bcl-XL and Bcl-2 on endoplasmic reticulum and reduces their anti-apoptotic activity. Oncogene *19*, 5736-5746.

Varjosalo, M., Sacco, R., Stukalov, A., van Drogen, A., Planyavsky, M., Hauri, S., Aebersold, R., Bennett, K.L., Colinge, J., Gstaiger, M., *et al.* (2013). Interlaboratory reproducibility of large-scale human protein-complex analysis by standardized AP-MS. Nat Methods *10*, 307-314.

Voeltz, G.K., Prinz, W.A., Shibata, Y., Rist, J.M., and Rapoport, T.A. (2006). A class of membrane proteins shaping the tubular endoplasmic reticulum. Cell *124*, 573-586.

Wang, J.L., Tong, C.W., Chang, W.T., and Huang, A.M. (2013). Novel genes FAM134C, C3orf10 and ENOX1 are regulated by NRF-1 and differentially regulate neurite outgrowth in neuroblastoma cells and hippocampal neurons. Gene *529*, 7-15.

Wu, Y.M., Whiteus, C., Xu, C.S., Hayworth, K.J., Weinberg, R.J., Hess, H.F., and De Camilli, P. (2017). Contacts between the endoplasmic reticulum and other membranes in neurons. P Natl Acad Sci USA *114*, E4859-E4867.

Yang, Y.S., and Strittmatter, S.M. (2007). The reticulons: a family of proteins with diverse functions. Genome Biol *8*, 234.

Zurek, N., Sparks, L., and Voeltz, G. (2011). Reticulon Short Hairpin Transmembrane Domains Are Used to Shape ER Tubules. Traffic *12*, 28-41.

Figure Legends

Fig. 1. RTN4B has many interaction partners in Huh-7 and HEK293 cells. Protein-protein interaction map of RTN4B generated with Cytoscape. The network represents interacting proteins from two cell lines and purification methods. Blue lines represent experimentally validated interaction by strep purification; green lines are for validated interactions from BioID purification; overlap of two purification methods is shown with light blue colour. Dashed lines represent known interactions derived from protein interaction network analysis (PINA2.0) platform (reference). The coloured circles represent tagged RTN4B prey proteins expressed in Huh-7 (left side) and HEK293 (right side) cells. Full protein names with their accession numbers are listed in Table 1.

Fig. 2. FAM134C and FAM134B interact with RTN4B. (A) Wide field light microscopy (LM) images of Huh-7 cells expressing BiFC constructs. (a-d) RTN4B (RTN4B-GFP 1-10-HA) or (e) FAM134C (FAM134C 1-10-HA) as baits (cyan, middle panels) show GFP signal (green, right panels) stating a positive interaction with (a) FAM134 and (b) FAM134B. (c) RTN4B was used as a positive control and (d) MYO1C as a negative control. (e) Positive interaction of FAM134C with itself. Left panels (flag tags, red) show the expression level of prey constructs. Scale bars: 10 μm. (B) Intensities from images after subtraction of background were quantified. The + symbol denotes outliers.

Fig. 3. FAM134C inserts into the membrane so that both N- and C-terminal ends face the cytoplasm. (A) Wide field LM images of HeLa cells mildly expressing N-terminally tagged FLAG-FAM134C or C-terminally tagged FAM134C-FLAG after digitonin or Triton X-100 permeablization and immuno-labelling with anti-FLAG and calreticulin antibodies reveal that both constructs were accessible to the anti-FLAG antibody in digitonin permeabilized cells (top row), whereas calreticulin was only labelled in Triton X-100 permeabilized cells (bottom row). (B) Quantification of intensities for images shown in A (>10 cells). Scale bars: 10 μm.

Fig. 4. FAM134C localizes to endoplasmic reticulum. (A) Confocal LM images showing Huh-7 cells mildly expressing FAM134C-FLAG (magenta) and its co-localization with FAM134C and organelles (in green) representing ER (calreticulin) (Aa), reticular ER (RTN4B) (Ab), Golgi (GM130) (Ac) and ERGIC (ERGIC-53) (Ad). Insets show higher magnification of boxed areas. The Merge panel is represents the extent of co-localization. (B) Co-localization between FAM134C-FLAG and indicated organelle markers were quantified using Pearson's correlation coefficient (~20 cells). For negative control (Neg Ctrl) one of the channels from the same ROI (region of interest) was rotated by 90°. Scale bars: 10 μm.

Fig. 5. FAM134C overexpression induces extensive ER tubulation. (Aa) LM images showing Huh-7 cells over-expressing FAM134C-FLAG (24 h) (magenta) co-stained with general ER marker calreticulin (green). The cells are observed to contain large globular structures co-localizing with calreticulin, co-existing with normal looking ER. Insets show higher magnification of boxed areas where ER tubules are seen co-localizing with FAM134C-FLAG. (Ab) Showing quantification of the size distribution for the globular structures shown in Aa (>20 cells). (B) Confocal LM images of three prominent phenotypes from FAM134C-eGFP overexpression (24 h) (green); large globular structures (Ba), long protrusions from the cell edge pertaining smaller globular structures (Bb) and long tubular unbranched profiles extending from the cell edge (Bc); also see Fig. S3 and Movies 1-3. (C) TEM

micrographs of Huh-7 cells, (Ca and Cb) showing highly branched smooth ER positive for cells co-expressing ssHRP-KDEL (darker ER) and FAM134C-eGFP representing the globular structures as shown in A and Ba. Red dotted line (in Ca) outlining a non-transfected control cell. (Cc) Golgi morphology appearing normal in FAM134C overexpressed condition. (Cd) Immuno-EM micrograph of FAM134C-eGFP overexpression induced heavily tubular and branched smooth ER positive for gold label (dark spots) recognizing GFP of FAM134C-eGFP. (Ce) Enlarged image of the red dashed box in Cc. Scale bars: 10 μm (A), 5 μm (B) and 1 μm (C).

Fig. 6. Depletion of FAM134C does not affect ER morphology in Huh-7 cells. (A) Confocal LM images of FAM134C depleted and mock treated cells expressing ER marker Hsp47-GFP (Aa). (Ab) EM micrographs of Huh-7 cells expressing ER marker Hsp47-Apex-RDEL with mock and FAM134C knockdown conditions. (B) Western blots of FAM134C in Huh-7 cells after 48 h silencing using GAPDH as loading control. Structural protein RTN4A is stably expressed in both mock and FAM134C depleted conditions. Scale bars: 10 μm (Aa) and 2 μm (Ab).

Fig. 7. FAM134C elevates upon starvation while FAM134C silencing does not affect bulk autophagy. (A) Western blots showing the rise of FAM134C upon 1h EBSS starvation in Huh-7 cells with quantification (Aa) and HeLa cells (Ab). (B) Western blots showing no change in FAM134C upon ER stress induced using 1h DTT treatment in Huh-7 cells while Phospho-elF2α, a marker for ER stress increase in levels. (C) Western blots showing no change in LC3 levels upon knockdown of FAM134C in Huh-7 cells.

Fig. 8. FAM134C is required for ER phagy. (A) Confocal LM images of U2-OS cells in FAM134C knockdown (Aa) or RTN4 knockdown (Ba) conditions for 48h with respective mock images. Red puncta representing ER-phagy (insets) is hampered in cells lacking FAM134C as compared to mock and RTN4 knockdown, upon 1h starvation with EBSS. Quantitation of the percentage of cells with acidified ER is shown in box plot and ER-phagy in terms of acidified ER vs area under the boundary of ER shown in violin plot for shFAM134C (Ab) and siRTN4 (Bb) conditions. Data showing median values in black bars for all violin plots from 3 experimental replicates.

Fig. S1. FAM134C is a relatively conserved protein. (A) Protein sequences of FAM134C from 6 representative species are aligned using MAFFT (MAFFT FFT-NS-i (v7.397)). Alignment shows that large parts of predicted transmembrane domains (shown in black outline box) and LIR motif (red outline box) fall into fully conserved regions. The following protein accession numbers from UniProtKB were used: *Homo sapiens* (Q86VR2-1), *Macaca mulatta* (F7CYZ2-1), *Callithrix jacchus* (F7HUC7-1), *Mus musculus* (Q9CQV4-1), *Rattus norvegicus* (B2GV94-1) and *Xenopus tropicalis* (Q0P4Z1-1). (B) Schematic representation of FAM134C depicting in black outline boxes four transmembrane domains forming the reticulon homology domain and in red outline box the LIR motif.

Fig. S2. FAM134C localizes to high curvature ER membranes. EM micrographs of Huh-7 cells expressing FAM134C-eGFP detected by anti-GFP gold particles. (Aa) TEM micrograph of FAM134C localizing heavily to peripheral ER containing more tubular ER profiles. (Ab) Magnified image from inset in Aa showing labelling of FAM134C around sheet edges and tubular ER profiles marked by arrow heads. (B) Micrograph showing FAM134C labelling pattern around fenestrations

on the ER sheet marked by arrows. (C) TEM image of FAM134C at high curvature ER of a mitochondrial-ER contact site. Scale bars 1 μm.

Fig. S3. Correlative light and electron microscopy (CLEM) and tomography reveals FAM134C overexpression phenotypes. (A) CLEM workflow of Huh-7 cells expressing Hsp47-GFP (Aa) or FAM134C-EmGFP (Ab). The GFP positive cell denoted by red asterisk is traced from light microscopy level (20X) (Phase-contrast and fluorescence) to scanning EM level (2000X). The control cell population represented by the non-transfected cells or the cells transfected with Hsp47-GFP can be seen with a smooth cell surface as compared to abnormal cell shape in FAM134C-eGFP overexpressing cells. FAM134C-EmGFP overexpressing cells portraying rounded cells with long protrusions extending form the cell surface. (B) Models generated from tomograms of 3 serial sections showing heavily tabulated and branched ER (green) connected to normal ER (yellow), upon FAM134C overexpression (24h). FAM134C-eGFP co-expressing ER marker Hsp47-APEX-RDEL (causing ER to darken) showing positive transfection (images in B are in perspective view). Scale bars: 20 μm (A) and 1 μm (B).

Fig. S4. FAM134C's RHD domain is necessary for membrane curvature. (A) FAM134C's RHD (Aa) was modified by extending its partial lipid bilayer inserting domains to develop MutFAM134C construct (Ab), thus abolishing membrane curvature. (B) TEM micrographs showing Huh-7 cells co-expressing MutFAM134C and ER marker Hsp47-APEX-RDEL. (C) LM images showing FAM134C-GFP (Cb) and MutFAM134C-GFP (Cc) detected by anti-GFP staining upon both semi-permeable (digitonin) and normal permeablization (Triton X-100), while ER marker calreticulin only detected by normal permeablization conditions (Triton X-100) (Ca) stating no change in topology of MutFAM134C-GFP as compared to FAM134C-GFP. Scale bars: 5 μm (B) and 10 μm (C).

Movie. 1. Live cell imaging of FAM134C induced large globular structures in Huh-7. FAM134C-EmGFP overexpression induces large globular structures at varied sizes randomly throughout the cell. The globular structures are non-dynamic in nature. Total movie length 1 min with frame rate 20, pixel size: 83 nm.

Movie. 2. Live cell imaging of FAM134C induced long protrusions in Huh-7. FAM134C-EmGFP overexpression induces long protrusions from the cell periphery. Small globular structures can be seen at random areas within the protrusions. These protrusions and globular structures are non-dynamic in nature. Total movie length 1 min with frame rate 20, pixel size: 83 nm.

Movie. 3. Live cell imaging of FAM134C induced long unbranched tubules in Huh-7. FAM134C-EmGFP overexpression induces long and unbranched tubules from the cell periphery. These long tubular structures are non-dynamic in nature. Total movie length 1 min with frame rate 20, pixel size: 83 nm.

Movie. 4. FAM134C overexpression causes a dense network of ER tubulation. Models generated from serial electron tomograms showing normal ER (yellow) connected to heavily branched and tabulated ER (green) in a Huh-7 cell co-expressing FAM134C-GFP and ER marker Hsp47-APEX-RDEL. Dual axis tilt series from three consecutive 250-nm thick sections were acquired using SerialEM software running on a Tecnai FEG 20 microscope (FEI). Voxel size: 2.28 x 2.28 x 2.28 nm.

Table. 1. RTN4B interacting proteins identified with strep purification and BioID approaches. Table showing individual proteins with the corresponding accession numbers and entry names along with the cell type in which the protein came out as a hit.

Figure 1.

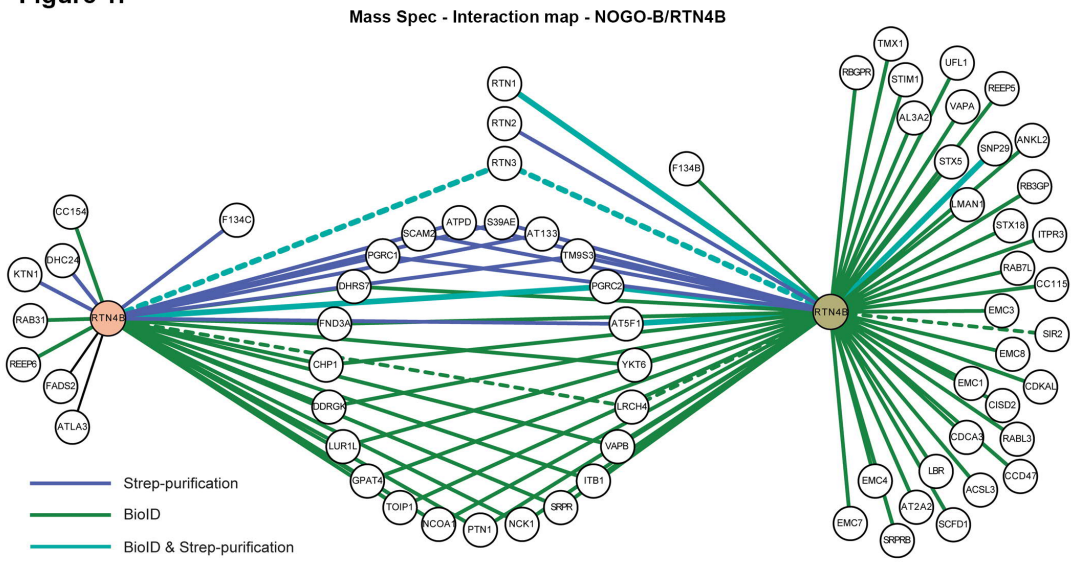
Mass Spec - Interaction map - NOGO-B/RTN4B
RTN1
RTN2
RTN3
F134B
CC154
F134C
SCAM2
ATPD
S39AE
AT133
KTN1
DHC24
PGRC1
TM9S3
DHRS7
PGRC2
RAB31
RTN4B
FND3A
AT5F1
REEP6
CHP1
YKT6
FADS2
DDRGK
LRCH4
ATLA3
LUR1L
VAPB
GPAT4
ITB1
TOIP1
SRPR
NCOA1
PTN1
NCK1
RTN4B
TMX1
RBGPR
STIM1
UFL1
REEP5
VAPA
AL3A2
ANKL2
SNP29
STX5
RB3GP
LMAN1
STX18
ITPR3
RAB7L
CC115
EMC3
SIR2
EMC8
EMC1
CDKAL
CISD2
CDCA3
RABL3
LBR
CCD47
EMC4
ACSL3
AT2A2
SCFD1
EMC7
SRPRB
Strep-purification
BioID
BioID & Strep-purification

Figure 2.

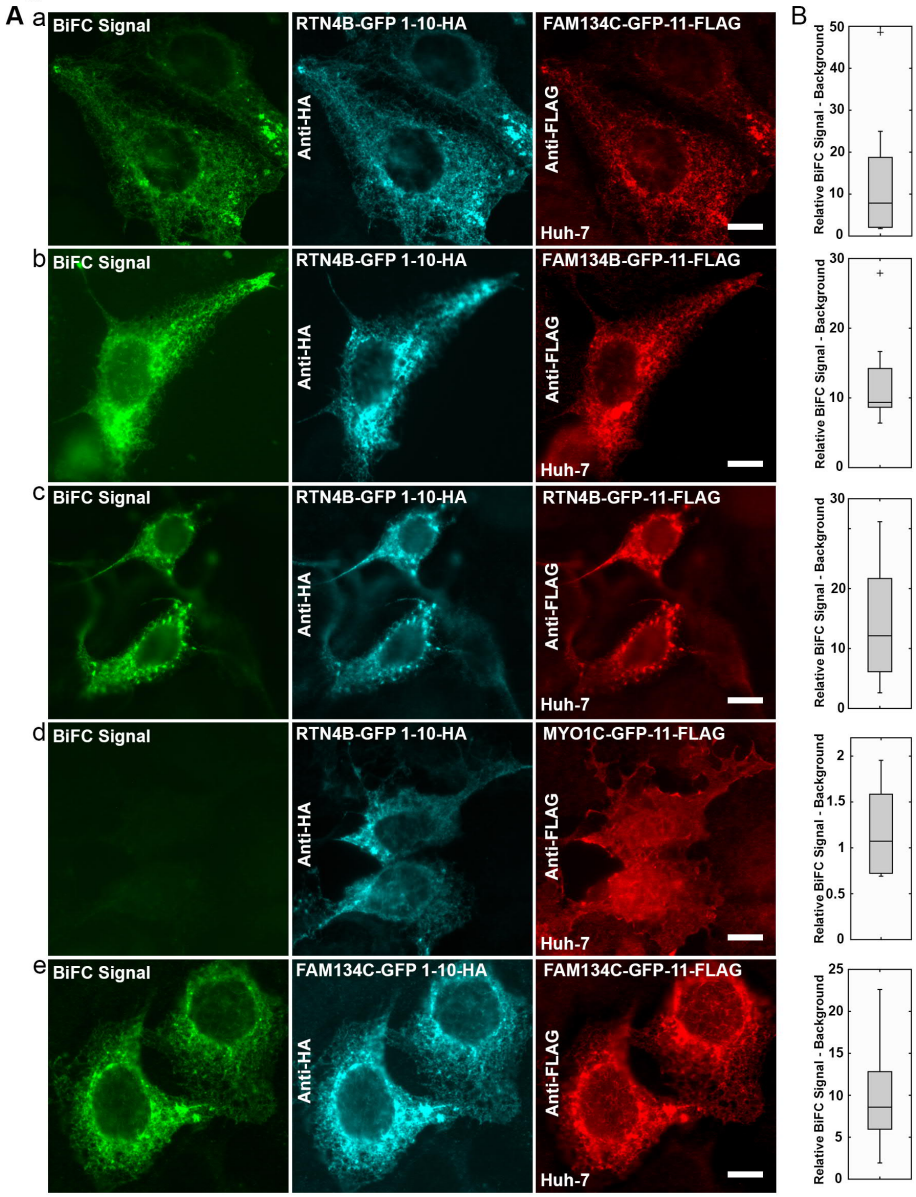
A
a
BiFC Signal
RTN4B-GFP 1-10-HA
Anti-HA
FAM134C-GFP-11-FLAG
Anti-FLAG
Huh-7
b
BiFC Signal
RTN4B-GFP 1-10-HA
Anti-HA
FAM134B-GFP-11-FLAG
Anti-FLAG
Huh-7
c
BiFC Signal
RTN4B-GFP 1-10-HA
Anti-HA
RTN4B-GFP-11-FLAG
Anti-FLAG
Huh-7
d
BiFC Signal
RTN4B-GFP 1-10-HA
Anti-HA
MYO1C-GFP-11-FLAG
Anti-FLAG
Huh-7
e
BiFC Signal
FAM134C-GFP 1-10-HA
Anti-HA
FAM134C-GFP-11-FLAG
Anti-FLAG
Huh-7
B
Relative BiFC Signal - Background
0
10
20
30
40
50
Relative BiFC Signal - Background
0
10
20
30
Relative BiFC Signal - Background
0
10
20
30
Relative BiFC Signal - Background
0
0.5
1
1.5
2
Relative BiFC Signal - Background
0
5
10
15
20
25

Figure 3.

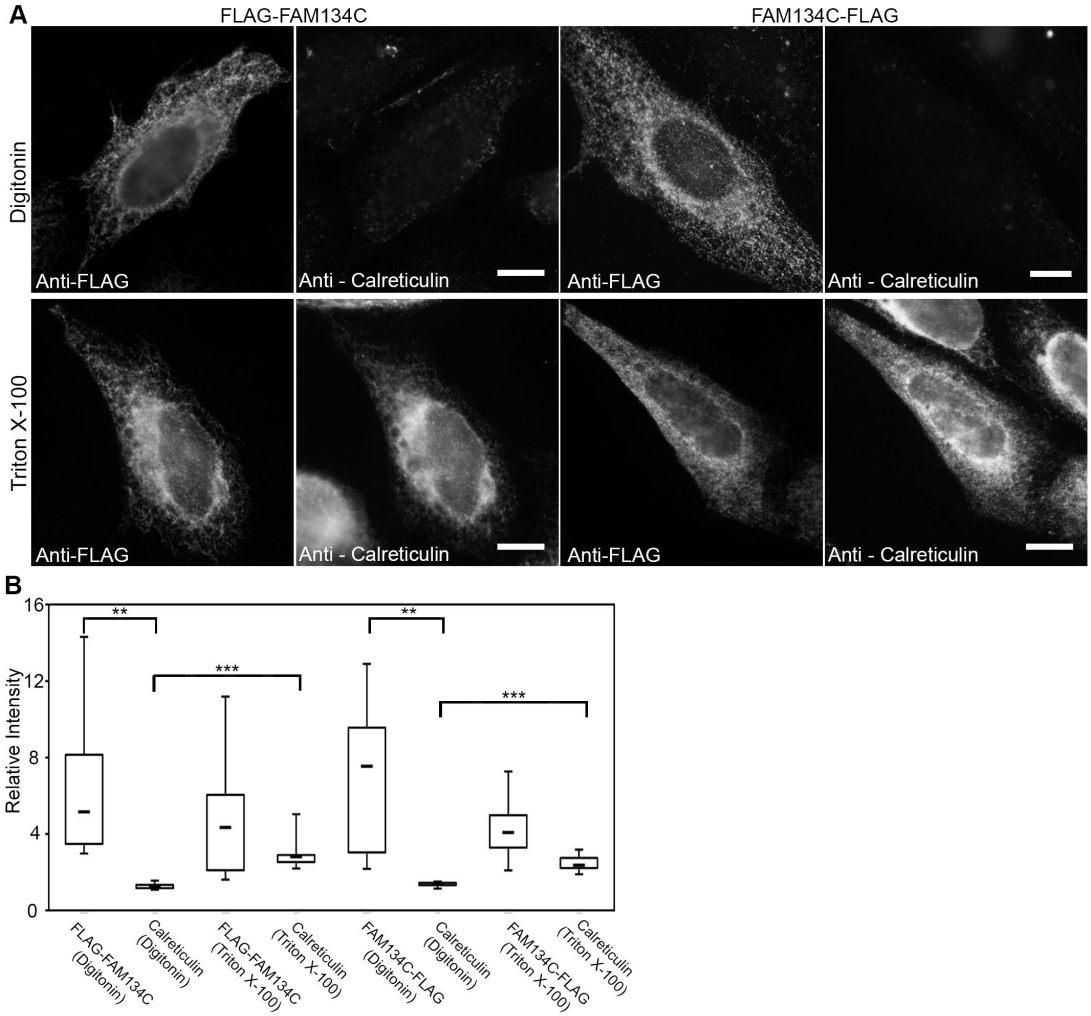
A
FLAG-FAM134C
FAM134C-FLAG
Digitonin
Triton X-100
Anti-FLAG
Anti - Calreticulin
Anti-FLAG
Anti - Calreticulin
Anti-FLAG
Anti - Calreticulin
Anti-FLAG
Anti - Calreticulin
B
Relative Intensity
16
12
8
4
0
**
***
**
***
FLAG-FAM134C (Digitonin)
Calreticulin (Digitonin)
FLAG-FAM134C (Triton X-100)
Calreticulin (Triton X-100)
FAM134C-FLAG (Digitonin)
Calreticulin (Digitonin)
FAM134C-FLAG (Triton X-100)
Calreticulin (Triton X-100)

Figure 4.

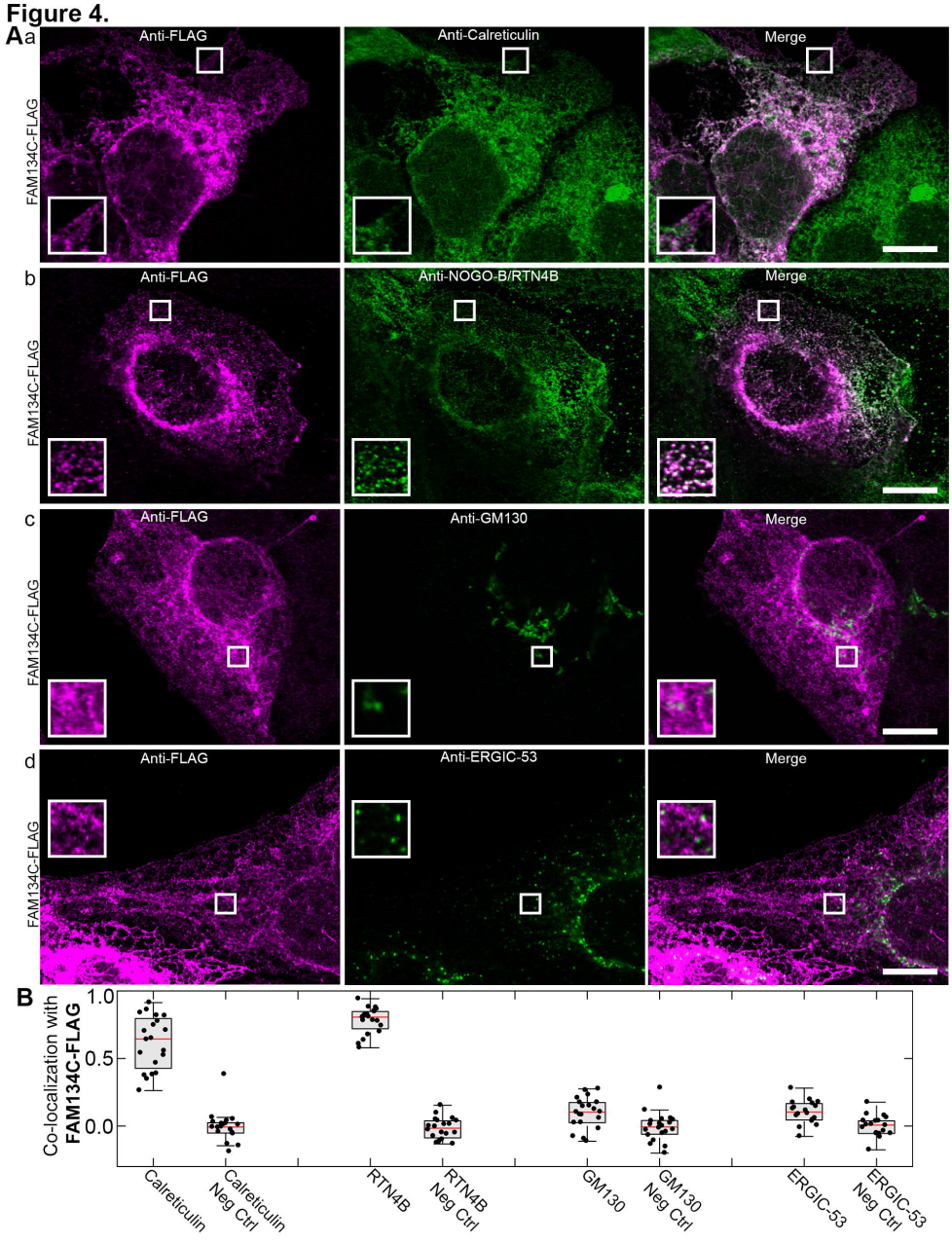
A
a
Anti-FLAG
Anti-Calreticulin
Merge
FAM134C-FLAG
b
Anti-FLAG
Anti-NOGO-B/RTN4B
Merge
FAM134C-FLAG
c
Anti-FLAG
Anti-GM130
Merge
FAM134C-FLAG
d
Anti-FLAG
Anti-ERGIC-53
Merge
FAM134C-FLAG
B
Co-localization with FAM134C-FLAG
1.0
0.5
0.0
Calreticulin
Calreticulin Neg Ctrl
RTN4B
RTN4B Neg Ctrl
GM130
GM130 Neg Ctrl
ERGIC-53
ERGIC-53 Neg Ctrl

Figure 5.

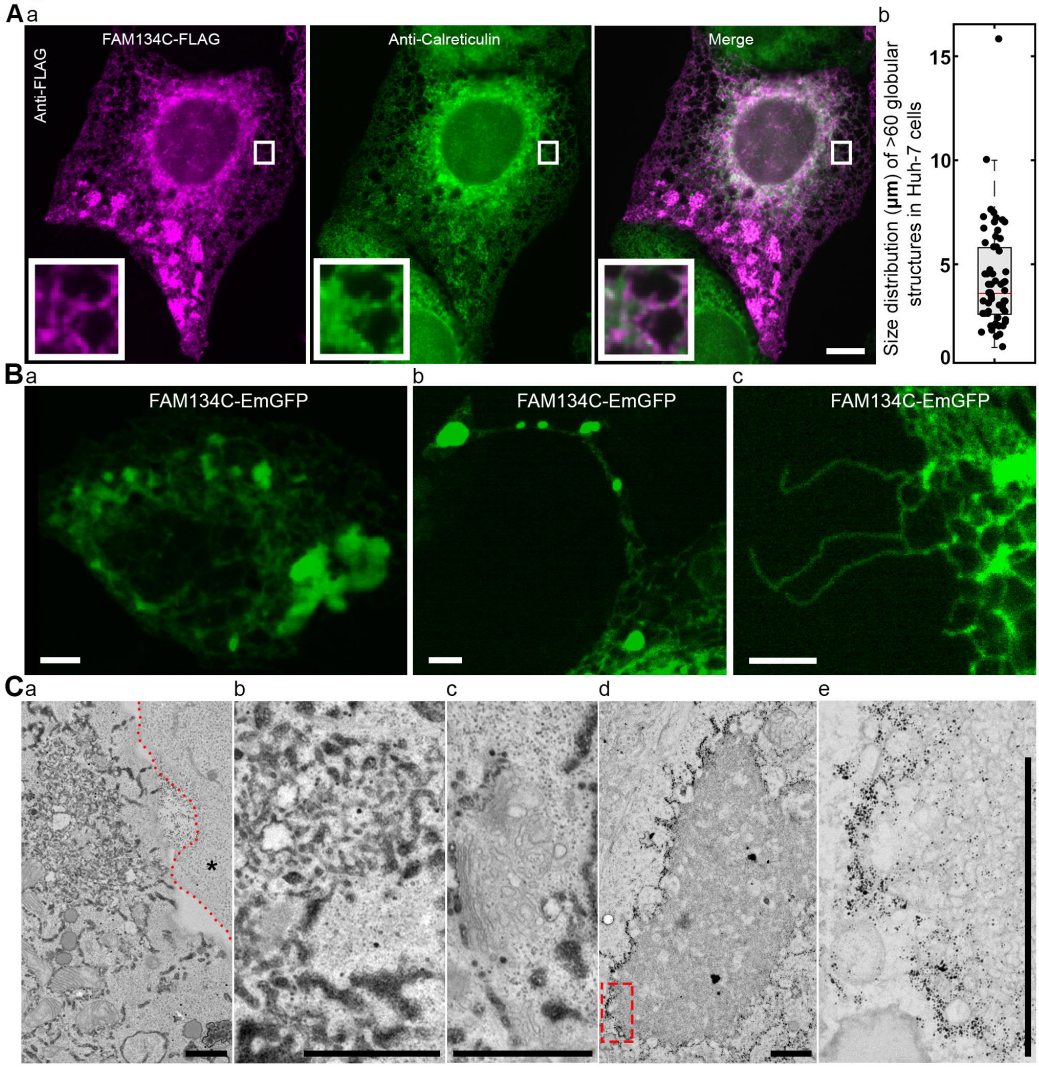
A
a
FAM134C-FLAG
Anti-FLAG
Anti-Calreticulin
Merge
b
Size distribution (μm) of >60 globular structures in Huh-7 cells
15
10
5
0
B
a
FAM134C-EmGFP
b
FAM134C-EmGFP
c
FAM134C-EmGFP
C
a
b
c
d
e
*

Figure 6.

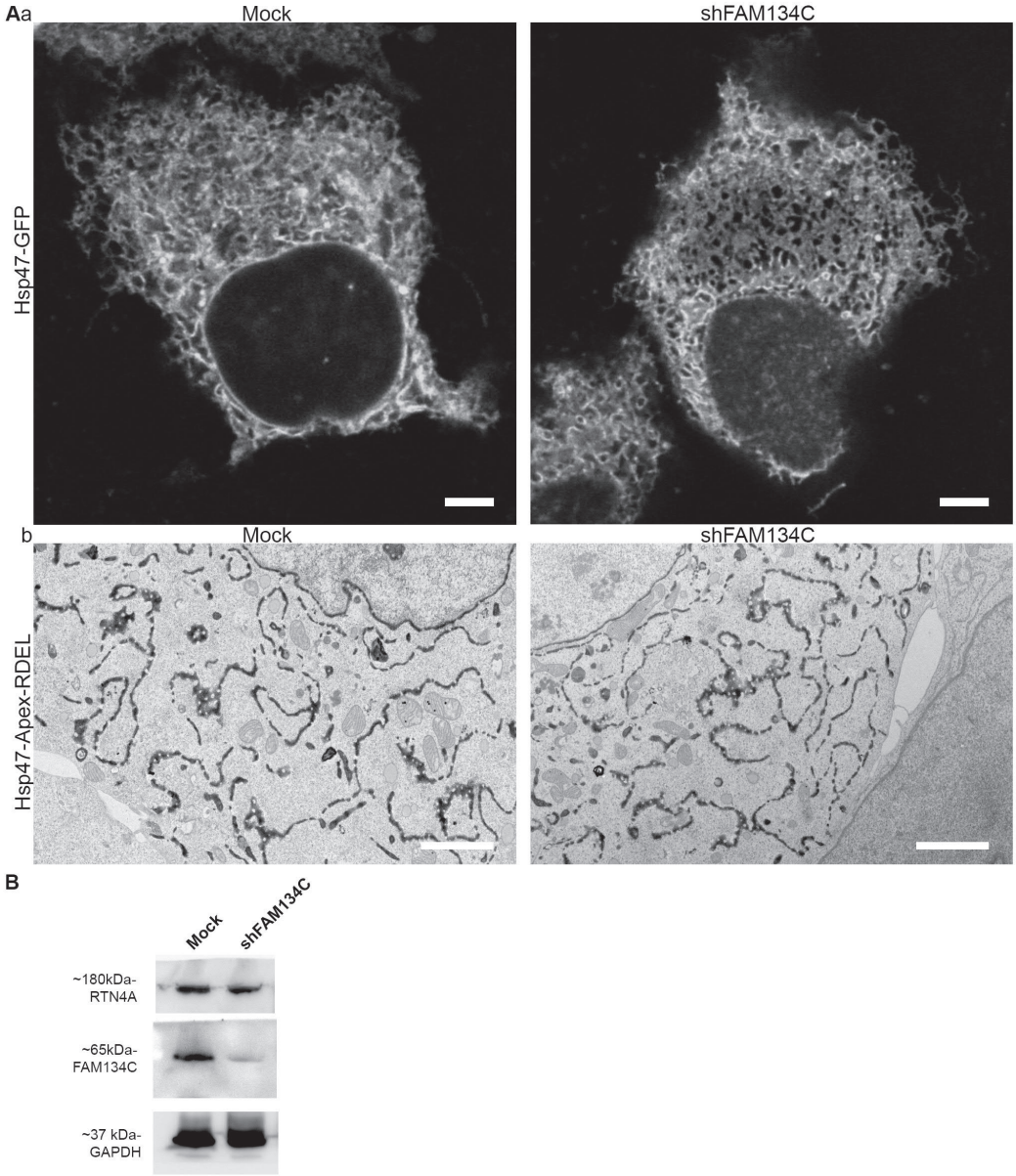
A
a
Mock
shFAM134C
Hsp47-GFP
b
Mock
shFAM134C
Hsp47-Apex-RDEL
B
Mock
shFAM134C
~180kDa-
RTN4A
~65kDa-
FAM134C
~37 kDa-
GAPDH

Figure 7.

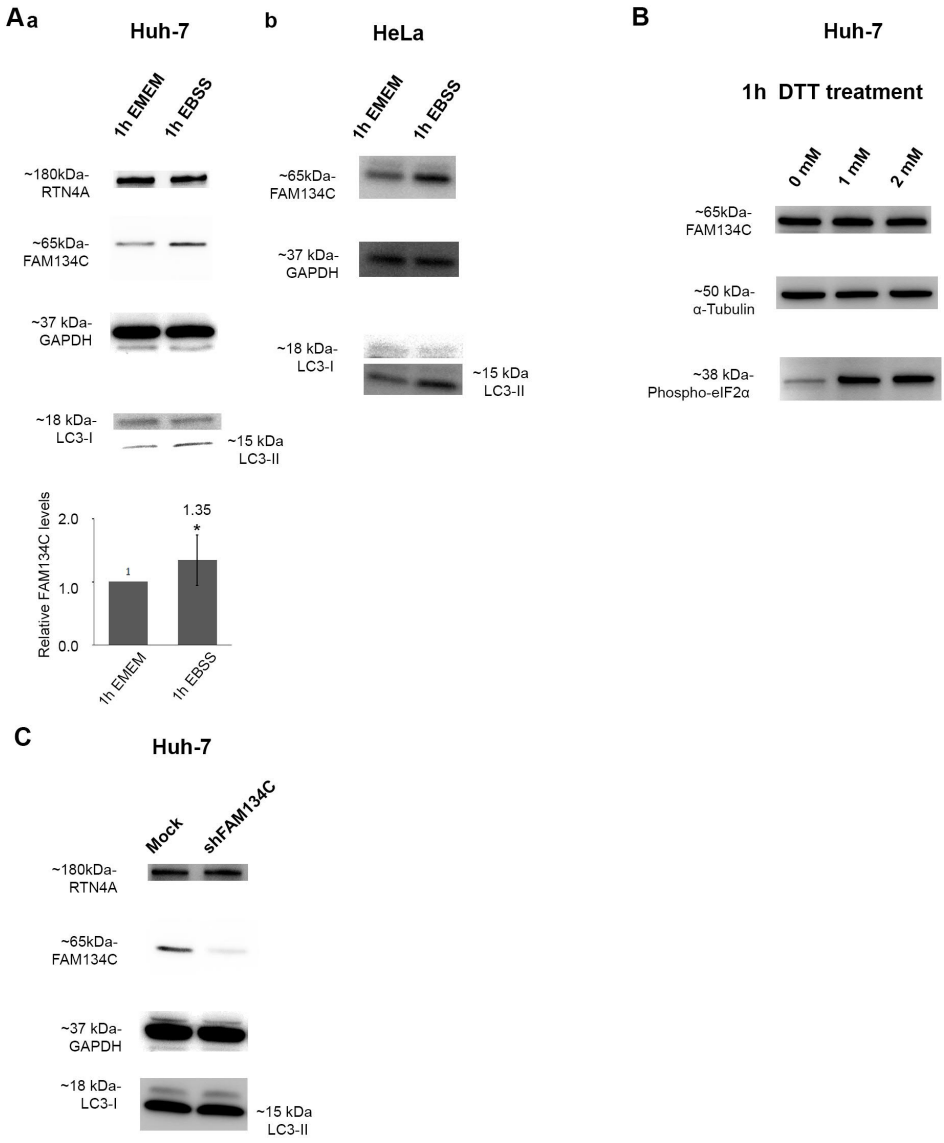
A
a
Huh-7
1h EMEM
1h EBSS
~180kDa-
RTN4A
~65kDa-
FAM134C
~37 kDa-
GAPDH
~18 kDa-
LC3-I
~15 kDa
LC3-II
Relative FAM134C levels
2.0
1.0
0.0
1
1.35
*
b
HeLa
B
Huh-7
1h DTT treatment
0 mM
1 mM
2 mM
~50 kDa-
α-Tubulin
~38 kDa-
Phospho-eIF2α
C
Mock
shFAM134C

Figure 8.

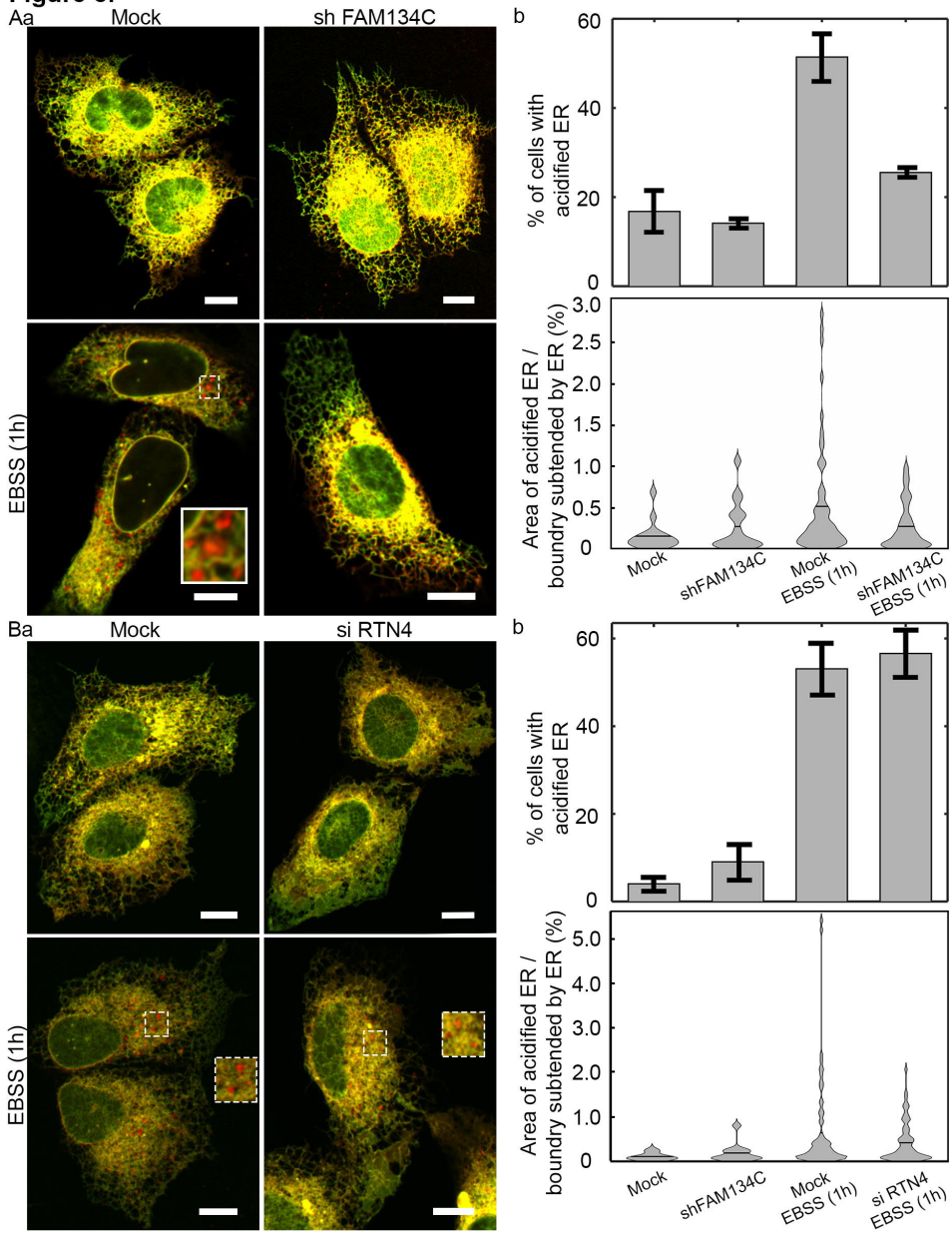
Aa
Mock
sh FAM134C
EBSS (1h)
b
% of cells with acidified ER
Area of acidified ER / boundry subtended by ER (%)
Mock
shFAM134C
Mock EBSS (1h)
shFAM134C EBSS (1h)
Ba
Mock
si RTN4
EBSS (1h)
b
% of cells with acidified ER
Area of acidified ER / boundry subtended by ER (%)
Mock
shFAM134C
Mock EBSS (1h)
si RTN4 EBSS (1h)

Figure S1.

A

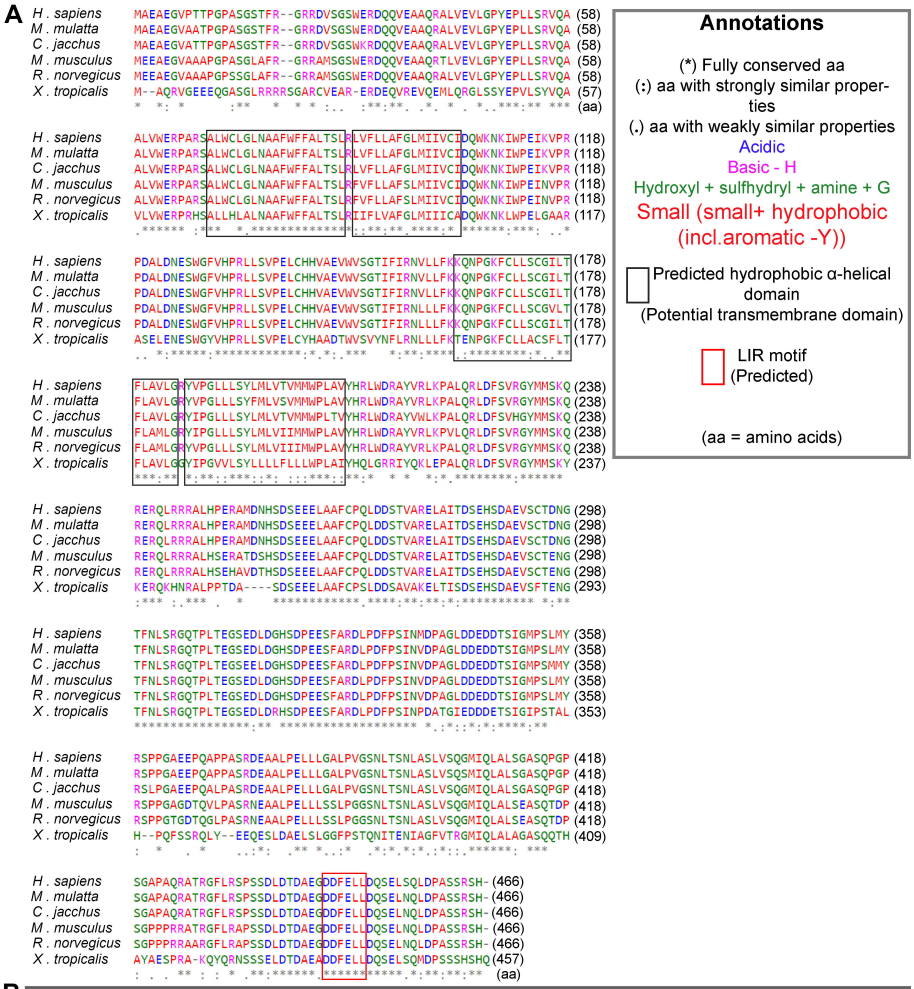
H . sapiens
M . mulatta
C . jacchus
M . musculus
R . norvegicus
X . tropicalis
Annotations
(*) Fully conserved aa
(:) aa with strongly similar properties
(.) aa with weakly similar properties
Acidic
Basic - H
Hydroxyl + sulfhydryl + amine + G
Small (small+ hydrophobic (incl.aromatic -Y))
Predicted hydrophobic α-helical domain (Potential transmembrane domain)
LIR motif (Predicted)
(aa = amino acids)

B

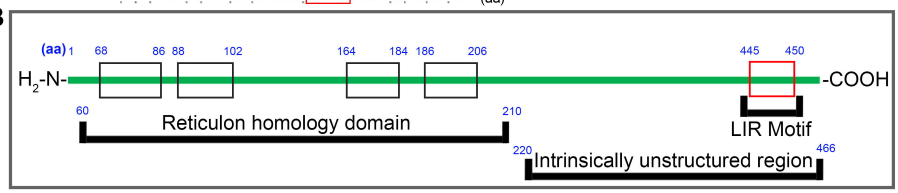
(aa)
H2-N-
-COOH
Reticulon homology domain
LIR Motif
Intrinsically unstructured region

Figure S2.

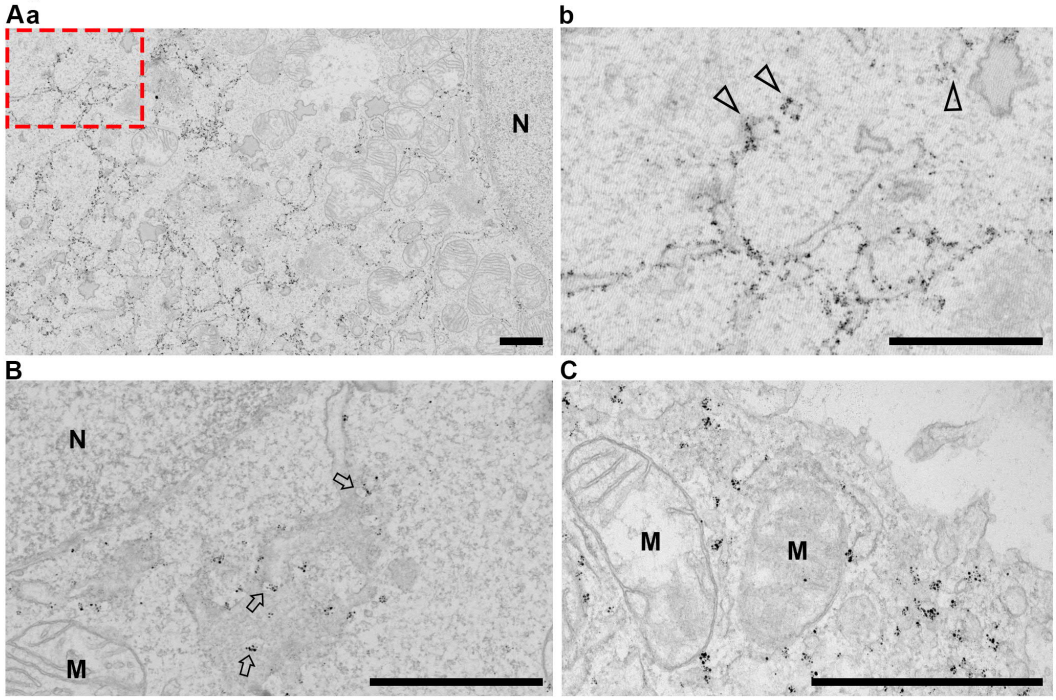

Figure S3.

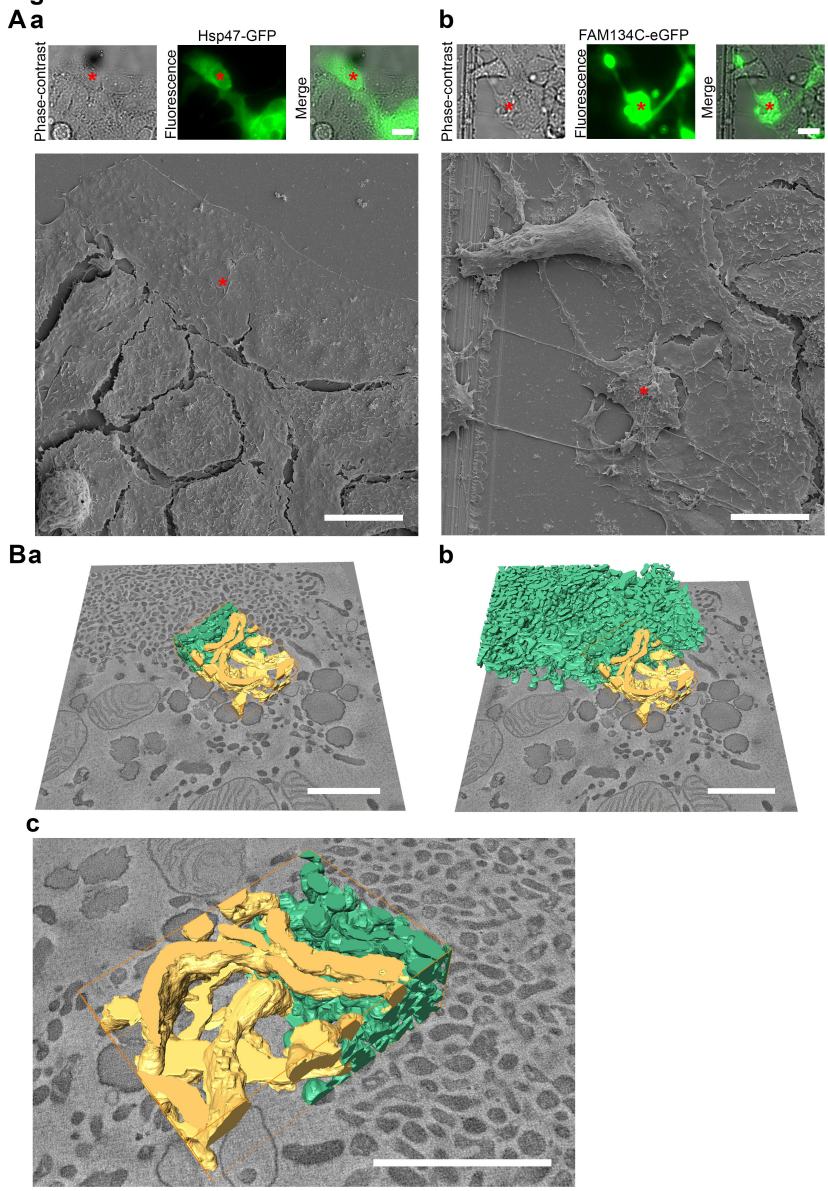
A a
Hsp47-GFP
Phase-contrast
Fluorescence
Merge
b
FAM134C-eGFP
Phase-contrast
Fluorescence
Merge
Ba
b
c

Figure S4.

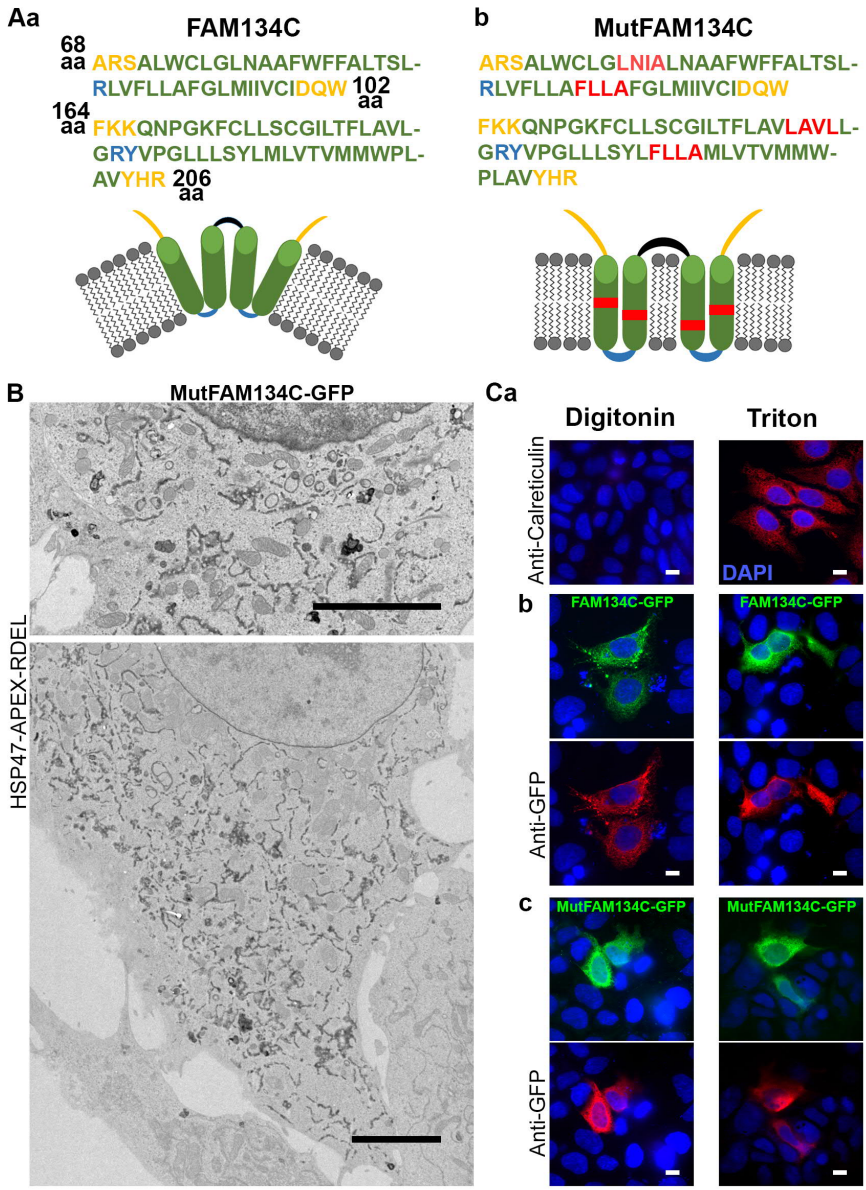
Aa
FAM134C
68 aa ARSALWCLGLNAAFWFFALTSL-
RLVFLLAFGLMIIVCIDQW 102 aa
164 aa FKKQNPGKFCLLSCGILTFLAVL-
GRYVPGLLLSYLMLVTVMMWPL-
AVYHR 206 aa
b
MutFAM134C
ARSALWCLGLNIALNAAFWFFALTSL-
RLVFLLAFLLAFGLMIIVCIDQW
FKKQNPGKFCLLSCGILTFLAVLAVLL-
GRYVPGLLLSYLFLLAMLVTVMMW-
PLAVYHR
B
MutFAM134C-GFP
HSP47-APEX-RDEL
Ca
Digitonin
Triton
Anti-Calreticulin
DAPI
b
FAM134C-GFP
Anti-GFP
c
MutFAM134C-GFP
Anti-GFP

Table. 1.

Cell Type	Entry Name	Protein names	Accession number
Huh-7	CC154	Coiled-coil domain-containing protein 154	A6NI56
	FADS2	Acyl-CoA 6-desaturase	O95864
	RAB31	Ras-related protein Rab-31	Q13636
	DHC24	Delta(24)-sterol reductase	Q15392
	ATLA3	Atlastin-3	Q6DD88
	KTN1	Kinectin	Q86UP2
	F134C	Reticulophagy regulator 3	Q86VR2
	REEP6	Receptor expression-enhancing protein 6	Q96HR9
Huh-7 and HEK-293	PGRC1	Membrane-associated progesterone receptor component 1	O00264
	SCAM2	Secretory carrier-associated membrane protein 2	O15127
	PGRC2	Membrane-associated progesterone receptor component 2	O15173
	YKT6	Synaptobrevin homolog YKT6	O15498
	LRCH4	Leucine-rich repeat and calponin homology domain-containing protein 4	O75427
	RTN3	Reticulon-3	O95197
	VAPB	Vesicle-associated membrane protein-associated protein B/C	O95292
	ITB1	Integrin beta-1	P05556
	SRPRA	Signal recognition particle receptor subunit alpha	P08240
	NCK1	Cytoplasmic protein NCK1	P16333
	PTN1	Tyrosine-protein phosphatase non-receptor type 1	P18031
	AT5F1	ATP synthase F(0) complex subunit B1, mitochondrial	P24539
	ATPD	ATP synthase subunit delta, mitochondrial	P30049
	S39AE	Zinc transporter ZIP14	Q15043
	NCOA1	Nuclear receptor coactivator 1	Q15788
	TOIP1	Torsin-1A-interacting protein 1	Q5JTV8
	GPAT4	Glycerol-3-phosphate acyltransferase 4	Q86UL3
	LUR1L	Leucine rich adaptor protein 1-like	Q8IV03
	DDRGK	DDRGK domain-containing protein 1	Q96HY6
	CHP1	Calcineurin B homologous protein 1	Q99653
	AT133	Probable cation-transporting ATPase 13A3	Q9H7F0
	TM9S3	Transmembrane 9 superfamily member 3	Q9HD45
	RTN4	Reticulon-4	Q9NQC3
	FND3A	Fibronectin type-III domain-containing protein 3A	Q9Y2H6
	DHRS7	Dehydrogenase/reductase SDR family member 7	Q9Y394
HEK-293	SRPRB	Signal recognition particle receptor subunit beta	Q9Y5M8
	STX18	Syntaxin-18	Q9P2W9
	VAPA	Vesicle-associated membrane protein-associated protein A	Q9P0L0
	EMC3	ER membrane protein complex subunit 3	Q9P0I2
	EMC7	ER membrane protein complex subunit 7	Q9NPA0
	F134B	Reticulophagy regulator 1	Q9H6L5

HEK-293	TMX1	Thioredoxin-related transmembrane protein 1	Q9H3N1
	RBGPR	Rab3 GTPase-activating protein non-catalytic subunit	Q9H2M9
	CDCA3	Cell division cycle-associated protein 3	Q99618
	CC115	Coiled-coil domain-containing protein 115	Q96NT0
	CCD47	Coiled-coil domain-containing protein 47	Q96A33
	SCFD1	Sec1 family domain-containing protein 1	Q8WVM8
	EMC1	ER membrane protein complex subunit 1	Q8N766
	CISD2	CDGSH iron-sulfur domain-containing protein 2	Q8N5K1
	SIR2	NAD-dependent protein deacetylase sirtuin-2	Q8IXJ6
	ANKL2	Ankyrin repeat and LEM domain-containing protein 2	Q86XL3
	CDKAL	Threonylcarbamoyladenosine tRNA methylthiotransferase	Q5VV42
	EMC4	ER membrane protein complex subunit 4	Q5J8M3
	RABL3	Rab-like protein 3	Q5HYI8
	RTN1	Reticulon-1	Q16799
	RB3GP	Rab3 GTPase-activating protein catalytic subunit	Q15042
	LBR	Delta(14)-sterol reductase	Q14739
	ITPR3	Inositol 1,4,5-trisphosphate receptor type 3	Q14573
	STIM1	Stromal interaction molecule 1	Q13586
	STX5	Syntaxin-5	Q13190
	REEP5	Receptor expression-enhancing protein 5	Q00765
	AL3A2	Fatty aldehyde dehydrogenase	P51648
	LMAN1	Protein ERGIC-53	P49257
	AT2A2	Sarcoplasmic/endoplasmic reticulum calcium ATPase 2	P16615
	SNP29	Synaptosomal-associated protein 29	O95721
	ACSL3	Long-chain-fatty-acid--CoA ligase 3	O95573
	UFL1	E3 UFM1-protein ligase 1	O94874
	RTN2	Reticulon-2	O75298
	EMC8	ER membrane protein complex subunit 8	O43402
	RAB7L	Ras-related protein Rab-7L1	O14966

IV

PLOS | BIOLOGY

COMMUNITY PAGE

Microscopy Image Browser: A Platform for Segmentation and Analysis of Multidimensional Datasets

Ilya Belevich, Merja Joensuu¤, Darshan Kumar, Helena Vihinen, Eija Jokitalo*

Electron Microscopy Unit, Institute of Biotechnology, University of Helsinki, Helsinki, Finland

¤ Current address: Single Molecule Neuroscience Laboratory, Queensland Brain Institute, Brisbane, Australia
* Eija.Jokitalo@Helsinki.fi

Citation: Belevich I, Joensuu M, Kumar D, Vihinen H, Jokitalo E (2016) Microscopy Image Browser: A Platform for Segmentation and Analysis of Multidimensional Datasets. PLoS Biol 14(1): e1002340. doi:10.1371/journal.pbio.1002340

Published: January 4, 2016

Funding: This work was supported by Biocenter Finland, Biological Imaging Network (EJ), Academy of Finland (projects 131650 and 1287975; EJ) and the Integrative Life Science Doctoral Program of the University of Helsinki (MJ and DK). The funders had no role in study design, data collection and analysis, decision to publish, or preparation of the manuscript.

Competing Interests: The authors have declared that no competing interests exist.

Abbreviations: EM, electron microscopy; ET, electron tomography; LD, lipid droplet; LM, light microscopy; MIB, Microscopy Image Browser; NRRD, nearly raw raster data; OMERO, open microscopy environment; SB-EM, serial block-face scanning electron microscope; SLIC, simple linear iterative clustering.

Abstract

Understanding the structure–function relationship of cells and organelles in their natural context requires multidimensional imaging. As techniques for multimodal 3-D imaging have become more accessible, effective processing, visualization, and analysis of large datasets are posing a bottleneck for the workflow. Here, we present a new software package for high-performance segmentation and image processing of multidimensional datasets that improves and facilitates the full utilization and quantitative analysis of acquired data, which is freely available from a dedicated website. The open-source environment enables modification and insertion of new plug-ins to customize the program for specific needs. We provide practical examples of program features used for processing, segmentation and analysis of light and electron microscopy datasets, and detailed tutorials to enable users to rapidly and thoroughly learn how to use the program.

Introduction

Imaging and image analysis are among the key methods in biosciences nowadays. The knowledge of complex 3-D structures of cells and cell organelles in their natural context is important for understanding the structure–function relationship. Moreover, statistical quantification of 3-D objects based on 2-D image information cannot be reliably made; therefore, segmentation, analysis, visualization, and comparison of whole 3-D volumetric datasets are required. Recently evolved 3-D/5-D light microscopy (LM) and electron microscopy (EM) techniques have enabled a new insight into the morphology of tissues, cells, and cell organelles that had not been conceivable before [1,2]. As the amount of collected data is exponentially increasing, the effectiveness of processing raw data into analyzed results has key importance. There are a number of both commercial (e.g., Amira and Imaris) and freeware image processing packages (e.g., ImageJ [3], Fiji [4], BioImageXD [5], IMOD [6], Ilastik [7], and 3D Slicer [8]) available. However, the performance and usability of image segmentation tools in most packages are still suboptimal, resulting in laborious and time-consuming workflows. Furthermore, with the wide range of software and applications used for data collection and image analysis, there is a clear

need for open-access programs that can be adjusted according to the needs of a specific project as well as for cross communication between existing programs.

Here, we present a new open-source software, Microscopy Image Browser (MIB) [9], that was designed for, but not limited to, easy and effective segmentation of multidimensional datasets, improving and facilitating the full utilization and quantitation of acquired data. MIB has a user-friendly graphical interface and is available for all common computer operating systems, either together with MATLAB (Windows, Linux, and Mac OS) or as a standalone package for Windows and Mac OS. At present, MIB has been utilized in more than ten different scientific projects, ranging from studies at the cellular level to those dealing with whole organisms; examples include projects on the endoplasmic reticulum (ER) and cytoskeletal filaments in cultured cells [10,11], the organ of Corti in mouse inner ear [12,13], the development of the sieve element in *Arabidopsis thaliana* root [14,15], and the characterization of cryptomonad *Rhinomonas nottbecki* n. sp. [16]. Although MIB was originally designed for the processing of relatively large EM datasets, it can be used for analysis of LM and any other microscopy datasets. Here, we provide several examples highlighting the various features of the program, and online tutorials have been made to provide detailed instructions on how to use them [17].

MIB Recognizes a Large Number of Imaging Formats and Offers a Variety of Image Processing Tools

The output files from different microscopes and programs are routinely stored in proprietary formats, and access to the collected images and corresponding metadata after acquisition often requires customized software from the manufacturer. MIB overcomes this problem by offering reading capabilities of up to 100 microscopy image and video formats powered by custom-made MATLAB and Bio-Formats [18] readers (Fig 1A; see MIB home page for the full list [9]). MIB was designed as an image browser to allow fast access to individual image datasets for viewing and assembling into 3-D and 4-D stacks (X:Y:Color:Z or X:Y:Color:Time). Up to eight datasets can be simultaneously opened and synchronized, facilitating the comparison and analysis of data from different experiments. The processed images can be exported using most frequently used output formats (Fig 1A).

Quantitative analysis and efficient segmentation of large or otherwise challenging datasets can be facilitated by preprocessing of images (Fig 1A): MIB can resize, flip, rotate, transpose, or crop the datasets as well as adjust brightness, contrast, and gamma settings. In all cases, the voxel (volume pixel) dimensions and the bounding box (exact coordinates of a data block in 3-D space) of the dataset are automatically controlled and adjusted with respect to the performed action. MIB also offers more advanced tools; for example, it has a tool to normalize intensities within the dataset. As intensity levels can easily fluctuate between different images, it is essential to normalize intensities prior to further processing. In many cases, normalization is done based on analysis of intensities of complete slices, while MIB offers additional options for normalization based on preselected areas, which allows normalization even for nonuniform images. Prefiltering of images, especially using anisotropic diffusion filters [19,20], facilitates the segmentation process because of simplification and noise reduction of the images (see MIB homepage for full list of available filters [9]). During a modelling workflow, the filters can be applied to certain arbitrarily shaped (rectangular, ellipsoidal, or polygonal) regions of interest. The alignment feature in MIB can be used to stitch together individual 3-D/4-D datasets while preserving and adjusting the voxel size and bounding box coordinates, correspondingly.

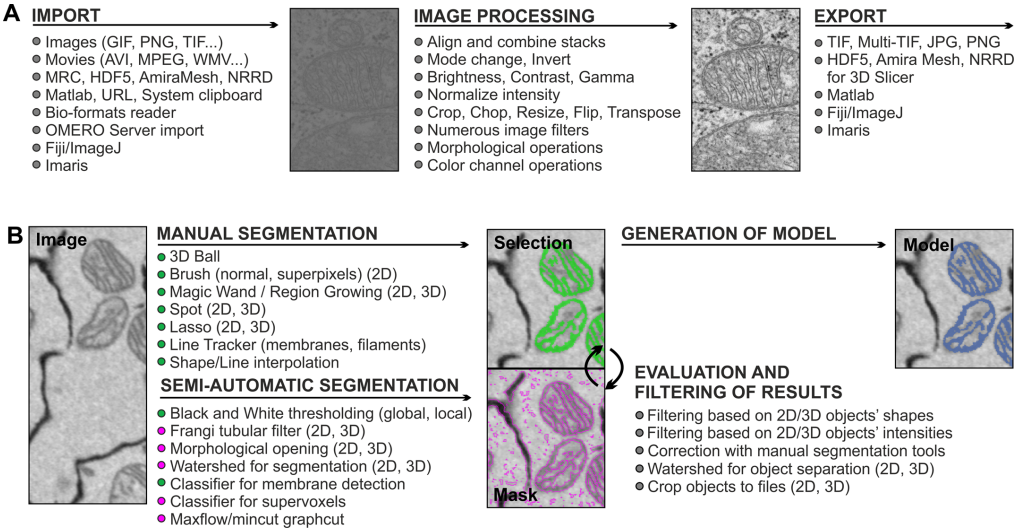

Fig 1. MIB recognizes a large array of imaging formats and offers many essential image processing tools. (A) Most common image formats can be imported to (left column) and exported from (right column) MIB. Most commonly used image processing tools are listed in the middle column (see MIB website for the full list). (B) Image segmentation workflow usually comprises a combination of several approaches. Datasets can be segmented iteratively using various manual and semiautomatic tools combined with quantification filtering of results in order to generate a model. Data in MIB are organized in four layers: Image (raw data), Selection (active layer for segmentation), Mask (an optional supporting layer for temporal storage of the segmentation results for evaluation and filtering), and Model (containing the final segmentation).

doi:10.1371/journal.pbio.1002340.g001

Multiple Manual and Semiautomatic Tools Are Gathered Together to Enable Segmentation of Various Specimens and Objects of Interest

Biological specimens vary greatly in regard to their shape, size, distribution, and intensity, thereby requiring multiple image segmentation procedures. The image segmentation in MIB combines manual and automatic approaches that may be further polished by filtering the segmented objects using quantification analysis (Fig 1B). This analysis can be easily performed on the shape or intensity properties of the resulting 2-D and 3-D objects. The main manual segmentation tools comprise of brush (normal or against superpixels [21] for faster selection), membrane click tracker (for tracing membrane profiles), magic wand and region growing, spot, and 3-D ball (S1 Video). When using these tools, the researcher interactively follows the modelling process slice by slice. To speed up the manual segmentation, MIB has shape and line interpolation algorithms that fill the gaps between objects drawn on two separated slices. The program also has several semiautomated routines, such as black and white thresholding, that can be applied to the entire dataset or to local selected (masked) area (S1 Video). Selection of such local areas is simple and usually done with the brush tool and the shape interpolation. This approach is especially useful for 3-D EM datasets, as the contrast differences are small and global thresholding (even with quantification filtering) is usually ineffective. The Frangi tubular filter [22] allows the detection of elongated, tubular structures in both 2-D and 3-D space, which is often useful for the segmentation of membranes or vessels.

The best suitable segmentation tool depends on the specimen, the imaging method, and the object of interest, and has to be found empirically. As an example, the brush tool was used for segmentation of individual Golgi cisternae (Fig 2A) and, in combination with shape interpolation, for segmentation of vesicles and ER (Fig 2A and 2B), while the line tracker tool was best suited for segmentation of microtubules (Fig 2B). Global thresholding and quantification filtering allow segmentation of high-contrast objects such as cytochemically stained ER (Fig 2C), whereas local thresholding combined with shape interpolation is better suited for segmentation of low-contrast objects such as different cell types in a tissue (Fig 2D). Use of semiautomated tools is essential for segmentation of large datasets and saves time, but as they are not applicable to all datasets, manual methods may be needed for segmentation of images with low-contrast variation, tightly packed areas, or heavily interconnected objects. Typically, modelling of a single dataset requires utilization of multiple segmentation methods. As an example, segmentation of different organelles in a densely packed mitotic cell, which has a high number of objects and is low contrast, is demonstrated by using basic MIB tools (Fig 2E; S1 Table).

Segmentation of Large Datasets Is Challenging and Requires a Special Set of Tools

Recent advances in both LM and EM have made it possible to acquire large volumetric datasets in a relatively easy manner. Those datasets may vary in size from moderately large volumes of up to 1,000 x 1,000 x 1,000 voxels to huge datasets of about three orders of magnitude higher (e.g., [23,24]). Manual segmentation of such datasets would be tedious, slow, and inefficient, and, as a result, a significant amount of high-quality data may stay unprocessed. Latest developments in image segmentation aim to minimize manual work by implementing automatic approaches of machine learning [25]. A promising example of the machine learning methods for image segmentation is the use of classifiers [7,23,26,27]. Classification starts by manual labelling of representative areas belonging to objects of interest and background. Next, by using various quantitative features (e.g., intensities, texture, and morphology) of the labelled area, the classifier can extend the local segmentation to cover the whole dataset. In some cases, the results can be improved when classification is combined with other methods, for example, the use of supervoxels with watershed [28] or graph-cut-based algorithms [29]. Usually, the use of supervoxels facilitates processing without significant degradation of segmentation results.

MIB currently includes two classifiers. The first one (called membrane detection) is based on a protocol developed by Kaynig et al. [27] for membrane detection from EM images. However, it is also suitable for segmentation of organelles from EM (S2 Video) and LM datasets (Fig 3A). We have used it to detect ER from time-lapse LM videos when, because of the gradient of the background intensities and variety of shapes (sheets and tubules), the standard thresholding methods are insufficient. The second classifier (called supervoxel classification) was designed to be fast and is based on classification of superpixels (2-D images) or supervoxels (3-D volumes) generated by the simple linear iterative clustering (SLIC) algorithm [21]. This classification uses only basic image intensity properties (e.g., minimal, maximal, average intensity, and cuts through the histogram) of each supervoxel and its neighbours. It is powerful in detection of objects that have distinct intensity features, for example, fluorescently labelled cells or organelles.

A graph-based semiautomatic segmentation in MIB starts by clustering of voxels to supervoxels [21] that are assigned to vertices of a graph, where the edges connecting vertices are defined by the difference between average intensities of the corresponding supervoxels. Once the user interactively labels the areas belonging to the target and background, MIB uses the

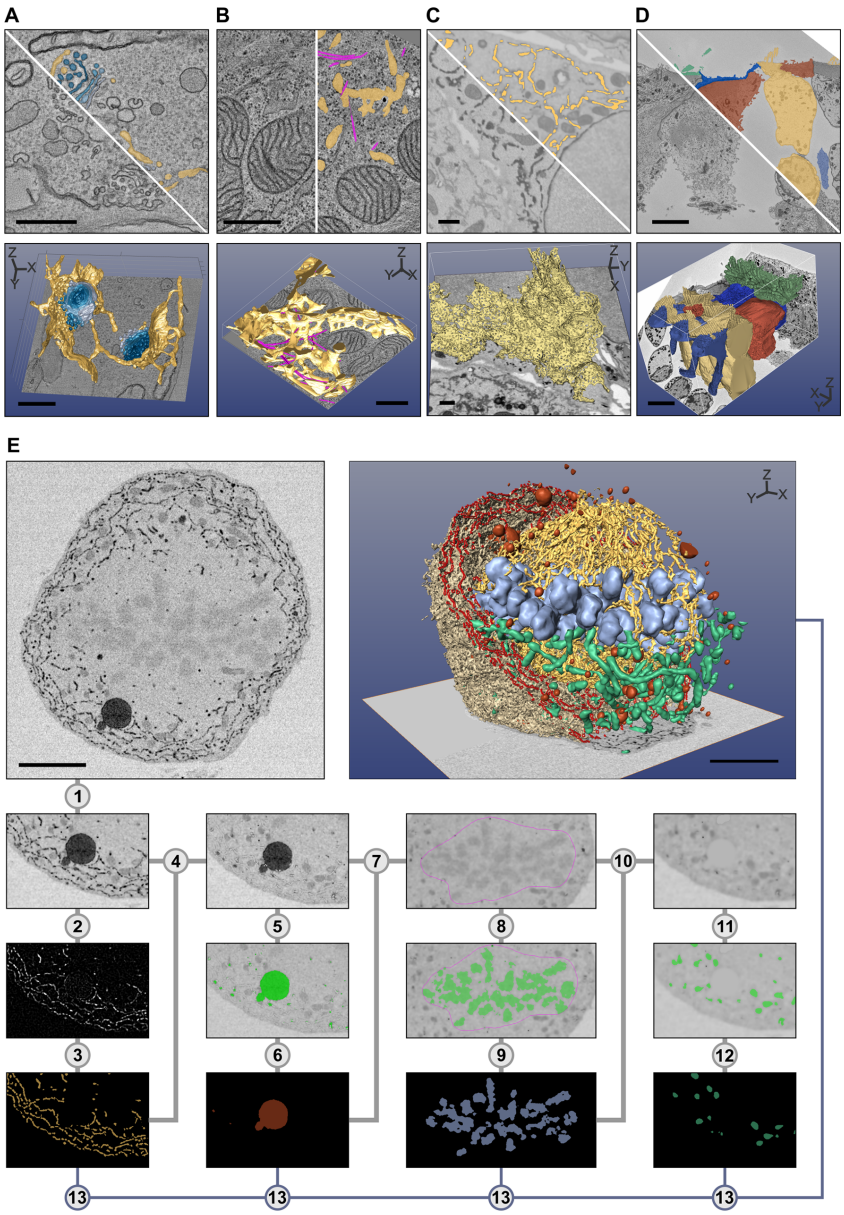
A
B
C
D
E
1
2
3
4
5
6
7
8
9
10
11
12
13
13
13
13

Fig 2. The selection of the best suitable tool for segmentation depends on specimen and object of interest. Five examples are given: in (A–D), the top row of each image shows a preprocessed slice and a segmentation overlay, and the bottom row shows the final 3-D visualization. Segmentation was done with MIB, and the 3-D rendering using different freeware (A–D) and commercial (E) software packages. (A) *Trypanosoma brucei* was chemically fixed and imaged with electron tomography (ET). Each Golgi cisternae (four shades of blue) was manually segmented using the brush tool, while ER and ER-derived vesicles (yellow) were segmented using a combination of the brush tool and shape interpolation. The resulting 3-D model was rendered directly in MIB. (B) A Huh-7 cell was high-pressure frozen and freeze-substituted, and a portion of the cell was subjected to ET [11]. ER (yellow) was segmented using the brush tool with shape interpolation and microtubules (magenta) using the line tracker tool. The resulting model was exported in the IMOD-compatible format and rendered in IMOD [6]. (C) A Huh-7 cell transiently expressing ssHRP-KDEL was cytochemically stained (dark precipitate) and imaged with a serial block-face scanning electron microscope (SB-EM) [11]. The ER network (yellow) was segmented semiautomatically using global black-and-white thresholding and further polished using quantification filtering [11]. The model was exported in the nearly raw raster data (NRRD) format and rendered in 3D Slicer [8]. (D) Mouse cochlea was perilymphatically fixed, and the sensory epithelium of the medial part of the cochlear duct was imaged with SB-EM [13]. Different cell types of the organ of Corti (inner hairs in green, outer hair cells in yellow, external rod in vermilion, internal rod in sapphire blue, and phalangeal part of the Deiters' cells in greyish blue) were segmented using local thresholding combined with shape interpolation and model rendered using 3D Slicer. (E) Stepwise segmentation workflow is needed to generate a 3-D model of a complex structure. A metaphase Huh-7 cell transiently expressing ssHRP-KDEL was cytochemically stained (dark precipitate in ER lumen) and imaged with SB-EM [10]. The modelling workflow for ER consists of 13 steps (S1 Table). For the visualization, the model was exported in the AmiraMesh format and rendered in Amira. Scale bars: A, B 500 nm; C, D, E 5 μm.

doi:10.1371/journal.pbio.1002340.g002

maxflox/min-cut algorithm [30] to perform the segmentation. For objects that have distinct boundaries, the watershed transformation [31] is extremely efficient. The marker-controlled watershed segmentation can be applied to detect both 2-D and 3-D objects. In practice, labelling the object(s) and background on a single slice allows segmentation of membrane-enclosed organelles in 3-D, as demonstrated for segmentation of the nucleus (Fig 3B and S2 Video) [14]. Objects that do not have clear boundaries and therefore would not qualify for segmentation using watershed can be preprocessed with the gradient filter to generate the required boundaries. Watershed can also be used to separate merged 2-D and 3-D objects even in anisotropic datasets [32], as exemplified by the separation of lipid droplets (LDs) (Fig 3C). For processing of large volumes, the chop tool can be used to divide the initial volume into smaller datasets for parallel segmentation on multiple workstations. Import of the chopped images then automatically assembles the segmented blocks together.

In automated segmentation, an essential part of the workflow is the estimation of accuracy of the applied method. As MIB was designed for segmentation of various objects coming from multiple imaging modalities, finding suitable parameters for accuracy metrics would be challenging, and the current version does not offer any. Therefore, MIB is most suitable for the processing of moderately large datasets, where the workflow can still be interactive and a researcher approves each step iteratively.

3-D Visualization and Quantification of Images and Models Are the Final Steps in Imaging

3-D visualization is an important part of any modelling. In contrast to segmentation, there are good 3-D visualization programs available already. While MIB can be used to visualize the models (Fig 2A), programs specialized to visualization might be more suitable. From MIB, the results of the segmentation (models) can be directly visualized using MATLAB engine (Fig 2A), Fiji 3-D viewer [33,34], and Imaris or saved in formats that are compatible with other visualization programs, i.e., IMOD (Fig 2B) [6,35], Amira (Fig 2E), or 3D Slicer (Fig 2C and 2D; Fig 3B and 3C) [8]. In other cases, the models may be saved in the TIF format for free packages such as BioImageXD [5], Drishti [36], or Vaa3D (Fig 4) [37].

For full utilization of the acquired data, the visualization should be complemented with numerical analysis. MIB provides several tools for numerical analysis of shapes (e.g., size, eccentricity, perimeter, and orientation) and intensities (e.g., minimum, maximum, and average) of 2-D and 3-D objects. These calculated parameters can either be used for filtering of objects as a part of the segmentation protocol or be exported to MATLAB and Microsoft Excel

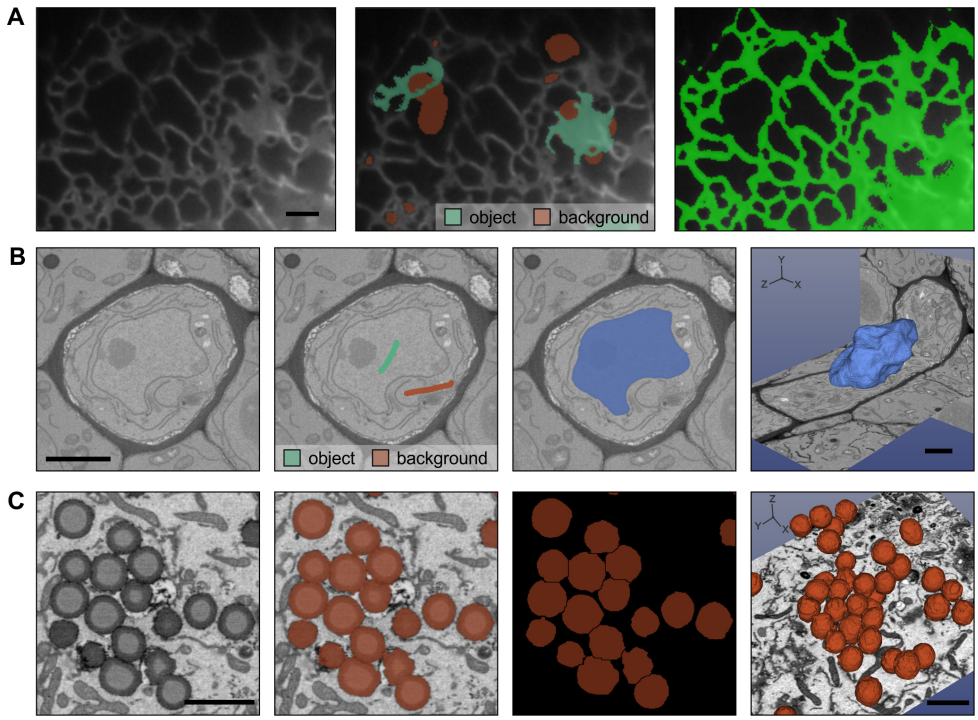

Fig 3. Semiautomatic image segmentation in MIB can dramatically decrease the time spent on modelling. (A) The Random Forest classifier was used to segment ER from wide-field time-lapse LM videos of Huh-7 cells. Labels were assigned (central image) to mark ER (Hsp47-GFP marker seen in green) and background (red), which were then used to train the classifier and segment ER throughout the time-lapse video (right image). (B) The semiautomatic watershed segmentation was used for segmentation of nucleus in the sieve element of *A. thaliana* root imaged with SB-EM [14]. Assigning of just two labels (green for nucleus and vermilion for background) was sufficient to segment the complete nucleus in 3-D (light blue, image on the right). (C) The separation of the fused objects using the watershed segmentation. The human U251MG astrocytoma cells were loaded with oleic acid producing a large amount of lipid droplets (LDs) (left image) that tend to form clusters. LDs were segmented using marker-controlled watershed; however, because of close proximity, most of the LDs appear merged (the second image). The object separation mode of the watershed tool was used to separate individual LDs for quantitative analysis (third and fourth images). The 3-D models were rendered with 3D Slicer [8]. Scale bars: 2 μm.

doi:10.1371/journal.pbio.1002340.g003

(Fig 4) for further statistical analysis. When needed, the automatic measurements can be complemented with the manual measurements of angles, distances, and radii (Fig 4) that also include an intensity profile of the image under the measured areas.

MIB Is a Freely Distributed Open-Source Program with a User-Friendly Graphical User Interface

MIB is written with MATLAB, which is available for all common computer operating systems (Windows, Linux, and Mac OS). As a high-level scientific programming language, MATLAB's program code is easy to understand, and, thus, its use for implementing image-processing routines is fast and cost efficient, not only for initial development but also for any enhancements of MIB with additional features, which can be achieved because of MIB's open-source code.

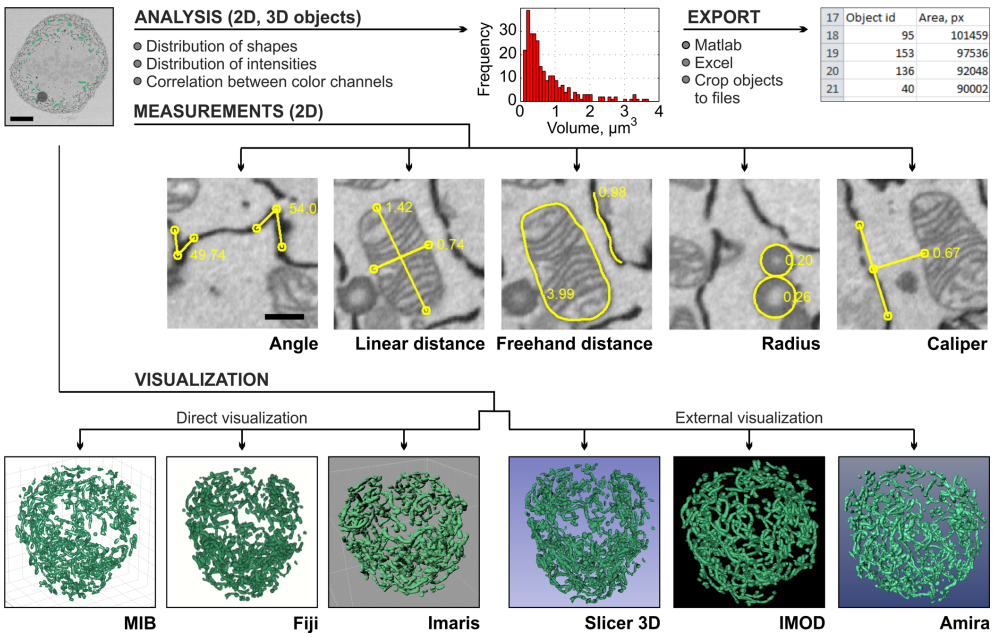

Fig 4. Quantification and visualization of results are the final steps of the imaging workflow. Generated models may be quantified to extract different parameters of the segmented objects and visualized using a number of programs. As an example, the volumes (μm^3) and numbers of segmented mitochondria were calculated (the plot in red). The quantifications results can either be plotted directly in MIB or exported to MATLAB or Microsoft Excel. The manual measurements of angles, distances, caliper, and radius complement automatic quantification. The visualization of the mitochondria model (in green) is demonstrated using six alternative programs (the lower row).

doi:10.1371/journal.pbio.1002340.g004

MATLAB has a large community of users who are developing and sharing algorithms using MATLAB Central File Exchange [38], an online library of over 20,000 user-contributed MATLAB files and toolboxes. Many of these submissions are dedicated to image processing and may easily be integrated into MIB, for example, as plug-ins. To support the development of plug-ins, MIB includes a description of its application programming interface that includes tutorials. MIB automatically detects all available plug-ins and initializes them during program start-up. For those researchers who are not familiar with MATLAB or who do not have a MATLAB license, we provide MIB as a stand-alone package (64-bit Windows and Mac OS) that can be freely downloaded and used on standard computers.

MATLAB itself is mostly a collection of functions that may be difficult to use by novices. To improve the usability, MIB includes an intuitive graphical user interface with standard components such as a menu, toolbar, and panels in the main window (Fig 5A). The toolbar and panels provide fast access to the most essential features described earlier, while the menu is used to access less frequently used actions. Some of the panels can be changed to adapt to the specific needs of a scientific project. MIB is designed to take the challenges of color-blind researchers into account, as we have selected a default color palette in which each color appears as a distinctive shade for color-blind users [39]. Alternatively, the default color palette can easily be replaced by one of the other color-blind-friendly ready assembled palettes [40] or each color

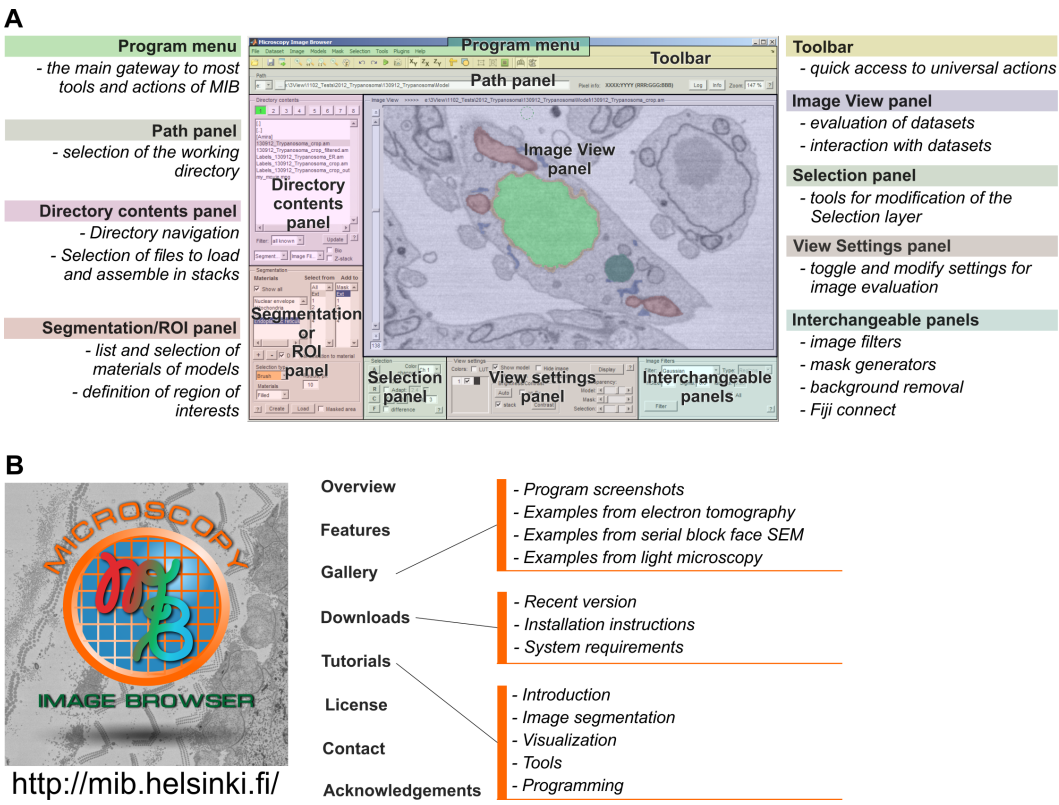

Fig 5. MIB has a user-friendly graphical user interface and is freely available from the website. (A) A screenshot of the MIB user interface. The program menu, toolbar, and panels are highlighted. A brief description of each element is provided. (B) A dedicated website includes direct links for software download and covers various topics and aspects of MIB functionality. *Image credit*: *Ilya Belevich*, *on behalf of MIB*.

doi:10.1371/journal.pbio.1002340.g005

can be individually selected. Each image-processing manipulation is logged, and the logs are stored with the data for future reference. To overcome accidental errors or to test most suitable tools and parameters during image processing, MIB has a flexible undo system that can erase recent changes made to the data or model. The number of undo steps for both 2-D and 3-D actions can be individually customized, thereby allowing optimized memory usage. MIB has a large variety of key shortcuts that improve segmentation performance and minimize unnecessary mouse movements. All details about the program usage are well documented and available from online tutorials on the MIB website (Fig 5B) [17] or from a built-in help system accessed through the Help menu or via dedicated buttons in each panel and auxiliary windows.

One of our aims during MIB development was to create a freely distributed open-source platform that would also allow a smooth cross talk with other image-processing programs. Depending on the program, the integration was accomplished with either direct data exchange or by data format compatibilities. The open microscopy environment (OMERO) image server

[41] can be directly accessed to download data, whereas the direct data exchange [33] with Imaris and Fiji [4] allows a large collection of their plug-ins to be used without generating space-consuming intermediate files. In cases where the direct link is not possible, the compatibility is achieved through use of common file formats. We anticipate that MIB will become a useful tool not only for biological researchers but also for mathematicians as a platform for implementation of new methods for image segmentation developed in MATLAB. We will also keep on upgrading and extending MIB with each new imaging project.

Supporting Information

S1 Methods. A description of cell lines, constructs, specimen preparation, and imaging conditions.
(DOCX)

S1 Table. Segmentation of a densely packed mitotic cell requires utilization of various segmentation tools provided by MIB (Fig 2E). First, the data was filtered using anisotropic diffusion filter (adapted from http://www.peterkovesi.com/matlabfns/) to eliminate the local noise while preserving the edges of the objects (step 1). As the ER network is extensive and makes contacts with nearly all other organelles, the removal of ER facilitates segmentation of all the other organelles later. Also in this example, the ER has a high contrast because of the luminal cytochemical staining making its segmentation feasible. In step 2, the morphological bottom-hat filter was used to temporally remove all large objects (such as mitochondria, chromosomes, and LDs). The Frangi vessel enhancement filter (adapted from http://www.mathworks.com/matlabcentral/fileexchange/24409-hessian-based-frangi-vesselness-filter) was then applied sequentially in the XY and ZX planes to segment ER tubules and sheet remnants (step 3: generation of the ER model). Next, the areas belonging to the ER in the anisotropically filtered image (from step 1) were replaced by the background color to generate degraded image without the ER (step 4). The resulting image was thresholded to select the dark singular objects such as LDs, peroxisomes, and lysosomes (step 5). To eliminate small objects, e.g., vesicles, the segmented areas were further smoothed using erosion followed by dilation in 3-D (step 6: generation of models for lysosomes, peroxisomes, and LDs). These areas were then replaced by the background color, similarly as in step 4 (step 7). As equatorially aligned chromosomes have contrast quite close to the mitochondria, global thresholding could not be used to discriminate them. Therefore, by using the brush tool and the shape interpolation, the central area of the cell was masked and thresholded to segment the chromosomes (step 8). The chromosomes were smoothed similarly as in step 6 (step 9: generation of the chromosome model). The chromosomal areas were replaced by the background color, and additional anisotropic diffusion filtering was applied (step 10). Segmentation of mitochondria was done by using the morphological image opening and thresholding (step 11), followed by smoothing and filtration of small objects (step 12: generation of the mitochondria model). The final model was assembled by combining all individual models and then visualized (step 13).
(DOCX)

S2 Table. List of all third-party tools and functions, including URL links.
(DOCX)

S1 Video. Basic segmentation tools of MIB. The video demonstrates the use of different basic image segmentation tools: (A) 3-D ball: modelling of LDs (00:04), (B) brush: modelling of Golgi stack (00:37), (C) brush with superpixels: segmentation of cells from LM (01:21), (C) magic wand: modelling of ER (01:50), (E) line tracker in 3-D: modelling of microtubules (02:22), (F) line tracker in 2-D and line interpolation: modelling of nuclear envelope (03:13),

(G) shape interpolation: modelling of mitochondria (04:04), and (H) global and local black and white thresholding: modelling of nuclear envelope with nuclear pores (04:38). Each clip contains screen capture taken during the segmentation process and the final 3-D visualization of the model. The starting point of each clip is given in brackets.
(MP4)

S2 Video. Advanced segmentation tools of MIB. The video demonstrates the use of advanced image segmentation tools: (A) random forest classifier: modelling of ER (00:01) and (B) watershed: modelling of a nucleus (01:23). Each clip contains screen captures taken during the segmentation process and the final 3-D visualization of the model. The starting point of each clip is given in brackets.
(MP4)

Acknowledgments

We would like to acknowledge the User Community of MATLAB-Central and the authors whose code was used during MIB development (S2 Table). We thank all beta testers for critical comments and suggestions. We also thank Mervi Lindman and Antti Salminen (University of Helsinki, Institute of Biotechnology, Electron Microscopy unit) for excellent technical assistance with ET and SB-EM specimen preparation, Cris de Graffenried and Kathy Schmidt (Max F. Perutz Laboratories, Vienna) for providing the fixed *T. brucei* specimen, and Yuki Ohsaki and Elina Ikonen (Faculty of Medicine, University of Helsinki) for providing lipid-loaded U251MG cells.

References

1. Knott G, Genoud C. Is EM dead? Journal of cell science. 2013; 126(Pt 20):4545–52. doi: 10.1242/jcs.124123 PMID: 24124192.
2. Lidke DS, Lidke KA. Advances in high-resolution imaging—techniques for three-dimensional imaging of cellular structures. Journal of cell science. 2012; 125(Pt 11):2571–80. doi: 10.1242/jcs.090027 PMID: 22685332; PubMed Central PMCID: PMC3706075.
3. Schneider CA, Rasband WS, Eliceiri KW. NIH Image to ImageJ: 25 years of image analysis. Nat Methods. 2012; 9(7):671–5. doi: 10.1038/nmeth.2089 PMID: 22930834.
4. Schindelin J, Arganda-Carreras I, Frise E, Kaynig V, Longair M, Pietzsch T, et al. Fiji: an open-source platform for biological-image analysis. Nat Methods. 2012; 9(7):676–82. doi: 10.1038/Nmeth.2019 PMID: WOS:000305942200021.
5. Kankaanpää P, Paavolainen L, Tiitta S, Karjalainen M, Päivärinne J, Nieminen J, et al. BioImageXD: an open, general-purpose and high-throughput image-processing platform. Nat Methods. 2012; 9(7):683–9. doi: 10.1038/nmeth.2047 PMID: 22743773.
6. Kremer JR, Mastronarde DN, McIntosh JR. Computer visualization of three-dimensional image data using IMOD. Journal of structural biology. 1996; 116(1):71–6. doi: 10.1006/jsbi.1996.0013 PMID: 8742726.
7. Sommer C, Straehle C, Kothe U, Hamprecht FA. Ilastik: Interactive Learning and Segmentation Toolkit. I S Biomed Imaging. 2011:230–3. PMID: WOS:000298849400054.
8. Fedorov A, Beichel R, Kalpathy-Cramer J, Finet J, Fillion-Robin JC, Pujol S, et al. 3D Slicer as an image computing platform for the Quantitative Imaging Network. Magnetic resonance imaging. 2012; 30(9):1323–41. doi: 10.1016/j.mri.2012.05.001 PMID: 22770690; PubMed Central PMCID: PMC3466397.
9. Belevich I, Joensuu M, Kumar D, Vihinen H, Jokitalo E. Microscopy Image Browser 2015. http://mib.helsinki.fi.
10. Puhka M, Joensuu M, Vihinen H, Belevich I, Jokitalo E. Progressive sheet-to-tubule transformation is a general mechanism for endoplasmic reticulum partitioning in dividing mammalian cells. Molecular biology of the cell. 2012; 23(13):2424–32. doi: 10.1091/mbc.E10-12-0950 PMID: 22573885; PubMed Central PMCID: PMC3386207.

11. Joensuu M, Belevich I, Rämö O, Nevzorov I, Vihinen H, Puhka M, et al. ER sheet persistence is coupled to myosin 1c-regulated dynamic actin filament arrays. Molecular biology of the cell. 2014; 25 (7):1111–26. doi: 10.1091/mbc.E13-12-0712 PMID: 24523293; PubMed Central PMCID: PMC3967974.

12. Anttonen T, Belevich I, Kirjavainen A, Laos M, Brakebusch C, Jokitalo E, et al. How to bury the dead: elimination of apoptotic hair cells from the hearing organ of the mouse. Journal of the Association for Research in Otolaryngology: JARO. 2014; 15(6):975–92. doi: 10.1007/s10162-014-0480-x PMID: 25074370; PubMed Central PMCID: PMC4389953.

13. Anttonen T, Kirjavainen A, Belevich I, Laos M, Richardson WD, Jokitalo E, et al. Cdc42-dependent structural development of auditory supporting cells is required for wound healing at adulthood. Scientific reports. 2012; 2:978. doi: 10.1038/srep00978 PMID: 23248743; PubMed Central PMCID: PMC3523287.

14. Furuta KM, Yadav SR, Lehesranta S, Belevich I, Miyashima S, Heo JO, et al. Plant development. Arabidopsis NAC45/86 direct sieve element morphogenesis culminating in enucleation. Science. 2014; 345 (6199):933–7. doi: 10.1126/science.1253736 PMID: 25081480.

15. Dettmer J, Ursache R, Campilho A, Miyashima S, Belevich I, O'Regan S, et al. CHOLINE TRANSPORTER-LIKE1 is required for sieve plate development to mediate long-distance cell-to-cell communication. Nature communications. 2014; 5:4276. doi: 10.1038/ncomms5276 PMID: 25008948.

16. Majaneva M, Remonen I, Rintala JM, Belevich I, Kremp A, Setälä O, et al. Rhinomonas nottbecki n. sp. (Cryptomonadales) and Molecular Phylogeny of the Family Pyrenomonadaceae. The Journal of eukaryotic microbiology. 2014; 61(5):480–92. doi: 10.1111/jeu.12128 PMID: 24913840.

17. Belevich I, Kumar D, Vihinen H. Microscopy Image Browser, on-line tutorials 2015. http://mib.helsinki.fi/tutorials.html.

18. Linkert M, Rueden CT, Allan C, Burel JM, Moore W, Patterson A, et al. Metadata matters: access to image data in the real world. The Journal of cell biology. 2010; 189(5):777–82. doi: 10.1083/jcb.201004104 PMID: 20513764; PubMed Central PMCID: PMC2878938.

19. Perona P, Malik J. Scale-Space and Edge-Detection Using Anisotropic Diffusion. Ieee T Pattern Anal. 1990; 12(7):629–39. doi: 10.1109/34.56205 PMID: WOS:A1990DK89400002.

20. Kroon DJ, Slump CH, Maal TJJ. Optimized Anisotropic Rotational Invariant Diffusion Scheme on Cone-Beam CT. Medical Image Computing and Computer-Assisted Intervention—Miccai 2010, Pt Iii. 2010; 6363:221–8. doi: 10.1007/978-3-642-15711-0_28 PMID: WOS:000287945600028.

21. Achanta R, Shaji A, Smith K, Lucchi A, Fua P, Susstrunk S. SLIC superpixels compared to state-of-the-art superpixel methods. IEEE Trans Pattern Anal Mach Intell. 2012; 34(11):2274–82. doi: 10.1109/TPAMI.2012.120 PMID: 22641706.

22. Frangi AF, Niessen WJ, Vincken KL, Viergever MA. Multiscale vessel enhancement filtering. Medical Image Computing and Computer-Assisted Intervention—Miccai'98. 1998; 1496:130–7. PMID: WOS:000082115900014.

23. Perez AJ, Seyedhosseini M, Deerinck TJ, Bushong EA, Panda S, Tasdizen T, et al. A workflow for the automatic segmentation of organelles in electron microscopy image stacks. Frontiers in neuroanatomy. 2014; 8:126. doi: 10.3389/fnana.2014.00126 PMID: 25426032; PubMed Central PMCID: PMC4224098.

24. Helmstaedter M, Briggman KL, Turaga SC, Jain V, Seung HS, Denk W. Connectomic reconstruction of the inner plexiform layer in the mouse retina. Nature. 2013; 500(7461):168–74. doi: 10.1038/nature12346 PMID: 23925239.

25. Sommer C, Gerlich DW. Machine learning in cell biology—teaching computers to recognize phenotypes. Journal of cell science. 2013; 126(Pt 24):5529–39. doi: 10.1242/jcs.123604 PMID: 24259662.

26. Breiman L. Random forests. Mach Learn. 2001; 45(1):5–32. doi: 10.1023/A:1010933404324 PMID: WOS:000170489900001.

27. Kaynig V, Fuchs T, Buhmann JM. Neuron Geometry Extraction by Perceptual Grouping in ssTEM Images. Proc Cvpr Ieee. 2010:2902–9. doi: 10.1109/Cvpr.2010.5540029 PMID: WOS:000287417502122.

28. Jones C, Liu T, Cohan NW, Ellisman M, Tasdizen T. Efficient semi-automatic 3-D segmentation for neuron tracing in electron microscopy images. Journal of neuroscience methods. 2015; 246:13–21. doi: 10.1016/j.jneumeth.2015.03.005 PMID: 25769273; PubMed Central PMCID: PMC4398646.

29. Lucchi A, Smith K, Achanta R, Knott G, Fua P. Supervoxel-based segmentation of mitochondria in em image stacks with learned shape features. IEEE transactions on medical imaging. 2012; 31(2):474–86. doi: 10.1109/TMI.2011.2171705 PMID: 21997252.

30. Boykov Y, Kolmogorov V. An experimental comparison of min-cut/max-flow algorithms for energy minimization in vision. IEEE Trans Pattern Anal Mach Intell. 2004; 26(9):1124–37. doi: 10.1109/TPAMI.2004.60 PMID: 15742889.

31. Couprie C, Grady L, Najman L, Talbot H. Power Watersheds: A Unifying Graph-Based Optimization Framework. IEEE Trans Pattern Anal Mach Intell. 2010. doi: 10.1109/TPAMI.2010.200 PMID: 21079274.

32. Mishchenko Y. A fast algorithm for computation of discrete Euclidean distance transform in three or more dimensions on vector processing architectures. SIViP. 2015; 9(1):19–27. doi: 10.1007/s11760-012-0419-9

33. Sage D, Prodanov D, J.-Y. T, Schindelin J. MIJ: Making Interoperability Between ImageJ and Matlab Possible. ImageJ User & Developer Conference; Luxembourg2012.

34. Schmid B, Schindelin J, Cardona A, Longair M, Heisenberg M. A high-level 3-D visualization API for Java and ImageJ. Bmc Bioinformatics. 2010; 11:274. doi: 10.1186/1471-2105-11-274 PMID: 20492697; PubMed Central PMCID: PMC2896381.

35. Nicastro D, Schwartz C, Pierson J, Gaudette R, Porter ME, McIntosh JR. The molecular architecture of axonemes revealed by cryoelectron tomography. Science. 2006; 313(5789):944–8. doi: 10.1126/science.1128618 PMID: WOS:000239817000036.

36. Drishti: volume exploration and presentation tool. http://sf.anu.edu.au/Vizlab/drishti.

37. Peng H, Ruan Z, Long F, Simpson JH, Myers EW. V3-D enables real-time 3-D visualization and quantitative analysis of large-scale biological image data sets. Nature biotechnology. 2010; 28(4):348–53. doi: 10.1038/nbt.1612 PMID: 20231818; PubMed Central PMCID: PMC2857929.

38. MathWorks. File exchange. http://www.mathworks.se/matlabcentral/fileexchange/.

39. Ichihara YG, Okabe M, Iga K, Tanaka Y, Musha K, Ito K. Color Universal Design—The selection of four easily distinguishahle colors for all color vision types. Proc Spie. 2008;6807. doi: 10.1117/12.765420 PMID: WOS:000255639200023.

40. Brewer C, Harrower M, Sheesley B, Woodruff A, Heyman D. ColorBrewer 2.0 2013. http://colorbrewer2.org/.

41. Allan C, Burel JM, Moore J, Blackburn C, Linkert M, Loynton S, et al. OMERO: flexible, model-driven data management for experimental biology. Nat Methods. 2012; 9(3):245–53. doi: 10.1038/nmeth.1896 PMID: 22373911; PubMed Central PMCID: PMC3437820.